Next Generation Mineral Mapping: Queensland Airborne HyMap and Satellite ASTER Surveys 2006-2008

Thomas Cudahy[1], Mal Jones[2], Matilda Thomas[3], Carsten Laukamp[4], Mike Caccetta[1], Rob Hewson[1], Andrew Rodger[1] and Mike Verrall[1]

CSIRO Exploration & Mining Report P2007 / 364

18 December 2008

[1] *CSIRO Exploration and Mining, ARRC, PO Box 1130, Bentley, WA 6102, Australia*
[2] *Geological Survey of Queensland, 80 Meiers Road, Indooroopilly, QLD 4068, Australia*
[3] *Geoscience Australia, GPO Box 378, Canberra, ACT 2601, Australia*
[4] *James Cook University, Economic Geology Research Unit, Townsville, QLD 4811 Australia*

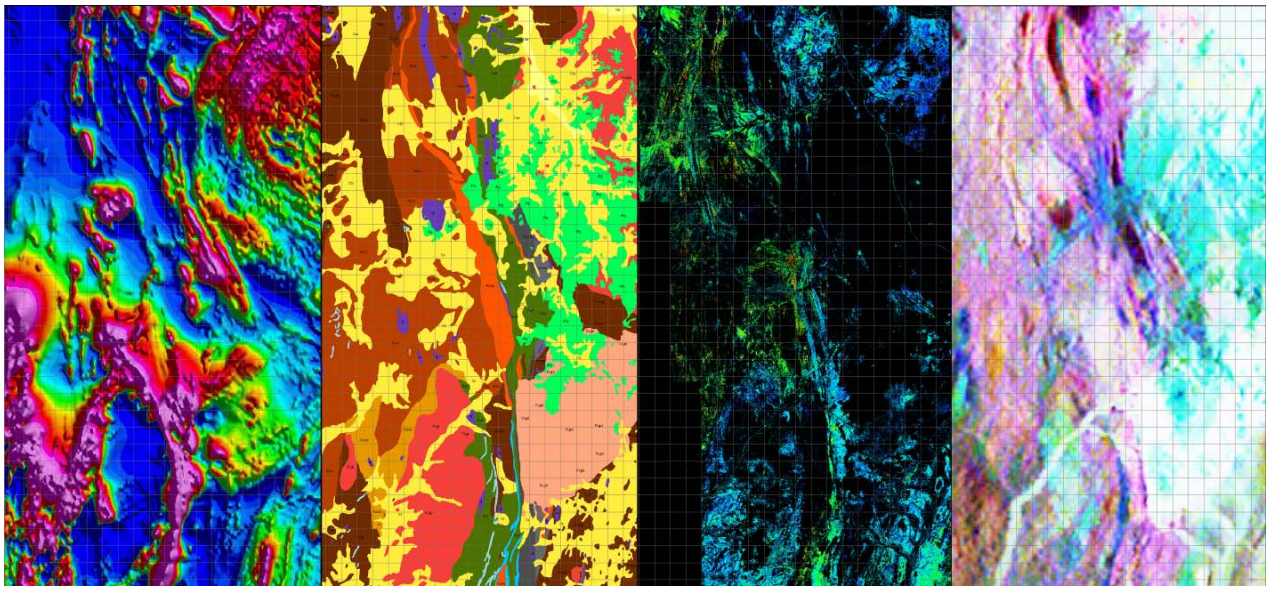

Queensland Government
Department of Mines and Energy

Australian Government
Geoscience Australia

JCU

Enquiries should be addressed to:

Dr Thomas Cudahy
Geologist and Group Leader for Minerals and Environmental Sensing
CSIRO Exploration and Mining
Australian Resources Research Centre (ARRC)
Street: 26 Dick Perry Avenue, Kensington, WA, Australia, 6151
Postal: PO Box 1130, Bentley, WA, Australia, 6102
phone: 61-8 6436-8630
mobile: 61-407-662-369
fax: 61-8 6436-8586
email: thomas.cudahy@csiro.au
http://www.csiro.au/csiro/content/standard/ps16a,,.html
http://www.em.csiro.au/NGMM

Copyright and Disclaimer

Important Disclaimer

Which way to go?

CONTENTS

SUMMARY

This two year collaborative project was established in July 2006 with the overall aim of developing, validating, evaluating and delivering a suite of publicly available, pre-competitive mineral mapping products from airborne HyMap hyperspectral imagery and satellite multispectral ASTER imagery. Moreover, it was important to establish whether these mineral maps would complement other precompetitive geological and geophysical data and provide valuable new information for enhanced mineral exploration by the Australian resources community.

The project was in several parts, including:

- Generating a suite of 15 mineral group maps of the Mount Isa Block (~500K km^2) from satellite multispectral ASTER imagery (~140 scenes);
- Stage 1 (2006-2007): acquisition and generation of a suite of 22 mineral abundance and mineral composition maps derived from airborne HyMap hyperspectral imagery (88 flight-lines) covering five structural/mineralised corridors (each about 15 km wide and 50 km long and covering 8250 km^2) across the Mount Isa Block; and
- Stage 2 (2007-2008): acquisition and generation of a suite of 29 mineral abundance and mineral composition maps derived from airborne HyMap hyperspectral imagery (204 flight-lines) covering four geological provinces (Mount Isa, Georgetown, Charters Towers and Hodgkinson) across geological/structural/mineralised corridors (each about 12 km wide and 50 km long and covering 16,000 km^2) in north Queensland.

The image processing methodology used to generate the current suite of mineral mapping products was designed to process multiple flight-lines/images based on a physical model that does not rely on levelling but instead normalises most/all of the inherent complications typical of remote sensing data (i.e. topographic shading, surface directional scattering, solar illumination, residual atmospheric/instrument effects). Furthermore, this methodology aims to be transferable, i.e. applicable to other similar data, and easily implemented by others wanting to reproduce similar products.

The mineral mapping processing methodology is based on the assumption that a given mineral abundance (or composition) is proportional to the normalised continuum-depth (wavelength, width, and asymmetry) of its diagnostic absorption bands, with zero abundance equal to no absorption developed. Currently, multiple masks are used to remove possible overlapping mineral absorptions and other effects like vegetation.

Even with this processing methodology, there remain significant product quality issues associated with instrument, atmospheric and pixel-unmixing effects. These include: (1) not all mosaics being seamless; and (2) masks/thresholds not transferable from one date of acquisition to another. These problems were caused by:

- Different HyMap instrument response functions for each airborne campaign producing different systematic residual effects;
- Water vapour (and other atmospheric) residuals with intensity proportional to the amount of water vapour. These generate along-track (flight-line), inter-block and inter-campaign errors;
- Small wavelength shifts (~1 nm) during the 2007 HyMap survey which produced along-track (flight-line) errors;

- Lichen, which affected the green vegetation masking;
- Vegetation mixing effects, both green and dry components, which affects the accuracy of the mineral abundances; and/or
- Environmental effects, including collecting airborne imagery while the ground was drying after rainfall.
- A new method for green vegetation masking was developed based on measuring leaf water rather than NDVI because of spectral complications associated with lichen. A new method was also developed to unmix the effects of green and dry vegetation. This method was validated and resulted in a new product for release, namely *Unmixed Al-clay content.* The other issues described above were characterised and where possible solutions implemented.

The mineral mapping products have been made available as JPEGs, ECW or TIFF by ftp via the www.em.csiro.au/NGMM webpage (~10 Gigabytes). The HyMap radiance and reflectance data, as well as the processed mineral map image files (BSQ format), are available from the Geological Survey of Queensland by external hard drive (~1 Terabyte).

At this stage, the associated product descriptions provide only a qualitative assessment of accuracy and what other effects may complicate the geoscience information. Ideally, all products require more quantitative error analysis, especially if the products are to be considered as standards. More objective methods are also required: (1) for establishing product threshold levels, especially with different instrument calibration; and (2) quality control of products in the processing chain, as there currently exists too much reliance on specialist interpretation.

As part of the mineral mapping product validation, over 200 field sites were visited and 500 samples collected and measured in the laboratory, including (1) reflectance spectra; (2) X-ray diffraction (XRD); (3) whole rock chemistry using X-ray fluorescence; (4) scanning electron microscopy including elemental analysis; (5) electron microprobe analysis of mineral chemical data; and (6) stable carbon isotopes. Among the key mineral information targeted in these studies were the (1) white mica (illite-muscovite) crystallinity based on the XRD 001 hkl peak width, which has been used by other workers as a measure of temperature/ pressure of formation; (2) white mica composition, especially the degree of Tschermak substitution (primarily driven by the tetrahedral Si-content); (3) and smectite clay composition. The validation work showed that all the tested remote mineral information products are significantly correlated with the ground validation data, including clay and iron oxide abundances and different clay mineralogies.

A mineral systems approach was used to appreciate the value of these mineral maps for exploration. That is, unlocking the value from these mineral maps is not simply by looking for the red bulls-eyes. Instead, mineral products need to be selected on the basis of critical parameters, such as what minerals are expected to develop as fluids migrate from source rocks to depositional sites and then to outflow zones with each associated with different physicochemical conditions (e.g. metasomatic metal budget, nature of the fluids, water-rock ratios, lithostatic pressure, pore fluid pressure, REDOX, pH, and temperature). Key products include: (1) opaques, which are a useful measure of reduced rock; and (2) white mica and Al-smectite compositions, which are useful for tracking chemical gradients; and (3) kaolin composition, which is useful for mapping regolith materials, especially “transported” from “*in situ*”. Two of the key messages are recognising mineral-chemical gradients and cross-cutting effects.

These principles were tested using a number of case histories including, (1) the Starra iron oxide Cu-Au deposit; (2) the Mount Isa Pb-Zn-Ag and Cu deposits; and (3) the Century Zn deposit, which are all in the Mount Isa Block. These case histories showed that the interpreted mineral alteration footprints of these mineral systems can be traced 10-15 km from the metal deposition sites, or in the case of Century, that no geobarometric gradient could be measured across the Termite Range Fault. In addition, it was found that most of the large open pit mines across all the Stage 1 and Stage 2 HyMap survey areas show the development of Si-poor white mica, irrespective of the age, host rock, commodity (Au or base metal) and deposit style. The recent Mount Dore molybdenum discovery announced by Ivanhoe is located along a structural pathway intersecting a REDOX gradient that is easily identified using the mineral maps and a mineral systems approach (see the figure below).

The technology transfer conducted in this project included: (1) five industry workshops (~120 partipants); (2) three in-house project team workshops; (3) 23 conference and other papers/publications; (4) two coordinated press releases with numerous uptakes by other media (local and national radio, newspapers and technical magazines); (5) numerous one-on-one company meetings; and (6) over 100 Gigabytes of mineral maps (>6500 maps at ~15 Mb each product) downloaded by ftp from the www.em.csiro/NGMM webpage. In summary, this project has shown that it is possible to generate accurate, large area mineral maps that provide new information about mineral system footprints not seen in other pre-competitive geoscience data and that the vision of a mineral map of Australia is achievable and of potential value for the resources industry.

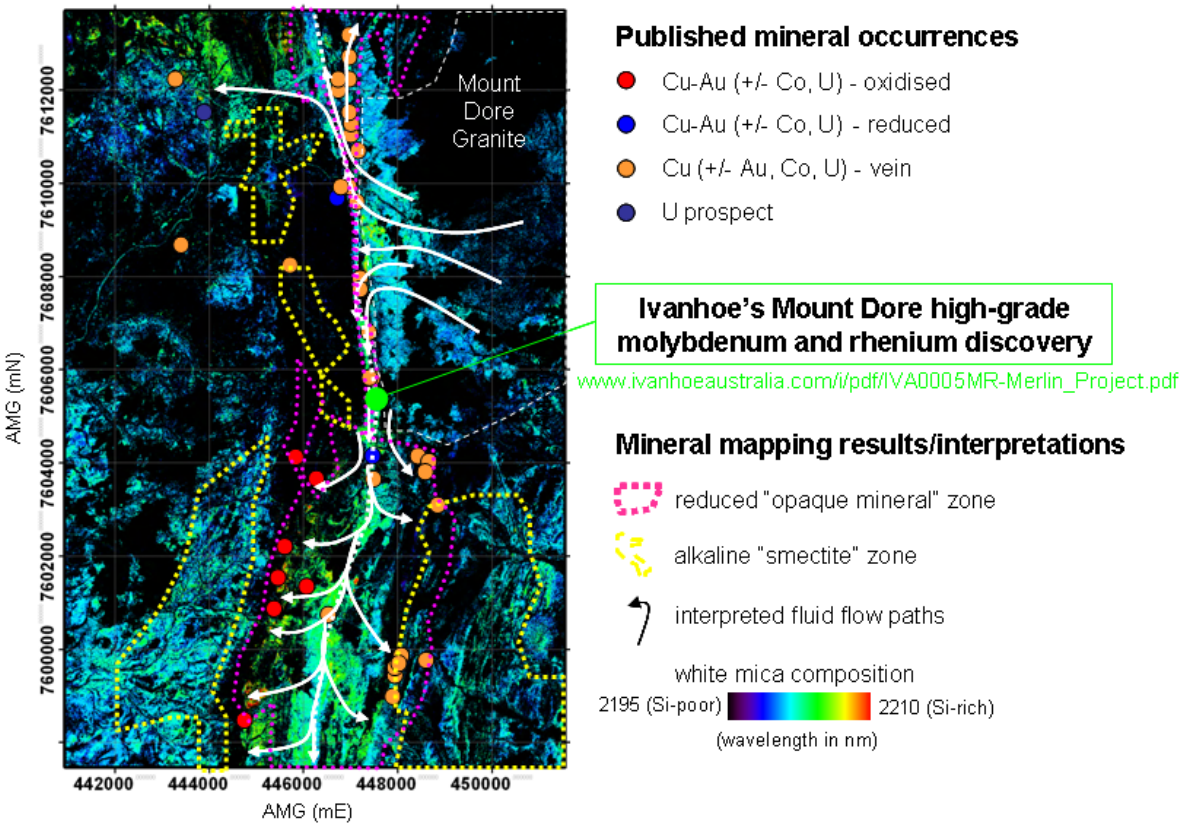

INTRODUCTION

Mineral Systems

A mineral system is defined as “all geological factors that control the generation and preservation of mineral deposits, and stress the processes that are involved in mobilising ore components from source, transporting and accumulating them in a more concentrated form and then preserving them throughout the subsequent geological history” (Wyborn and others 1994). The mineral system concept emphasises that although the volume of rock containing economic mineralisation is typically <1 km^3, the total system of fluid-rock interactions responsible for mineralisation can extend tens to hundreds of kilometres around the deposit. For example, hydrothermal white mica associated with hematite-chlorite has been recognised 80 km from the Olympic Dam Cu-Au-U deposit and supports a regional flow of oxidised fluids at about 1590 Ma (AUSGEO News, 2002). Recognising these “big footprints” is a key to unlocking the wealth of yet undiscovered economic mineralisation in Australia and beyond.

Geophysics will continue to provide valuable local- to regional-scale exploration information about facets of mineral systems (Goleby and others 2002; Blewett and Hitchman, 2004). From such data, the geological architecture, the plumbing systems that channel the mineralising fluids and the subsequent fluid-rock and/or fluid-fluid interactions can be modelled. This modelling of reactive transport processes can then be used to predict the 3D patterns of superimposed alteration geochemistry and mineralogy (Kühn, 2004).

However, inverted geophysical and numerical reactive transport models lack the critical component of mineralogy. Mineralogy is fundamental to all mineral deposits and is a barometer to the physicochemical drivers (temperature, pressure, REDOX, pH, chemical activities) of mineral systems. Access to spatially-comprehensive mineralogy would thus better constrain mineral system analysis by providing both seed and validation information. In addition, mineralogy could be used as a targeting tool by explorers to track big footprint alteration signatures and as a vector to economic mineral deposits which are commonly located at the steepest physicochemical gradients (Walshe and others, 2003).

Mineral Mapping

Mineral mapping is based on the specific interactions of geological materials with electromagnetic radiation anywhere across the wavelength region from 0.4 to 14 μm (or 400 to 14000 nanometres). This interaction occurs in just the top few microns of a given geological material and can be measured from the micron-scale in the laboratory with microscopes to the continental-scale with imaging satellites. The measured reflectance or emissivity data contains spectral features related to the mineral composition. Laboratory studies have shown that most of the major rock-forming minerals have diagnostic spectral absorptions (Lyon, 1965; Hunt and Salisbury, 1971; Clark, 1983, 1999), which can also include information about their physicochemistry (Duke, 1994; Crowley and Vergo, 1988).

The three main wavelength regions available for optical spectral sensing through the available atmospheric windows include:

- 400 to 1000 nm - visible to near infrared (VNIR);

- 1000 to 2500 nm - shortwave infrared (SWIR); and
- 7600 to 14000 nm - thermal infrared (TIR).

Materials with diagnostic absorption features in the VNIR include:

- Fe-, Mn-, Cr-, Mn-bearing minerals: e.g. hematite, goethite, jarosite, crocoite and pyrolusite;
- Minerals containing rare earth elements; and
- Vegetation: e.g. chlorophyll and leaf water.

Materials with diagnostic absorption features in the SWIR include:

- AlOH-bearing minerals: e.g. white mica (paragonite, muscovite, phengite, illite, pyrophyllite), kaolin (e.g. kaolinite, halloysite, dickite and nacrite) and smectite (montmorillonite and beidellite);
- Sulphates: e.g. alunite, jarosite and gypsum;
- Si(OH): e.g. opaline silica;
- Fe(OH)-bearing minerals: e.g. nontronite and Fe-chlorite;
- MgOH-bearing minerals: e.g. saponite, vermiculite, epidote, chlorites (Mg/Fe), biotite, phlogopite, antigorite, tremolite, actinolite, talc, serpentine and hornblende;
- Carbonate: e.g. calcite, dolomite, magnesite, ankerite and siderite;
- Vegetation components: e.g. cellulose, lignin, waxes, oils, proteins and leaf water; and
- Hydrocarbons: e.g. plastics and soil contaminated with fuel oil.

Materials with diagnostic absorption features in the TIR include:

- Silica: e.g. quartz and opaline silica;
- Feldspars: e.g. microcline, albite and anorthite;
- Pyroxenes: e.g. orthopyroxenes (such as enstatite) and clinopyroxenes (such as diopside);
- Garnets: e.g. almandine, spessartine, pyrope, andradite and grossular;
- Olivines: e.g. forsterite and fayalite;
- Carbonates: e.g. calcite, aragonite, dolomite, magnesite, ankerite, siderite and cerrusite ;
- Sulphates: e.g. jarosite, alunite and gypsum; and
- Vegetation: including composition and structure.

There is now a range of airborne and satellite spectral sensing systems available for geological applications. Figure 1 shows a selection of these which span the different wavelength regions and different spectral resolutions. Those with a hundred (or greater) spectral bands are typically called “hyperspectral” which enables the measurement of often small but diagnostic mineral absorptions. These hyperspectral systems include: the airborne VNIR-SWIR HyMap system (www.hyvista.com), which is well suited for mapping OH-bearing silicates (clays, chlorite, amphibole and talc) and iron oxides; and the SEBASS TIR system, which is useful for non-OH-bearing silicates (quartz, feldspars, garnet, pyroxenes and olivine) as well as carbonates. Multispectral imaging systems have fewer spectral bands (2-50) making them less useful for capturing the detailed spectral information content from minerals.

These systems include the Japanese satellite-borne ASTER (www.gds.aster.ersdac.or.jp) on board the US TERRA platform (http://terra.nasa.gov/), which now provides complete coverage of the Earth's land surface (three times over) for 14 spectral bands across the VNIR (3 bands @ 15 m pixel resolution), SWIR (6 bands @ 30 m pixel resolution) and TIR (5 bands @ 90 m pixel resolution). ASTER's multispectral resolution allows for the mapping of broad mineral groups, such as the abundances of iron oxides, AlOH "clays", MgOH/carbonates and SiO_2. Landsat Thematic Mapper has even poorer spectral resolution (seven bands) and so its ability to map mineralogy is all the more restricted.

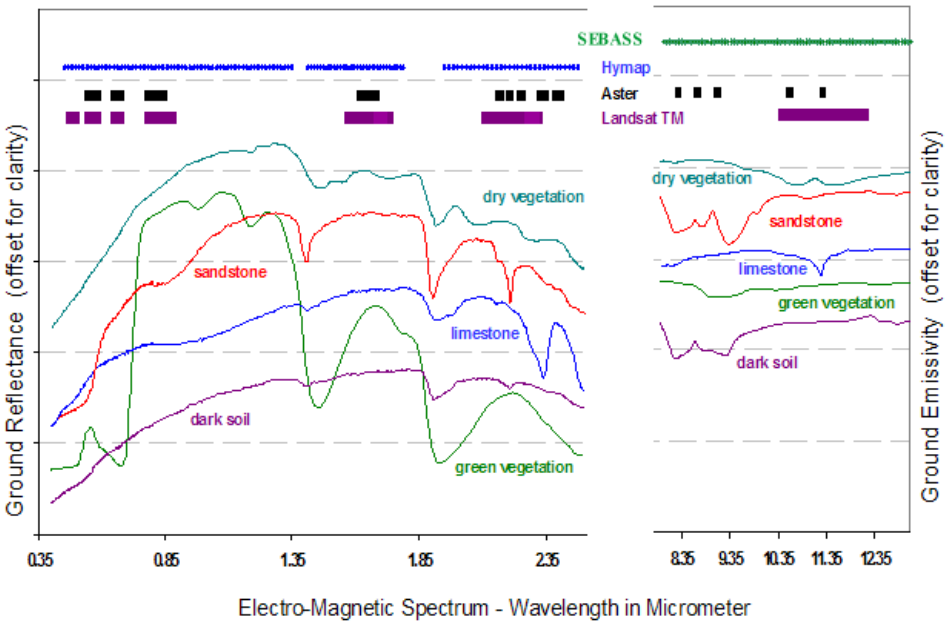

Figure 1. The band-passes of SEBASS, HyMap, ASTER and Landsat TM together with selected mineral and vegetation library spectra (from Hausknecht, *pers. comm*. 2003).

Global-scale mineral maps from remote sensing systems have now been generated for Mars using thermal infrared hyperspectral data collected from the Mars-orbiting Thermal Emission Spectrometer (*TES*- http://jmars.asu.edu/data/). In particular, the Martian TES sensor maps feldspar, pyroxene, olivine and quartz abundances. Other mineral maps of Mars are now being assembled using the recently launched Compact Reconnaissance Imaging Spectrometer (*CRISM* - http://crism.jhuapl.edu/), to include sulphates, kaolinite, illite/muscovite, chlorites, carbonate and water/ice (www.lpi.usra.edu/meetings/7thmars2007/pdf/3270.pdf). However, the opportunity to generate global scale mineral maps of the Earth's land surface has yet to be realised.

The opportunity for hyperspectral mineral mapping of the Earth to date has largely been left to the private sector, which has impacted on data access (cost and timeliness), reliability of sensor performance, cross-calibration of sensors/data and standardisation of derived geoscience products. This lack of coordination/standardisation has resulted in many users being unsatisfied, especially as these non-standard geoscience products have often been inaccurate and not reproducible. However, in the next seven years there will be a suite of hyperspectral imaging satellites coming on stream (see http://www.isiswg.org/), delivering global-scale publicly available radiance/reflectance data. Combined with the airborne systems, it is imperative that solutions to these challenges be found if this technology is to be valued alongside airborne magnetic and other pre-competitive geoscience data by the

resources industry. However, the greatest challenge to successful implementation of mineral mapping in the resources industry is the establishment of viable mineral system models that link exploration criteria to spectrally mappable mineralogy (Bierwirth and others, 2002; Cudahy and others, 2005).

Next Generation Mineral Mapping

Next Generation Mineral Mapping (NGMM) is a CSIRO Minerals Down Under initiative aimed at addressing the challenges of delivering a new range of pre-competitive geoscience information to the Australian resources industry (http://www.csiro.au/science/ps16a.html; http://www.csiro.au/org/MineralsDownUnderOverview.html). The objective is to develop remote sensing capabilities in collaboration with the government geological agencies across Australia. The vision is a comprehensive suite of web-accessible, seamless, accurate maps of mineral abundances and mineral physicochemistries of the Australian continent at high spatial resolution (<30 m pixels or >1:25,000 scale mapping). This requires suitable:

- Airborne and satellite hyperspectral imaging systems that capture the full complement of spectral-mineralogy (visible to thermal infrared wavelengths);
- Methods and systems for handling, calibrating and processing large volumes (terabytes) of multi-scene imagery;
- Validated, pre-competitive geoscience product standards with error assessments;
- Web-based delivery tools/systems;
- Mineral system models that relate spectral mineralogy to geological (and environmental) processes to help target footprints larger than the deposits themselves; and
- Technology transfer through case histories, workshops and seminars.

As a step towards achieving this vision, a two year project was established in July 2006 between the Geological Survey of Queensland (GSQ) (www.dme.qld.gov.au/mines/hyperspectral.cfm) and CSIRO Exploration and Mining (www.csiro.au/science/ps16a.html) with close collaboration with Geoscience Australia (www.ga.gov.au), James Cook University and Curtin University. The project was supported by the Queensland Government's Smart Exploration/Mining initiatives (www.dme.qld.gov.au/zone_files/geoscience_pdf/webbrochure.pdf), CSIRO Minerals Down Under (MDU - www.csiro.au/science/MineralsDownUnder.html), the Cooperative Research Centres for Predictive Mineral Discovery (pmd*CRC) and Landscape Environment and Mineral Exploration (LEME) and HyVista Corporation (www.hyvista.com). Data resources for the project included 25000 km^2 of airborne HyMap imagery (~250 flight-lines at 5m pixel resolution), over 100 ASTER scenes and associated ground and laboratory validation data collected along major structural/geological corridors across Queensland. The project follows a similar mineral mapping demonstration in Western Australia where 28 flight-lines of HyMap data spanning the 1:100 000 scale Kalgoorlie-Kanowna region were processed to generate a suite of seamless, validated maps of regolith and primary rock mineralogy (Cudahy and others, 2005).

The surface mineral mapping initiative complements the Auscope National Virtual Core Library (ANVCL) project which is another MDU initiative supported by the Federal government NCRIS (www.ncris.dest.gov.au/) program through Auscope (www.auscope.org.au/). The ANVCL will deliver to each Australian State and Territory

geological survey, a full-spectrum (0.4 to 14 μm) drill core/chip HyLogging™ system that will be used to measure their archives of drill. The resulting mineralogy interpreted from the spectral measurements will be delivered via the web (nvcl.csiro.au), a new suite of publicly available geoscience information of "subsurface" mineralogy. Linking the ANVCL subsurface mineralogy with the NGMM surface mineralogy is the objective of the WA Centre of Excellence for 3D Mineral Mapping.

OBJECTIVES

The overall aim of this collaborative project was to support the objectives of the Smart Mining – Future Prosperity programs and the Queensland Smart Exploration Development initiative by acquiring new geoscientific data. In particular, remote mineral mapping was targeted within priority and frontier regions of the State to attract increased exploration investment. This project is focused on the Mount Isa, Georgetown, Charters Towers, Drummond Basin and Palmerville Fault areas where remote mineral mapping data were collected to complement publicly available pre-competitive geoscience data, including airborne geophysics and geological mapping. The selected areas targeted major faults, seismic transects and prospective mineralised ground.

Specific objectives included:

- Delivering a new GIS-compatible suite of pre-competitive mineral maps;
- Validation of the mineral maps through ground sampling and associated analyses;
- Assessment of the geological/exploration significance of the mineral maps, especially for better understanding of the published geology and distinguishing previously unrecognised alteration zonation associated with mineral deposits (e.g. Cu, Pb, Zn, Ag, Au, and U);
- Technology transfer of NGMM capabilities/products to the geological survey geoscientists and publicly;
- Improving web-based delivery systems for better public access to pre-competitive mineral information products; and
- Attracting investment to Queensland by providing valuable new geoscience information to explorers.

EXPECTED DELIVERABLES

The proposed HyMap and ASTER products are similar to those generated for the Kalgoorlie-Kanowna 1:100 000 scale mapsheet (Cudahy and others, 2005). Specific deliverables include:

- HyMap radiance-at-sensor data (without atmospheric corrections);
- HyMap atmospherically corrected radiance-at-sensor data, e.g. apparent reflectance;
- Approximately 15 processed mineral information products generated from the airborne HyMap data;
- Associated metadata descriptions for all remote sensing products;
- All mineral maps to be presented as GIS-compatible maps (ArcMap and MapInfo). All data to conform to UTM/GDA94 map projection with format suitable for ERMapper (www.ermapper.com/) and ENVI (www.ittvis.com/ProductServices/ENVI.aspx)

software. However, the data supplier of the HyMap data, HyVista Corporation, is only able to provide UTM/WGS84 map projection for radiance at sensor and reflectance products. Given the similarity between these datums (within 5 metres), all data maps were provided as UTM/WGS;

- Collection and analysis of at least 300 ground-validation samples. Analyses to comprise spectral measurements of all samples, and XRD and or XRF/ICPMS/LOI on approximately half of the samples; and
- Final report including mineral map interpretations.

STRATEGY

The overall strategy to achieve the project objectives included:

- Pursuing image processing methods that generate seamless, accurate, standardised, transferrable mineral maps. That is, the detectable sensitivity of products, such as kaolinite abundance generated for a map at Mount Isa, should be the same as those for Kalgoorlie;
- Testing the effectiveness of new vegetation unmixing algorithms;
- Validating through ground and laboratory analysis, a selection of those remote sensing geoscience information products not tested in earlier studies, e.g. Cudahy and others (2005);
- Investigating a selection of key mineralogical issues that are potentially of value for understanding the geology of north Queensland. These include:
    - Illite crystallinity as a potential geobarometer for metamorphic grade following on from the XRD studies in the Mount Isa region by Golding and others (2006);
    - Tschermak substitution in white mica ($Al \leftrightarrow [Si+(Fe^{2+}/Mg)]$) for measuring chemical gradients associated with contrasting conditions in hydrothermal systems; and
    - Smectite clay mineralogy, especially identifying beidellite from montmorillonite, as these have different cation exchange capacities available to plants.
- Generating mineral product descriptions which describe the qualitative accuracy and how each was generated so that others can reproduce the same results; and
- Building case histories that demonstrate a mineral systems approach to using mineral mapping products in combination with geophysics and other pre-competitive geoscience data for targeting economic mineralisation.

DATA AND COVERAGE

Airborne HyMap sensor

The HyMap™ (Hyperspectral Mapper) system is an operational, airborne imaging VNIR-SWIR spectrometer designed and built by Integrated Spectronics Proprietary Limited (ISPL) (www.intspec.com) and commercially operated by HyVista Corporation (www.hyvista.com). The features of the HyMap system include:

- Operates in aircraft equipped with standard aerial camera ports;
- Whiskbroom imaging;
- 3-axis gyro-stabilised platform with C-migits IMU/GPS system for derivation of parameters required for precise geometric rectification (+/- 2 pixels with a geo-referenced digital elevation model applied);
- 450-2500 nm spectral coverage;
- 126 spectral bands across three wavelength regions. There are 62 bands in the VNIR region from 450-1400 nm, 32 bands in the SWIR-1 region from 1400-1900 nm and 32 bands in the SWIR-2 from 1900 to 2500 nm;
- Bandwidths of 10-20 nm;
- High signal to noise ratio for all bands (>400:1 for a 60% reflectance standard illuminated at mid latitude summer conditions);
- 512 pixel swath;
- 3-10 m spatial resolution (depending on flying height);
- 61.3 degrees swath width; and
- On-board radiometric calibration (gain and dark current) collected for each scan line.

Airborne HyMap data coverage

The HyMap data was acquired in two stages in 2006 and 2007. Stage 1 was flown in September/October 2006 and focused on the Mount Isa region while Stage 2 was collected in August 2007 and was more widespread across northern Queensland (Figure 2) and included the Georgetown, Hodgkinson, Pajingo as well as the Mount Isa area. Stage 1 covered 8250 km^2 and Stage 2 16,000 km^2 from along corridors approximately 15 km wide (~10 overlapping HyMap flight-lines). The details of the areas/blocks covered by the two HyMap surveys are provided in Appendix 1 and the associated geometric datums for each of the HyMap Blocks are provided in Appendix 2. Note also that HyVista Corporation re-collected Stage 2 Mount Isa Block A^I in August 2008 because of technical problems with the original data. The dates and times of each flight-line are provided in Appendix 3 and the Bureau of Meteorology weather records for the Stage 1 survey over Mount Isa are provided in Appendix 4.

For each survey, calibration of the HyMap sensor is conducted by HyVista Corporation. This means that the centre wavelengths and full-widths at half height (FWHH) for each band are different for each survey. Appendix 5 provides a listing of the band centres for Stages 1 and 2, together with the differences in wavelength between them. Note that the spacing between spectral bands (~spectral resolution) is typically ~14 nm for the VNIR and SWIR 1 (450-1800 nm) and ~18 nm for the SWIR 2 (2000-2500 nm).

Prior to HyMap data acquisition, the expected geoaccuracy of the airborne data was:

- 3 pixels between overlapping flight-lines for the area of overlap; and
- 50 m absolute.

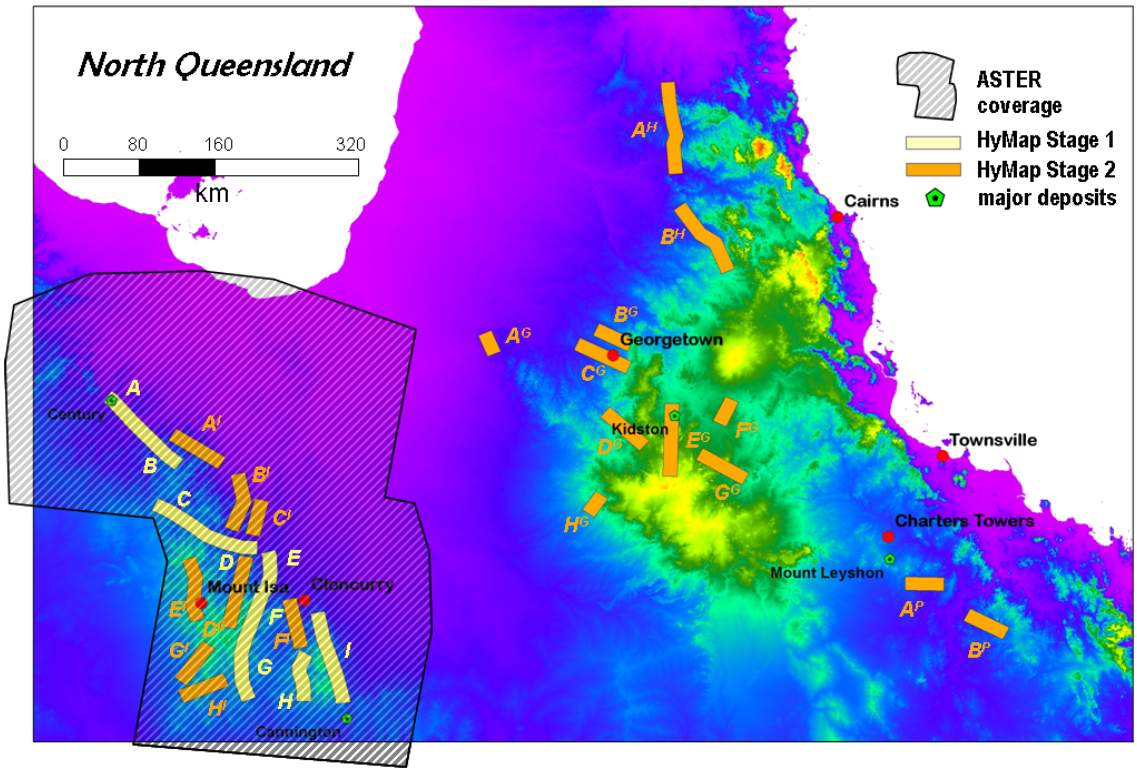

Figure 2. Location map of the airborne HyMap and satellite ASTER coverage across north Queensland. HyMap block numbers are shown with superscripts for Stage 2 (see Appendix 1 for details).

Satellite ASTER sensor

The satellite-borne ASTER multispectral VNIR-SWIR-TIR sensor on board the TERRA platform (Yamaguchi and others, 2001) was successfully launched into a sun-synchronous orbit in December 1999 with a 10.30 AM equatorial crossing time. ASTER acquires imagery within a 60 x 60 kilometre scene area from three 15 m pixel resolution VNIR channels (bands 1-3), six 30 m pixel resolution SWIR channels (bands 4-9) and five 90 metre pixel resolution TIR channels (bands 10-14) (Yamaguchi and others, 2001). The VNIR and SWIR modules consist of push-broom detectors arranged as a 5000-element linear array and 2048-element staggered arrays, respectively, while the TIR uses a whiskbroom detector with a scan mirror for across track sampling. The VNIR and SWIR are available in 8-bit dynamic range and the TIR in 12-bit quantisation. There is also a backward looking VNIR telescope that provides stereo coverage and enables the generation of digital elevation models (DEM) with a base-to-height ratio of 0.6. ASTER-derived 30 m pixel resolution DEMs were sourced from the USGS (http://edcimswww.cr.usgs.gov/pub/imswelcome) and were generated for specific areas.

The ASTER images for the Mount Isa area (Figure 2) were assembled from the Geoscience Australia archive (www.ga.gov.au/acres/prod_ser/aster.jsp). Approximately 140 ASTER Level 1B (radiance-at-sensor) images were required to cover the entire Mount Isa Block. These were sourced from many different dates of acquisition over a five year period and from different times of the year. The main factor in determining a suitable scene was the lack of cloud cover followed by high sun angle (summer). Level 1B data were chosen over any Level 2 products as further correction is required for additive effects (in addition to standard

corrections), especially atmospheric scattering in the VNIR and instrument cross-talk effects in the SWIR.

SWIR Cross-talk effect

The SWIR crosstalk effect represents a leakage of photons from one detector element to other detector elements producing an additive increase in photons for these other detector elements (Iwasaki and others, 2001). This cross-detector leakage is most pronounced in bands 5 and 9, mainly because these detectors receive relatively few photons and their neighbour, band 4, generally receives the most photons. However, this leakage affects all SWIR bands. Similar but significantly smaller instrument additive effects have also been detected in the VNIR bands during ASTER imaging of the moon (Hugh Keifer, USGS, *pers. comm*., 2003).

A spatially-dependent correction for SWIR crosstalk has been developed by Iwasaki and others (2001) and has since been incorporated by the Japanese ASTER Ground Data System (GDS) at ERSDAC (www.ersdac.gov.jp) as part of its L1A to L1B pre-processing and is now also available from the USGS. This method involves using a defocused band 4 to provide a spatially-dependent estimate of the crosstalk effect. The related software is also available from the GDS.

All of the ASTER scenes from Mount Isa were processed using the GDS SWIR cross-talk correction software prior to implementing CSIRO's cross-calibration software (discussed below).

Airborne geophysics

Publicly available airborne gamma radiometric and magnetic data were used for comparison with the mineral maps. These data (www.geoscience.gov.au/gadds) were collected at 200-400 m line spacing and resampled/interpolated to 50 m pixels (Jayawardhana and Sheard, 2000).

Field sampling

Approximately 600 field samples from 212 field localities were collected from most of the HyMap Blocks during three field campaigns. Information acquired at field site included: the geology type, percent-exposure (rock:soil:vegetation); field photographs (close up and overview) as well as structural and landform characteristics. The field samples included weathered and fresh rocks as well as soils sampled from the top 10 mm. The GDA94 coordinates of these field sites together with their associated analytical measurements are provided in Appendix 6 and from the web (http://www.em.csiro.au/NGMM).

Laboratory Analyses

Reflectance

A single beam, Analytical Spectral Devices (ASD) FieldSpec Pro spectrometer (www.asdi.com) was used to measure the 350 to 2500 nm bi-directional reflectance of field samples. A 100% reflectance Spectralon™ panel (http://www.labsphere.com/) was used as

the reference standard, with both the target and reference illuminated in series, either (1) under the same optical geometry (off the specular angle) with a 1000 W Quartz Halogen light source; or (2) using the contact-probe attachment which has its own illumination source.

Emissivity

The emissivity of field samples was measured using a portable FTIR (Fourier transform infrared) spectroradiometer designed and built by Designs and Prototypes (Hook and Kahle, 1996; Korb and others, 1996). This instrument measures emissivity in the 3-5 and 8-14 µm wavelength regions at approximately 6 wavenumber resolution. The area sensed is approximately 20 mm diameter or less. Measurements of hot and cold blackbodies establish calibration to radiance at sensor. A correction for background or sky down welling irradiance is implemented using a brass reference plate to retrieve absolute surface radiance. The method for temperature-emissivity separation and extraction of surface emissivity involved an assumption for an emissivity at the Christiansen Frequencies (e.g. where emissivity ~ 1.0).

X-Ray Fluorescence

Samples were sent to a commercial laboratory (Ultra Trace Pty Ltd) for routine XRF analysis.

X-Ray Diffraction

Laboratory X-Ray Diffraction (XRD) analyses of samples was undertaken using a Philips X'Pert MPD. Prior to April 2008 the system was fitted with a Cu tube operated at 40kV, 40mA and a curved Graphite Monochromator. Since April 2008, the system has been fitted with a Co tube operating at 40kV, 40mA and an iron filter. Samples were prepared as random powders (nominally 80% <75 µm) and back mounted into circular holders. Samples were typically scanned from 2-70˚ 2θ at with a 0.02˚ or 0.03˚ 2θ size increments and 1 or 2 seconds counting time/increment. More detailed analysis involved slower scan rates over a narrower angle range (e.g. for clays – see below). Where quartz was identified in the diffraction patterns, this was used as an internal standard to correct for any instrumental shifts in 2θ position due to sample displacement.

Mineral interpretation

First pass mineral identification was facilitated using the CSIRO XPLOT software program (Raven and Self, 1988). This is based on the search-match of peak positions with respect to the ICDD mineral standards library (http://www.icdd.com/).

Clay identification

The samples for detailed clay analysis (i.e. Al-smectite mineralogy) were mixed with a 0.6% calgon (sodium hexametaphosphate) solution and allowed to settle. The clay fraction was then removed by pipette and placed on a ceramic disk for XRD. The collected clay fraction was then dried on the circular mounts before being Li saturated and heated overnight at 200ºC. Samples were then treated with ethylene glycol and XRD measured at a slow scan rate.

Oriented air dried untreated samples were measured on the XRD. The samples were then treated with ethylene glycol and analysed again. A modified Green-Kelly test was used to

differentiate montmorillonite from beidellite. In this test, Li-saturated clay is heated to 200ºC and then treated with ethylene glycol. After heating, all smectites collapse to approximately 10Å, and after subsequent ethylene glycol solvation, beidellite expands to 17Å whereas the collapse of montmorillonite is irreversible (Greene-Kelly, 1953). There is some concern that interactions with the sodium in the glass used as a substrate may have affected the results and lead to only a partial collapse of the montmorillonite (Volzone, 1992).

Scanning electron microscope

Selected samples were examined using a Philips (now FEI) XL40 controlled pressure SEM (scanning electron microscope) fitted with and EDAX EDS (energy dispersive X-ray spectrometer). The SEM was typically operated at chamber pressure of between 0.1mbar and 1.0mbar and an accelerating voltage of 30kV.

Electron microprobe

Samples for electron microprobe work were coated with a conductive carbon layer approximately 25nm thick using a Dynavac high vacuum coating unit. The microprobe used was a Cameca SX50 fitted with 3 WDS (wavelength dispersive spectrometers).

IMAGE PROCESSING

The image processing strategy for generating the remote sensing image geoscience information products includes:

- Ensuring that data are well calibrated to radiance-at-sensor or surface (apparent) reflectance (quality check or QC);
- Avoiding any levelling and statistics-based methods as these introduce undesired scene-dependencies, such that image products from different areas are not comparable;
- Using physics-based reduction models and removing complicating effects (additive and/or multiplicative) in their order of development (e.g. instrument first followed by atmospheric, and then surface effects) through either offsets or normalisation;
- Assuming that mineral abundances/compositions/crystallinity are proportional to diagnostic absorption depths/wavelengths/widths, respectively;
- Capturing the diagnostic absorption information involves using:
    - continuum band normalisation (ratios); and/or
    - fitted polynomials;
- Assuming that when the diagnostic mineral absorption is not evident, then that mineral is not present. That is, the “background” to a given mineral abundance is defined as the pixel-spectrum’s absorption hull. Pure pixels (100% abundances) are gauged using library mineral data (particle size >250 μm);
- Assuming linear mixing at the pixel-scale for mixtures of soil/rock with vegetation (dry and green), which enables rescaling of apparent to absolute mineral abundances.
- Increasing the accuracy of a given mineral interpretation/abundance by using multiple diagnostic absorption features; and
- Removing any complications such as spectrally overlapping materials by applying set thresholds.

Figure 3 presents a schematic diagram of the basic image processing steps from radiance@sensor data through to the final GIS-compatible products (geoTIFs, JPGs). More detail is provided in the next sections.

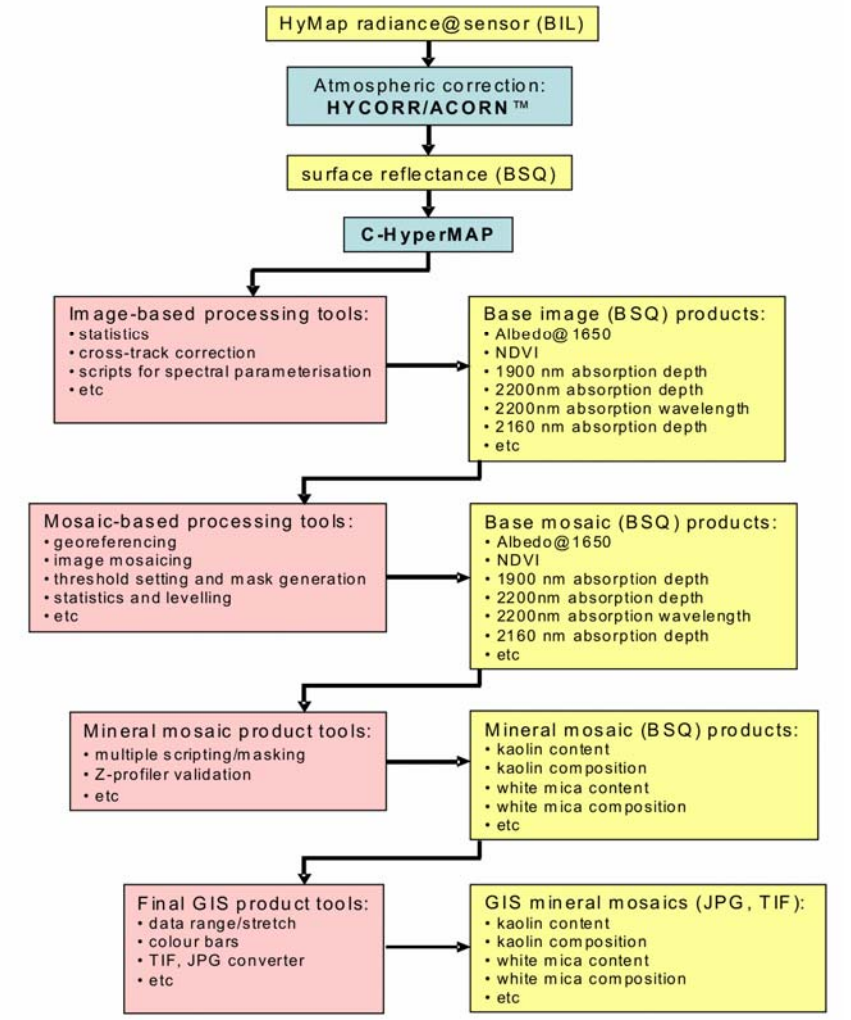

Figure 3. Flow diagram showing the hyperspectral image processing steps, including software (blue boxes) like, CSIRO's C-HyperMAP and its sub-routines (pink boxes), as well as the various types of data (yellow boxes). The ASTER processing is similar though instead of atmospheric correction, CSIRO's image cross-calibration software is implemented followed by reduction to reflectance (based on HyMap or ground reflectance data) before information extraction using CSIRO's C-SatMAP software.

HyMap

Atmospheric correction

The HyMap L1B radiance-at-sensor data were processed to apparent reflectance by HyVista Corporation Pty Ltd using CSIRO's *HYCORR* software (Figure 3). *HYCORR* is an IDL-based front-end widget to ATREM, which is based on 6S (Gao and others, 1993; Clark and others, 1993; http://cires.colorado.edu/cses/atrem.html), both of which are no longer publicly available or supported. No attempt was made to remove systematic, high-frequency,

residual atmospheric absorption-line features as this typically involves the use of scene-dependent statistics, e.g. EFFORT™ correction in ENVI™.

Multi-scene information extraction

The multi-scene HyMap apparent reflectance data were processed to extract mineral maps using CSIRO's *C-HyperMAP* software, which is based on IDL™ and can be imported into ENVI™ (http://www.ittvis.com) as a processing module. *C-HyperMAP* is currently a research prototype with potentially a more robust version being made available in the future to the geosurveys to assist with developing national standards in processing mineral mapping data.

> *C-HyperMAP* (Figure 3) is a collection of linked software modules/steps designed to rapidly generate accurate seamless mineral maps from large volume (Gigabytes to Terabytes), multi-run, hyperspectral surveys. *C-HyperMAP* is based on a programmable feature extraction-processing pipeline where scripts can be designed based on capturing spectral parameters (absorption depths, wavelengths, widths and asymmetries). It comprises a set of routines implementing functionality for spectral pre-processing (mean normalisation, continuum removal, Savitzky-Golay smoothing) and feature parameter extraction (feature depth, feature area, feature width, wavelength at minima, ratios, arithmetic and logical operators). These modules can be chained together to create simple or complex processing algorithms. The hyperspectral data are processed on a per-flight-line basis and not as a single large mosaic. Mosaicing is completed at the final stages of mineral map production, where georeferencing and output to standard map GIS formats are generated. Additional algorithms are included to remove for example, systematic cross-track variations or minimising residual radiometric errors between adjacent flight lines, where required. Note that most processing does not require this type of correction because of the potential negative effect of introducing scene-dependencies, such that image products from different areas may not be comparable.

The procedure for mineral information extraction using C-HyperMAP is based on measuring the diagnostic absorption bands, including their depths, wavelengths and geometries (full-width half height and asymmetry). This is demonstrated in Figure 4. Essentially, band depth (relative to the background continuum) is assumed to be proportional to the mineral abundance. That is, no absorption measured equates to no mineral present. Absorption wavelength is assumed to be proportional to the cation composition (e.g. Tschermak substitution) of minerals like white mica (e.g. muscovite) and chlorite. Absorption band width can be assumed to be proportional to the crystal order/disorder. That is, the range of vibrational states (degrees of freedom) is increased (spread) with increasing disorder (long and short range molecular structural order). Multiple diagnostic features are used to mask in (or out) specific minerals/materials. For example, all pixels are measured for their green and dry vegetation contents, and if above a certain threshold, are then masked out. This effectively excludes or nulls many of the pixels available in a given image. Areas of standing water and deep topographic shading are also masked out. In future, C-HyperMAP is expected to be able to "unmix" the vegetation components (green and dry) leaving as residual weighted mineral contents as if the pixel contained no vegetation. The current suite of mineral content images have been converted to apparent % abundance where appropriate assuming the USGS library spectra (speclab.cr.usgs.gov/spectral-lib.html) of "pure" minerals equate to 100% abundance.

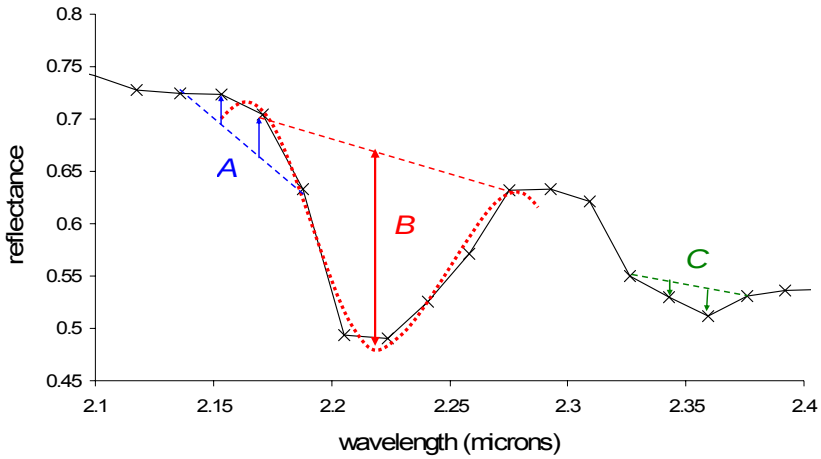

Figure 4. Schematic representation of the spectral parameterisation method used to measure mineral abundances/physicochemistries.

The example in Figure 4 is of a HyMap pixel spectrum of white mica. The abundance of white mica measured using multiple criteria. First, the pixel is assessed for the presence of any AlOH clay (i.e. kaolin, Al-smectite, illite/muscovite) by measuring the depth/area of the 2200 nm AlOH combination tone absorption. This can be done by several continuum-removal based methods. In this case, a 4th order polynomial curve (red dotted line) is fitted to the spectrum (black cross and lines) between wavelengths of 2120 and 2270 nm. The fitted curve has been normalised with respect to a continuum stretched between the wavelength endpoints. Note that the normalised depth/area is assumed to be linearly proportional to the abundance of the AlOH mineral/s. Next, the Al-clay abundance is masked for any contribution by kaolin. Kaolin is gauged using a continuum reflectance ratio $((R_{2136}+R_{2188})/(R_{2153}+R_{2171}))$ that targets the diagnostic kaolin (kaolinite, halloysite and dickite) absorption features from 2160 to 2175 nm (A in blue), which must be smaller than a given threshold (i.e. <1 in this example) for the spectrum to represent white mica (illite/muscovite). The separation of Al-smectite (e.g. montmorillonite, beidellite) from white mica is based on the development of a white mica absorption at 2350 nm (C - green) which is measured using a continuum reflectance ratio $((R_{2326}+R_{2376})/(R_{2343}+R_{2359}))$, designed to minimise complications caused by the presence of MgOH minerals and carbonates. Again, a threshold is applied to bin the result into either dominantly white mica or dominantly Al-smectite. As a result, this spectrum indicates the presence of white mica. To measure the level of Tschermak substitution in white mica, the 1st derivative of the same 4th order polynomial is used to track the precise wavelength of AlOH absorption, which is correlated with Al-content (Duke, 1995). Other masking criteria are also applied related to mixing with green and dry vegetation as well as low SNR, the details of which are provided in Appendices 7 (HyMap geoscience products) and 8 (ASTER geoscience products).

Survey calibration

Figure 5 plots HyMap band number versus the difference in band wavelength position for Stages 1 and 2 (i.e. = Stage 1 – Stage 2). The data show a range from -5.7 to 7.5 nm. This change in wavelength position can impact on the information extraction processing as specific bands are used for each mineral mapping product. The potential effect is demonstrated in Figure 6a and 6b where a 4th order polynomial was fitted to all spectra in the USGS mineral spectral library ("*USGS_min.sli*") after it had been convolved to the HyMap responses for Stages 1 and 2. Both the absorption depth and wavelength (1st derivative)

were calculated. Only those samples with absorption greater than 0.1 and between 2180 and 2230 nm were included in the analysis. Comparison of the absorption depths between Stage 1 and Stage 2 (Figure 5) shows correlation, though there is a root mean square (RMS) error +/- 0.05 (approximates 10% clay abundance) and the fitted regression line is not "*y=x*" as expected.

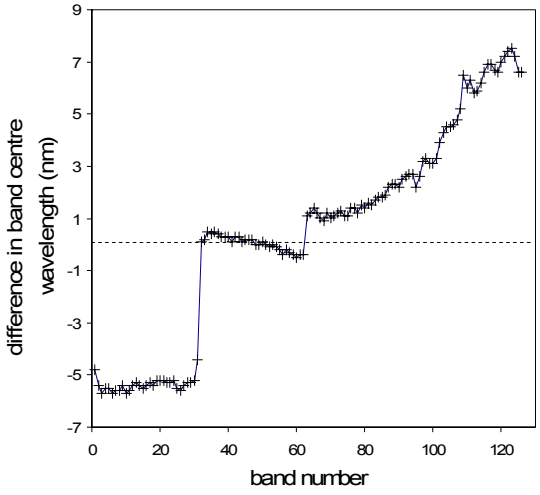

Figure 5. Scattergram of the HyMap band-number versus the difference in HyMap band centre wavelength position between Stages 1 and 2. (=Stage 1-Stage 2). Increasing band number correlates with increasing wavelength. For bands 1-31, the bands for Stage 1 were sampling shorter wavelengths than the same bands for Stage 2. Bands 32-62 inclusive measured similar wavelengths in both surveys whereas bands 63 and above during Stage 1 sampled progressively longer wavelengths than during Stage 2.

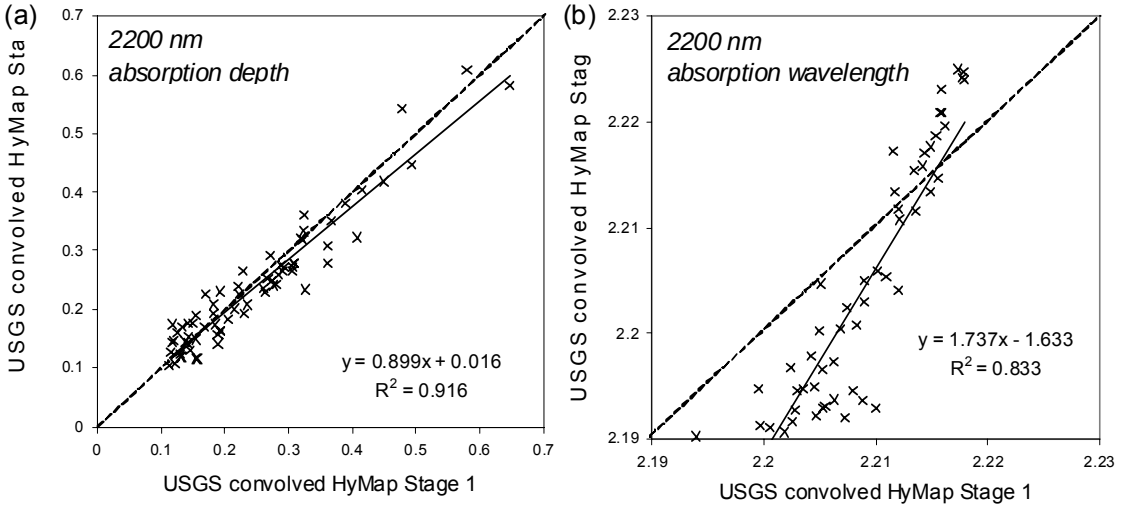

Figure 6. Comparison of the (a) depth of the 2200 nm absorption feature calculated from the USGS library spectrum for white mica (muscovite, paragonite, lepidolite, illite) using a 4th order fitted polynomial for data convolved using the HyMap band centres from Stages 1 and 2; and (b) the wavelength of the 2200 nm calculated from the USGS library using a 4th order fitted polynomial for data convolved using the HyMap band centres from Stages 1 and 2.

The calculated wavelength position shows greater difference (Figure 6) with even greater departure from the "*y=x*" axis. Only at 2215 nm are the wavelength values the same. Away from here, Stage 2 results are up to 10 nm less at shorter wavelengths and 7 nm more at longer wavelengths compared to Stage 1. This is a significant problem and has meant that scaling factors as well as new masking and product thresholds have had to be generated to bring many of the information products into agreement between the two HyMap airborne campaigns. Current research is working on developing new methods that are sensor-independent, including library-seeded Gaussian modelling.

ASTER

The ASTER-HyMap calibration component was set up to enhance and develop work that had been undertaken by Geoscience Australia as part of pmd*CRC activity (van der Wielen and others, 2005) in keeping with a larger strategy of generating accessible, continental-scale ASTER geoscience maps developed by CSIRO in collaboration with ERSDAC (Japan).

Multi-scene cross-calibration

The cross-calibration of the ASTER Level 1B imagery was conducted using software developed by CSIRO Mathematics and Information Sciences for processing Landsat Thematic data (www.cmis.csiro.au/rsm/research/index.htm). The software uses a kernel-type approach that reduces the various physical effects (date, latitude/longitude, view and solar angles, bi-directional reflectance distribution function or BRDF, atmosphere) to a spatially-dependent, linear combination of spectral bands.

The next step in the reduction of the ASTER cross-calibrate mosaic to (apparent) surface reflectance involved a transformation based on a least squares regression between the ASTER and HyMap data.

Multi-scene information extraction

Similar to *C-HyperMAP*, *C-SatMAP* is a prototype software package developed in IDL™ by CSIRO for the processing of multi-scene, multi-spectral image data such as ASTER. The processing methodology and functionality is also similar and operates as an ENVI™ add-on module.

Output Image Format

The processed ASTER and HyMap geoscience image products were converted to GIS compatible format as geoTIFF colour images, which are supported by both MAPINFO (extranet.mapinfo.com/products) and ESRI's ArcMap (www.esri.com). HyVista Corporation HyMap currently provide their data products using a WGS84 datum and not GDA94. However, there is essentially no difference between these datum points at the accuracy of HyMap geo-positioning. The ASTER mineral maps are provided in WGS84 UTM projection.

VALIDATION

ASTER cross calibration

The accuracy of the ASTER cross-calibration was validated using the airborne HyMap reflectance data, which was first convolved to the ASTER response functions. Over 60 coincident regions of interest (ROI) were collected from both data sets (spread over five HyMap blocks) and spanning a range (bright to dark) of surface types. Areas of variable vegetation cover were avoided.

The results of the regression analyses of the ROIs are presented in Figure 7, which shows significant correlation (at 99% confidence level) for all ASTER bands 1-9. This is an excellent result and validates the stability of both the ASTER and HyMap sensors as well as the effectiveness of CSIRO's cross-calibration software. The before and after cross-calibration mosaics are presented in Figure 8, which shows the seamless nature of the

calibrated product for most of the scenes. However, there are issues between scenes associated with unavoidable seasonal vegetation differences.

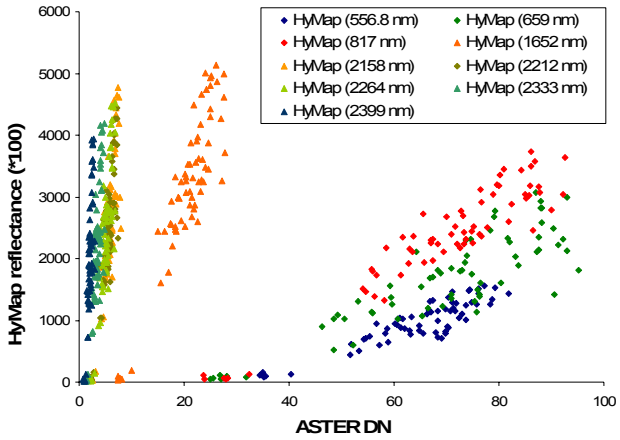

Figure 7. Scattergrams of the processed ASTER mosaic DN and the convolved HyMap reflectance data for 67 coincident ROIs collected from 5 HyMap blocks near Mount Isa (Blocks C, D, F, G, H). The associated regression coefficients are provided in Table 1.

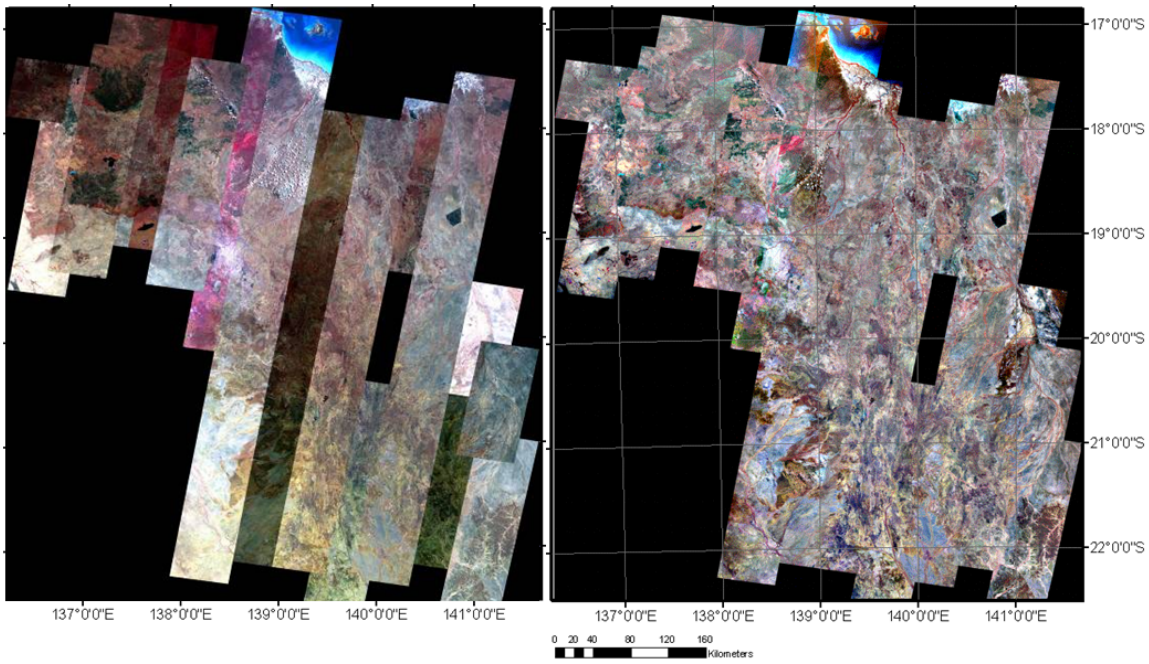

Figure 8. False colour mosaic of approximately 140 ASTER scenes spanning the Mount Isa Block (a) L1B radiance-at-sensor mosaic, SWIR cross-talk corrected; (b) CSIRO cross-calibrated mosaic provides a seamless image of the region.

The associated gains and offsets (Table 1) provide both a mechanism to transform the cross-calibrated ASTER digital data to (apparent) ground reflectance, consistent with the HyMap reflectance data as well as helping to better understand calibration issues, especially ASTER additive effects such as SWIR cross talk, given the assumption that the CSIRO cross-calibration software has not introduced significant gain/offset effects. The VNIR bands show decreasing offset values with increasing wavelength. This is consistent with the expected aerosol scattering effect, which was not corrected. However, an offset value equal to the mean reflectance for all the ROIs is significant, as it indicates that an aerosol correction is required for these data if standard radiative transfer correction procedures were to be

applied. Similar large offsets are recorded for all the SWIR bands, including band 4. This is an important result and is consistent with the results of Hewson and Cudahy (2008) who found that the current cross-talk correction under compensates for this additive effect and challenged the assumption that ASTER band 4 has no crosstalk effect.

Table 1. Regression coefficients for the cross-calibrated ASTER mosaic and the HyMap reflectance data shown in Figure 4.

Band	band centre (nm)	R^2	gain	offset	ROI mean	% offset/mean
1	556	0.81	29.79	-958.54	955.09	100
2	661	0.76	36.57	-901.22	1634.42	55
3	807	0.90	51.47	-1249.81	2319.71	54
4	1656	0.83	232.84	-1654.99	3147.78	53
5	2167	0.73	754.41	-1726.21	2578.13	67
6	2209	0.75	715.13	-1467.00	2425.82	60
7	2262	0.72	812.40	-1695.37	2378.86	71
8	2336	0.70	1027.03	-1321.10	2116.64	62
9	2400	0.65	1679.30	-1484.40	2008.02	74

HyMap

Validation of the HyMap radiance-at-sensor and apparent reflectance data has already been established in previous studies (Cudahy and others, 1999, 2005). Many of the HyMap derived mineral information products have also been validated using independent field/laboratory data as part of the Kalgoorlie study (Cudahy and others, 2005), including: kaolin abundance, kaolin crystallinity, white mica abundance; white mica composition (muscovite versus paragonite); iron oxide content; hematite-goethite ratio; and sulphate (gypsum) abundance. Therefore, there is less need to re-establish the efficacy of these derived products for the Queensland HyMap mineral mapping results. However, extensive ground sampling and laboratory data collected in the current project are valuable for better understanding the accuracy of the HyMap products, especially for new products not previously released. These are described in more detail in the following sections.

LABORATORY VALIDATION STUDIES

A series of laboratory studies targeted specific mineral information issues related to a number of the key remote mineral mapping products generated from this project. These issues included:

- White mica physicochemistry, including:
    - level of Tschermak substitution;
    - crystallinity;
- Surface water abundance and bonding;
- Al-smectite mineralogy;
- Mineral mapping and spectral resolution; and
- Implications for HyMap information extraction processing.

White mica physicochemistry

White mica is used here to describe a range of primarily dioctahedral (but also the trioctahedral K-rich lepidolite), Fe- and Mg-poor and Al-rich sheet silicates, which have a general formula of $(K,Na)_2(Al,Fe^{2+},Mg)_4(Al,Si)_8O_{20}(OH)_4$. Compostional endmembers include: muscovite ($K_2Al_4[Al_2Si_6O_{20}][OH]_4$), paragonite ($Na_2Al_4[Al_2Si_6O_{20}][OH]_4$), margarite ($Ca_2Al_4[Si_4Al_4O_{20}](OH)_4$) and celadonite ($K_2[(Al,Fe^{3+})_2(Mg,Fe_{2+})_2]Si_8O_{20}[OH]_4$). These have less ordered, hydrated equivalents, including illite (K-rich) and brammallite (Na-rich) that typically form in lower temperature environments.

White micas are commonly formed in a range of metamorphic (including diagenetic) and metasomatic conditions and have been used as physicochemical barometers (T, P, REDOX, pH, chemical activities). For example, García-Casco and others (1993), Guidotti and Sassi (1976) and Duke (1994) found that the level of Tschermak substitution [e.g. $(Al\leftrightarrow Si)_{tet}=(Al\leftrightarrow\{Fe^{2+},Mg,\text{ site vacancy}\}_{oct})$] was useful for measuring metamorphic grade. Similarly, Pollastro (1993) and Dalla Torre and others (1998) found that illite/smectite structural transformations were sensitive to temperature.

The potential to use reflectance spectroscopy to measure white mica physicochemistry has been explored by various workers (Kruse and Hauff, 1991; Post and Noble, 1993; Duke, 1994; Scott and Yang, 1997; Longhi and others, 2000). However, care is required in making geobarometric inferences from this type of data (Rieder and others, 1992) as well as using the term “crystallinity” (Guggenheim and others, 2002).

In the current study, two aspects of white mica physicochemistry are examined in more detail, namely:

- Tschermak substitution – Cudahy and others *(*1997, 1999, 2005), Yang and others (2001) and Ruitenbeek and others (2005) have shown the potential of this information for mapping chemical gradients associated with mineralised hydrothermal systems; and
- Crystallinity – Gibson and others (2005), found regional changes in the XRD Illite ‘*Kubler Index*” (Kubler and Jaboyedoff, 2000) consistent with lower grade regional metamorphic patterns in the western part of the Mount Isa Block.

White mica from Mount Isa

Figure 9 shows two examples of white mica from the Mount Isa area. Locality MI059 is from a strongly foliated metasediment from the Mount Dore Shear Zone close to the Starra IOCG deposits in the south-eastern part of the Mount Isa Block (discussed in more detail below). This rock comprises large (200 μm) muscovite (lighter grey) plates aligned within at least two tectonic foliation planes. The large size of these muscovite plates makes them suitable for electron microprobe analysis.

Locality *MI077* is from a weakly foliated metasediment from the Century area in the northwest part of the Mount Isa Block and comprises small (~10-20 μm) white mica plates. This small size makes them a difficult target for accurate electron microprobe analysis.

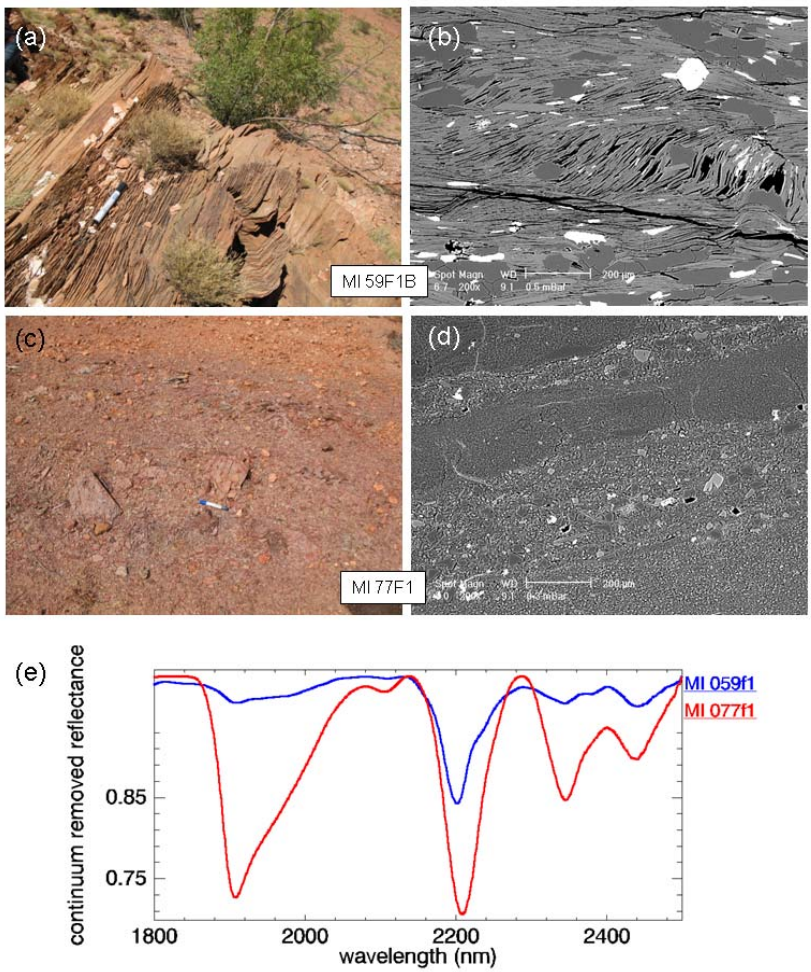

Figure 9. (a) Field photograph at locality "*MI059*" of foliated metasediments near the Starra IOCG deposits (GDA94: 446826mE, 7601310mN); (b) SEM photomicrograph of a rock sample from *MI059*; (c) Field photograph at locality "*MI077*" of foliated metasediments near the Century Zn deposit (GDA94: 243599mE, 7933859mN); (d) SEM photomicrograph of a rock sample from *MI077*; (e) ASD continuum-removed SWIR reflectance spectra of samples from *MI059* and *MI077*.

The associated reflectance spectra (Figure 9e) of these two samples show a number of major differences including:

- All the absorption features in *MI077* can be explained by white mica (1910, 2120, 2200, 2350 and 2450 nm). *MI059* shows these as well as additional features at 2000, 2380 and 2245 nm, which could be explained by the presence of chlorite;
- Despite the apparent dominance of large grained white mica, the associated 2200 nm AlOH absorption for sample *MI059* is half the depth of *MI077*;
- The secondary AlOH absorption at 2350 nm is very weakly developed compared with the 2200 and 2450 nm features in *MI059*. This is unusual behaviour and can be indicative of Al-smectite rather than white mica. Al smectite is typical for the Mount Isa region, including a number of deposits like Century (discussed in more detail below). This contrasts with the spectral behaviour of *MI077* which shows strong 2350 nm absorption, more consistent with the USGS library data (ENVI™); and
- Water absorption in the 1900 nm region displays a shorter wavelength (~1910 nm minimum for both samples indicating "bound" water) and is much stronger (deeper)

for *MI077*. Given that this bound water is associated with white mica then this indicates that *MI077* comprises illite rather than muscovite.

Tschermak substitution

Following on the results of Scott and Yang (1997), the current study conducted an electron microprobe study of a selection of rock samples from the Mount Isa area. A number of the original samples selected for analysis were subsequently found to have a mica grain size too small for accurate probing. Those with sufficiently large grain size (listed in Table 2) show octahedral (Figure 10) and interlayer compositions consistent with the results from previous studies of white mica (Scott and Yang, 1997). That is, the wavelength of the 2200 nm absorption is inversely correlated with the mica octahedral sheet trivalent cation content.

Table 2. Regression coefficients for the cross-calibrated ASTER mosaic and the HyMap reflectance data shown in Figure 4.

Sample	Number of analyses	wavelength (nm)	Al oct	R^{III}_{oct}	K/(K+Na)
MI58F2	50	2214	3.285	3.287	0.983
MI59F1	50	2203	3.621	3.622	0.915
MI82F4	25	2211	3.186	3.188	0.967
MI82F5	45	2208	3.450	3.450	0.925
MI83F1	57	2211	3.265	3.267	0.981

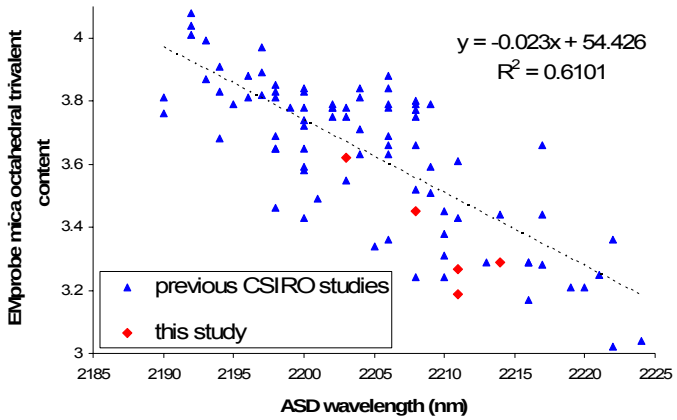

Figure 10. Scattergram of the ASD wavelength position of the 2200 nm white mica absorption minimum versus the calculated total number of trivalent cations in the white mica octahedral layer from EMprobe analyses (from Table 2). Results from this study (red diamonds) are compared with the results from Scott and Yang (1997) (blue triangles) and show that increasing wavelength is associated with decreasing trivalent cation content (increasing Si).

Illite crystallinity

The crystallinity of white mica is complex and can be affected by: interstratification within smectite/chlorite layers; different structural polytypes (e.g. 2M versus 1M illites); changes in cation composition/density (e.g. Tschermak substitution, site vacancies); particle size and

shape. One measure of white mica crystallinity, namely the XRD-based "illite crystallinity index" of ICI (Kubler and Jaboyedoff, 2000), has been used by the hydrocarbon exploration industry since the 1960's to identify unproductive rocks caused by over maturation of organic matter. This index is based on the full width at half height maximum (FWHH) of the first illite diffraction peak (10 Å = *001hkl* peak). It is useful only for studying low-grade metamorphism, especially the range from diagenesis to greenschist facies. As a consequence, Gibson and others (2005) used this index to map metamorphic zonation in the low grade northwest part of the Mount Isa Block. The ICI value is in reality not a measurement of the crystallographic order of illite, but rather an indirect measurement of the amount of expandable (montmorillonite) interlayers in between illite tetrahedral-octahedral-tetrahedral layers.

Kruse and Hauff (1991) also examined a range of illites of different polytypes from relatively ordered 2M illites to relatively poorly ordered 1M illite. Both XRD and reflectance data showed variations consistent with these polytypes. In addition, all the 1M illites show a wide 10 Å peak (i.e. expandable interlayers), and the reflectance spectra show the 1M illites have a broader 2200 nm absorption, often with right-hand asymmetry. The XRD data also showed that some of the 2M illites also had expandable layers. These same samples show deeper, sharp water absorption at 1910 nm in the reflectance data.

XRD analysis

Following the above context, 15 Mount Isa samples, rich in white mica, were selected for XRD analysis using the FWHH of the 10 Å peak. The correlation matrix for a selection of the XRD and reflectance parameters is given in Table 3. Figure 11 ranks the associated ASD reflectance spectra of these samples in order of their 001hkl FWHH. These data show some correlation with the best correlation between (R^2 = 0.415) the XRD *001hkl* FWHH and the reflectance 2200D/1900D index.

Table 3. Regression correlation matrix (R) for selected XRD and reflectance parameters calculated for 15 Mount Isa white-mica-rich samples. *2200D* = depth of 2200 nm absorption; *2200W* = wavelength of 2200 nm absorption; *2200A* = area of the 2200 nm absorption; *2200Ass* = asymmetry of the 2200 nm absorption. The same is the case for the *1900** parameters. All the XRD parameters relate to the 10 Å white mica *001hkl* peak. The *2200A/2200D* is proportional to the FWHH of the 2200 nm absorption.

	XRD 001hkl peak position	**XRD 001hkl peak height**	**XRD 001hkl peak FWHH**	**2200W**
2200D	-0.481	0.036	0.176	0.509
2200W	**-0.515**	-0.243	0.283	1.000
2200A	**-0.509**	0.015	0.182	0.570
2200Ass	**-0.548**	-0.341	0.343	0.642
2200A/2200D	-0.380	-0.069	0.092	**0.921**
1900D	-0.486	-0.129	**0.522**	0.456
1900W	0.170	-0.272	-0.197	-0.294
1900A	-0.498	-0.142	**0.532**	0.475
2200D/1900D	0.080	0.246	**-0.644**	-0.418

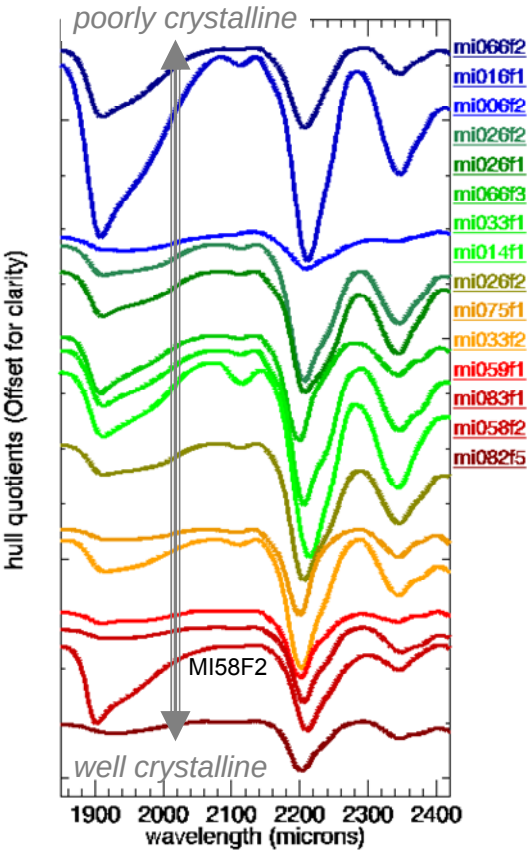

Figure 11. ASD reflectance spectra of white mica samples from the Mount Isa area ranked in order of their XRD 001hkl (10 Å) FWHH. Note the general decrease in water absorption at 1900nm with increasing white crystallinity.

In an attempt to improve this correlation, partial least squares (PLS – Haaland and Thomas, 1988) analysis was applied to the full spectrum ASD reflectance spectra with the XRD 001hkl FWHH parameter as the target variable. The results showed slight improvement (R^2=0.44) with the Final Regression Coefficients (FRC - Figure 12) showing the importance of the molecular water absorption at 1900 nm and to a lesser degree, though still important, the (inverse) 2200 nm absorption to generate this correlation. This is consistent with the simple parameter approach (Table 3) showing increased XRD 001hkl FWHH with decreasing AlOH to water content in the reflectance spectra.

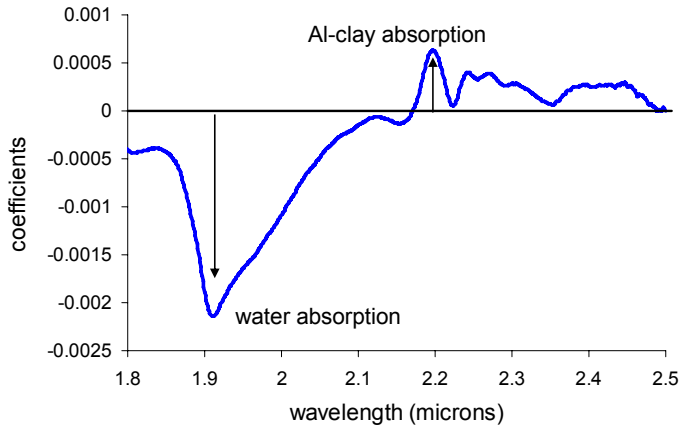

Figure 12. The PLS final regression coefficients (FRC) responsible for the correlation between the ASD reflectance spectra and the XRD 001hkl (10 Å) FWHH parameter. The large weightings, both +ve and –ve, are key drivers for observed correlation.

The implication of this result is that it may be possible to broadly map the "illite crystallinity" and hence temperature using HyMap data for at least low-grade rocks given that:

- Molecular water can be measured with HyMap spectral resolution;
- This water is present in white mica and not another mineral and/or vegetation; and
- White mica is not the product of recent weathering.

To test whether molecular water at 1900 nm can be measured at HyMap spectral resolution (i.e. bands omitted because of atmospheric water vapour absorption), ASD reflectance spectra of field samples were first convolved to the HyMap responses. Then the depth of the 1900 nm absorption before and after convolution was calculated. Figure 13 plots the results which show significant correlation (at 99% confidence level) and provides strong evidence to support the generation of accurate maps of surface water content using HyMap data based on the depth of the 1900 nm absorption.

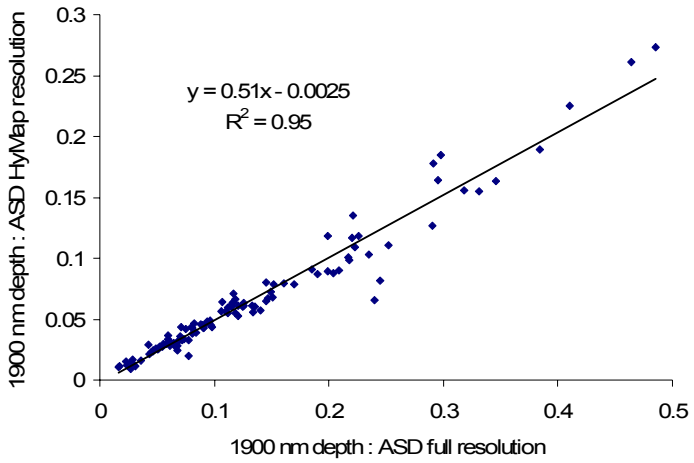

Figure 13. Scattergram of the depth of the 1900 nm absorption at full ASD spectral resolution versus the same data convolved using the HyMap band-passes. This shows that even though HyMap bands are not located across most of the 1900 nm region because of strong atmospheric water vapour, the few bands on the shoulders nevertheless provide a useful measure of the water absorption.

Even though Table 3 shows no apparent correlation between the FWHH of the 2200 nm absorption (approximated using the *2200A/2200D* index) at the XRD 001hkl FWHH parameter (R^2= 0.008), these data show a strong correlation (R^2= 0.848) between with 2200 nm wavelength and the 2200 nm FWHH. Figure 14 plots these same parameters for a larger suite of Mount Isa field samples containing white mica, which confirms this close relationship. It indicates that increasing Tschermak substitution (increasing wavelength) is correlated with increasing absorption width, both of which can be inferred to be related to increasing disorder.

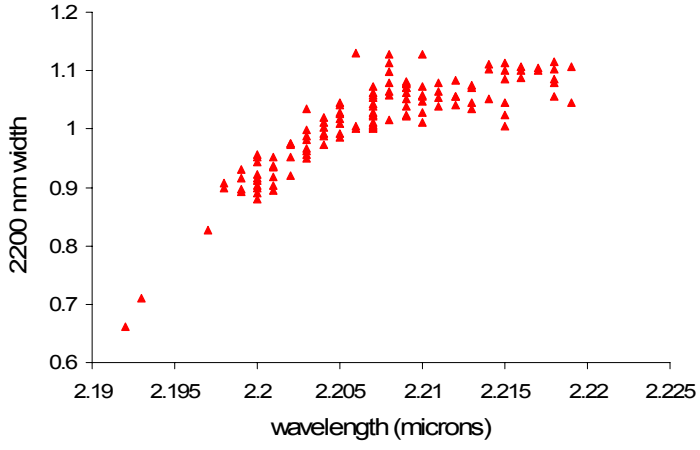

Figure 14. Scattergram of the wavelength of the 2200 nm absorption minimum versus the FWHH of the 2200 nm absorption calculated using 2200A/2200D (Table 3) and showing the correlation between these two parameters.

Al-smectite mineralogy

In addition to kaolin and white mica, Al-smectite is also found in the in the study area. The presence of Al-smectites provides information regarding pH, REDOX, water/metal activities and permeability. Al-smectites include beidellite and montmorillonite with the latter having higher cation exchange capacity and the ability to undergo Tschermak substitution similar to white micas. Post and Noble (1993) showed that the difference in Al-content between beidellite and montmorillonite is measurable as a change in the wavelength of the AlOH absorption minima in the 2200 nm wavelength region, with the montmorillonite absorption exhibiting a longer wavelength. The question is whether remote hyperspectral data, such as airborne HyMap imagery, can be processed to yield Al-smectite content and even the separation of beidellite and montmorillonite.

Figure 15 shows XRD and reflectance data for four soil samples that contain Al-smectite as well as kaolinite and a mixed-layer clay, possibly kaolinite-smectite. The XRD results (Figure 15a) show that samples *MI114* and *MI123* remain mostly collapsed with very little evidence of re-expansion and therefore the smectite in these samples is believed to be mostly montmorillonite. For samples *MI120* and *MI122* some re-expansion is evident although the expansion is only to about 15Å. It is believed that these samples therefore contain a mixture of beidellite and montmorillonite.

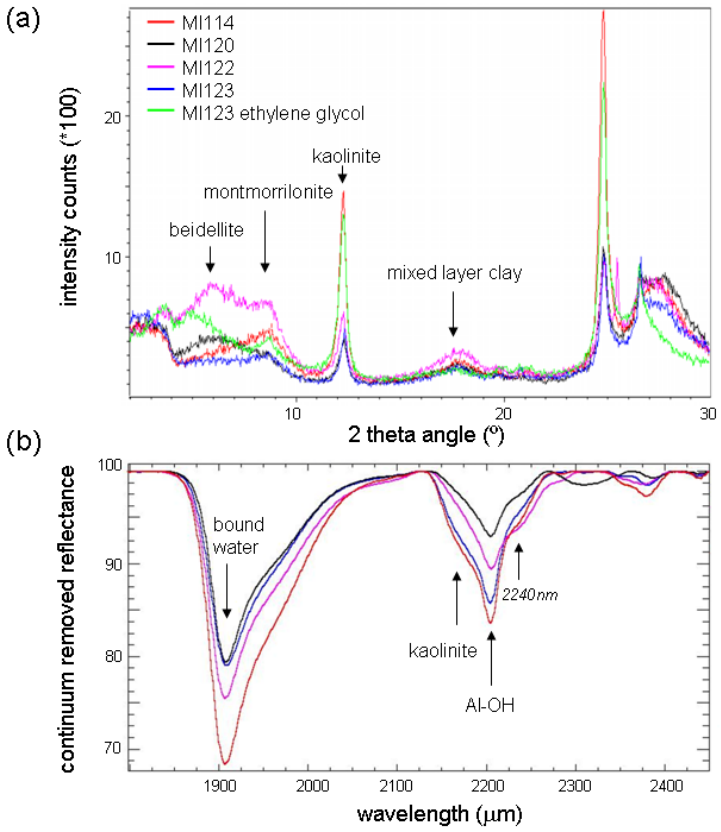

Figure 15. (a) XRD traces of soil samples showing diagnostic peaks related to the Al-smectites beidellite and montmorillonite as well as kaolinite and a mixed-layer clay. (b) ASD reflectance spectra of the same soil samples in (a) showing abundant bound water at 1910 nm as well as kaolin and another AlOH clay, presumably Al-smectite, in the 2200 nm region.

The associated reflectance spectra (Figure 15b) show abundant bound water at 1910 nm as well as kaolin and another AlOH clay, presumably Al-smectite, in the 2200 nm (+ 2240 nm) wavelength region. There is no white mica feature at 2350 nm. This apparent mineralogy in the reflectance spectra is consistent with the XRD results. However, there is no evidence in the spectra of a wavelength shift between the beidellite-rich samples (*MI120* and *MI122*) from the montmorillonite-rich samples (MI114 and MI123), as found by Post and Noble (1993). Thus, it is unlikely that montmorillonite can be separated from beidellite using the airborne HyMap data.

Mineral mapping and spectral resolution

Three datasets have been used to interpret the mineralogical significance of spectral measurements. These are:

- Coarse spectral resolution ASTER satellite data – 9 VNIR-SWIR channels;
- Moderate-high spectral resolution HyMap airborne data – VNIR-126 SWIR channels in the Visible – SWIR wavelength range; and
- High spectral resolution field ASD data – ~1000 VNIR-SWIR channels.

Comparing a high spectral resolution data with another of lower resolution requires the first to be resampled to the poorer resolution of the second.

The effect of spectral resolution on the ability to accurately measure and map the abundance and composition of specific minerals is assessed using the ASD reflectance spectra of rocks collected from the Mount Isa area. This analysis is first examined with respect to mineral group type. Key features to note include:

- The intensity of the 2160 nm absorption in the kaolin spectra (Figure 16) decreases in intensity with decreasing crystallinity (Figure 16). Separating this behaviour becomes more challenging both with decreasing kaolin content as well as decreasing spectral resolution.
- The wavelength position of the 2330 nm carbonate absorption, which changes from dolomite (2320 nm) to calcite (2335 nm), appears to be achievable at all spectral resolutions, albeit with varying levels of accuracy (Figure 17). Complications arise when MgOH minerals are also present (e.g. epidote-chlorite in Figure 18 and amphibole in Figure 19) for the same sample. Distinction from these other minerals depends on other features (discussed below);
- Both epidote and chlorite share a similar small absorption at 2255 nm, which is clearly evident at HyMap resolution but not apparent at ASTER resolution (Figure 18). The separation of chlorite from epidote can be achieved by using the 1550 nm absorption, which is only developed in epidote. The 2000 nm chlorite absorption could also be used but can easily be complicated by broad absorption of cellulose and water at similar wavelengths. Ferrous-rich chlorite (as well as ferrous amphiboles) has characteristic absorption from 2100 nm towards 1000 nm. This can be seen in the top two chlorite spectra (Figure 18) and can be mapped at all spectral resolutions;
- Amphibole is characterized by a small absorption at 2380 nm which is detectable at HyMap resolution but not at ASTER resolution (Figure 19). Talc shares similar features to amphibole, including the 2304 and 2387 nm absorptions, which are both fixed in wavelength. Mixing with other minerals causes these absorptions to change geometry/wavelength as shown by the lower few spectra which are mixtures with white mica;

- The diagnostic white mica absorptions at 2200, 2350 and 2450 nm are clearly seen at HyMap resolution though the 2350 and 2450 nm features are poorly resolved at ASTER resolution. Changes in 2200 nm absorption wavelength, related to Tschermak substitution, are also well tracked at HyMap resolution though at ASTER resolution the precise position of the absorption minimum is lost and only a relative change in the height of the shoulders can be used to infer mica composition. However, the resolution of the white mica absorption wavelength is complicated by the presence of kaolinite (Figure 16).

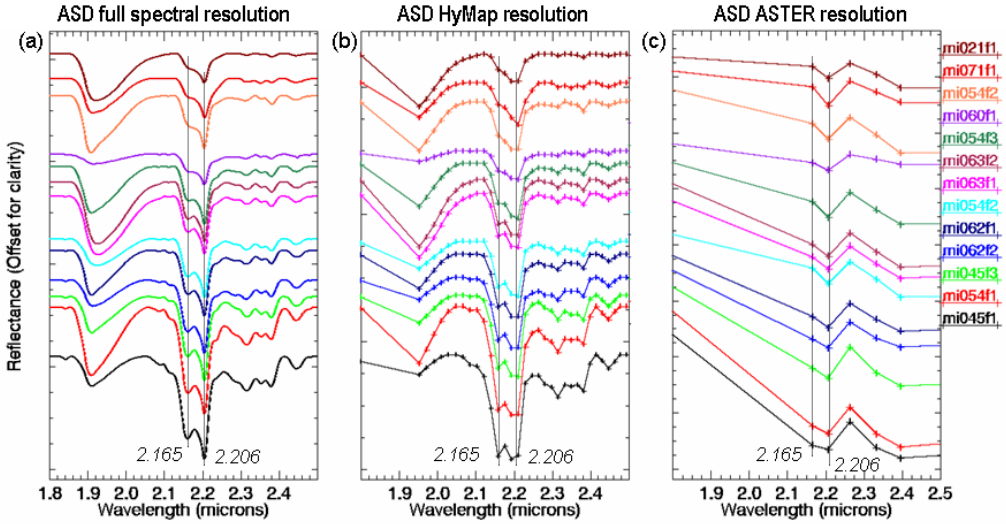

Figure 16. Kaolin-rich samples (a) ASD spectra at full resolution; (b) the same ASD spectra convolved to HyMap responses; and (c) the same ASD spectra convolved to ASTER responses. Samples are ordered from poorly crystalline kaolin (halloysite) at the top to well-ordered kaolinite at the bottom.

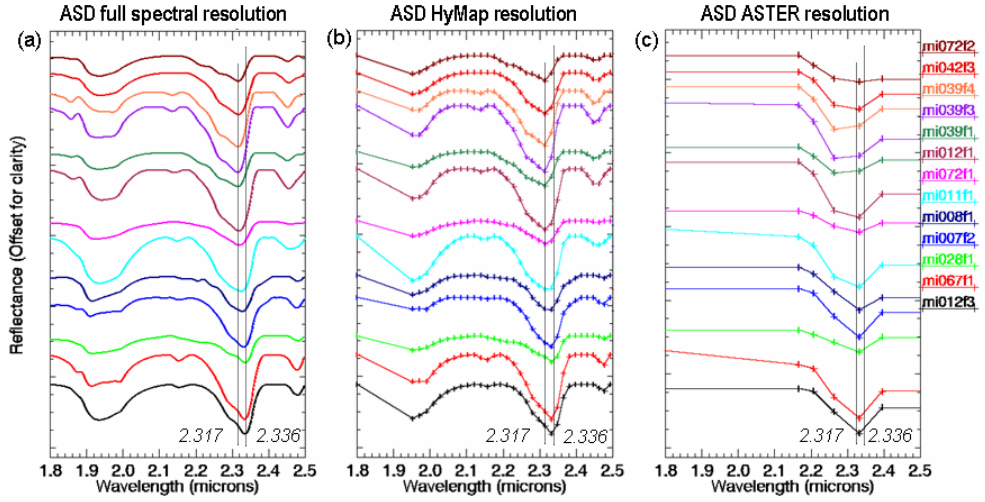

Figure 17. Carbonate-rich samples (a) ASD spectra at full resolution; (b) the same ASD spectra convolved to HyMap responses; and (c) the same ASD spectra convolved to ASTER responses. Samples are ordered from dolomite (top) to calcite (bottom).

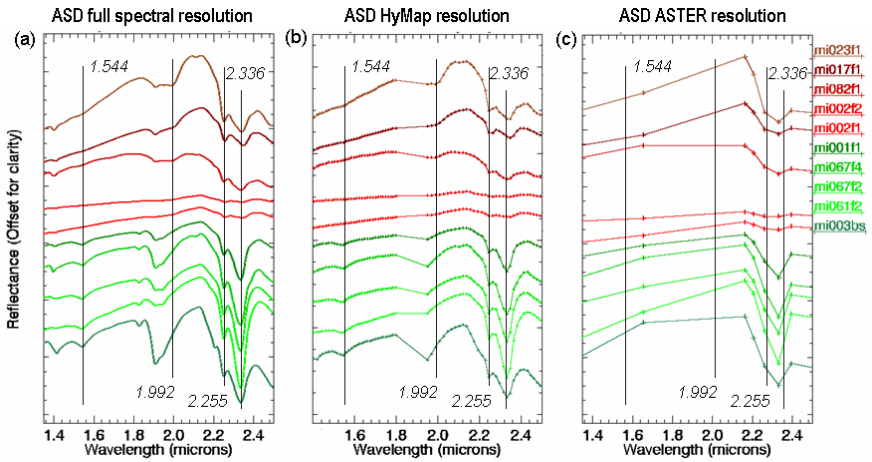

Figure 18. Epidote/chlorite-rich samples (a) ASD spectra at full resolution; (b) the same ASD spectra convolved to HyMap responses; and (c) the same ASD spectra convolved to ASTER responses. Samples are ordered from chlorite (top & red) to epidote (bottom & green).

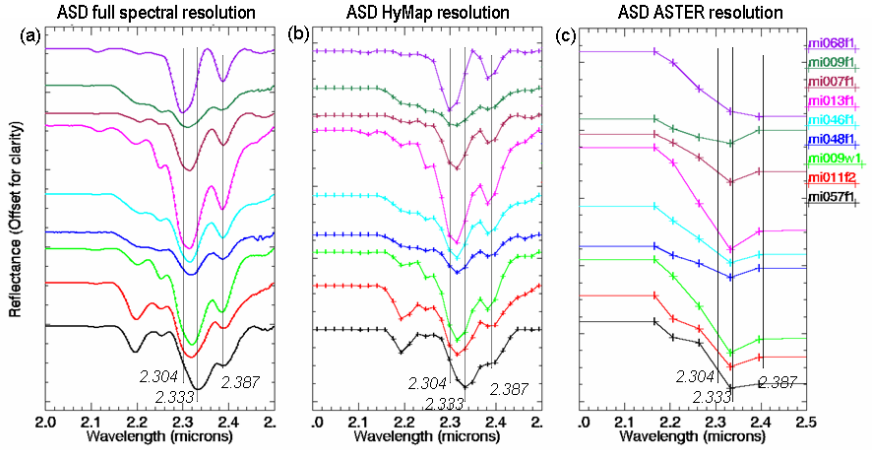

Figure 19. Amphibole-rich samples (a) ASD spectra at full resolution; (b) the same ASD spectra convolved to HyMap responses; and (c) the same ASD spectra convolved to ASTER responses. Samples are ordered from relatively pure amphibole (top) to mixtures (bottom).

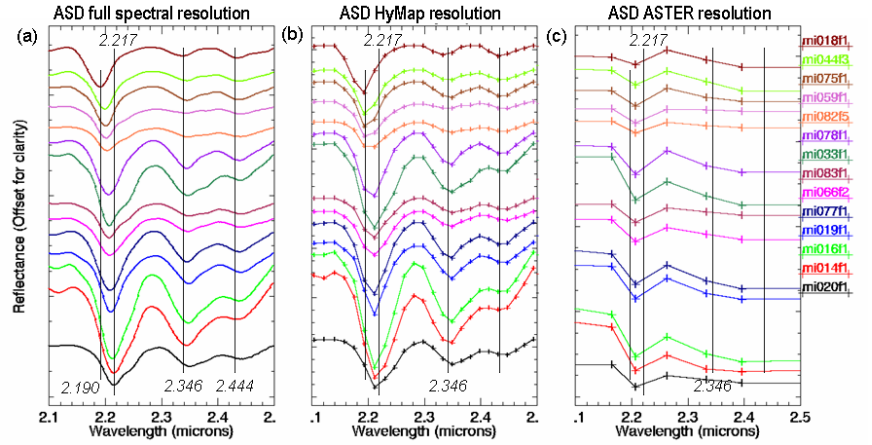

Figure 20. White mica-rich samples (a) ASD spectra at full resolution; (b) the same ASD spectra convolved to HyMap responses; and (c) the same ASD spectra convolved to ASTER responses. Samples are ordered from Si-poor mica (muscovite/paragonite - top) to Si-rich mica (phengite) mica.

Information extraction

From the above results, a series of spectral parameters were designed to separate the various minerals at HyMap and ASTER spectral resolutions. These are described in more detail below.

White mica

The presence/absence of the 2350 nm is critical for identifying and separating white mica from other minerals like Al-smectite. However the white mica 2350 nm absorption also strongly overlaps with 2330 nm absorption caused by MgOH and carbonate minerals. Figure 21 shows how the HyMap spectral parameters (Appendix 7) are able to effectively resolve these complications. In this plot, samples have been sourced from the USGS spectral library (ENVI™) and convolved to HyMap responses (Stage 1). The white mica group, which includes illite, muscovite and lepidolite, are clearly separated from the MgOH (chlorites, epidote, amphiboles and carbonates), Al-smectites (montmorillonite) and kaolin (kaolinite, interstratified kaolinite-smectite, dickite and halloysite) groups using a combination of these spectral parameters.

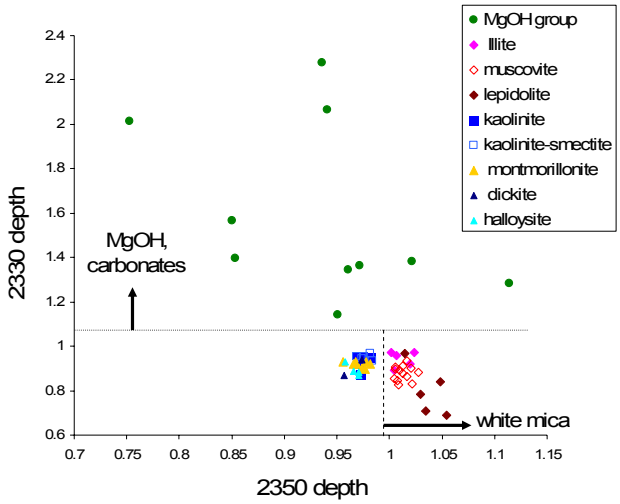

Figure 21. Comparison of the calculated depths of the 2350D and 2330D parameters using the USGS library spectra of selected minerals convolved to the HyMap Stage 2 bandpass centres. See Appendix 7 for details regards these spectral parameters.

The ability at ASTER spectral resolution to measure the change in wavelength of the white mica 2200 nm absorption using the relative shoulder heights of 2200 nm absorption (B_5/B_7) is tested in Figure 22, with high values related to phengite and low values to muscovite/paragonite. Using this parameter alone does not capture these white micas as most of the high B_5/B_7 values are related to MgOH and carbonate minerals. Thus a first pass cull is required to capture only the AlOH minerals. This is achieved using a $[(B_5+B_7)/B_6)]$ combination as shown in Figure 22. Following a threshold to mask in these Al-clays, the (B_5/B_7) ratio can then be used to measure composition information. However, these data also show that "long-wavelength" phengite samples are not well resolved from "short-wavelength" muscovite samples both in regards to the overlap with other AlOH minerals, such as kaolin. In addition, there is a broad positive correlation between these two spectral parameters which indicates that they are not independent variables. Related to this, well-ordered kaolin as well as other AlOH minerals like pyrophyllite with a strong 2160 nm

absorption relative to the 2200 nm feature, become increasingly difficult to measure/capture using the [(B_5+B_7)/B_6)] combination.

Thus the ability for ASTER to measure mineral composition as specific as “phengite” is poor. It is thus recommended that mineral maps based on ASTER should be more conservative and instead describe mineral groups, such as AlOH abundance [(B_5+B_7)/B_6)] or AlOH composition {(B_5/B_7) masked by [(B_5+B_7)/B_6)]}.

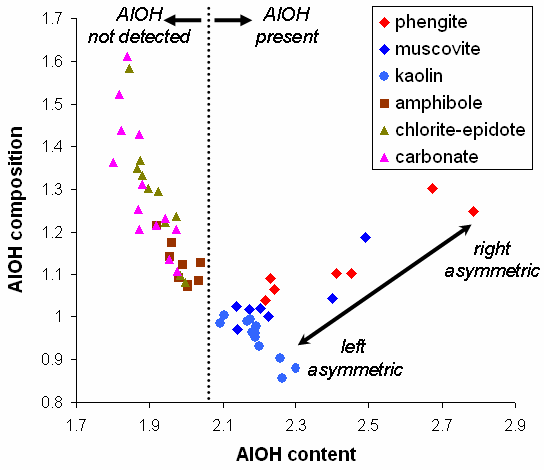

Figure 22. Scattergram of USGS mineral library spectra convolved to ASTER band-passes and then processed to capture AlOH information using band combinations, namely: AlOH content (B_5+B_7)/B_6) and AlOH composition (B_5/B_7).

Figure 23 also shows the importance of using the correct ASTER band combination to capture a given mineral group. In this case, using [(B_7+B_9)/B_8] to capture MgOH (and carbonate) content, which spans the 2330 nm absorption, is not as effective as [(B_6+B_9)/(B_7+B_8)], which spans a wider wavelength interval but better separates MgOH (and carbonates) from AlOH clays.

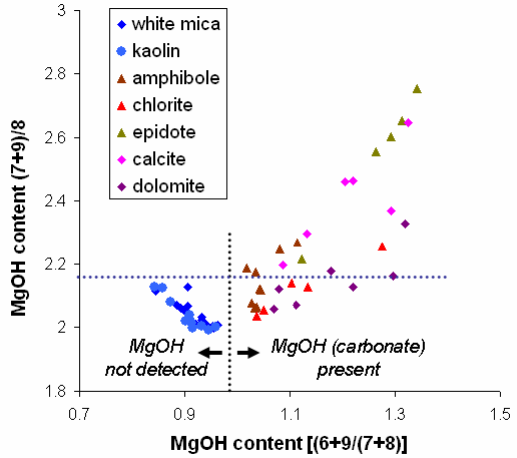

Figure 23. Scattergram of USGS mineral library spectra convolved to ASTER band-passes and then processed to capture MgOH content using two band combinations, namely: (B_6+B_9)/(B_7+B_8) versus (B_7+B_9)/(B_8).

The ability at ASTER spectral resolution to measure MgOH/carbonate information, both content and composition is examined in Figure 24. Similar to the AlOH information, a mask must first be applied to separate the desired MgOH and carbonate minerals from the AlOH

(and other) minerals, using the $[(B_6+B_9)/(B_7+B_8)]$ combination. Then with a $(B_7)/(B_8)$ combination, broad separation of the MgOH group is possible, including: dolomite from calcite; and chlorite from epidote. Amphiboles span the complete range and absorption features due to dolomite-chlorite is not separated from those due from calcite-epidote.

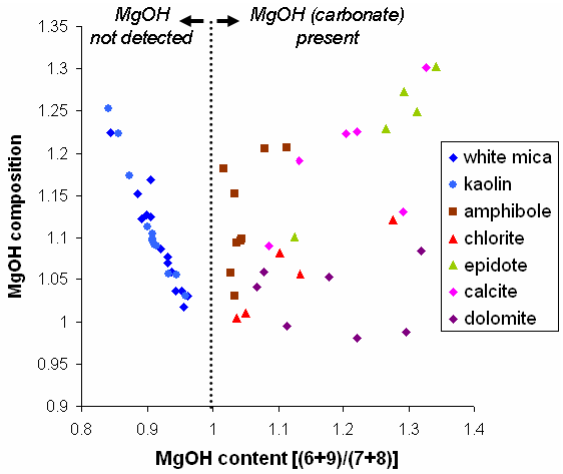

Figure 24. Scattergram of USGS mineral library spectra convolved to ASTER band-passes and then processed to capture MgOH information using band combinations, namely: MgOH content $(B_6+B_9)/(B_7+B_8)$ versus MgOH composition (B_7/B_8).

A range of minerals have ferrous and ferric iron as part of their composition, including amphiboles (e.g. actinolite) and chlorites (e.g. clinochlore). ASTER has poor spectral coverage of the ferric iron absorptions in the VNIR though it is better suited for the measuring of the broad absorption of ferrous iron. This is demonstrated in Figure 25 which plots these two parameters and shows that all of the MgOH minerals are well separated from the AlOH minerals using the ferrous iron ratio.

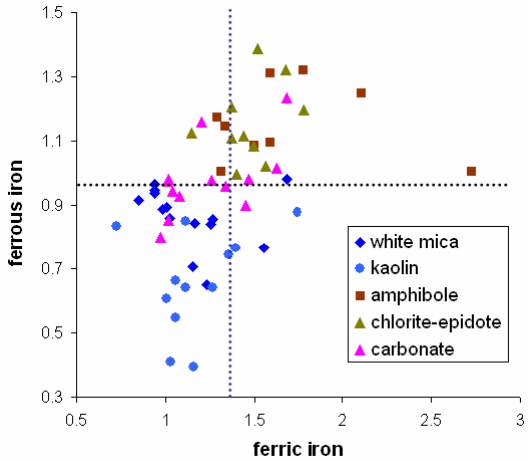

Figure 25. Scattergram of USGS mineral library spectra convolved to ASTER band-passes and then processed to capture ferrous iron (B_5/B_4) versus ferric iron (B_4/B_3).

As mentioned above, the ASTER spectral band configuration is not well designed to map iron oxides (instead it was designed similar to Landsat TM for mapping green vegetation) as it misses the important iron oxide crystal field absorption at 900 nm. This is demonstrated in Figure 26 which plots these two parameters for a suite of 39 rock and soil samples. The iron oxide content is assumed to be proportional to the XRF $\%Fe_2O_3$ content. The results show

that both ASTER ratios do not show significant correlation with the chemical data though the B_4/B_3 is a marked improvement over the B_2/B_1 suggesting that it is a better measure for iron oxide content. The other important consideration is the role of atmospheric scattering which increases with shorter visible wavelengths. That is, ASTER bands 1 and 2 are the most susceptible to this potential additive error due to uncorrected aerosol atmospheric effects.

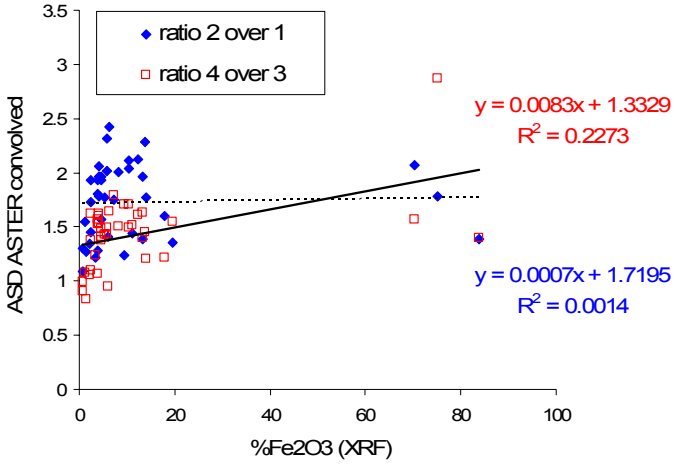

Figure 26. Scattergram of the Fe_2O_3 contents of field samples versus the predicted iron oxide content calculated from the ASD reflectance measurements of the same samples but convolved to ASTER spectral resolution and processed using two ratios, namely B_2/B_1 and B_4/B_3.

REMOTE GEOSCIENCE INFORMATION PRODUCT VALIDATION

The validation of the derived geoscience information products from the calibrated ASTER and HyMap surface reflectance data is based on field ASD spectral measurements, primarily of soils samples, convolved to both the ASTER and HyMap bandpass configurations. The decision to use soil sample spectra was chosen to mitigate complications in accurately deriving a "pixel" estimate for comparison from a range of field samples and spectra taken from any one locality. These samples included all the typical rock and soil types. The ASD spectra were taken from both the fresh and weathered surfaces such that 3-10 spectra were taken from any given locality. This is a major complication and is compounded by the mixing effects of both green and dry vegetation at the pixel-scale.

To overcome these issues, the validation procedure selected a relatively vegetation-free area in the vicinity of the former Tick Hill Au mine, 100 km southeast of Mount Isa (Figure 2: Stage 1: Block G) that was dominated by soil spectral features. The assumption being that there was little contribution from any rock (or vegetation) signature such that the soil spectra could be used alone for validation of the HyMap and ASTER products. Given the number of products generated from ASTER and HyMap (~40), the validation presented here is restricted to only a few basic ASTER and HyMap geoscience products, namely the iron oxide, Al-clay content and water content, though other mineral product validation data (e.g. white mica content) are provided elsewhere in this report (below).

This type of validation is also subject to complications. The major one being that a sample of only a few cm^2 from a heterogeneous field site is assumed to be the same as a remotely sensed pixel of >20 m^2 with both assumed to be from the same location but with the accuracy of their geo-location position being +/- 30 m. To help reduce this uncertainty in pixel positioning, regions of interest (ROI) spanning 4-40 coincident pixels over the expected field sample point were collected from the processed HyMap data.

Iron oxide content

The iron oxide content is indicated by the depth of the 900 nm absorption feature. The HyMap spectral data (Figure 27a) shows significant correlation (at 99% confidence level) with the spectral data from field soil samples (Figure 27b). This is also apparent in Figure 27a where comparable colours to the image are applied to the field samples according to the measurement of the 900 nm absorption depth. The colours of the field data are consistent with the HyMap product, even at this small scale. This is an excellent result and shows that the processing methodology applied to the HyMap is accurately measuring the iron oxide content. However, the resultant scattergram shows a relationship that is not "*y*=*x*". That is there is slight curvature to the trend where the HyMap predictions are increasingly over estimating the depth of the iron oxide crystal field absorption feature at 900 nm with increasing iron oxide content. The reason for this non-linear behaviour is unclear though could be a mixing effect with the little vegetation present. Or more likely, this is a mixing effect with an iron oxide poor rock component as iron oxides are *trans-opaque* at these wavelengths while clays and quartz are transparent, with the mixing of the different material being non-linear (Clark, 1983). The general over-estimation by the processed HyMap data is for at least two reasons: (1) iron oxide rich rocks being captured at the pixel level or not captured by use of the soil spectra alone; and (2) the HyMap reflectance spectra having systematic, high frequency noise related in large part to residual atmospheric correction errors.

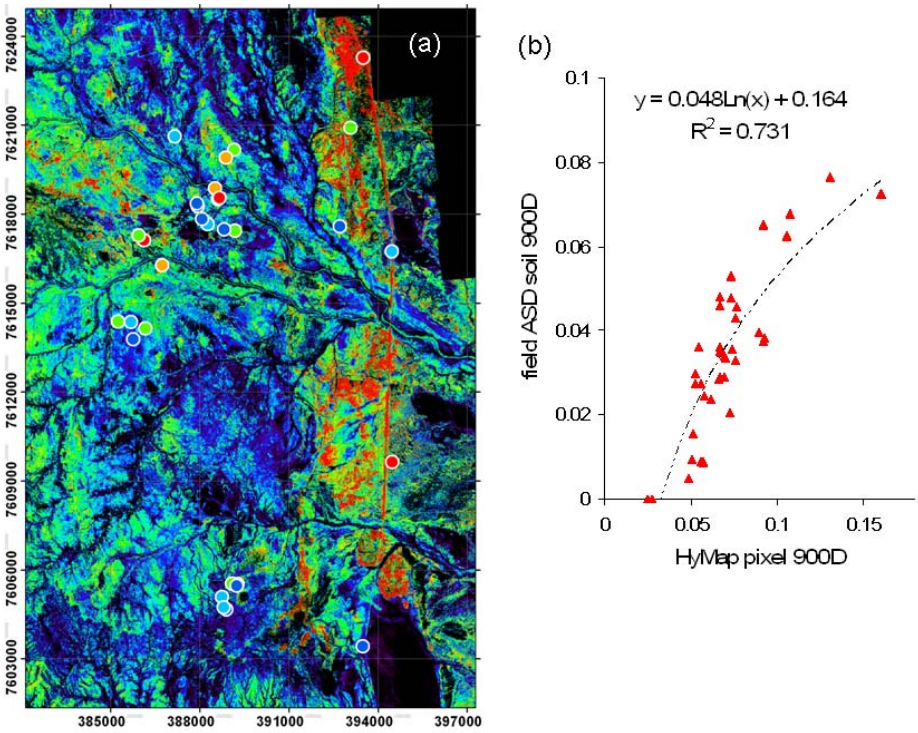

Figure 27. (a) Iron oxide content map of the Tick Hill area, derived from HyMap reflectance data together with field ASD spectra of soil samples from 33 sites (coloured circles). The field spectra were convolved to the HyMap band-pass responses and processed using the same algorithms as the HyMap data. The rainbow-scale of colours range from blue = low detectable abundance to red = maximum detectable abundance. Note these data have been masked to exclude pixels with green and dry vegetation above a certain threshold as well as dark pixels (see Appendix 7 for details). (b) Scattergram for the predicted iron oxide content from the HyMap ROIs versus the soil sample data from the same areas/sites. Iron oxide abundance is indicated by the depth of the 900 nm absorption feature, referred to as 900D.

Figure 28 compares HyMap pixel spectra from iron-oxide poor (blue) and rich (red) areas collected during different airborne campaigns in the Mount Isa area in 2006, 2007 and 2008 (Figure 2, Blocks A^l, H and F^l). For a given campaign, the same systematic (gain effect) high-frequency noise is apparent. This is largely a residual error from the atmospheric radiative transfer correction, which is common and expected given the accuracy of the models and the instrument wavelength calibration which is at best accurate to 1 nm (Terry Cocks, pers. comm.). Importantly, for a given campaign, this high-frequency noise is systematic for the whole survey and can be reduced in appearance, but not necessarily effect, using various multiplicative "smoothing" routines, such as EFFORT polishing in ENVI™. The cross-calibration between campaigns and its impact on generating transferable, seamless mineral maps thus remains problematic. For example, using the same 2nd order polynomial fitting method to the spectra in Figure 29 to measure the depth of the 900nm iron oxide crystal field absorption will generate different depths (contents) each campaign even though the ground targets may have the same iron oxide amounts. The products for different campaigns currently need to have re-scaling factors (e.g. Figure 6) to ensure that they are comparable. This is a fundamental problem with the existing methods and current research is pursuing solutions to removing these systematic residuals.

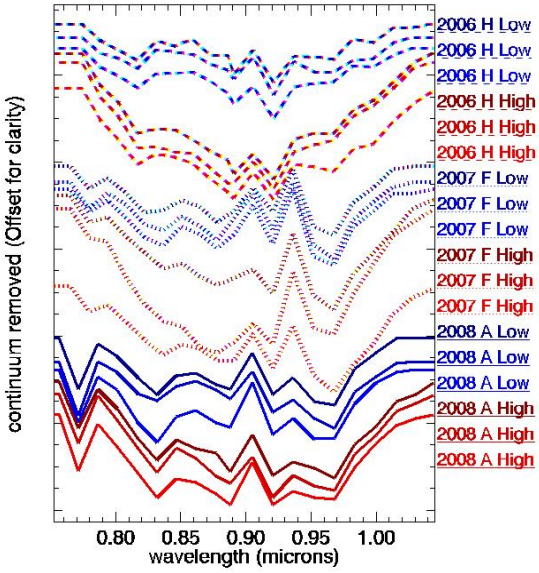

Figure 28. HyMap spectra collected from high iron oxide- content (red) and low iron oxide content (blue) pixels from three different airborne campaigns at Mount Isa in 2006, 2007, and 2008.

Even though ASTER (like Landsat) is not well designed for mapping iron oxides, a ratio of B_4/B_3 can provide some information on iron oxide content. Figure 29 presents this band ratio for the calibrated ASTER data over the Tick Hill area together with ASD spectra of soil samples collected from the field that have been convolved to the ASTER band response functions and have had a similar ratio implemented. The bigger pixel 30 m footprint of ASTER makes the task of this type of validation even more difficult compared with HyMap (Figure 27). Despite these complications there is some broad correlation (at 90% confidence level) evident (Figure 29b). This broad correlation is evidence to suggest that the reduction of the ASTER data to reflectance, including additive aerosol effects, has been effective. However, despite these useful results, a comparison between this ASTER derived iron oxide map (Figure 29a) and the HyMap iron oxide map (Figure 27) shows very limited correlation. These areas include "A" and to a lesser degree "B" (in Figure 29). However, other areas, such as "C" and "D" are opposite to the patterns observed in the HyMap product (Figure 27). One main reason for this "error" in ASTER mapping of the iron oxide content is the difficulty

of unmixing the dry vegetation component as most of these “false positives/negatives” described above are related to spinifex grass and other dry plant materials, especially after seasonal rainfall. This is not a problem with the HyMap data as it has spectral bands that adequately capture the related cellulose absorption of dry plant material at 2080 nm and so dry vegetation can be removed from the derived products.

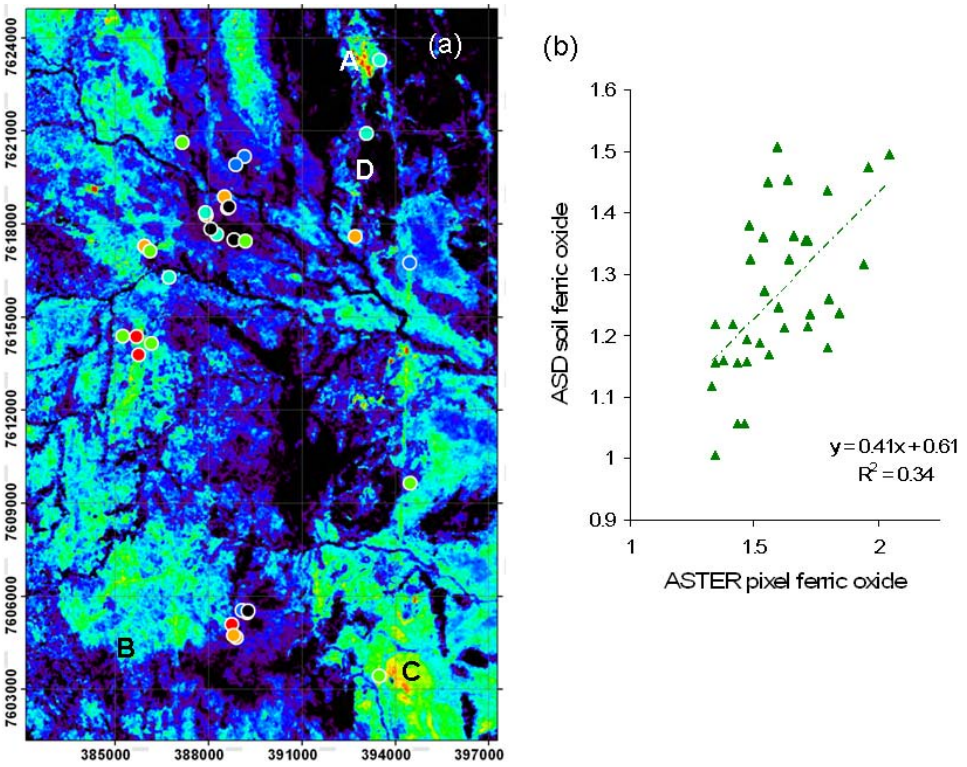

Figure 29. (a) Iron oxide content map of the Tick Hill area, derived from ASTER calibrated reflectance data using a ratio of B_4/B_3, together with field ASD spectra of soil samples from 33 sites (coloured circles). The field spectra were convolved to the ASTER band-pass responses and processed using the same algorithms as the ASTER data. The rainbow-scale of colours range from blue = low detectable abundance to red = maximum detectable abundance. Note these data have been masked to exclude pixels with green vegetation above a certain threshold as well as dark pixels (see Appendix 8 for details). (b) Scattergram for the predicted iron oxide content (value of the B_4/B_3 ratio) from the ASTER ROIs versus the soil sample spectral ratios from the same area/site.

Al-clay content

The Al-clay content, which in this case includes the kaolin, white mica and Al-smectite mineral groups, was measured from the HyMap reflectance data using a fitted 4th order polynomial and also included several masks (see Appendix 7 for details). The depth of the 2200 nm absorption feature is used to indicate Al-clay abundance. Figure 30 presents a comparison of the field ASD spectra and processed HyMap imagery. Both the image (Figure 30a) and scattergram (Figure 30b) show high correlation, which highlights the high quality of the HyMap data and the veracity of the assumptions used in this validation. The significance of this result for regional mapping of clay content for soil mineral mapping is discussed in the case histories below.

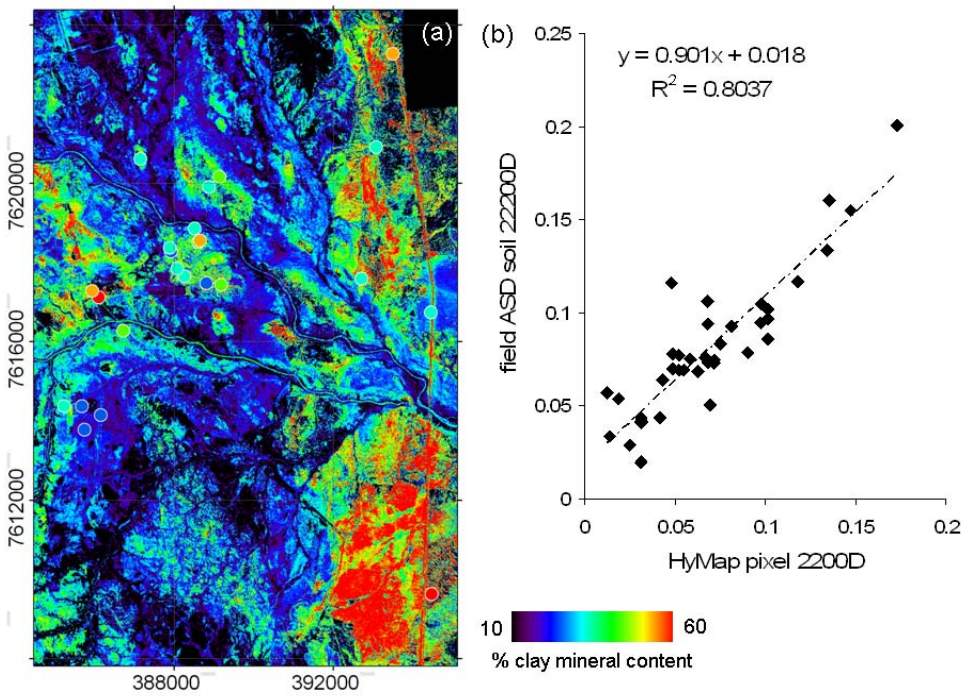

Figure 30. (a) Al-clay content map of the Tick Hill area, derived from HyMap reflectance data together with field ASD spectra of soil samples from 33 sites (coloured circles). The field spectra were convolved to the HyMap band-pass responses and processed using the same algorithms as the HyMap data. Note these data have been masked to exclude pixels with green and dry vegetation above a certain threshold as well as dark pixels (see Appendix 7 for details). (b) Scattergram for the predicted Al-clay content based on the depth of the 2200 nm absorption feature (2200D) from the HyMap ROI's versus the soil sample spectral data from the same area/site.

Figure 31 shows the validation results for processing of the three ASTER bands suitable for capturing Al-clay content, namely $(B_5+B_7)/B_6$. An obvious image scene edge is apparent angled down the centre of the study area that is not observed at shorter wavelengths (Figure 29a). This is interpreted to be related to local differences in vegetation content and its probable impact (as a bright material, especially in Band 4) on the magnitude of the spatially-dependent ASTER SWIR cross-talk effect. Even though all the recommended, as well as additional steps, were taken to reduce the impacts of this effect, it can still have some influence at a local-scale. Note that towards the bottom and top in this image, as well as beyond the image limits, this problem disappears. This effect has thus had an impact on the predicted Al-clay content with the left image showing relatively lower abundances compared to the right image. Combined, the correlation between the field and ASTER data is broad (R^2= 0.26). When separated (Figure 30b), the correlation increases only marginally (R^2= 0.36). This is a poorer result compared with the HyMap predictions (Figure 30) and highlights the fact of the major differences in the abilities of these sensors to provide accurate geoscience information products. Unlike, the iron oxide results, the ASTER Al-content shows closer spatial correlation with the HyMap Al-content map. For example, areas "A" and "B" are high clay contents and "C" and "D" are low contents observed in both products, but there still remain opposing patterns, such as "E" and "F". These differences are likely in large part to be caused by the difficulty of removing the effects of dry vegetation in the ASTER data.

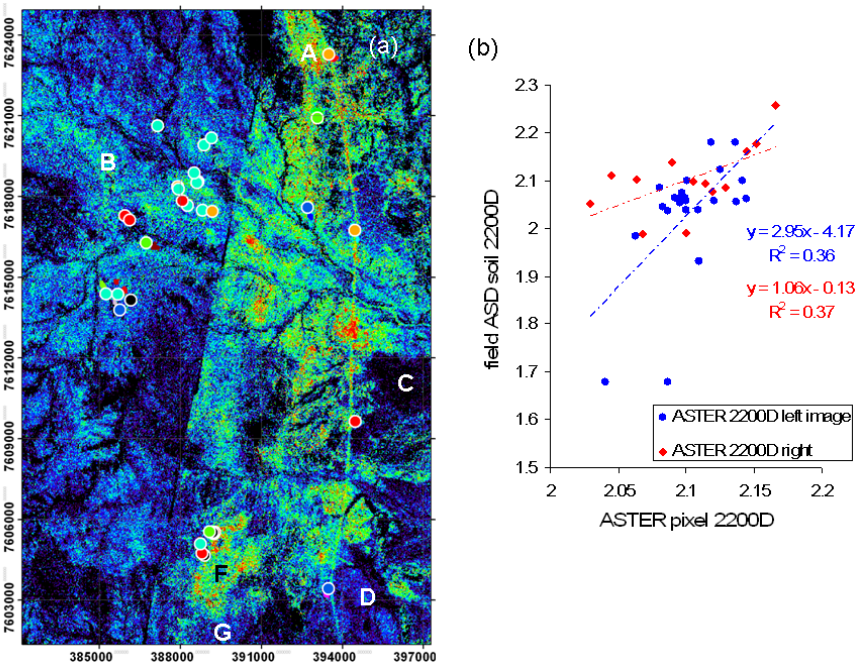

Figure 31. (a) Al-clay content map of the Tick Hill area derived from ASTER reflectance data using (B_5+B_7)/ B_6, together with field ASD spectra of soil samples from 33 sites (coloured circles). The field spectra were convolved to the ASTER band-pass responses and processed using the same algorithms as the ASTER data. The rainbow-scale of colours range from blue = low detectable abundance to red = maximum detectable abundance. Note these data have been masked to exclude pixels with green vegetation above a certain threshold as well as dark pixels (see Appendix 8 for details). (b) Scattergram for the predicted Al clay content from the ASTER ROIs versus the soil data from the same area/site, using the same ratios ((B_5+B_7)/ B_6) as an indicator of abundance.

Vegetation effects

The amount and nature of vegetation of any area can change over time depending on rainfall, growing season, fire and other environmental effects. As a consequence, the generation of seamless mosaics from multiple flight-lines acquired at different times becomes challenging, (*e.g.* ASTER mosaic, Figure 8). As a result of these temporal changes in vegetation cover and the objective to generate accurate estimates of the surface mineral abundance, it is important to be able to remove, or at least reduce, the effects of the vegetation components.

In the broadest sense, vegetation can be considered as either green (actively photosynthesizing) or dry (cellulose and lignin). The task of removing their contribution at the pixel-scale is to then estimate the effects of these two vegetation endmembers and then remove their contribution from the desired mineral product.

The spectral parameter approach contribution being developed by CSIRO (Rodger and Cudahy, in prep) to unmix the vegetation is tested for only one vegetation-unmixed product, namely “vegetation-unmixed Al-clay content” (Appendix 7) and has been released as part of the Stage 2 data release only. An example of the “vegetation-free” AlOH clay content product is presented from the Georgetown area (Block G) in Figure 32c, together with the original AlOH clay content (Figure 32b). The locations and nature of the vegetation at the field sample sites are shown in Figures 32a and 33, together with ASD spectra of “fresh”

rocks from these sites, in Figure 34. The field sites were situated within natural vegetation dominated areas, away from the dirt track and estimated at 70%+ vegetation cover (Figure 33).

These image products show that:

- The unsealed tracks traversing the centre of the image, display high clay contents all along their length before unmixing (Figure 32b) but after unmixing, they blend in with their background geology (Figure 32c);
- The field ASD spectra (Figure 34) show that sites 23, 24 and 27 have similar large AlOH absorption depths at 2200 nm whereas samples from sites 25 and 26 have smaller AlOH absorption depths. This pattern is best illustrated with the vegetation unmixed product, especially sample site 24, which shows low clay content before unmixing but high clay content after unmixing; and
- After unmixing, there is a very pronounced NNE-SSW trending zone of high (red tones) AlOH clay content, flanked by continuous zones of low (blue tones) AlOH clay content (Figure 32c). These mineral trending zones are only weakly apparent before unmixing (Figure 32b).

These results show that this new vegetation unmixing process provides valuable, accurate new information regarding the geology by lifting the geological-mineralogical response as if there were no vegetation cover for those pixels with <70% vegetation.

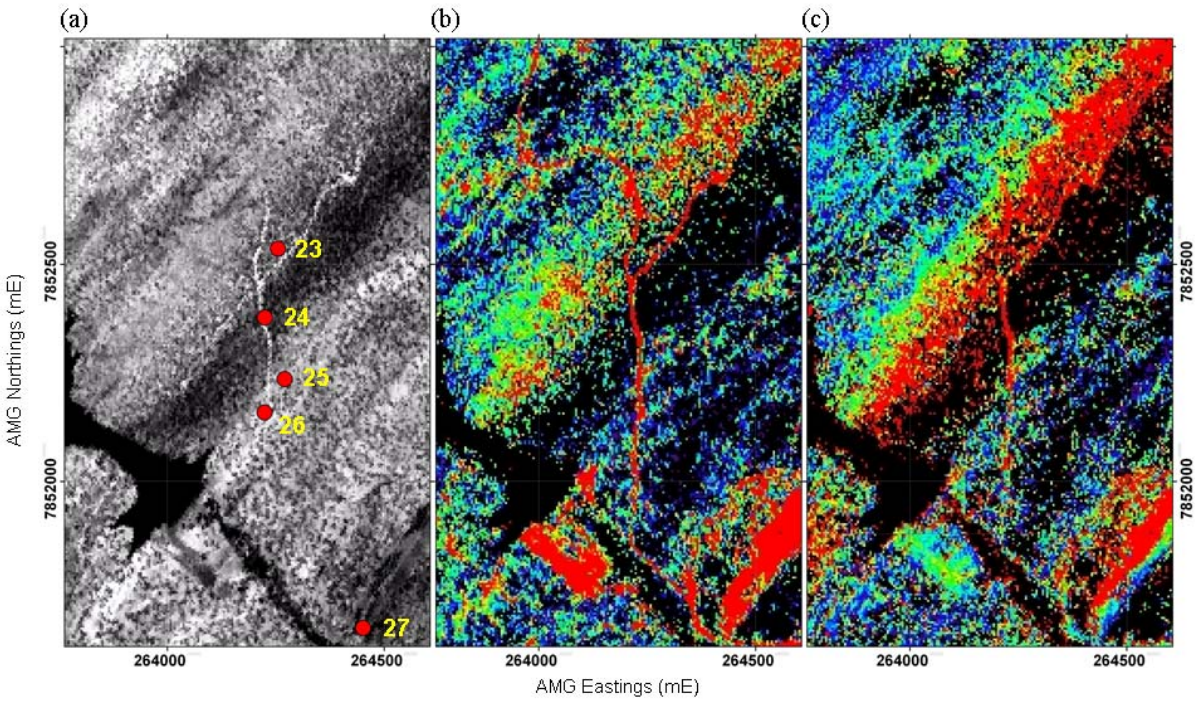

Figure 32. (a) HyMap "albedo" image (reflectance @ 1650 nm) with location of field validation sites. Note the darker eastern slope of NNE-trending ridge in the centre due to topographic shading; (b) Standard AlOH clay content image generated using the continuum-depth of the 2200 nm absorption. Note the "clay-rich" tracks running N-S through the centre of the image; (c) Vegetation unmixed AlOH clay content image. Note how the tracks have changed their response, blending in with the surrounding vegetated landscape.

Figure 33. Field photographs of the (a) Site 23 at the top of the hill; (b) Site 25; (c) Site 24; and (d) 26. Note the differences in vegetation cover and type, especially the density of trees and (dry) grasses.

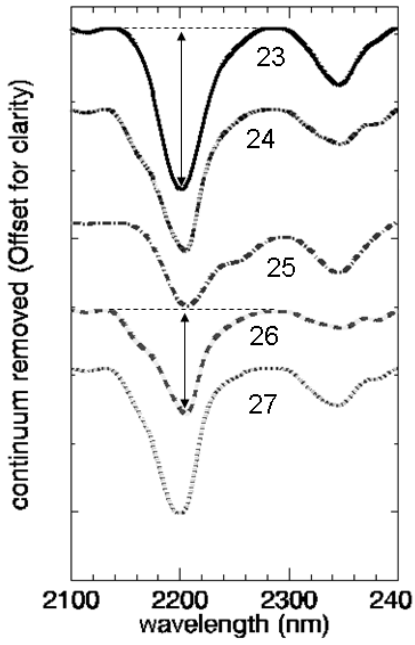

Figure 34. Field ASD spectra of fresh rock samples taken from the field sites (numbered 23-27). Note that samples 23, 24 and 27 have relatively deep AlOH absorption at 2200 nm compared with samples 25 and 26. Refer to Figures 32 and 33 for their location and vegetation cover.

To further validate the reliability of this new product, the field data were quantitatively compared with the HyMap predictions for AlOH clay content. There were over 40 sample sites, including the five shown in Figure 32a, where visual estimates were made in the field of the proportions of rock, soil, dry plant material (including leaf and dry grasses) and green plant material (trees and bushes) cover. The ASD spectra of the weathered rock and soil were then linearly combined in the proportion noted for each site and then rescaled to compensate for the estimated vegetation content. These scaled estimates of the AlOH clay content were then assessed against the HyMap clay contents (before and after unmixing) for ROIs over these field sites. The results (Figure 35) show that the unmixing procedure has:

- Increased the correlations between the field and airborne data; and
- Increased the slope closer to the desired y=x line.

This is a significant improvement, providing a strong impetus to apply this method for each mineral product at a future date.

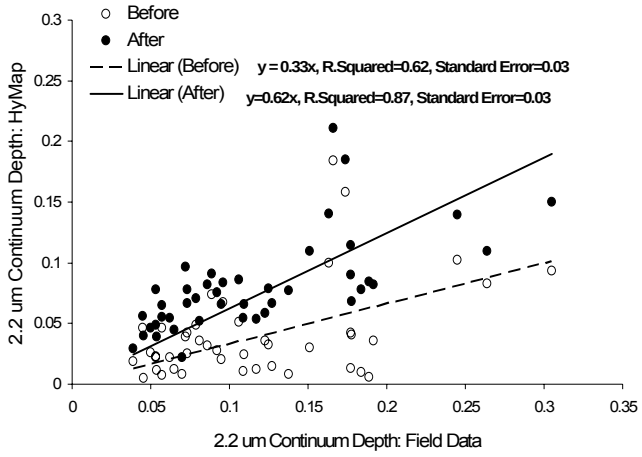

Figure 35. Scattergram of the continuum-depth of the AlOH absorption at 2200 nm for field samples (x-axis) versus HyMap ROI (y-axis) before (open circles) and after (solid circles) vegetation removal. Note that after vegetation unmixing, (1) there is an increase in slope approaching the ideal y=x relationship; (2) there is an increase in correlation between the field and airborne data.

Lichen effects

During the course of the Stage 2 processing it became apparent that many of the well exposed outcrops of limestones in the Hodgkinson and Georgetown areas (Figures 36a and b, respectively) were not being mapped using the MgOH product, even though both the airborne and field spectral signatures showed a significant absorption at 2335 nm (Figure 35d). The problem was found to be related to the green vegetation mask which mapped even 100% outcrop of limestone as green vegetation as measured using the NDVI (Merton) index. Both the ASD and the airborne signatures of the weathered rock surfaces showed absorption at 693 nm, as would be expected from chlorophyll, and also a steady rise in reflectance at longer wavelengths into the NIR, although the typical NIR shoulder/plateau of green vegetation is not apparent. It was also noted that there is no apparent development of “leaf” water absorption at 970 and 1200 nm in the HyMap or field spectra. These spectral properties are similar to the crustose lichens developed in sub-polar regions (Rees and others, 2004). Close inspection of the exposed versus broken rock surfaces (Figure 36c) showed a dark patchy surface covering which is considered to be this lichen.

To solve this problem of incorrect green vegetation masking, a new mask was developed based on the continuum-depth of the “leaf” water at 1200 nm, which is well-developed in green vegetation but not apparent in the dry lichen spectra (Figure 36f). This new mask was implemented on the Stage 2 Georgetown, Hodgkinson and Pajingo Blocks only as similar problems were not apparent for the Mount Isa area.

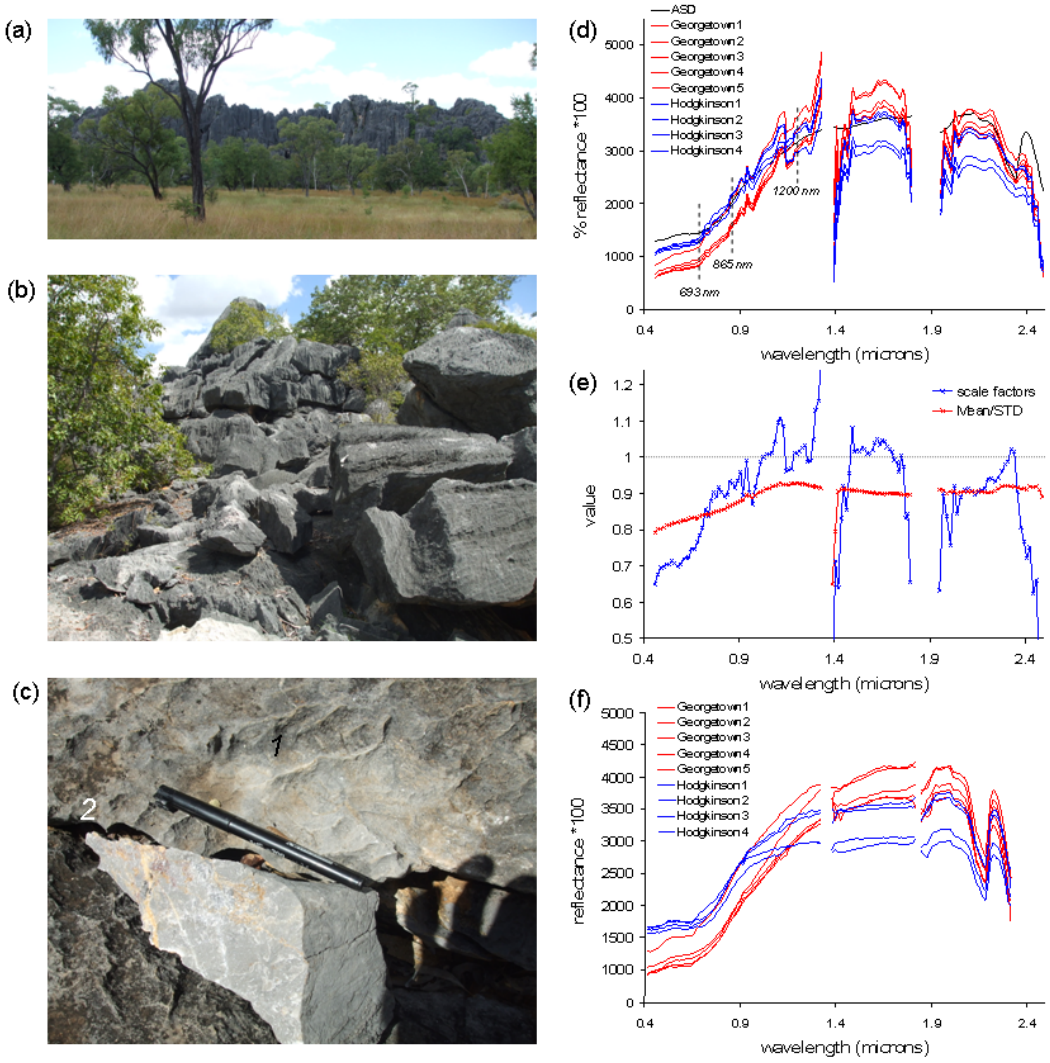

Figure 36. (a) Extensive flat-lying limestone outcrop at a tourist cave entrance near Chillagoe, Hodgkinson Block B (GDA94 MGA Zone55 233890 mE 8098400mN); (b) Limestone outcrop in Georgetown Block G (QS21: GDA94 MGA Zone54 269925E, 7850083); Note that between the isolated large green trees are extensive areas of exposed rock; (c) Close up of the weathered, and partly dark lichen covered surface as well as a broken rock that shows “fresh” limestone (QS21: GDA94 MGA Zone54 269925E, 7850083); (d) HyMap pixel spectra and an ASD field reflectance spectra of the limestones shown in Figures 36 a-c; (e) Scattergram showing (i) an estimate of the HyMap signal to noise (red curve) based on statistics generated from the large area (200 pixels) of exposed limestone shown in Figure 36a (standard deviation divided by the mean for 200 pixels) and (ii) scale factors that can be used to remove the systematic, high frequency, atmospheric residuals apparent in the HyMap non-EFFORT corrected spectra as shown in Figure 36d, and calculated by dividing the mean HyMap spectrum by the mean ASD spectrum for all selected limestone pixels/samples; (f) The same HyMap pixel spectra presented in Figure 36d but corrected using the scale factors presented in Figure 36e. Note the removal of the high frequency atmospheric residuals and the enhancement of the calcite absorption at 2335 nm.

Signal to Noise

The presence of large areas of flat lying, vegetation-free (except lichen) limestone outcrop in the Chillagoe area covered by the Hodgkinson Block B survey, provided an opportunity to examine the HyMap SNR. Approximately 200 pixels were selected as a ROI from which the mean and standard deviation (STD) were generated. A qualitative measure of SNR was subsequently calculated using the mean divided by the STD but without normalising with respect to a 50% reflectance target as per the method described by Kruse and others (2003). Although this method attempts to remove the effect of the target spectral shape, the calculated SNR typically has some residual shape, which is shown to be the case in Figure 36e (red spectrum). That is, the SNR should in theory be much higher for the VNIR bands compared with the SWIR bands given the amount of sun illumination available and the performance of the detectors. Nevertheless, the results show an overall similar SNR at all wavelengths, except in the vicinity of 1400 nm, which is on the long wavelength edge of the strong water vapour absorption. Interestingly, there is not a similar affect for the stronger 1900 nm water vapour absorption, consistent with the airborne AVIRIS SNR results calculated by Kruse and others (2003).

Compensation for atmospheric residuals

The same data presented in Figure 36 can be used to help correct the systematic, high frequency noise attributed to atmospheric residuals apparent in Figure 36d. That is, the mean of all HyMap ROIs were normalised with respect to the mean of the ASD spectra of weathered rock surfaces from the same sites. The resultant set of coefficients (Figure 36e - blue spectrum) was then applied to the HyMap spectra on Figure 36d to yield the corrected spectra in Figure 36f. The results remove the systematic high frequency noise as well as broader effects (e.g. >2300 nm reduction in reflectance) in all spectra and better highlights the mineralogical information, especially the calcite absorption at 2335 nm. However, as Figure 28 shows, a separate set of coefficients are required for each airborne campaign, assuming that there are no changes in instrument calibration during any given survey.

Figure 37 presents continuum-remove HyMap spectra collected from vegetation-free pixels (e.g. from along dirt tracks) from three different Stage 2 HyMap Blocks with varying amounts of HYCORR modelled water vapour, namely:

- Mount Isa Block G : ~700 atmospheres-cm water vapour;
- Mount Isa Block D – “dry” ground : ~ 690 atmospheres-cm water vapour;
- Mount Isa Block D – “wet” ground : ~ 3000 atmospheres-cm water vapour; and
- Pajingo Block A – 2600 atmospheres-cm water vapour.

The dry versus wet ground issue will be addressed in more detail in the next section. At this stage, the focus is on the relationship of the atmospheric residuals to the overall water vapour content.

These spectra show a number of patterns including:

- The “dry” ground pixels from Mount Isa Blocks D and G produce similar spectral shapes, especially around bands 32-30 and 35-36;
- The “wet” ground spectra from Mount Isa Block D, which have the highest modelled water vapour, also display a deep absorption (water vapour residual) between bands

32 and 30, as well as deeper absorption centred at band 36, relative to the Mount Isa "dry" samples. This comparison suggests that the residual water vapour errors have an impact on the spectral shape on the 900 nm region and thus on any derived geoscience information products, such as ferric oxide content.

- The Pajingo A spectra have slightly smaller band 32 to 30 depths, compared to the wet Mount Isa Block D spectra. This result is consistent with the slightly lower retrieved water vapour values where the depth at band 36 is the largest and the geometry of bands 35 and 36 is different from all other spectra. This suggests an instrument calibration issue which is discussed in more detail below.

The current iron oxide images of these three blocks all reflect these pixel-spectral patterns, including:

- Mount Isa Block D, showing a major step across the image mosaic, including higher predicted ferric oxide content associated with wet ground (next section);
- The dry section of Mount Isa Block D and Mount Isa Block G show similar ferric oxide content histograms;
- The histogram of ferric oxide contents for Pajingo Block A spans much higher values, which suggests generally much higher iron oxide contents compared with, for example, anywhere in the Mount Isa region. This is expected not to be the case and simply an artefact of the large uncorrected water vapour residuals for the Pajingo HyMap data.

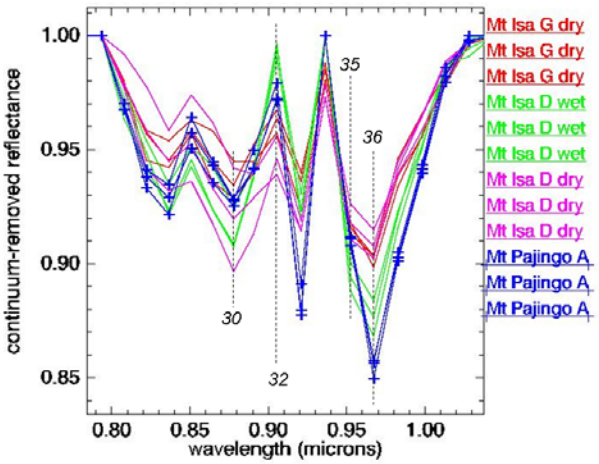

Figure 37. Selected HyMap continuum-remove spectra (780-1070 nm) from vegetation-free pixels collected from three different HyMap Blocks from Stage 2. All of these pixels produce a mid-level iron oxide absorption depth at 900 nm using the current processing. The positions of the selected band channel numbers are annotated. Note the change in geometry between the Pajingo (blue) and data from other areas, especially channels 35 and 36.

Surveying wet ground

One of the problems in mosaicing the Stage 2 HyMap Blocks is associated with data being collected while parts of the survey area were wet. This is demonstrated for Mount Isa Block D, where HyMap data was acquired the day after rainfall was recorded on the 17th (2.4 mm) and 18th (1.2 mm) August 2007 (Appendix 4, Bureau of Meteorology; http://www.bom.gov.au/). Figure 38a presents the HYCORR estimated water vapour image of Block D, indicating a pronounced difference in spectral response between HyMap flight-lines 2-7 (19th August 2007) and HyMap flight-lines 8-12 (20th August 2007). The relative

humidity interpreted from the HyMap data was at moderate levels throughout this period, including: 63% (17th); 45% (18th); 53% (19th); and 42% (20th) with tempertures on the 18-19th being 12ºC (min) to 24ºC (max) and wind speeds ~45 km. The surface water product (Figure 38b) shows a marked difference between these two dates of acquisition, with wetter ground associated with data collected on 19th August. Most of the derived geoscience information products were affected to some degree by this wet ground. However, the greatest effect was on those products sensitive to "water" absorption, such as the Surface Water Bonding image where wet ground is highlighted as unbound water, and also ferric/ ferrous iron products. Major problems of this kind were also recognised in other Blocks, especially Hodgkinson Block A. To avoid this problem, the survey ground should be allowed to dry for at least a day before the survey begins, though this is not always practical operationally.

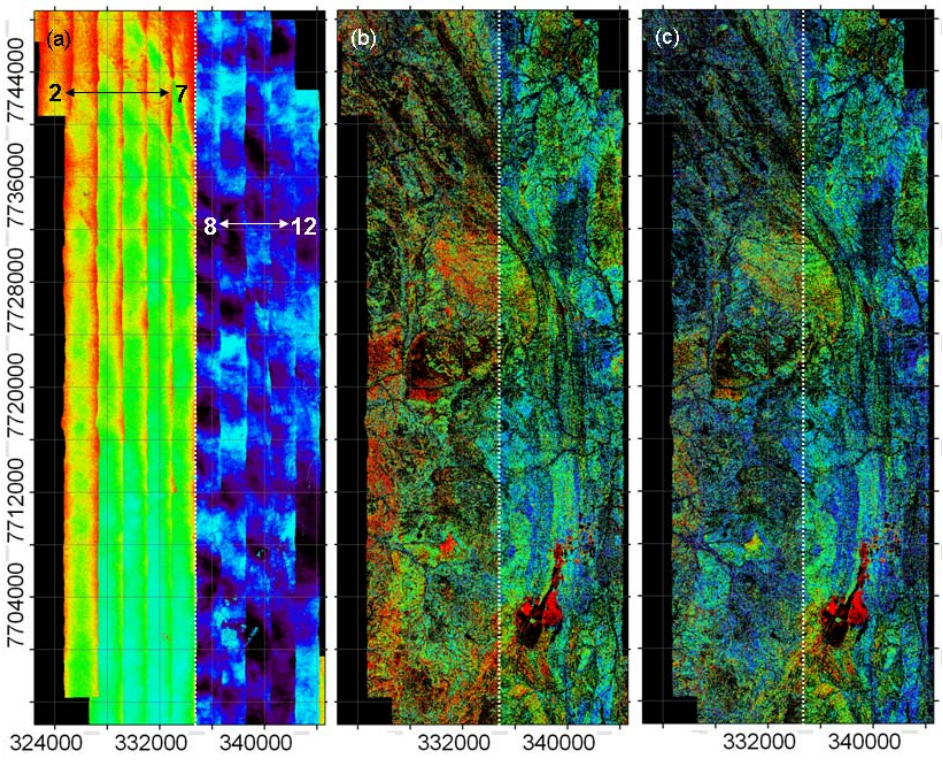

Figure 38. (a) Water vapour image of Mount Isa Block D (Stage 2) estimated using the continuum-depth of the 940 nm absorption derived from the HyCORR/ACORN atmospheric correction of radiance-at-sensor to surface reflectance; (b) surface water content generated using the continuum-depth of the 1900 nm absorption and masked for the effects of vegetation. Note the high water contents on the western half of the Block; (c) Same data as in (b) but levelled using equalisation of scene overlaps to reduce the effects of residual water (surface and/or atmospheric). Flight-lines 2-7 and 8-12 are shown within the western and eastern halves, respectively.

To help resolve this problem related to ground moisture in the current Stage 2 data, affected Blocks were levelled (normalised), based on the statistics generated from the areas of scene overlaps, and referenced to the "dry" flight-lines. The main objective was to apply the same product thresholds for the entire survey, though this would not be practical for any Blocks that are entirely affected by wet ground, which may have been the case for Stage 2 Mount Isa Block E. The effectiveness of this levelling procedure is demonstrated for the surface water content in Figure 37b, with the corrected product shown in Figure 38c. Using this method, problems occur if the ground is variably wet along the length of the flight-line. This along-track problem is examined in the next section.

Along track noise

A large number of flight-lines suffer from along-track effects that also render the derived mineral products difficult to mosaic. The example provided in Figure 39a for the "hematite-goethite ratio" product for Mount Isa Stage 2 Block B, shows one aspect of this problem which causes most of the flight-lines to produce a similar north-south trend but by different amounts.

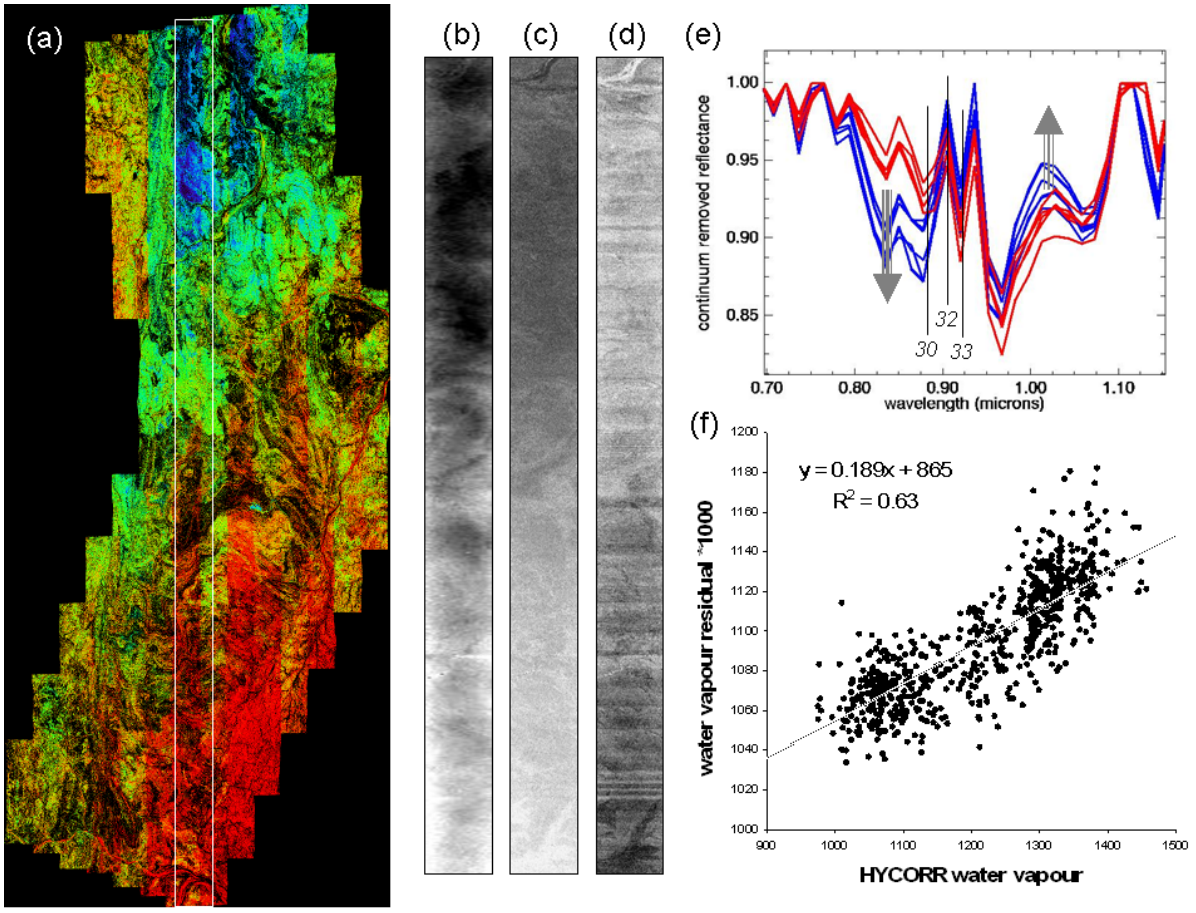

Figure 39. (a) Stage 2 Mount Isa Block B, interpreted wavelength position of the 900nm iron oxide crystal field absorption derived using the 1st derivative of a least squares fitted 2nd order polynomial between 760 (blue) and 1070 (red) nm. Note the changes in colour along flight-line; (b) HYCORR (ATREM) per-pixel water vapour estimate of flight-line 9 (white rectangle in (a)); (c) ratio of the atmospherically corrected HyMap bands 32 over 30 for flight-line 9 aimed at capturing residual (uncorrected) water vapour (see (e)); (d) ratio of the atmospherically corrected HyMap bands 32 over 33, which are both deep in the atmospheric water vapour absorption. Note that scan-line instrument noise is now apparent, though there remains an along-track intensity effect; (e) selected HyMap pixel spectra from the blue and red areas along Flight-line 9 (a). Positions of the bands used in the ratios in (c) and (d) are shown. Note how the blue spectra are deeper at wavelengths <880 nm and shallower at wavelengths >940 nm. This interpreted water vapour residual error effect produces a significant change in geometry of the broad ferric iron crystal field absorption. Unless corrected, accurately tracking the wavelength (and depth) of this iron oxide absorption will remain a problem; (f) scattergram of the HYCORR (ATREM) water vapour estimate versus the ratio of HyMap bands 32/30, related to water vapour residual error. The apparent correlation of these parameters provides a means of predicting the systematic water vapour residual error.

There are several potential reasons for this effect, including:

- variably wet ground;

- other ground conditions, such as flush of green vegetation or fire;
- different surface scattering phenomena linked to illumination/view angle (bi-directional reflectance distribution functions or BRDF);
- atmospheric residuals; and
- Changes in operating instrument performance/calibration.

There is evidence to show that the last two of these effects have caused problems in generating seamless mosaics of the derived geoscience information products, especially for the Stage 2 data. An example of this is presented in Figure 39a, for the hematite-goethite ratio which is based on tracking the wavelength position of the iron oxide absorption between 760 and 1070 nm (Figure 39e) (Cudahy and Ramanaidou, 1997). Clearly, each flight-line does not seamlessly match its neighbouring flight-lines, with (or even without) the same stretch limits applied. Note that this particular product has presented problems in seamless mosaicing for most blocks of the Queensland HyMap surveys in 2006, 2007 and 2008 (Mount Isa Block A) as well as the Kalgoorlie HyMap survey (Cudahy and others, 2005).

To understand what is driving this along track problem, spectra (Figure 39e) from either end of flight-line 9 (white box in Figure 39a) were extracted from iron oxide-rich, vegetation free pixels. The spectral range also encompasses the water absorption between 870 and 950 nm. The image spectra were corrected for atmospheric effects, including water vapour. The question is whether the atmospheric residuals, especially those of water vapour, are influencing the interpreted wavelength of the iron oxide absorption. The spectra from the northern end (blue) versus the southern end (red) of the flight-line show two important features (Figure 39e). First, the blue spectra show a relative reduction (grey arrow) at approximately 850 nm and a rise (grey arrow) at approximately 1000 nm. This could be associated with changes in the hematite-goethite ratio, with the blue spectra being more hematite-rich compared with the red spectra. However, the blue spectra also show a systematic larger step down from channels 32 to 30 compared to the red spectra. As these channels are on the edge of the water vapour absorption, then it is possible that this is a residual effect that can impact on the geometry (wavelength) of the superimposed iron oxide absorption.

To test the influence of water vapour on iron oxide products, the HYCORR water vapour image (Figure 39b) for flight-line 9 is compared side by side with images of two ratios, namely:

- bands 32 over 30 (B_{32}/B_{30} - Figure 39c), designed to measure the short-wavelength edge of water vapour absorption at 900 nm; and
- Bands 32 over 33 (B_{32}/B_{33} - Figure 39d), located over the centre of the 900 nm water vapour absorption.

Both the water vapour and the B_{32}/B_{30} images show a similar decrease in brightness from bottom to top of the flight-line. This relationship is further demonstrated in the scattergram between these parameters (Figure 39f). In contrast, the B_{32}/B_{33} ratio image shows a reversed trend that is much weaker in intensity as well as showing the strong development of cross-track “noise” striping effects. That is, the B_{32}/B_{33} ratio is not as sensitive to this apparent along-track trend.

These artefacts introduced by the water vapour residuals have not been corrected in the current mineral mapping release at this stage. They affect a range of products that use bands that overlap water vapour absorption, including:

- ferric oxide content;
- hematite-goethite ratio;
- ferrous iron content;
- surface water content; and
- surface water bonding.

Wavelength calibration

The possibility of the instrument calibration, and in particular the spectral response functions or wavelength calibration, changing during the course of the campaign or even during an individual flight-line acquisition, is a concern for ensuring seamless, transferrable, accurate geoscience products. Ideally, the instrument should be stable throughout a survey, and ground-based calibration of the sensor should be conducted before and after the campaign to ensure the integrity of the applied calibration data.

Most of the difficulties in generating seamless products can be attributed to atmospheric or surface phenomena (above) though there are rare examples when an instrument effect looks to be at fault. Figure 40a presents the iron oxide content product for Georgetown Block G, which shows a coherent map except for one strip, flight-line 3 which is highlighted by a white dashed box. This flight-line was flown from NE to SW (top to bottom). About one-third of the way down this flight-line, something happened that caused the modelled iron oxide abundances to be much lower than on the adjoining flight-lines. The error was then partly corrected, but continued throughout the remainder of the line at a different level, producing slightly lower levels of modelled iron oxide content compared to the start of the line and to its neighbouring lines. To highlight this effect, Figure 40b presents a ratio of B_{34}/B_{35} generated from the radiance-at-sensor data. This product shows clear steps in behaviour that cannot easily be explained by environmental effects. Three coherent blocks are evident and these are labelled A, B and C. The ROI spectra of these blocks are presented in Figure 40c which show this subtle change in geometry of the water vapour absorption.

To investigate this change in geometry, the radiative transfer software package MODTRAN™ (Version 4) was used to model the effects of different wavelength calibrations. This involved stepping though 0.5 to 1 nm intervals for +/- 10 nm from the actual band centres of the Stage 2 HyMap calibration file. After stepping through, each modelled response was then assumed to be undetected and so given the original calibration file wavelength position. Figure 40d presents a selection of these models and shows very similar spectral behaviour to that observed in the actual HyMap radiance data (Figure 40c). No similar effect could be observed with the CO_2 absorption in the SWIR, suggesting that this problem is restricted to the HyMap VNIR module only.

From this analysis, it was gauged that the change in VNIR wavelength calibration from “A” to “B” was 1.2 nm (shorter) and from “A” to “C” 0.1 nm shorter. This shift in wavelength calibration is near the current accuracy limits of the procedures used to calibrate the HyMap instrument pre(post)-flight on the ground, which is ~1 nm. That is, the sub-nm shift from A to C is much less than the accuracy of the current calibration procedures and thus would be difficult to measure/monitor using current calibration procedures. However, its effect on water vapour correction and downstream mineral products are significant. Thus, new post data collection software procedures for <1nm wavelength calibration are required.

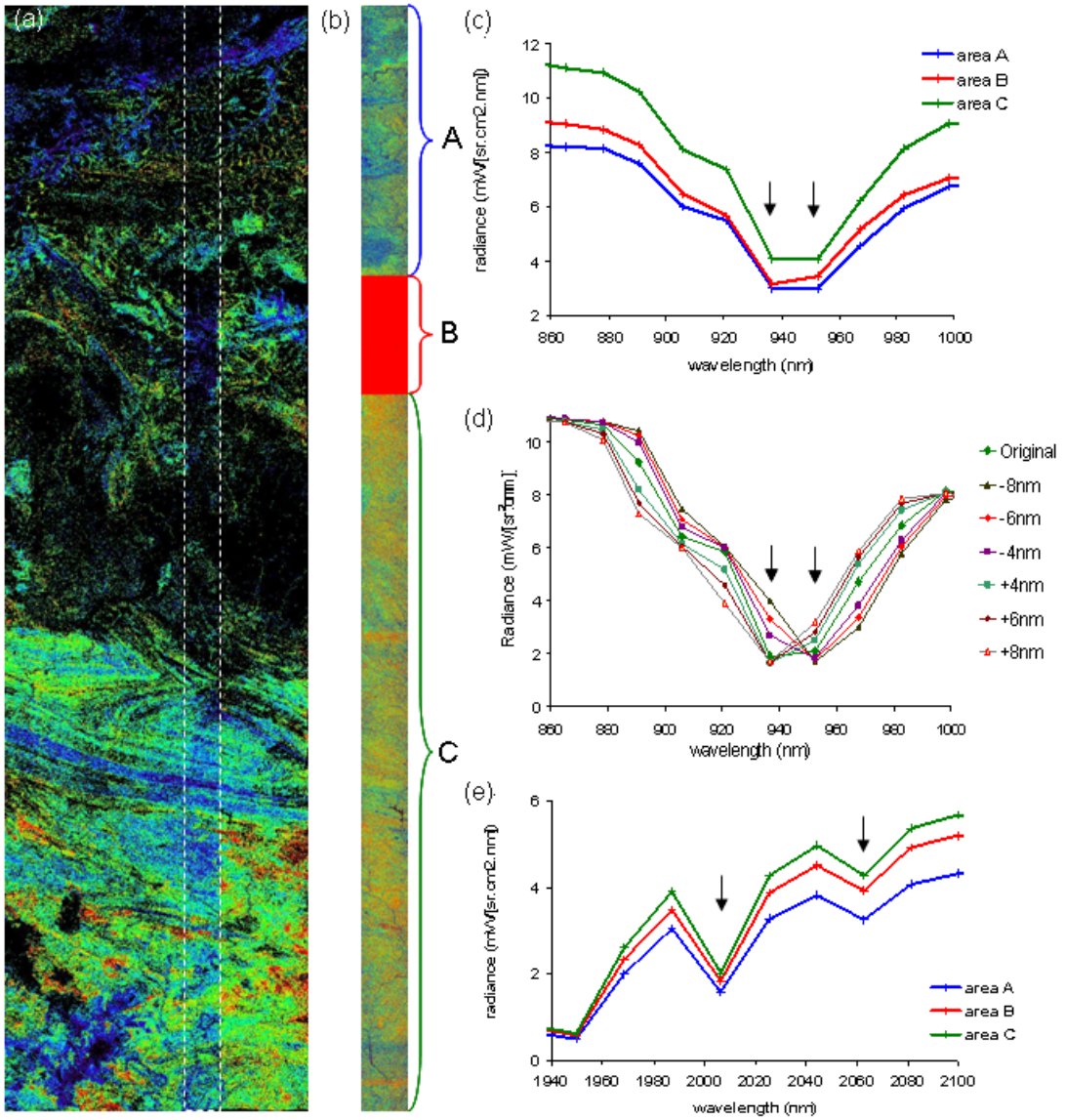

Figure 40. (a) Georgetown Block G iron oxide content image. Flight-line 3 is shown as a white dashed rectangle. Note that this flight-line does not merge seamlessly with the adjoining lines. (b) Ratio image B_{34}/B_{35} of flight-line 3 highlights changes in the geometry of water vapour absorption. Rainbow colour chart applied. Note the three sharply bound and contrasting domains, A, B and C, with domain C associated with the anomalously low iron oxide contents in (a). (c) ROI radiance-at-sensor means from the three blocks shown in (b) for the 860 to 1000 nm region. (d) MODTRAN™ Version 4 water vapour model with band centres shifted incrementally by up to 10 nm longer/shorter but binned as the same band wavelength position to test for possible in-flight wavelength shifts. Note the change in slope of the bottom of the water vapour absorption (arrows). Note the similar change in geometry of the base of the water vapour absorption marked by the arrows. (e) ROI radiance-at-sensor means from the three blocks shown in (b) for the 1940 to 2100 nm region. Note that there is no apparent change in geometry of the CO_2 absorptions marked by arrows.

Comments from Terry Cocks (pers. comm. 2008) about this issue:

"Our (HyVista Corporation) experience of this relates to flights where extreme turbulence was encountered and it is our theory that the scanner on occasions experienced mechanical shock sufficient to move the NIR focal plane. On the next occasion it experiences such a shock the focal plane snaps back to its original position …. hence the blocky nature of the effect…. The consequence

of this NIR focal plane movement is to essentially change the band centre wavelengths in the NIR module…."

"While the wavelength shift is a NIR phenomena only, the effect ripples thro' to other modules when atmospheric water vapour is applied. HYCORR doesn't know there has been a wavelength shift in the block and so will return a different water vapour values to that out side the block (before and after the turbulence jolt)."

"We have subsequently modified the focal plane mechanics and have not seen any re-occurrence in the last 6 months"

RELEASED GEOSCIENCE PRODUCTS

All of the processed geoscience products generated from the ASTER and HyMap sensors, as well as the field-laboratory data, site and sample photos and field site descriptions can be downloaded via ftp pull from the webpage www.em.csiro.au/NGMM through the associated *"Precompetitive data download"* link (Figure 41). Further details of these data are given below.

Figure 41. The front page of the NGMM website (www.em.csiro.au/NGMM). Note the location of the "Precompetitive Data Download" in blue on the left side of the page which is the ftp link to the GIS data.

ASTER

The GIS-compatible ASTER geoscience information raster products are publicly available via ftp transfer through the www.em.csiro.au/NGMM webpage through the *"Precompetitive data download"* link (Figure 41) and under the "*ASTER Geoscience Products*" directories, which have a date attached related to the various versions of released products. It is recommended the

most recent product release be used as updates are generally posted because improved processing methods have been applied. Products have also been released in a variety of GIS-compatible formats including, JPEG, JPEG2000 and geoTIFF. These range in size from 20-100 Mbytes. The current recommendation is to use the geoTIFF files because:

- there is minimal loss of information content; and
- GIS packages, such as ARCMAP™, can more easily identify null values.

The BSQ/BIL format processed image data is also available through the Geological Survey of Queensland and in time limited areas will be available through the CSIRO webpage being developed through AuScope. These files are much larger, being approximately 700 Mbytes each, and can be used in image processing systems such as ENVI™. The 9 band calibrated reflectance file is 7 Gigabytes. Access to the calibrated ASTER reflectance mosaic is copyright protected by ERSDAC (Japan).

This project generated 15 geoscience information products from the 140 cross-calibrated ASTER scenes of the Mount Isa area. There is also an associated meta-data file called:

"*Mount Isa Project Stage 1 ASTER Geoscience Product Descriptions.doc*"

This word file provides:

- The product name, e.g. *"ASTER AlOH group content";*
- The minerals that can be mapped by this product, e.g. *"ASTER AlOH group content"* can comprise: illite, muscovite, phengite, montmorillonite, kaolinite, (and Al-clays);
- The band combinations used to generate this product so that others can replicate the processing, e.g. for *"ASTER AlOH group content"*, involved (1) $(B_5+B_7)/B_6$, (2) and a composite mask of green vegetation and albedo (B_4);
- Details of the thresholds for both the masking and the resultant image product;
- The nature of the colour rendition, including whether a linear or histogram equalization stretch was applied and whether a rainbow colour chart or gray-scale was applied; and
- A qualitative assessment of the accuracy of the product, including the source of likely error or spectral "contamination" from overlapping minerals.

An example of the composite ASTER mineral group map is provided in Figure 42 which presents the AlOH content (Figure 42a) and the AlOH group composition (Figure 42b). Important things to note from these images include:

- No apparent correlation (similarity in colour) between these products. That is, these products are independent from one another even though these use the same 2-3 spectral bands;
- Minimal development of edges between scenes. This demonstrates the success of the scene cross-calibration. Note that ~90% of the signal (=albedo) has been removed though the ratio process, which would accentuate any additive mis-calibration between scenes.

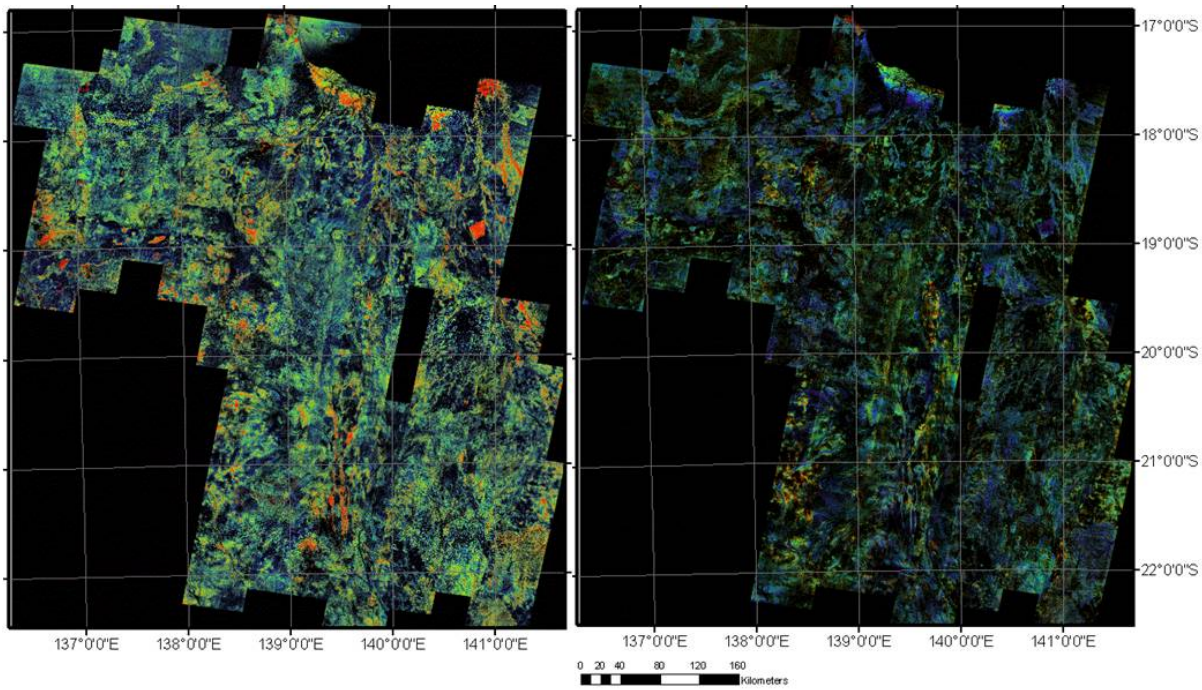

Figure 42. (a) ASTER mosaic of the AlOH group content generated using a (B_5+B_7)/B_6 combination with red tones representing high abundances and blue tones low abundances. Areas of black are masked out because they are below the threshold for clay content and/or contain excessive green vegetation, water, deep shade or were not covered by the available ASTER imagery. (b) AlOH group composition is based on a B_5/B_7 and masked for those pixels with sufficient AlOH group clay content as well as the other masks used for the AlOH group content.

HyMap

This study generated up to 25 geoscience information products from each of the 25 Blocks (9-16 flight-lines for each Block) of HyMap reflectance data from across northern Queensland (Figure 2). Details of the number, dates and times of flight line acquisition is given in Appendix 3. There are also a number of associated meta-data files that describe these geoscience products, including:

- *Mount Isa Stage 1 HyMap Geoscience Product Descriptions.doc*"
- *"Stage 2 HyMap Geoscience Product Descriptions D.doc"*

As with the ASTER products and metadata files, the HyMap GIS-compatible geoscience information raster products are publicly available via ftp transfer through the www.em.csiro.au/NGMM webpage and the *"Precompetitive data download"* link and under the "*HyMap Geoscience Products*" directories, which are also date stamped. There are also a number of sub-directories for different dates (Stages) and under these are a further series of subdirectories for each product type, e.g. "*white mica content*". Each mineral map product (geoTIFF, JPEG, JPEG2000) is between 10 and 200 Mbytes in size. Copies of the BSQ/BIL format processed image data for use in image processing systems can be obtained through the Geological Survey of Queensland and in time through the CSIRO webpage (AuScope). The HyMap radiance-at-sensor and reflectance data is owned by Geological Survey of Queensland and available at the cost of hard drive media and postage. The size of the entire data set is close to 1Terabyte.

Figure 43 provides an example of the HyMap mineral products, namely "white mica content" for Stage 1 Blocks G and H, which are plotted with a backdrop of the ASTER "false colour" image. This figure shows several things:

- The seamless nature of the processed HyMap flight-lines within each block and the apparent continuity in colour range between blocks, i.e. both have blue through to red tones. Note that the same data stretches were applied to all blocks for the normalised products;
- The separation in distance between HyMap blocks; and
- Locations of the Tick Hill and Starra case history test sites (discussed below).

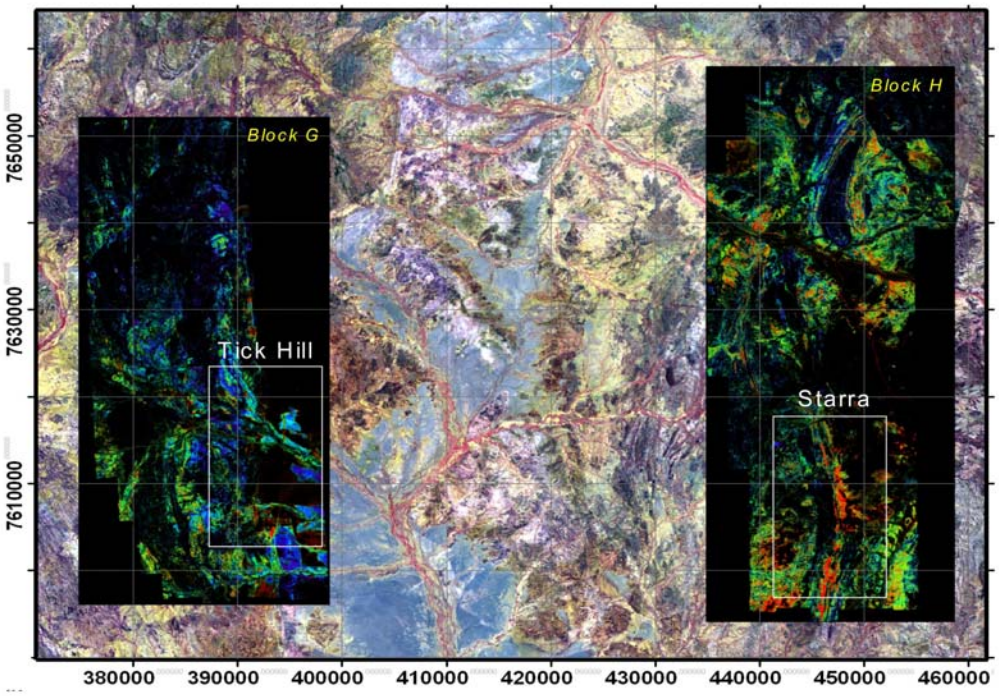

Figure 43. Mosaic image showing the white mica content images for Mount Isa Stage 1 Blocks G and H with a back drop of the ASTER false colour image. The locations of two of the detailed case histories are shown by white boxes.

Field and laboratory data

Appendix 6 provides a list of the of field and laboratory analyses. The data includes:

- ASD spectral reflectance of all field samples (~1000) in text format;
- Electron microprobe analyses of white mica composition from five samples in EXCEL table format;
- X-Ray diffraction spectra from ~300 samples in text format;
- Carbon C13 stable isotope data from 1 sample;
- Field sample photos of all 211 field sites in jpeg format;
- Photos of all samples in jpeg format;
- Field descriptions of all samples and sample sites including MGA coordinates in EXCEL format.

CASE HISTORIES

The value from the mineral maps becomes tangible when considered within the context of an exploration geological model. Unlike some other pre-competitive geoscience data, mineral maps will provide limited value if only used for finding linear features or looking for "red bull's eyes", though there are times when this may be useful. The recommended strategy is a mineral systems approach. This includes: tracking the source and pathways of the mineralising fluids and recognising mechanisms that may force these fluids to drop their metal load, especially contrasting physicochemical conditions - map the gradients (Walshe and others, 2003)!

The following IOCG case history of the Proterozoic Starra Cu-Au system in the Eastern Succession of the Mount Isa Block shows the process of building a suitable mineral system model which allows the selection of the necessary geoscience information products, whether they are mineral maps, geophysics or geology. This case history was also presented as part of the proceedings for the PACRIM 2008 conference (Cudahy and others, 2008).

Also in this section, airborne mineral maps are tested for recognising big footprint alteration associated with the Mount Isa Pb-Zn and Cu deposits using the published geology. This is followed by testing the illite crystallinity index product as a geobarometric tool in the Century area. Finally, various open pit mines imaged using HyMap are examined for their alteration mineralogy, especially white mica composition. A soil mapping case history has also been developed for the Tick Hill area (Figure 43) and published by Cudahy and others (2009) but will not be presented in this report.

Proterozoic IOCG Mineral System Analysis

The source of the mineralising fluids for Proterozoic IOCG deposits remains unresolved with both magmatic (Pollard, 2000) and intrusion heated sedimentary brine (Cox and Singer, 2007) models, with the latter supported by the observation that Na-alteration is typical in most IOCG systems. Whatever the mechanism is, oxidized fluids rich in K, Fe, Cu, Au and other metals migrated from source rocks into surrounding country rocks with ore deposition occurring where the metal-rich fluids mixed with reduced fluids/rocks.

Using geophysical data (magnetics, radiometrics, gravity), Williams and Pollard (2001) concluded that IOCG deposits in the Mount Isa area are inherently difficult to find as there are no reliable relationships between the location of ore and any specific combination of geophysical characteristics. Furthermore, Mark (1999) concluded that despite the temporal association between magmatism and epigenetic Cu-Au mineralization (ca. 1.59-1.50 Ga), close spatial relationships between intrusions and Cu-Au deposits (i.e. connecting fluid pathways) are rarely observed in the Eastern Succession. Rare examples are intra-ore intermediate dykes at the Mount Elliott Cu-Au deposit (Wang and Williams, 2001), pre- to syn-ore pegmatites at the Osborne Cu-Au deposit (Gauthier and others, 2001) and magmatic-hydrothermal magnetite-rich mineralisation within the Squirrel Hills Granite (Perring and others, 2000).

Finally, the recognised spatial extent of IOCG related alteration zonation is typically small (<1 km). For example, the IOCG-related alteration in the Starra area has been recognised to extend <400 m eastward and only a few metres westward from the orebody (Rotherham, 1997).

Given these challenges, can hyperspectral mineral mapping data provide complementary information to existing geophysical and geological data that delivers new information regarding:

- Fluid pathways from oxidized granites to reduced domains;
- Large footprint alteration signatures (scale of kilometres); and
- Chemical gradients that show rapid changes in physicochemical conditions as these are potential sites for metal precipitation and thus for targeting exploration.

Starra location and geology

The Starra study area is approximately 100 km south of Cloncurry (Figure 43). Figure 44 presents a summary of the published 1:100,000 geology (Mount Merlin and Selwyn mapsheets) which includes a range of Proterozoic rocks (after Foster and Austin, 2008) including: granites (Mount Dore and Gin Creek), calcareous and calc-silicate rocks, non-calcareous rocks (slates, arenites, greywacke, phyllites, rhyolites, quartzites, schists) of the Kuridala Formation (Soldiers Cap Group), Staveley Formation (Cover Sequence 3), Answer Slate Formation (Cover Sequence 3). Major structures in the area include the 1km wide, ductile Starra Shear Zone (SSZ - Adshead-Bell, 1998) and the Mount Dore Shear Zone (MDSZ).

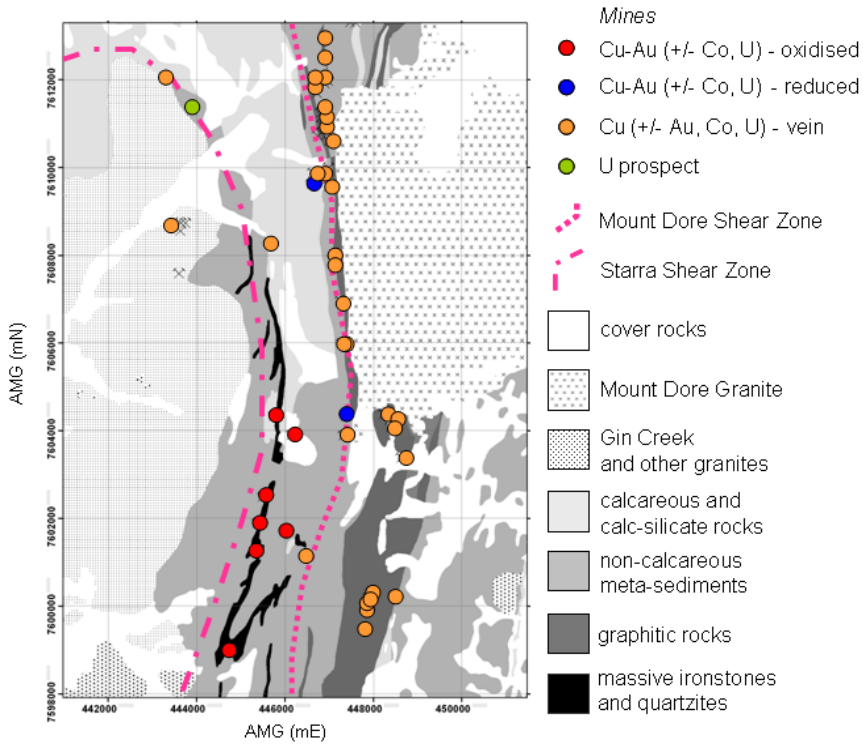

Figure 44. Published 1:100, 000 scale geology of the Starra area showing major rock units (from the Geological Survey of Queensland) as well as Cu +/- Au mineral occurrences.

Rotherham (1997) detailed the geology and alteration of the IOCG deposits of the Starra area. The major IOCG Cu-Au deposits of the area (red dots - Figure 44) are hosted within massive ironstone units aligned N-S over a strike length of 5 km with smaller sub-economic zones extending for a further 5 km within this zone and partly within the SSZ. These magnetite ironstones occur at a lithological contact of metamorphosed sandstones and

siltstones of the Staveley Formation and foliated chlorite-biotite-magnetite schists of the Answer Slate (Figure 44) and are easily mapped using magnetic data (Williams and Pollard, 2001, Figure 45a). Textures are generally massive in appearance, but relict deformed breccia and foliation textures are locally preserved. Sulphide ore textures are more brittle and consist of fine, pervasive brecciation of the ironstones and host rocks. Further to the east in the Staveley Formation are hematite ironstones, which Rotherham (1997) considered to be the product of increasingly oxidised conditions eastward.

The mineral paragenesis for the Starra Cu-Au deposit developed by Rotherham (1997) is presented in Table 4. Several post-metamorphic alteration phases are recognised including: (a) Na, (b) Fe-K; and (c) S and Cu-Au. Key associated minerals detectable using VNIR-SWIR hyperspectral sensing include: (a) actinolite; (b) magnetite and biotite; (c) hematite, white mica (muscovite and sericite), calcite and chlorite. The Cu-Au related alteration halo persisted up to 400 m eastward but only metres westward from the magnetite-hosted IOCG ore bodies and comprises chiefly biotite and chlorite with minor white mica.

Table 4. Alteration mineral paragenesis of the Starra Cu-Au deposit developed by Rotherham (1997). Alteration minerals that developed during the time of Cu-Au mineralisation and are detectable using HyMap are highlighted in magenta.

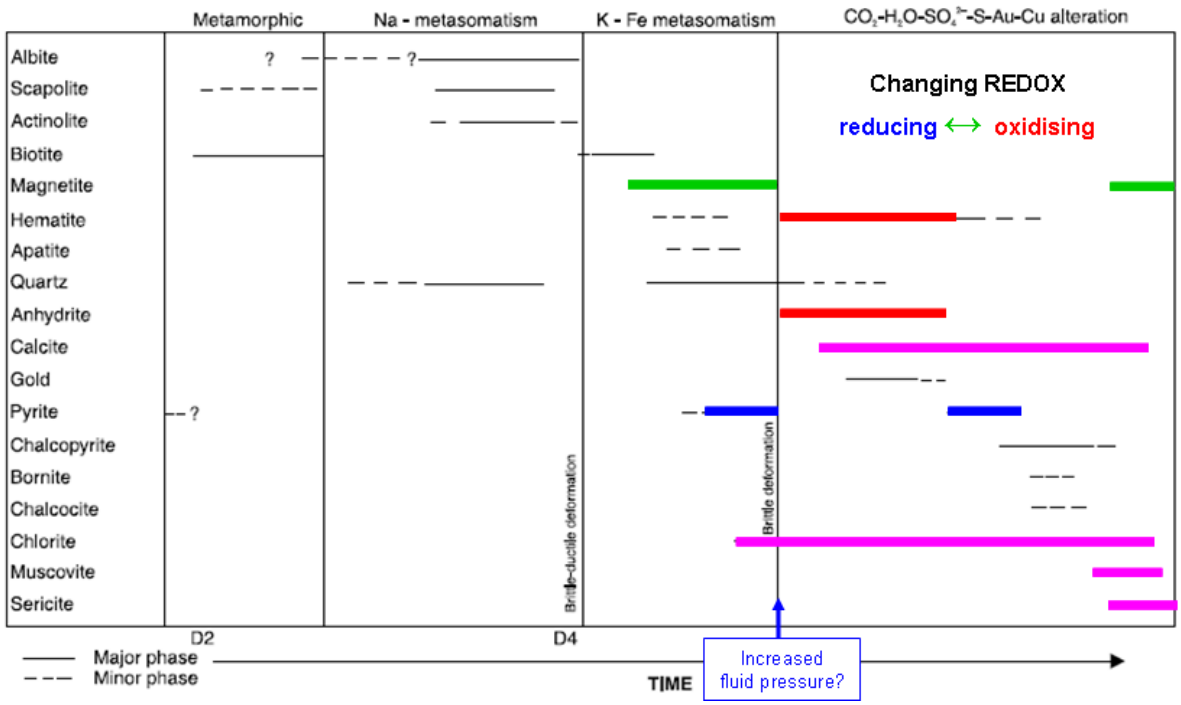

There are numerous other Cu deposits (orange dots in Figure 44) in the study area associated with graphitic units.

IOCG mineral system model

The mineral system model proposed here for the targeting of Cu-Au deposits in the Starra area infers the sourcing, transport and deposition of metals from Fe-K rich fluids driven by contrasting physicochemical conditions especially REDOX. In particular, Fe-K rich fluids are sourced from oxidised granites, transported along intersecting conduits which transport the fluids to reduced rocks that result in metal deposition. Using the hyperspectral mineral maps

and other pre-competitive geoscience data to recognise the mineral expressions of these mineral system components, especially the mineral-chemical gradients, is described in more detail below.

Fluid source

The IOCG model tested here requires a suitable source of oxidised fluids from granites of post-peak metamorphic age. These granites in theory will also be oxidised as well as rich in K and Fe. Figure 45 presents a selection of mineral and geophysical maps of the Starra area, as well as the outlines of the Mount Dore Granite (A) and Gin Creek Granite (B). These two granite types show contrasting behaviour, with the Mount Dore Granite showing:

- High ferric oxide content (red-green tones);
- High white mica content (red tones); as well as
- Relatively high magnetic susceptibility (red-yellow-green tones); and
- High levels of radiometric K, U and Th (white).

The Gin Creek Granite (B) has essentially opposite characteristics. Thus, from the model, the Mount Dore Granite represents a viable source of oxidised fluids rich in K and Fe as well as potentially dissolved Cu, Au and U.

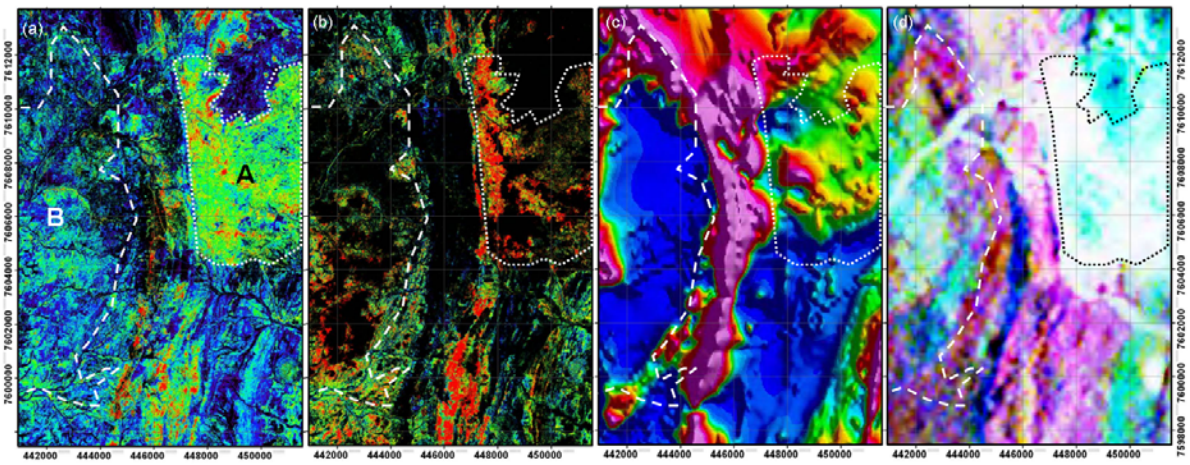

Figure 45. Selected mineral and geophysical maps of the Starra area showing attributes of granites that may provide a suitable fluid source for Cu-Au mineralisation (a) ferric iron mineral map; (b) white mica content mineral map; (c) magnetic susceptibility; and (d) radiometric ternary image. The dotted/dashed outlines of the Mount Dore granite (A) and the Gin Creek granites (B) are shown.

Figure 46 presents field spectra of fresh rock samples taken from the Mount Dore (site 157 MGA Zone 54 447910mE, 7604627mN) and Gin Creek Granite (site 160 MGA Zone 54 442869mE 7600755mN). These show iron oxide and white mica information consistent with the HyMap mineral maps in Figures 45a and 45c. That is, the Mount Dore Granite is relatively rich in ferric oxide (deep 900 nm absorption) and white mica (deep 2200, 2350 and 2450 nm absorptions) compared to the Gin Creek granite.

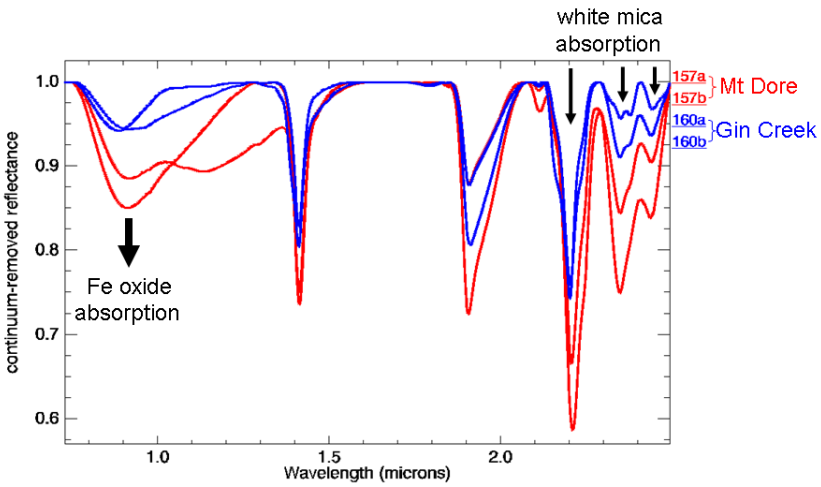

Figure 46. Continuum-removed ASD spectra of field samples taken from fresh rock samples from the Mount Dore Granite (red spectra of site 157) and Gin Creek Granite (blue spectra from site 160). These confirm the HyMap results which show that the Mount Dore Granite is relatively rich in iron oxide and white mica (deeper absorption features).

Depositional environment

The deposition of Cu-Au from oxidised fluids requires a significant physicochemical gradient, such as reduced rocks/fluids. Potential "reduced" rocks in the Starra area include:

- Magnetite ironstones; and
- Graphitic shales.

The airborne magnetic susceptibility data can be used to indentify the magnetite-rich ironstones. There are a number of mineral mapping products that can also be used to target reduced rocks, including:

- Opaque mineral products, which are sensitive to strong absorption at all optical wavelengths by minerals such as magnetite, sulphides and carbon black (e.g. in graphitic shales); and
- Ferric oxide abundance, which can detect the weathering of magnetite ironstones to ferric oxides.

Figure 45a shows high ferric oxide contents over the magnetically high (Figure 45c) massive ironstones (Figure 44) consistent with weathering and oxidation of abundant magnetite. The opaque product (Figure 47a) provides information that crosscuts the geology (Figure 47a) and geophysical data (Figures 45c and d) and shows two large coherent domains immediately to the north and south of the western margin of the Mount Dore Granite. The lack of a similar response in the meta-sedimentary rocks immediately west of the Mount Dore Granite correlates with a thick unit of dominantly calc-silicate rocks (brown unit in Figure 47c). This unit is well mapped using the smectite-content product (Figure 47b) which is developed as a weathering product in this area and typically forms in more alkaline conditions (Van der Merwe and others, 2002).

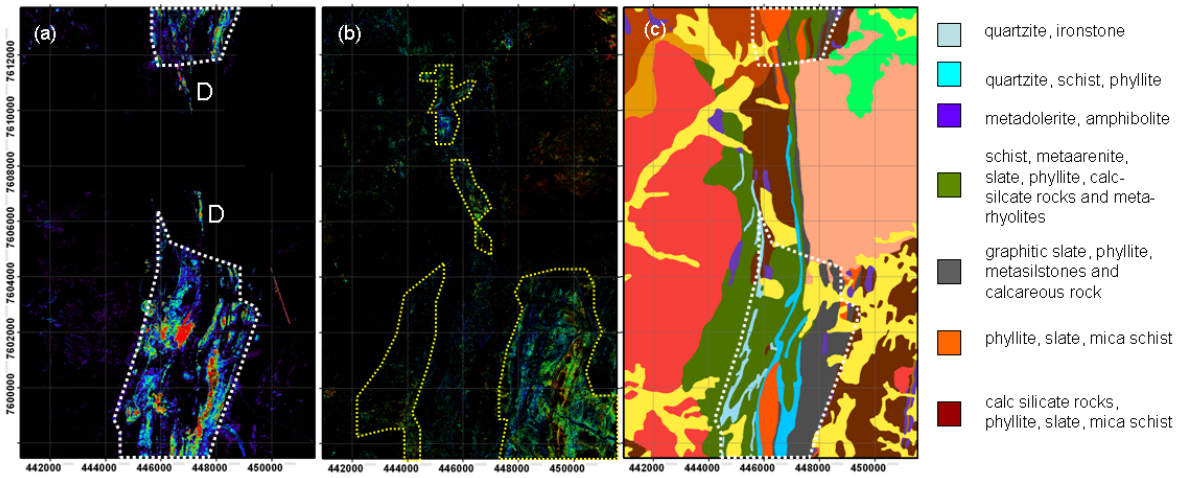

Figure 47. Starra area: (a) Opaque mineral map with the limits of large interpreted "reduced zone" shown by white dotted line; (b) smectite content map with the apparent boundary highlighted by a yellow dotted line; and (c) 1:100,000 geology and associated legend. The dotted lines show the boundary of apparent domains of opaque minerals.

Fluid pathways

Fluid pathways can be either along large open structures associated with brittle deformation (e.g. faults/fractures/shear zones) and associated high water-rock ratios or pervasive diffusion along grain boundaries associated with low water-rock ratios. Both can exist in any system depending on fluid/rock pressures and temperatures, such as in volcanic massive sulphide systems (Cudahy and others, 1999). These fluid pathways must also intersect the source of the fluids as well as suitable depositional sites. Laukamp and others (submitted) noted from the work on Stage 1 Block I over the Cloncurry Fault area that fluid migration can be of at least four types namely:

- Pervasive (low water-rock ratio) in metasediments (e.g. Snake Creek Anticline);
- Pervasive (low water-rock ratio) in igneous bodies (e.g. Camel Hill/Cloncurry Fault gabbros; granites at Mallee Gap);
- Discrete fluid channels (high water-rock ratios) such as faults (e.g. Cloncurry Fault, Mt Dore Fault and parallel shear zones); and
- Discrete fluid channels such as breccia pipes (e.g. Suicide Ridge north of the Saxby Granite).

The two main faults/shear zones in the Starra area are the Mount Dore Shear Zone (MDSZ) and the Starra Shear Zone (SSZ) (Figure 44). The two shear zones are essentially parallel, about 2 km apart, and oriented N-S. The MDSZ intersects the eastern edge of the Gin Creek Granite. The MDSZ is more like a "classic" fault zone, whereas the SSZ is more like a melange-zone, where clasts of the Gin Creek Granite and amphibolites lie in a sheared matrix. Also the thickness of the SSZ is much larger than of the MDSZ. Thus there are more architectural reasons for enhanced focussing of fluids in the MDSZ.

Given that the mineralising fluids were K-rich, then it is clear from Figure 45b that only the MDSZ is associated with abundant white mica (assumed rich in K and not Na[1]) and thus the

[1] Na in paragonite versis K in muscovite-phengite. Note that the XRD analysis of all samples collected from the Mount Isa region in this project did not find the presence of any paragonite but only muscovite.

potential conduit for fluid flow. Importantly, the MDSZ can be mapped for the entire length of the study area using the white mica content (Figure 45b) and intersects reduced rocks along its length (Figure 47a).

The mineral maps can also provide information about the possible composition of the mineralizing fluids. Figure 48 provides the mineral maps "white mica crystallinity" (Figure 48a) and "white mica composition" (Figure 48b). The crystallinity index map is a ratio of the white mica content (2200 nm absorption depth) and the surface water content (1900 nm absorption depth) and is sensitive to the disorder of the white mica, especially illite, as discussed above. The high values for the MDSZ indicate abundant, "dry", muscovite-rich rocks, which is confirmed in the ASD spectra (sample 59 - Figure 48c). Inferred, "lower crystallinity" white mica is mapped away from the MDSZ towards both Cu vein deposits to the east and the oxidised Cu-Au deposits to the west. Field spectra from site 82 from one of the oxidised Cu-Au deposits (Figure 48a) show the development of bound water, which could be associated with illite. The sample from the Gin Creek Granite (site 160 – Figure 48a) shows abundant, unbound water (long-wavelength, deep and broad 1900 nm absorption) and an AlOH clay without the diagnostic white mica absorptions at 2350 and 2450 nm. The mineral mapping results also showed smectite as well as white mica (Figures 47b and 46b, respectively).

The white mica composition (Figure 48b), which is sensitive to the level of Tschermak substitution, shows a distinct zone of relatively Al-poor mica (red-yellow tones), especially between the MDSZ and the SSZ. There is also a zone of decreased Al-content of the white mica near the western margin of the Mount Dore granite (F – Figure 48b) indicating possible evolution of the fluid in its passage from the granite into the country rock. The white mica patterns, although structurally bounded, are typically pervasive within these 2+km wide zones indicating that there was low water-rock interaction for the interpreted metasomatic fluid. However, the deposits themselves are characterised by veins and breccias typical of high fluid pressures and water-rock ratios.

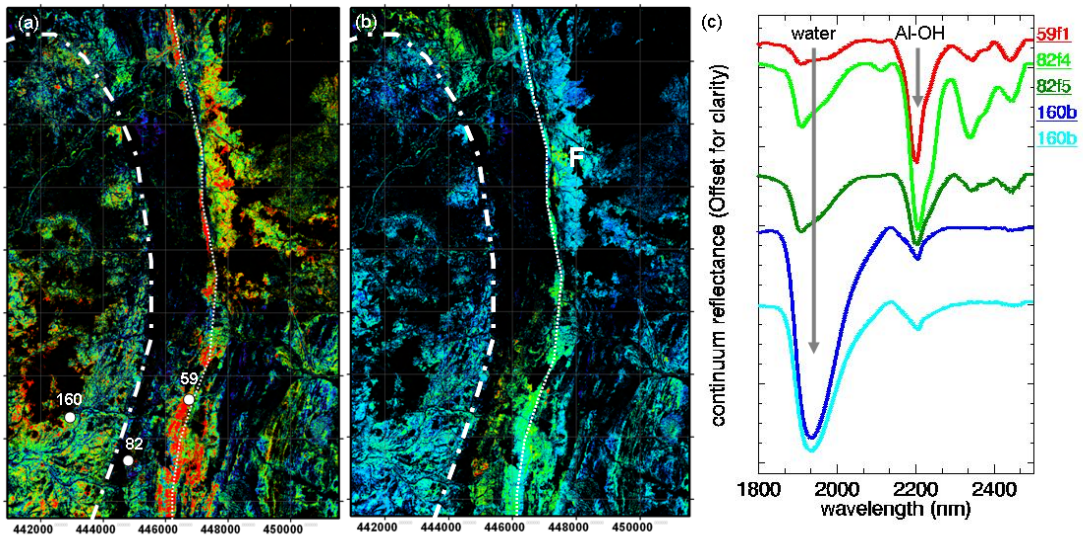

Figure 48. Mineral maps and field spectra of the Starra area, including: (a) Mica crystallinity index map (2200D divided by the 1900D); (b) white mica composition map; (c) field ASD spectra of sample sites shown in (a). The MDSZ (white dots) and SSZ (dot-dash) are annotated.

Mineral system summary

Figure 49 presents a summary of the interpreted fluid flow lines from the source of the mineralising fluids in the Mount Dore granite to the reduced rocks of the Staveley Formation. The white mica composition map is a key mineral product that helps define both the extent of the related alteration system and also the likely sites of metal deposition - in areas of maximum chemical gradient change. That is, where the mica changes rapidly both in composition (from Si-rich (red-yellow tones) to Si-poor (blue tones)) and abundance is where the mineral deposits have formed, both to the west and east (~ 2 km) from the MDSZ. On the western side, this maximum gradient change occurs along the magnetite ironstones, whereas in the east, the chemical gradient is greatest along graphitic shales, both of which represent reduced sites that strongly interacted with the metal-bearing oxidising fluids.

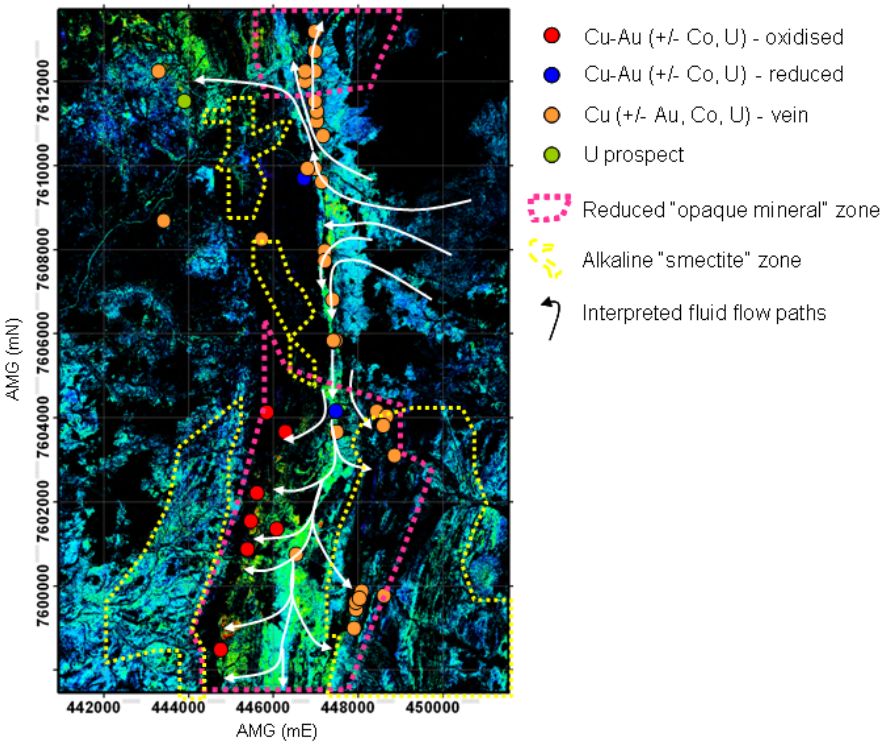

Figure 49. White mica composition map of the Starra area with a number of features annotated, including the interpreted fluid flow lines from the source of the mineralising fluids from the Mount Dore Granite to the reduced rocks of the Staveley Formation.

ASTER mapping

Can ASTER be used to generate similar mineral system architecture? Figure 50 presents the four mineral maps that in theory would provide comparable information to the HyMap mineral maps described above, including: (a) ferric oxide (Figure 50a); (b) opaques (Figure 50b); (c) AlOH group content (Figure 50c) and (d) AlOH group composition (Figure 50d). Unlike the HyMap product (Figure 45a), the ASTER ferric oxide image (Figure 50b) does not highlight the Mount Dore Granite as being ferric oxide rich. This poor result is not surprising given the validation studies described above. In contrast, the ASTER opaque image (Figure 50b) is very similar to the HyMap derived opaque image (Figure 47a). The AlOH group content and composition maps cannot easily be related to the white mica information available in the HyMap mapping, as kaolin and smectite will also affect the ASTER information. The Mount Dore Granite is mapped as AlOH-rich in the ASTER data (Figure 50c) similar to the HyMap data, but the related compositional information is affected by both kaolin and white mica. This problem is particularly evident because the MDSZ is not a zone

of pronounced abundant AlOH mineral (white mica) unlike the HyMap mapping (Figure 45b). Also, the zone between MDSZ and the SSZ is not mapped as Si-rich clay (white mica), again in contrast to the HyMap mapping (Figure 48b). Thus the ASTER mineral mapping is of some value only for defining the Starra IOCG mineral system.

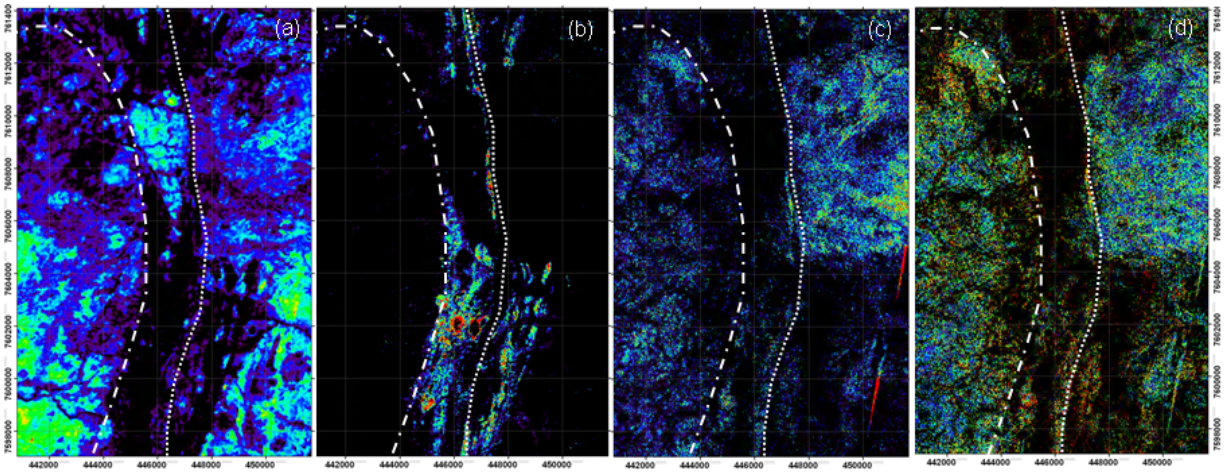

Figure 50. Various ASTER mineral group maps of the Starr area, including: (a) ferric oxide content; (b) opaque mineral content; (c) AlOH mineral group content; (d) AlOH group composition. The traces of the MDSZ and SSZ are shown.

Summary

In summary, the hyperspectral mineral mapping data of the Starra area provides evidence that the alteration footprint associated with the Starra IOCG extends from metres to kilometres. In contrast to the available geophysics, the mineral mapping data provide evidence for a direct link between the likely source fluid/rock and the main site of Cu-Au metal deposition 4-10 km south. The MDSZ is interpreted as the pathway for fluid flow during mineralisation, especially as the chemical gradient observed in the mica composition are symmetric about this fault zone with the highest gradients at the locations of known Cu-Au mineralisation. REDOX is considered to be the main driver for fluid-mineral processes. ASTER is of restricted value for mapping the iron oxide and Al-clay information but is useful for mapping the opaques, which is critical for recognition of potential “reduced” rocks.

Using the geology to analyse mineral maps

Another method for analysing the mineral maps for their exploration potential is to use the existing geology map for establishing “anomalous” behaviour such as:

- The development of white mica in rocks that would not normally contain it, like basalts and gabbros;
- Changes in white mica crystallinity (used as a geobarometer tool) to establish whether there has been:
    - significant vertical displacement across a suspected growth fault; contact metamorphism; or
    - injection of hot fluids;
- Lateral changes in mineralogy for a given geology unit (i.e. cross-cutting).

The latter two of these are considered in more detail below for: (1) the Century deposit associated with the Termite Range "growth" fault; and (2) quartzites nearby the Mount Isa Pb-Zn and Cu deposits. The prevalence of "Si-rich" white mica (phengite) in mineral deposits across Queensland in different types and ages of geology is also briefly examined.

Quartzites around the Mount Isa Pb-Zn and Cu deposits

Background

The precise nature of the fluids and (structural) pathways responsible for generating the Pb-Zn and Cu deposits around Mount Isa are still resolved. Perkins (1984) proposed that the Pb-Zn-Ag mineralization accumulated either syn-genetically or at a very early stage in diagenesis and that the copper was introduced at least 150 My later and coincidentally into similar stratigraphic/structural sites (e.g. Urquhart Shale - Figure 51). Heinrich and others (1995) suggested that high-grade Cu ore-bodies formed as a result of large hydrothermal system with regional scale fluid flows. Matthäi and others (2004) added that an "oxidized" Cu-rich fluid was sourced from underlying meta-basalts which entered a brecciated contact zone in meta-sedimentary rocks of overlying Mount Isa Group with a "reduced" S-rich fluid.

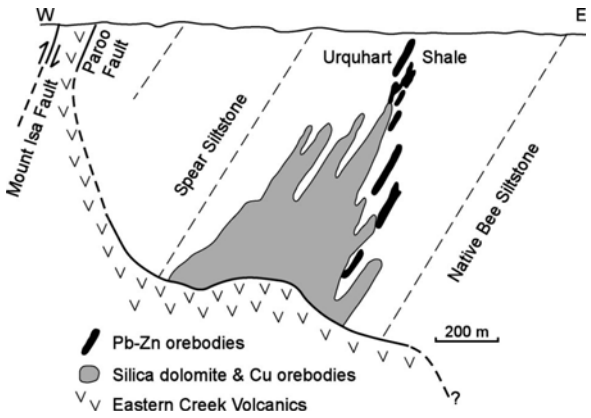

Figure 51. Schematic cross-section of the Mt Isa Mine showing the anomalous east-dipping to sub-horizontal fault contact controlling mineralisation (from Heinrich and others, 1995).

Recognising the alteration footprint of this mineralised system using airborne hyperspectral systems has been tested by Yang and others (2003). Minerals identified and mapped included talc, epidote, white mica (two types comprising both Si-rich and Si-poor varieties), chlorite, phlogopite/biotite, carbonate, amphibole, kaolin and iron oxides. Key amongst these minerals for defining the alteration were:

- talc in the dark and fine-grained sedimentary rocks, which was considered of hydrothermal origin and associated with Cu mineralisation; and
- epidote, which was mapped in the meta-basalts and interpreted to be the result of oxidizing hydrothermal fluids from the Eastern Creek Volcanic rocks.

White mica was considered to be generally non-metasomatic and lithology-dependent, with Si-poor white mica (long AlOH wavelength) found in quartzites and sandstones and the Si-poor white mica (short AlOH wavelength) developed in shales and siltstones. However, Yang and others (2003) also recognised that locally, Si-poor white mica is developed close to small faults near the contact between sedimentary rocks and Eastern Creek Volcanics, which they interpreted as possibly metasomatic.

Current mineral mapping results

The current suite of mineral mapping products is broadly similar to the unmixed mineral products described by Yang and others (2003). The details why these information extraction methods differ was discussed above. The point to reiterate here is that the current processing methods used to generate information allows the user to more independently interpret mineralogical significance by examining a number of related products, e.g. mapping epidote content (deep 1550 nm absorption) would also involve using the chlorite-epidote content (deep 2250 nm absorption), MgOH content (deep 2300 nm absorption), MgOH composition (long 23330 nm absorption) and ferrous iron (low ferrous iron in MgOH) to be confident in the identification of epidote for a given area.

Figure 52 provides a selection of the current hyperspectral mineral maps for the Stage 2 Mount Isa Block D. The *ferrous iron content in MgOH* associated (Figure 52b) shows the extent of the ferromagnesian rocks in the Eastern Creek Volcanics. Note the distinct break from blue tones (ferrous poor) in the south to red tones (ferrous rich) in the middle and north of the Block (marked by a white dotted line). This separation can also be seen, although more subtly, in the *false colour* image (Figure 52a), which suggests that the mapped ferrous iron is possibly affected by vegetation cover. This is an important consideration when interpreting these products, especially those minerals that overlap with strong vegetation effects, such as iron oxides and ferrous iron in the VNIR. Also note that in some cases, abundant, well-ordered kaolinite can produce strong absorption in the 2300 nm region and thus be included in this ferrous iron in MgOH product. Kaolin will typically have low ferrous iron and thus show blue tones. This situation could also be responsible for the southern area in Figure 52b, as Figure 52c shows that well ordered kaolin is also developed in these areas.

The *kaolin composition* product (Figure 52c) shows well ordered kaolin that has developed especially in quartzites. The opportunity this presents for mapping within unit mineral variations is described in more detail below. The one point to be made here is that the well orderd kaolinite marked “A” appears to disappear northward across the white dotted line. Changes in vegetation cannot explain this pattern though geological reasons like sedimentary provenance or structural offsetting are possibilities.

Figure 52 presents the *hydrated silica* (Figure 52d) *mica crystallinity* (Figure 52e) and *opaque* (Figure 52f) products. These products also have other effects that can complicate their mineral mapping interpretation. For example, *hydrated silica* (Figure 52d), which is based on mapping broad Si-OH absorption at 2250 nm, can be complicated by strong absorption by AlOH and MgOH minerals. This may be the case in Figure 52d as areas such as “B” are also areas of high clay content. Similarly, given that the *white mica crystallinity* product (Figure 52e) is measured using the amount of AlOH clay normalised by the amount of water, then if the soil water content is a relative constant across the area, then the resultant colours will be driven by the white mica content and not white mica crystallinity. Therefore, it is also useful to check the *surface water content* to see if it shows variation consistent with the geology or mapped mineralogy. Finally, both the opaque products are sensitive to a given pixel’s radiance (energy “reflected” off the surface) which is a function of its albedo (overall brightness or reflectivity) as well as surface geometry (topographic shading), surface wetness (especially in the SWIR where water strongly absorbs) and incoming energy (primarily solar irradiance). To help appreciate any complication induced by surface geometry effects, it is useful to examine products like the *albedo* or *false colour* imagery (Figure 52a) to establish which pixels are affected by shading.

Having provided some cautionary tips, the selected mineral maps presented in Figure 52 nonetheless show interesting behaviour peripheral to the known Pb-Zn and Cu mineralisation. For example, the apparent association of abundant “dry” white mica and opaques within 5 km of the Mount Isa deposits (”C”) and smaller areas in the north (“D”) and south (“E”). This possible “footprint” zonation is discussed in more detail below.

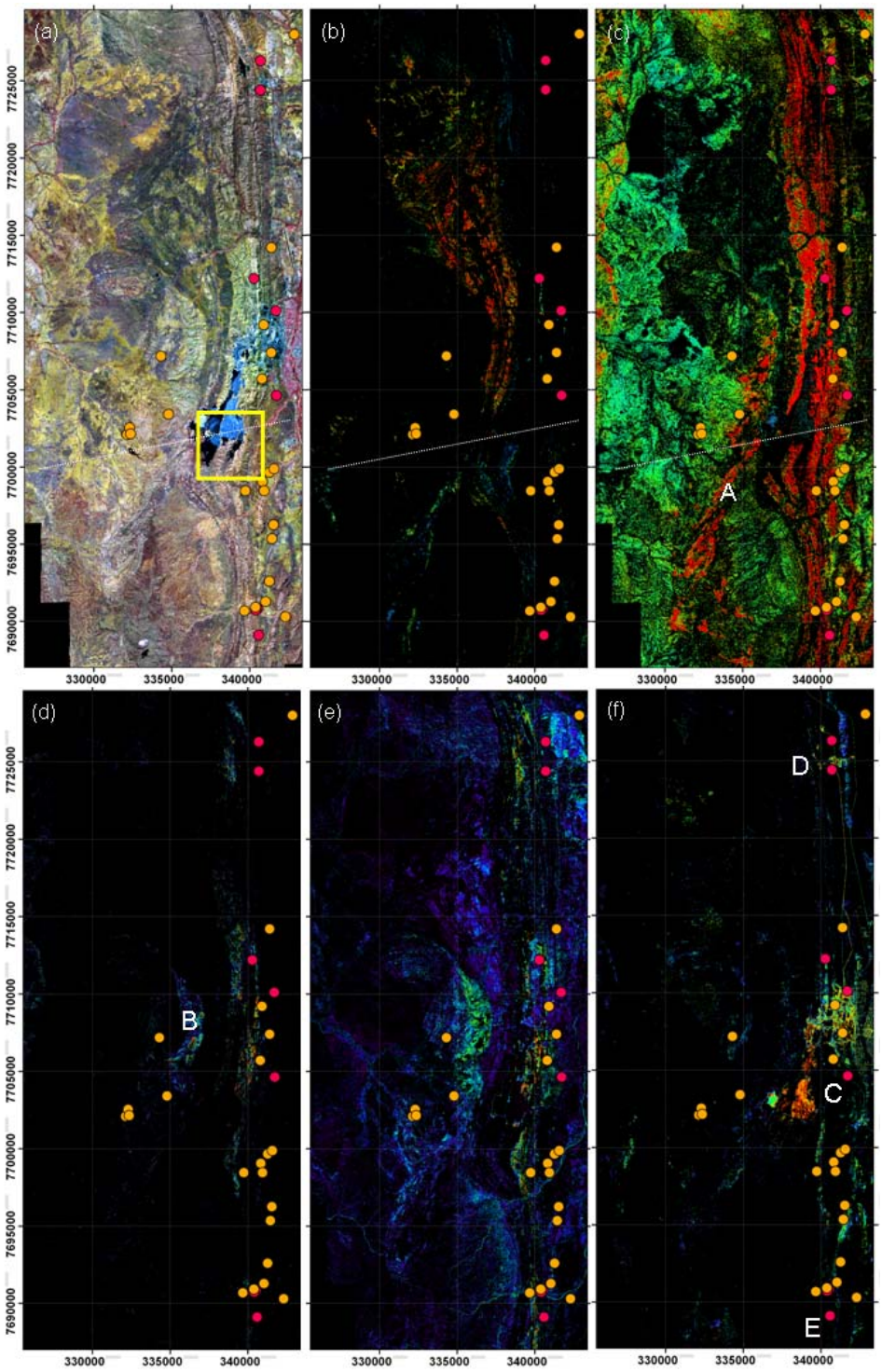

Figure 52. Mineral maps of Mount Isa Stage 2 Block D over Mount Isa area, including (a) false colour; (b) Ferrous iron in MgOH minerals; (c); kaolin composition; (d) hydrated silica; (e) mica crystallinity, and (f) opaques.

An area just south of the Mount Isa lodes (yellow box in Figure 52a) was selected to examine in greater the spatial detail of these mineral maps as well as mineralogical variation within a given geological unit. Figure 53a shows the lithology striking NNE-SSW, with a large part covered by tailings dams, which are highlighted by the *opaque* product (Figure 53b). This *opaque* product also shows a NNW-SSW striking zone ("A") which cannot be explained by topographic shading. From the published geology, this zone corresponds to a dolomitic siltstone. Both the *ferrous iron in MgOH* image (Figure 53c) and *chlorite-epidote content* image (Figure 53d) show similar highlighted pixels (though different colours), including a sharp break across the stratigraphic strike from "B" to "C" (Figure 53a). There is no evidence from any of the images of a change in vegetation, dust or water content that can explain this change in MgOH related mineralogy. South of this break (C) there exists an MgOH mineral poor in ferrous iron, with moderate to strong absorption at 2250 nm (related to chlorite-epidote), and relatively deep 1550 nm absorption (in parts), which suggests the presence of epidote rather than chlorite. However, the published geology does not describe this as an epidote-bearing quartzite. Note also that MgOH mineralogy contrasts with an area in the northwest ("C") which is interpreted to be chlorite and lesser amount of epidote, based on the higher *ferrous iron content* and weaker 1550 nm absorption (and longer wavelength MgOH absorption, i.e. not Fe-amphibole). Importantly, the MgOH mineral disappears across the break from "C" to "B" in the same unit.

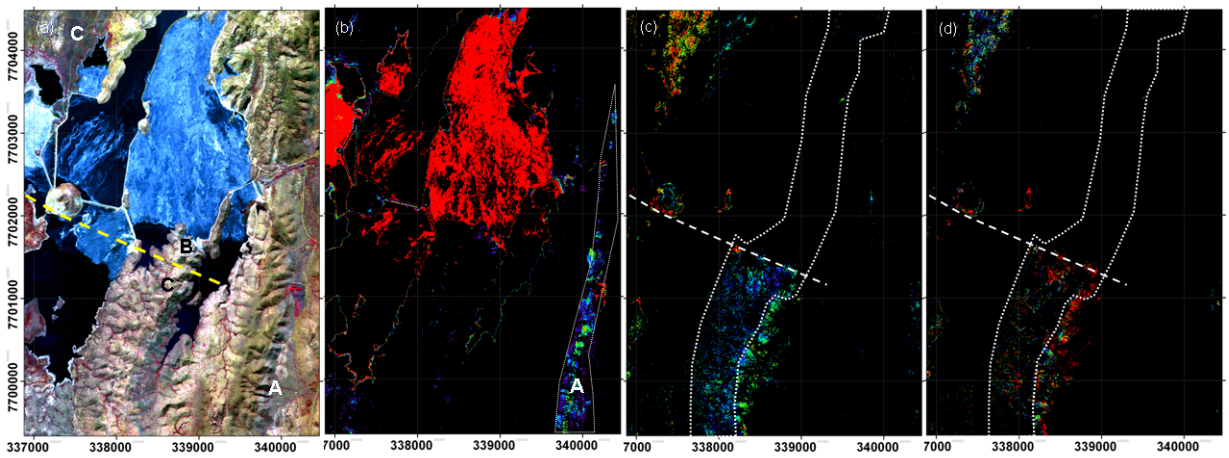

Figure 53. Mount Isa Stage 2 Block D zoom window (see Figure 52 yellow box for location): (a) false colour image; (b) opaques 1; (c) ferrous iron and MgOH; and (d) chlorite-epidote content.

Figure 54a shows that the areas "B" and "C" (Figure 53a) have both been mapped in the published 1:100,000 scale geology as quartzite, feldspathic quartzite and/or minor schist. Importantly, the break (white dashed line) separates kaolin (Figure 54c) on one side (B) from white mica (Figure 54d) on the other (C). This white mica is Si-rich (Figure 54e) and continues to the north within the same mapped unit ("D") as well as in quartzites and feldspathic sandstones immediately to the east (E). As described above, this relationship between Si-rich mica and quartzites was noted by Yang and others (2003) though these current data show that quartzites can also be white mica-poor and kaolin-rich. Si-rich white mica is also developed in other lithologies including dolomitic siltstones ("F") and meta-siltstones ("G"). The Si-rich white mica zone (yellow dotted polygon) also correlates with the zone of hydrated silica (Figure 54e). Whether this zone also marks the termination of an interpreted WNW-ESE fault (white dashed line), which coincides with a number of offsets in the published geological units, is unclear.

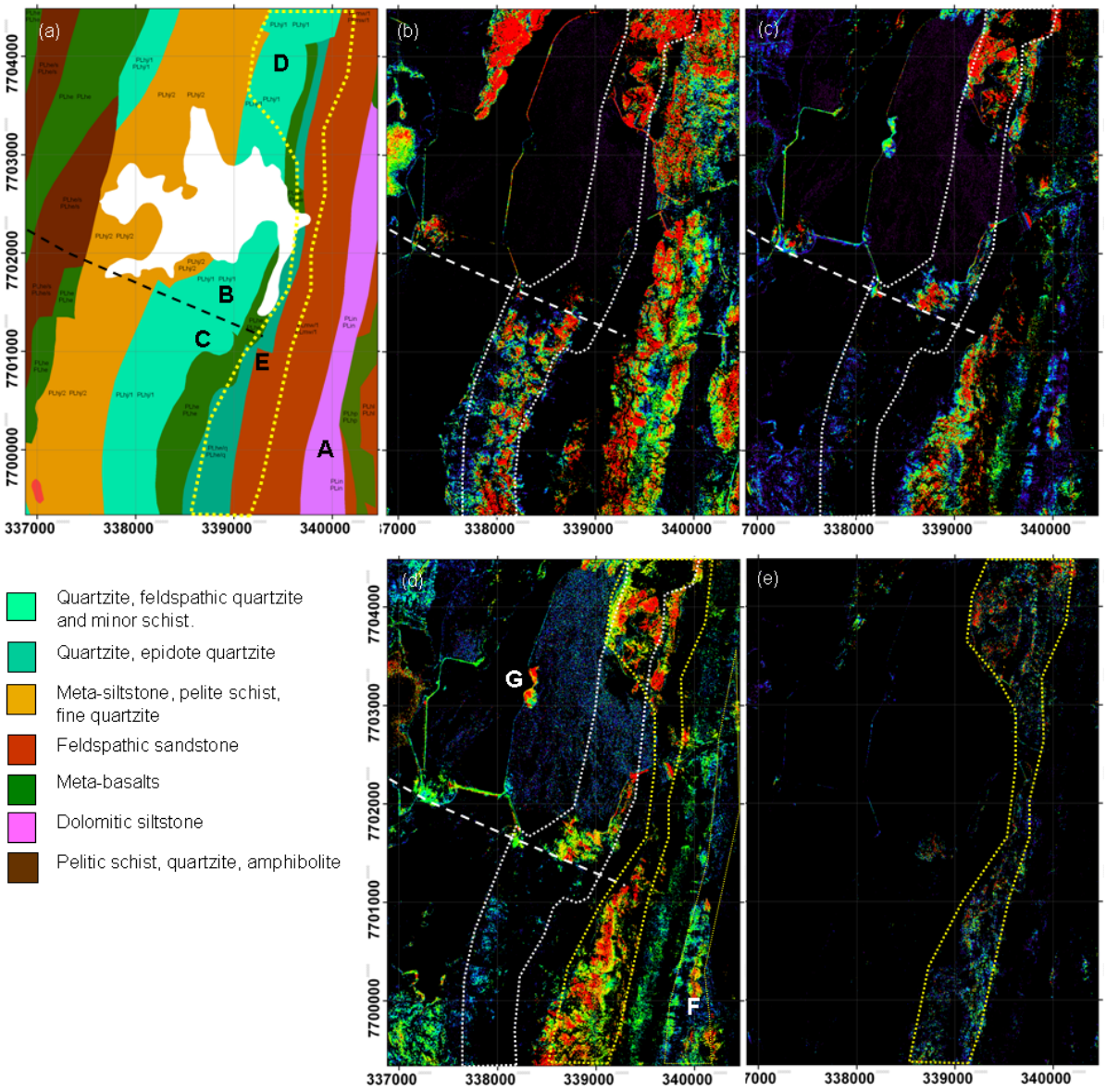

Figure 54. (a) Published 1:100 000 scale geology; (b) kaolin content; (c) white mica content; (d) white mica composition; and (e) hydrated silica.

Figure 55 presents selected AlOH mineral products within the published quartzite units only. The unmixed Al-clay content (Figure 55a) shows elevated levels around three areas that span the known Pb-Zn deposits. The width of the Al-clay zone in the quartzites around the Mount Isa deposits is approximately 18 km in apparent strike length. The other two zones are smaller (<10 km). The quartzites lower in the Eastern Creek Volcanics (5 km to the west) do not show a similar pattern. This is an important result for at least two reasons:

1. The pattern of lower vegetation content around the Mount Isa area is not apparent in the unmixed product mineral, suggesting that this new processing method is effective;
2. The apparent elevated Al-clay footprint to the mineralisation is extensive along strike (up to 18km?) but not deeply penetrating (<5 km west), which is consistent with previous studies (Heinrich and others, 1995).

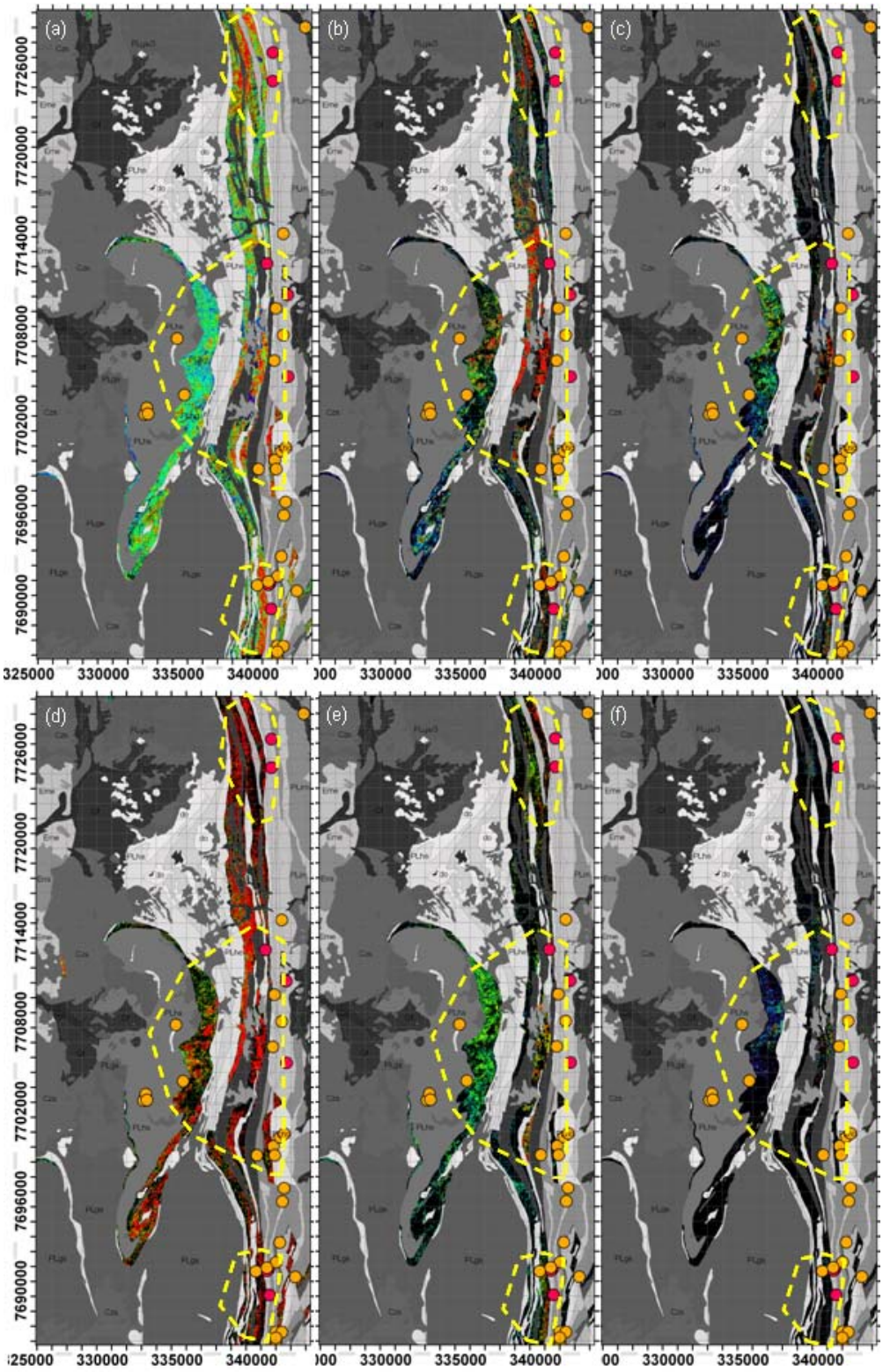

Figure 55. Published 1:100 000 scale geology with the quartzite units made transparent to allow for the underlying mineral maps to show their behaviour, including (a) vegetation unmixed AlOH clay content; (b) kaolin content; (c) white mica content; (d) kaolin composition; (e) white mica composition; and (f) white mica crystallinity. The location of the Cu deposits (yellow dots) and Pb-Zn deposits (pink dots) are shown. The yellow dashed polygons show the approximate limits of interpreted alteration mineral footprints.

Unmixing of the vegetation components has not yet been implemented on specific clay products like the kaolin, white mica and Al-smectite contents. This is expected to be completed in the future. Nevertheless, the current maps show that both kaolin and white mica (Figure 55b and c, respectively) are developed in the elevated clay zone close to mineralisation (Figure 55a). Unlike the *unmixed Al-clay* map though, white mica (and kaolin) is also developed in the lower quartzite unit 5 km to the west of Mount Isa. Elsewhere in background areas, only kaolin is developed. This is evidence for a "larger footprint" in the quarzites.

To help confirm this footprint, the clay composition products are examined. Unlike the mineral content products, mineral composition is generally independent of vegetation effects. The kaolin composition (Figure 55d) and white mica composition (Figure 55e) show that:

- Kaolin composition is well ordered everywhere, except with more moderately ordered kaolin in places 5 km west of Mount Isa;
- White mica composition is Si-rich near mineralisation (red-yellow tones) with moderate levels of Si content (green tones) 5-10 km away from the Mount Isa deposits (but with lesser distances for other deposits like George Fisher) and then Si-poor in background areas (cyan-blue tones).

These results provide further evidence for large alteration footprints. Field verification of these mineralogocally cross-cutting patterns has yet to be conducted.

White mica crystallinity and the Termite Range "growth" fault

There are a range of models to explain the development of the Century Pb-Zn deposits including syngenetic and diagenetic (Huston and others, 2006) though all essentially rely on the movement of mineralising fluids along large, active faults, such as the Termite Range Fault, into reactive lithologic units (Broadbent and others, 1998), such as graphitic shales. The Termite Range Fault is considered to have reactivated during the Paleoproterozoic and Mesoproterozoic in response to major tectonic events. Higher temperatures (up to 300°C), at around 1400 Ma and driven by fluid flow, are recorded in the immediate vicinity of the Termite Range Fault, followed by enhanced cooling, possibly due to thermal relaxation or further crustal exhumation (Golding and others, 2006).

These structural and metamorphic processes could have generated rocks that formed under different P-T conditions being juxtaposed on either side of the Termite Range Fault. To test this possibility, the HyMap *illite crystallinity* index product was selected because of its potential use as a geobarometer following on from this project's laboratoriy studies described above. Note that the XRD-based illite crystallinity index (Kübler index) used as a basis for geobarometry in this project and by Golding and others (2006) is affected not just by temperature (and pressure) but also by the primary lithology and the presence of any smectitic phase. Note that smectite was mapped using both the airborne HyMap and field/laboratory data in this area.

Figure 56a presents a part of the Stage 1 Block A airborne HyMap white *mica crystallinity* product (Figure 55a) and the Al-smectite-composition product (Figure 56b) with the Termite Range Fault shown as a white dashed line. Note that similar geological units are exposed on either side of this fault. Features to note include:

- There is no apparent change in the *mica crystallinity* index across the Termite Range Fault indicating either that:

- There is no temperature (inferred) difference measurable in the exposed rocks; or
- The resolution of the HyMap data and/or the spectral index used here is not precise/accurate enough to measure/detect the temperature difference.

- The rocks from within the Century open pit are a relatively Si-poor Al-clay. Note that this clay is mapped as Al-smectite in the HyMap processing but the laboratory XRD studies have shown this to be illite though it lacks absorption at 2350 nm, which is unusual. This type of illite is also found in other deposits, such as Trekelano (discussed below).

Thus, the current processed data do not provide any evidence to suggest significant vertical displacement along the Termite Range Fault and/or that hot fluids passed up along/near this fault. However there is evidence for Si metasomatism as shown by the Si-poor smectite (illite).

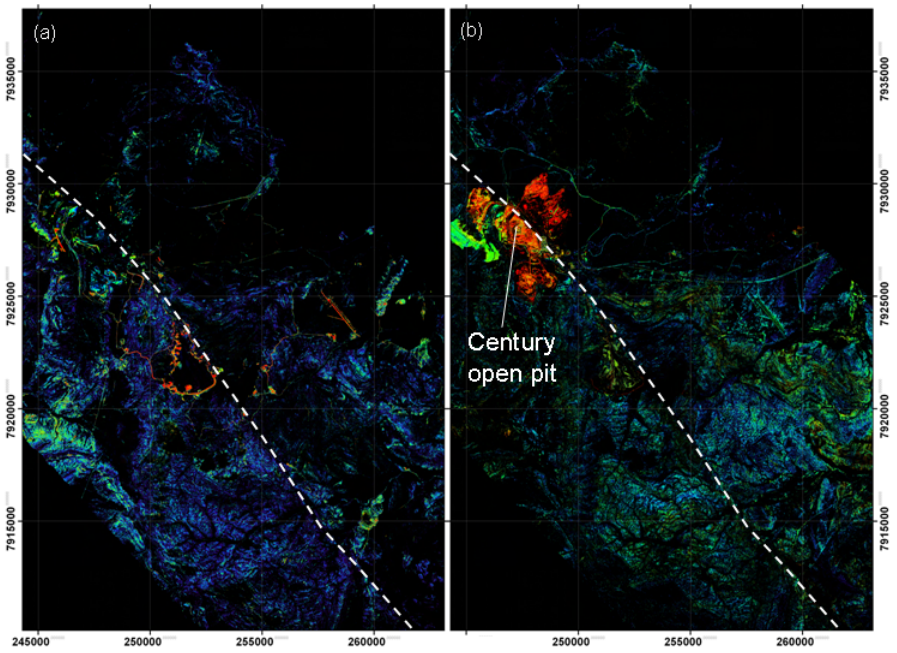

Figure 56. Mineral maps from the Century Pb-Zn mine area, including (a) white mica crystallinity (blue = water-rich; red is water poor); and (b) Al-smectite-composition (red = Si-rich mica; blue = Si-poor mica). The trace of the Termite Range fault is shown as a white dashed line.

Snapshots of open pit mines

The following series of images are of open pit mines covered by the Stages 1 and 2 HyMap surveys. These mines span different geological ages, host rocks, commodity types and mineralising styles and include:

- Kidston Au mine (Figure 57): Stage 2, Georgetown, Block F;
- Croydon area Au mines (Figure 58): Stage 2, Georgetown, Block A;
- Red Dome Au mines (Figure 59): Stage 2, Hodgkinson, Block B;
- Tick Hill Au mine (Figure 60): Stage 1, Mount Isa, Block G;
- Mount Warner base metal mine (Figure 61): Stage 2, Mount Isa, Block C;

- Georgetown area Au mines (Figure 62): Stage 2, Georgetown, Block C;
- Trekelano base metal mine (Figure 63): Stage 1, Mount Isa, Block G; and
- Unknown mine SE of Georgetown (Figure 64): Stage 2, Georgetown, Block E.

The most obvious feature from all of these examples is the development of Si-poor white mica in the rocks within the open pits. This suggests that there is fundamental process in K-rich mineralising fluids that drives Si activity (P, T, fluid/rock composition?).

Similar to the Starra example described above, a number of the deposits also show a broad zone (2+ km) of white mica that rapidly changes in chemical towards the edge(s) of the zone and where mineralisation has occured, e.g. Mount Warner (Figure 61) and Georgetown (Figure 62). This is an important exploration clue. Note that some of the other deposits shown here are complicated by mining activity (e.g. Red Dome, Figure 59) and/or cover (e.g. Tick Hill – Figure 60).

At first glance, the extent of the *in situ* Si-rich "phengite" could be considered as being restricted to only the walls/floor of the open pit, possibly because weathering (illitisation) would in theory preferentially attack Mg and/or ferrous iron in the mica structure and leave only Si-poor illite in the weathered regolith. Given that this is a real complication, then targeting the "fresh rock" deposited/exposed along active drainage channels would solve this potential problem. Using this approach for the Kidston area (Figure 57b), the Si-rich phengitic mica (red tones) can be traced 11 km upstream (to point A) from the eastern point immediately alongside the Kidston open pit mine (8 km direct along geological strike) as well as for all the observed distance downstream. Other drainage in the area either does not show this phengitic signature (e.g. B) or does not comprise white mica (e.g. C).

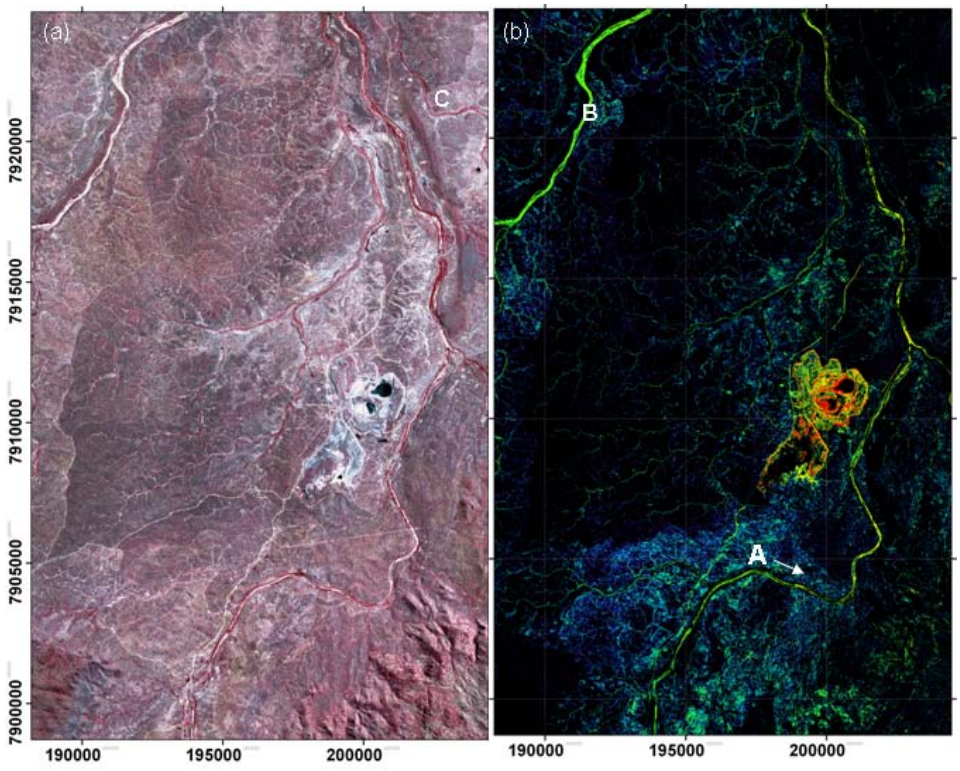

Figure 57. HyMap mineral mapping products from over the Kidston Au mine, (a) false colour image; (b) white mica composition (blue = Si-poor; red = Si-rich).

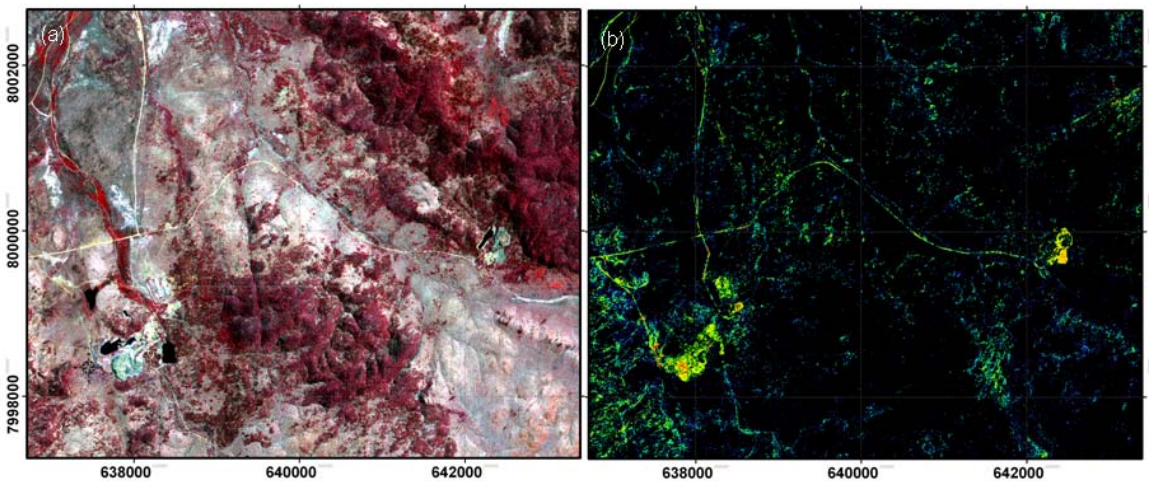

Figure 58. HyMap mineral mapping products from over the Croydon area Au mines, (a) false colour image; (b) white mica composition (blue = Si-poor; red = Si-rich). Note the two small open pit mines.

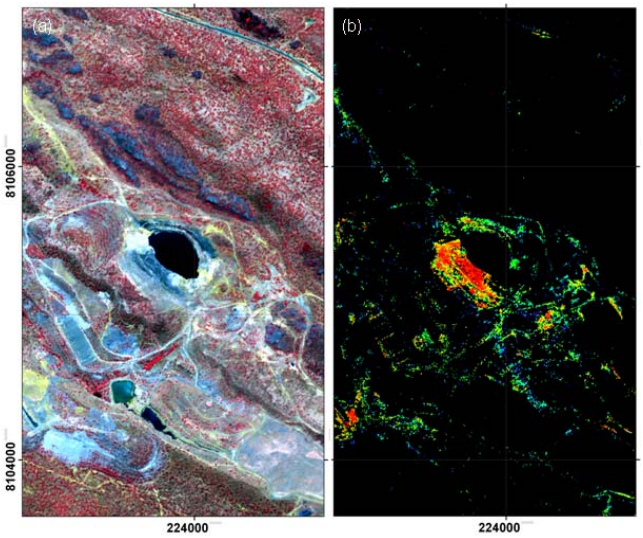

Figure 59. HyMap mineral mapping products from over the Red Dome Au mine, (a) false colour image; (b) white mica composition (blue = Si-poor; red = Si-rich).

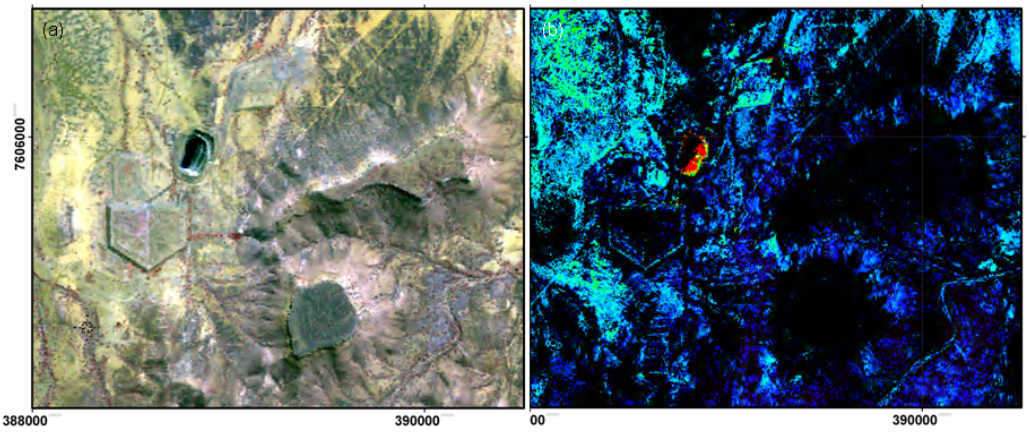

Figure 60. HyMap mineral mapping products from over the Tick Hill Au mines, (a) false colour image; (b) white mica composition (blue = Si-poor; red = Si-rich).

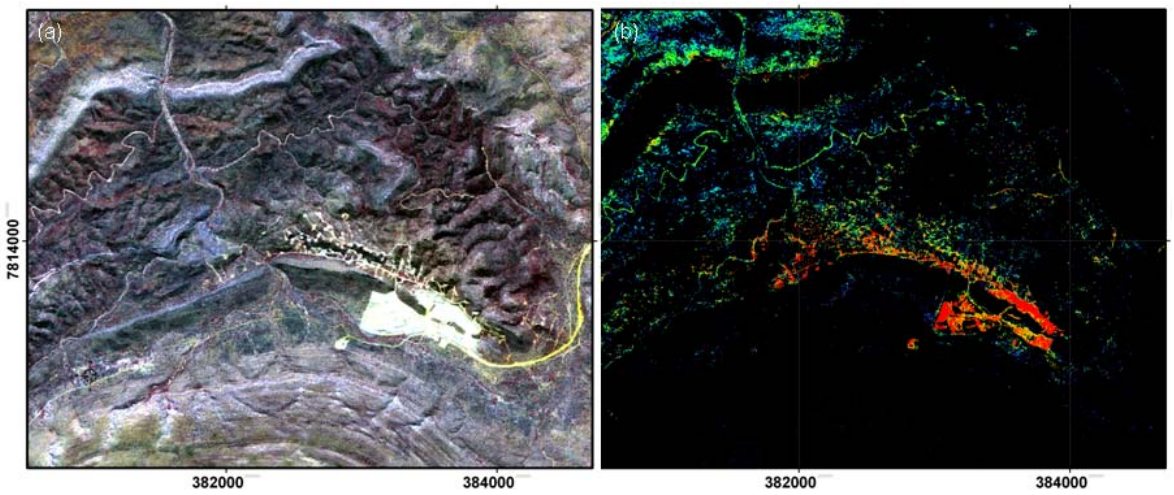

Figure 61. HyMap mineral mapping products from over the Mount Warner base metal mine, (a) false colour image; (b) white mica composition (blue = Si-poor; red = Si-rich).

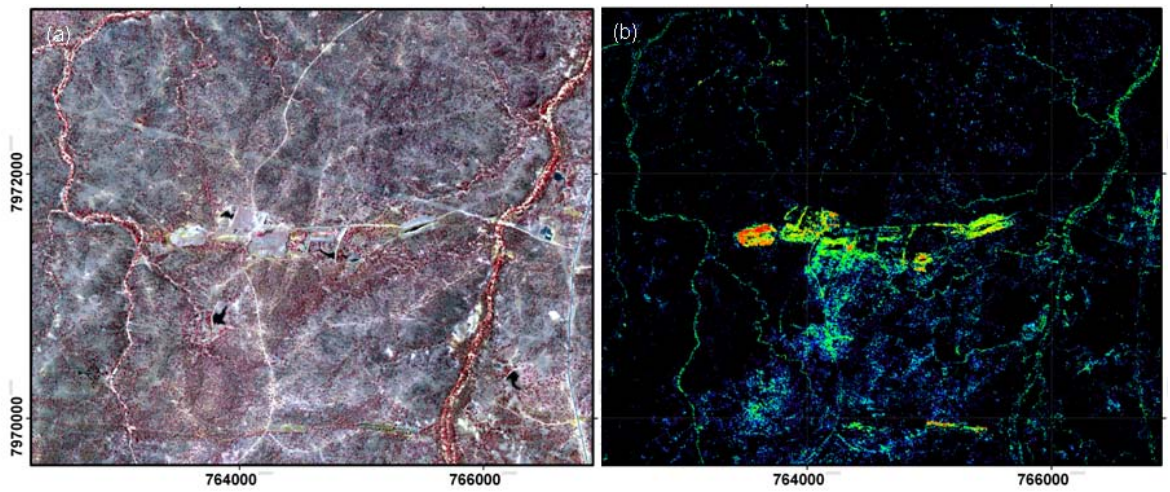

Figure 62. HyMap mineral mapping products from over some of the Georgetown Au mines, (a) false colour image; (b) white mica composition (blue = Si-poor; red = Si-rich).

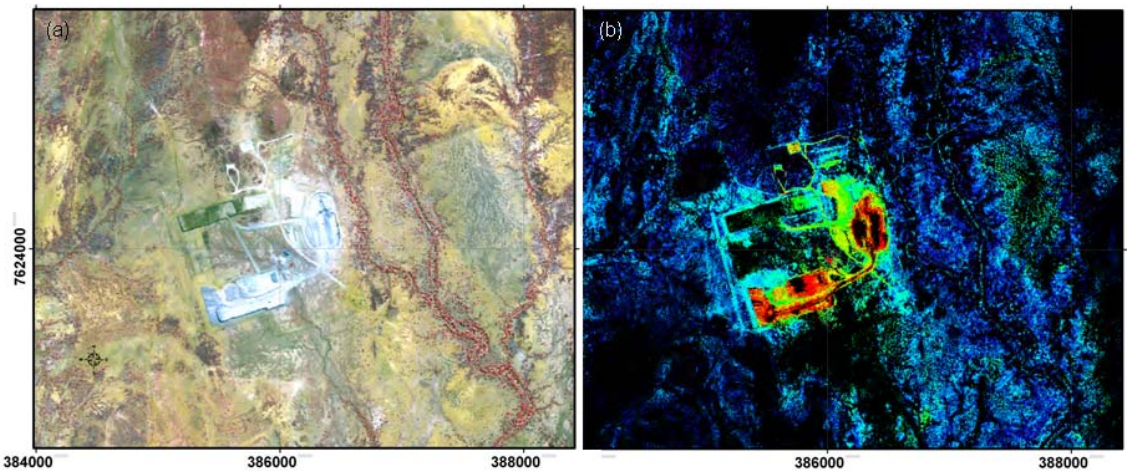

Figure 63. HyMap mineral mapping products from over some of the Trekelano base metal mines, (a) false colour image; (b) Al-smectite composition (blue = Si-poor; red = Si-rich).

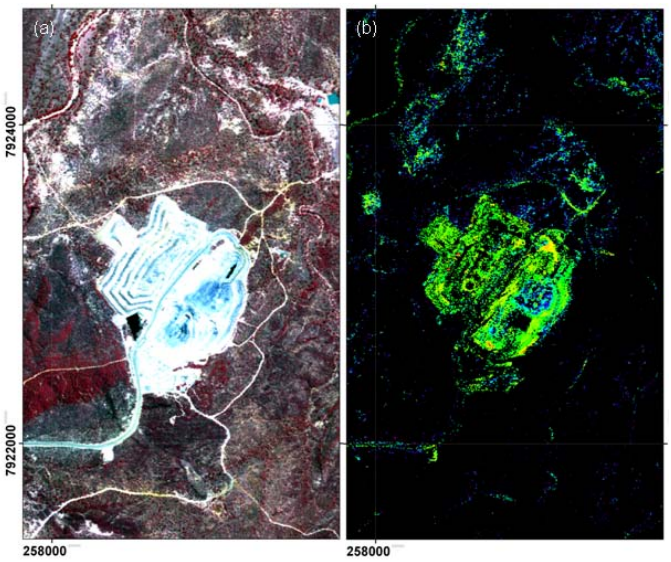

Figure 64. HyMap mineral mapping products from over the Balcooma open pit mine on Stage 2 Georgetown Block E (mine type unknown), (a) false colour image; (b) white mica composition (blue = Si-poor; red = Si-rich).

FURTHER WORK

This project has been diverse in its scope from investigating atmospheric residuals and their impact on accurate information extraction of mineralogy to exploring the potential significance on the mineral maps using a mineral systems approach to technology transfer via workshops, conference papers and other communications (a full list is provided below). This report shows that mineral mapping products can be used for mineral exploration but that there also remain some challenges if we are to achieve the vision of an accurate mineral map of the Australian continent. Some of these challenges include:

- Testing the mineral maps for their value in exploration, especially using a mineral systems approach, as this allows the appropriate questions to be asked of the data;
- Developing more effective web delivery systems, including moving from delivery of simply JPEGS or TIFFS, to quantitative mineral information products (e.g. BSQ) that can be imported into modelling packages;
- Training many more geoscientists in how these mineral maps can be used to help their exploration more effectively;
- Developing new methods that makes mineral mapping processing independent of instrument calibration and bandpass configuration and moving away from the current “instrument-focus”, i.e. ASTER or HyMap, to a “mineral product-focus”. That is, users should need to only specify what level of product accuracy is required for their application;
- Solving vegetation and other mineral unmixing effects for a wider suite of minerals; and
- Linking the surface mineral maps with ANVCL drill core mineral profiles to generate 3D mineral maps.

Most (all) of these steps will be tackled by the new WA Government Centre of Excellence for 3D Mineral Mapping (C3DMM) which will begin in early 2009.

ACKNOWLEDGEMENTS

This project has benefited from the support of and interactions with many individuals and organisations. First, thanks to Dave Mason and his team at the Geological Survey of Queensland, especially the geoscientists that have taken the time to geologically assess these new data. Thanks also to Geoscience Australia, especially Andrew Barnicoat and Lesley Wyborn for their support in this new technology and to James Johnson and Neil Williams for allowing this work to be published. Nick Oliver from James Cook University and Mehrooz Aspandiar from Curtin University provided support through their supervision of post doctoral (Carsten Laukamp) and post graduate (Fitri Augustin) students. Terry Cocks and his team from HyVista Corporation were fast to respond to questions regarding HyMap data issues and to solve any major associated problems, including the re-collection of airborne data in 2008. Many people from CSIRO also provided valuable assistance, including Peter Caccetta and Xiaoliang Wu from Mathematics and Information Sciences, who provided access and support to their satellite cross-calibration software, which was critical in the processing of the ASTER data. From CSIRO Exploration and Mining, the project benefited from the following people: Andrew Hackett, who provided assistance with sample preparation; Tim McLennan, Leanne McLennan, Neil Ballment and Rebecca Walls, who provided assistance with contracts preparation; Grahame Cooper who assisted with finances; Bob Chamberlain who helped with marketing and communications in collaboration with Jim Beeston and Sharon Beeston from the Geological Survey of Queensland; Chris Yeats who provided overall leadership; and special thanks to Cheryl Harris, who helped in so many areas from administration to arranging travel and preparations for workshops. Finally, we appreciate the financial support from the Queensland Government's Smart Mining and Exploration initiatives, and CSIRO's MDU, as without this help the project and the opportunity to move towards acheiving the vision of a mineral map of the Australian continent would not be possible.

COMMUNICATIONS RELATED TO THE PROJECT

The following lists the papers presented at conferences, workshops, journal papers and book chapters generated from this project.

Cudahy, T.J. and Jones, M., 2007. Hypersectral mineral mapping report. Digging Deeper 5 symposium, Geological Survey of Queensland. 28 November 2008 (oral paper).

Cudahy, T.J., Jones, M. Thomas, M., Laukamp, C., Hewson, R.D. and Hussey, M., 2007. Hyperspectral Mineral Mapping Workshops. 29 November, Brisbane, 30 November, Townsville.

Cudahy, T.J., 2007. Airborne hyperspectral mapping for drill targeting. AMEC Congress, 7-9 June, Perth (oral paper).

Cudahy, T.J., Jones, M., Thomas, M., Laukamp, C., Hussey, M., Caccetta, M., Hewson, R.D., Verrall, M. and Hacket, A., 2007. Next Generation Mineral Mapping: The Mount Isa Project, Queensland. Exploration 2007 Workshop on Remote Sensing and Spectral Geology Workshop, 8-9 September, 2007, Toronto (oral paper).

Cudahy, T.J., Jones, M., Thomas, M., Laukamp, C., Hewson, R.D., Caccetta, M., Rodger, A. Verrall, M. and Agustin, F., 2008. Towards global hyperspectral mapping of surface mineralogy: Fundamental information for understanding Earth's soils and geology.

Proceedings LEME Mineral Exploration Seminar, 4 June 2008, ARRC, Perth, 8 pages.

Cudahy, T.J., Jones, M., Thomas, M., Laukamp, C., Caccetta, M., Hewson, R.D., Verrall, M. and Hacket, A., 2008. Continental-scale mineral maps as standard government pre-competitive geoscience data in Australia. International Society for Photogrammetry and Remote Sensing Conference, Beijing, 3-11 July 2008, 1 page.

Cudahy, T.J., Jones, M., Thomas, M., Laukamp, C., Caccetta, M., Hewson, R.D., Verrall, M., Hacket, A. and Rodger, A., 2008. Mineral Mapping Queensland: IOCG Mineral System Case History, Starra, Mount Isa Inlier. PACRIM conference, Jupiters Casino, 24-26 November, 2008. AUSIMM, 6 pages (in press).

Cudahy, T.J., 2008. 3D (Hyperspectral) Mineral Mapping to Expedite the Exploration Process and Discovery. Mineral Exploration Technology Summit, Singapore, 8-9 April, 2008. Keynote paper.

Cudahy, T.J., 2008. Remote and field spectral sensing for the resources industry: empowering the geoscientist with mineralogy. Masterclass Workshop presented at the Mineral Exploration Technology Summit, 7 April, 2008.

Cudahy, T.J., Jones, M., Thomas, M., Cocks, P., Augstin, F., Caccetta, M., Hewson, R.D., Verrall, M. and Rodger, A., 2008. Soil mineral mapping using airborne hyperspectral data, Tick Hill, Mount Isa region, Queensland. 1st Global Workshop on High Resolution Digital Soil Sensing and Mapping, 5-8 February, 2008, Sydney, 14 pages.

Cudahy, T.J., Jones, M., Thomas, M., Cocks, P., Augstin, F., Caccetta, M., Hewson, R.D., Verrall, M. and Rodger, A., 2009. Mapping soil surface mineralogy at Tick Hill, Northwest Queensland. using airborne hyperspectral imagery. Chapter 17, Digital Soil Mapping, Published by Elseveier Press, 19 pages (in press).

Cudahy, T.J., Jones, M., Thomas, M., Laukamp, C. Caccetta, P., Caccetta, M., Hewson, R.D., Verrall, M. and Rodger, A., 2008. Next generation mineral mapping in Queensland: Another piece to the pre-competitive geoscience data puzzle. Australian Earth Sciences Convention, 2-24 July, Perth, p.74. (oral paper).

Cudahy, T.J., Jones, M., Thomas, M., Laukamp, Hewson, R.D. and Hussey, M., 2008. Smart exploration with pre-competitive hyperspectral mineral mapping data from Queensland. Workshop at the AESC, 25 July, Perth.

Hewson, R.D. and Cudahy, T.J., 2008. Hyperspectral mineral mapping for the Geosciences in Australia. 33rd International Geological Convention, 6-14 August, Oslo, Norway (keynote paper).

Jones, M. and Cudahy, T.J., 2008. Hyperspectral mineral maps and beyond. Digging Deeper 6 Symposium, Geological Survey of Queensland, 10 December 2009 (oral paper).

Jones, M., Cudahy, T., Thomas, M. and Laukamp, C., 2008. Hyperspectral and ASTER mineral maps of Queensland - Preview. Australian Society of Exploration Geologists, 136, 28-29.

Laukamp, C., Cudahy, T., Oliver, N.H.S. and Cleverley, J.S., 2008. Detection of K-alteration in the Cloncurry District, NW Queensland, using Hyperspectral Mineral Maps. AESC 2008, Perth, Australia, Program & Abstract Booklet, 159-160.

Laukamp, C., 2007. Recognition of Hydrothermal Footprints in the Eastern Fold Belt of the Mount Isa Inlier Using Geophysical-Geochemical Spatial Data.- EGRU Newsletter, Dec 2007, p. 20-22.

Laukamp, C., Cleverley, J., Cudahy, T., Hewson, R., Jones, M., Oliver, N. and Thomas, M., 2008. Validation of spectral remote sensing data for geological mapping and detection of hydrothermal footprints in the Mount Isa Inlier (final report and database). pmd*CRC Report, 60pp.

Laukamp, C., 2008. Report on the validation of spectral techniques for exploration in the Mount Isa terrane. Enabling technology Final Report pmd@CRC, Chapter 2.2.8, 5pp.

Laukamp, C., Cudahy, T., Thomas, M., Jones, M., Cleverley, J.S. and Oliver, N.H.S., 2008. Recognition of hydrothermal footprints in the Eastern Fold Belt of the Mount Isa Inlier using geophysical-geochemical spatial data. pmd*CRC I7 final report, 18 pp.

Rodger, A. and Cudahy, T.J., (in prep). Vegetation Corrected Continuum Depths at 2.20 µm: An Approach for Hyperspectral Sensors. Remote Sensing of Environment.

Thomas, M., 2008. ASTER – HyMap Hyperspectral calibration report. pmd*CRC I7 final report, 9pp.

Thomas, M., Laukamp, C., Cudahy, T. and Jones, M., 2008. Flowpaths and Drivers: New spectral methods and products for resource and surface materials mapping in Queensland, Australia - methods and applications for industry. In: Korsch, R.J. & Barnicoat, A.C. (eds.): New Perspectives: The foundations and future of Australian exploration, abstracts for the June pmd*CRC Conference, Perth, Australia, p.99-105.

Thomas, M., Laukamp, C., Cudahy, T. and Jones, M., 2008. Exploration advances: New developments in spectral remote sensing in the Mount Isa region, Australia. IGC Oslo, 6th-14 August 2008.

Thomas, M., Laukamp, C. and Hewson, R., 2008. Get closer to the Truth with Hyperspectral Mineral Maps from Queensland. AESC 2008, Perth, Australia, Program & Abstract Booklet, p.149.

Thomas, M., Cudahy, T. and Jones, M., 2008. Spectral and remote-sensing techniques for regolith-landform characterization and mapping in Queensland, Australia. Australian and New Zealand Geomorphology Group Conference Queenstown, Tasmania, Proceedings.

In addition, over 100 Gigabytes of mineral maps had been downloaded by ftp from the www.em.csiro.au/NGMM webpage one year after the realease of the Stage 1 data (July 2008). This equates to over 6500 individual images (~15 Mbytes each) from Stage 1 alone.

REFERENCES

Adshead-Bell, NS, 1998. Evolution of the Starra and Selwyn high-strain zones, Eastern fold belt, Mount Isa Inlier; implications for Au-Cu mineralization. Economic Geology; Vol. 93; no. 8, 1450-1462.

AUSGEO News, 2002. In depth study of mineral province evolution. Issue no. 68, page 18. http://www.ga.gov.au/pdf/Corp0113.pdf

Bell, T.H., 1991. The role of thrusting in the structural development of the Mount Isa mine and its relevance to exploration in the surrounding region. Economic Geology, Vol. 86, 1602–1625.

Bierwirth, P., Huston, D. and Blewett, R., 2002. Hyperspectral mapping of mineral assemblages associated with mineralization in the Central Pilbara, Western Australia. Economic Geology, Vol. 97, 819-826.

Blewett, R.S. and Hitchman, A.P. (editors), 2004. pmd*CRC Final Report Project Y2, 2004. Geological models of the eastern Yilgarn Craton. http://www.pmdcrc.com.au/pdfs/Y2_final_report_digital4.pdf .

Boardman, J.W., 1998. Post-ATREM polishing of AVIRIS apparent reflectance data using EFFORT: A lesson in accuracy versus precision. In Summaries 7th JPL Airborne Earth Science Workshop, Pasadena, CA, Vol. 1.

Broadbent, G.C., Myers, R.E., and Wright, J.V., 1998. Geology and origin of shale-hosted Zn-Pb-Ag mineralization at the Century deposit, northwest Queensland, Australia: Economic Geology, Vol. 93, 1264–1294.

Clark, R.N., 1983. Spectral properties of mixtures of montmorillonite and dark carbon grains: Implications for remote sensing minerals containing chemically and physically absorbed water. Journal of Geophysical Research, 88(B12): 10,635-10,644.

Clark, R.N., 1999. Chapter 1: Spectroscopy of Rocks and Minerals, and Principles of Spectroscopy, in Manual of Remote Sensing, Volume 3, Remote Sensing for the Earth Sciences, (A.N. Rencz, ed.) John Wiley and Sons, New York, p 3- 58.

Cox, D.P. and Singer, D.A., 2007. Descriptive and Grade-Tonnage Models and Database for Iron Oxide Cu-Au Deposits. USGS Open-File Report 2007-1155.

Crowley, J.K. and Vergo, N., 1988. Near-infrared reflectance spectra of mixtures of kaolin-group minerals: use in clay mineral studies. Clays and Clay Minerals, Vol. 36., No. 4, 310-316.

Crowley, J.K. and Zimbelman, D.R., 1977. Mapping hydrothermal altered rocks on Mount Rainer, Washington, with airborne visible/infrared imaging spectrometer (AVIRIS) data. Geology, Vol. 25, No. 6, 559-562.

Cudahy, T.J. and Ramanaidou, E.R., 1997. Measurement of the hematite-goethite ratio using field VNIR spectrometry in channel iron deposits, Western Australia. Australian Journal of Earth Sciences, Vol. 44, No. 4, 411-421.

Cudahy, T.J., Okada, K., Ueda, K. Brauhart, C., Morant, P., Huston, D., Cocks, T., Wilson, J., Mason, P. and Huntington, J.F., 1999. Mapping the Panorama VMS-style alteration and host rock mineralogy, Pilbara Block, using airborne hyperspectral VNIR-SWIR data. MERIWA Report No. 205, CSIRO Exploration and Mining Report 661R, 107 pages.

Cudahy, T.J., Okada, K., Cornelius, A. and Hewson, R.A., 2002. Regional to prospect-scale exploration for porphyry-skarn-epithermal mineralisation at Yerington, Nevada, using ASTER and airborne hyperspectral data. CSIRO Exploration and Mining Report, 1122R, 26 pages.

Cudahy T.J., Caccetta, M., Cornelius, A., Hewson, R.D., Wells, M., Skwarnecki, M., Halley, S., Hausknecht, P., Mason, P. and Quigley, M.A., 2005. Regolith geology and alteration mineral maps from new generation airborne and satellite remote sensing technologies and Explanatory Notes for the Kalgoorlie-Kanowna 1:100,000 scale map sheet, remote sensing mineral maps. MERIWA Report No. 252, 114 pages.

Cudahy, T.J., Caccetta, M, Wells, M.A. and Skwarnecki, M., 2006. Mapping alteration through the regolith at Kalgoorlie using airborne hyperspectral data. Australian Earth Science Convention, July 2006, Melbourne, 8 pages. http://www.earth2006.org.au/papers/extendedpdf/Cudahy.pdf.

Cudahy, T.J., Jones, M., Thomas, M., Laukamp, C., Caccetta, M., Hewson, R.D., Verrall, M., Hacket, A. and Rodger, A., 2008. Mineral Mapping Queensland: IOCG Mineral System Case History, Starra, Mount Isa Inlier. PACRIM conference, Jupiters Casino, 24-26 November, 2008. AUSIMM, 6 pages (in press).

Cudahy, T.J., Jones, M., Thomas, M., Cocks, P., Augstin, F., Caccetta, M., Hewson, R.D., Verrall, M. and Rodger, A., 2009. Mapping soil surface mineralogy at Tick Hill, Northwest Queensland. using airborne hyperspectral imagery. Chapter 17, Digital Soil Mapping, Published by Elseveier Press, 19 pages (in press).

Dalla Torre, M., De Capitani, C., Frey, M., Underwood, M.B., Mullis, J. and Cox, R., 1996. Very low-temperature metamorphism of shales from the Diablo Range, Franciscan Complex, California: New constraints on the exhumation path. GSA Bulletin, Vol. 108, No. 5, 578-601.

Duke, E.F., 1994. Near infrared spectra of muscovite. Tschermak substitution and metamorphic reaction process. Implications for remote sensing. Geology, Vol. 22, 201-219.

Foster, D.R.W. and Austin, J.R., 2008. The 1800–1610 Ma stratigraphic and magmatic history of the Eastern Succession, Mount Isa Inlier, and correlations with adjacent Paleoproterozoic terranes. Precambrian Research, Vol. 163, 7-30.

García-Casco, A, Sánchez-Navas, A. and Torres-Roldán, R., 1993. Disequilibrium decomposition and breakdown of muscovite in high P-T gneisses, Betic alpine belt (southern Spain). American Mineralogist, Vol 78, pp. 158-177.

Gauthier, L., Hall, G., Stein, H. and Schaltegger, U., 2001. The Osborne Deposit, Cloncurry District: A 1595 Ma Cu-Au Skarn Deposit. In: Williams P.J., ed, 2001: A hydrothermal Odyssey Extended Conference Abstracts. Economic Geology Research Unit, James Cook University, Contribution, Vol. 59, 58-59.

Gibson, G.M., Offler, R. and Henson, P.A., 2006. Thermobarometric constraints on depth of tectonic burial. Chapter 6, pmd*CRC I1 Project Final Report, 10 pages.

Golding, S.D., Uysal, I.T., Glikson, M., Baublys, K.A. and Southgate, P.N., 2006. Timing and chemistry of fluid-flow events in the Lawn Hill platform, Northern Australia: Economic Geology, Vol. 101, 1231–1250.

Goleby, B.R., Korsch, R.J., Fomin, T., Bell, B., Nicoll, M.G., Drummond, B.J. and Owen, A.J., 2002. Preliminary 3-D geological model of the Kalgoorlie region, Yilgarn Craton, Western Australia, based on deep seismic-reflection and potential field data. Australia Journal of Earth Sciences, Vol. 49, No. 6, 917-933.

Greene-Kelly, R., 1953. Identification of montmorillonoids. Journal of Soil Science. 4:233-237.

Guidotti, C.V. and Sassi, F.P., 1976. Muscovite as a petrogenetic indicator mineral in pelitic schists. N. Jb. Mineral. Abh., 127, 97-142.

Guggenheim, S., Bain, D.C., Bergaya, F., Brigatti, M.F., Drits, V.A., Eberl, D.D., Formoso, M.L.L., Galan, E., Merriman, R.J., Peacor, D.R., Stanjek, H. and Watanbe, T., 2002. Report of the Association Internationale pour l'Etude des Argiles (AIPEA) Nomenclatire Committee for 2001: Order, disorder and crystallinity in phyllosilicates and the use of the 'Crystallinity Index'. Clay Minerals, Vol. 37, 389-393.

Haaland, D.M. and Thomas E.V., 1988. Partial least-square methods for spectral analyses. 1. Relations to other quantitative calibration methods and the extraction of qualitative information. Analytical Chemistry, Vol. 60 No. 11, 1193–1202.

Heinrich, C.A., Bain, J.H.C., Mernagh, T.P., Wyborn, L.A.I., Andrew, A.S. and Waring, C.L., 1995. Fluid and mass transfer during metabasalt alteration and copper mineralisation at Mount Isa, Australia, Economic Geology, Vol. 90, 705-730.

Hewson, R.D. and Cudahy, T.J., 2009. Accurate geological mapping in Australia with ASTER Data. Chapter in ASTER User Manual, Springer-Verlag, 37 pages.

Hook, S.J. and Kahle, A.B., 1996. The micro Fourier transform interferometer (mFTIR) – A new field spectrometer for acquisition of infrared data of natural surfaces. Remote Sensing of Environment, Vol. 56, 172-181.

Hunt, G.R. and Salisbury, J.W., 1971. Visible and near infrared spectra of minerals and rocks: III. Silicates, Modern Geology, 1: 283-300.

Huston, D.L., Stevens, B., Southgate, P.N., Muhling, P. and Wyborn, L., 2006. Australian Zn-Pb-Ag ore-forming systems: A review and analysis. Economic Geology, Vol. 101, 1117–1157.

Hyperion, 2005. Evaluation of the Hyperion performance at Australian hyperspectral calibration and validation sites. NASA NRA-99-OES-01, 51 pages. http://eo1.gsfc.nasa.gov/new/validationReport/Technology/JoeCD/Jupp_FinalReport.doc

Iwasaki, A., Fujisada, H., Akao, H., Shindou, O. and Akagi, S., 2001. 'Enhancement of spectral separation performance for ASTER/SWIR.' Proceedings of SPIE - The International Society for Optical Engineering, Vol 4486, 42-50.

Jaques, A.L., Jaireth, S. and Walshe, J.L., 2002. Minerals systems of Australia: an overview of resources, settings and processes. Australian Journal of Earth Sciences, Vol. 49, 623-660. http://www.blackwell-synergy.com/doi/abs/10.1046/j.1440-0952.2002.00946.x

Javawardhana, P.M and Sheard, S.N., 2000. The use of airborne gamma-ray spectrometry: A case study from the Mount Isa inlier, northwest Queensland, Australia. Geophysics, 65(6):1993-2000.

Korb, A.R., Dybwad, P., Wadsworth, W. and Salisbury, J.W., 1996. Portable Fourier transform infrared spectroradiometer for field measurements of radiance and emissivity. Applied Optics, Vol. 35, No. 10, 1679-1692.

Kruse, F.A. and Hauff, P.L., 1991. Identification of illite polytype zoning in disseminated gold deposits using reflectance spect6roscopy and X-Ray diffraction – Potential for mapping with imaging spectrometers. IEEE Transactions on Geoscience and Remote Sensing, Vol. 29, No. 1, 101-104.

Kruse, F.A., Boardman, J.W. and Huntington, J.F., 2003. Comparison of airborne hyperspectral data and EO-1 Hyperion for mineral mapping. IEEE Transactions on Geoscience and Remote Sensing, Vol. 4, No. 6, 1388-1400.

Kübler, B. and Jaboyedoff, M., 2000. Illite crystallinity. Earth and Planetary Sciences, Vol. 331, 75-89.

Kühn, M., 2004. Reactive flow modelling of hydrothermal systems. Springer, 261 pages.

Longhi, I., Mazzoli, C. and Sgavetti, M., 2000. Determination of metamorphic grade in siliceous muscovite-bearing rocks in Madagascar using reflectance spectrosopy. Terra Nova, Vol. 12, No.1, 21-27.

Lyon, R.J.P., 1965. Analysis of rocks and minerals by reflected infrared radiation. Economic Geology, 60: 715-736.

Mark, G., 1999. Petrogenesis of Mesoproterozoic K-rich granitoids, southern Mt Angelay igneous complex, Cloncurry district, northwest Queensland. Australian Journal of Earth Sciences, Vol. 46, 933-949.

Matthäi, S.K., Heinrich, C.A. and Driesner, T., 2004. Is the Mount Isa copper deposit the product of forced brine convection in the footwall of a major reverse fault?, Geology, V32, No. 4, 357-360.

Perkins, W.G., 1984. Mount Isa silica dolomite and copper orebodies: the result of a syntectonic hydrothermal alteration system. Economic Geology, Vol. 79, No. 4, 601-637.

Perring, C.S., Pollard, P. J., Dong, G., Nunn, A.J. and Blake, K.L., 2000. The Lightning Creek Sill Complex, Cloncurry District, Northwest Queensland: A Source of Fluids for Fe Oxide Cu-Au Mineralization and Sodic-Calcic Alteration. Economic Geology, Vol. 95, 1067–1089.

Pollard, P.J., 2000. Evidence of a magmatic fluid and metal source for Fe-oxide Cu-Au mineralization. In Porter, T.M., ed., Hydrothermal iron oxide copper-gold and related deposits: a global perspective. V.1 PGC Publishing, Linden Park, Australia, 27-42.

Pollastro, R.M., 1993. Consuderations and applications of the illite/smectite geothermometer in hydrocarbon-bearing rocks of Miocene to Missipian age. Clays and Clay Minerals. Vol. 41, No.2, 119-133.

Post, J.L. and Noble, P.N., 1993. The near-infrared combination band frequencies of dioctahedral smectites, micas and illites. Clays and Clay Minerals, 41(6): 639-644.

Raven, M.D. and Self, P.G., 1988. Xplot User Manual, Manipulation of Powder X-ray Diffraction Data. CSIRO Division of Soils Tech. Mem. No. 30/1988.

Rees, W.G., Tutubalina, O.V. and Golubeva, E.I., 2004. Reflectance spectra of subarctic lichens between 400 and 2400 nm. Remote Sensing of Environment, Vol. 90, 281-292.

Rodger, A. and Cudahy, T.J., (in prep). Vegetation Corrected Continuum Depths at 2.20 µm: An Approach for Hyperspectral Sensors. Remote Sensing of Environment.

Rotherham, J.F., 1997. A metasomatic origin for the iron-oxide Au-Cu Starr ore bodies. Eastern Fold Belt, Mount Isa Inlier. Mineralium Deposita, Vol. 32, 205-18.

Scott, K. and Yang, K., 1997. Spectral Reflectance Studies of white micas. CSIRO Exploration and Mining Report No. 439R, 41pp.

van der Merwe, G.M.E., Laker, M.C. and Bühmann, C., 2002. Clay mineral associations in melanic soils of South Africa. Australian Journal of Soil Research, Vol. 40, pp. 115-126.

van der Wielen, S.E., Oliver, S., Kalinowski, A.A. and Creasy, J., 2005. Remotely sensed imaging of hydrothermal footprints in Western Succession, Mount Isa Inlier. In: Gibson GM & Hitchman P

(eds). pmd*CRC I1 Project Final Report—3D Basin Architecture and Minerals Systems in the Mt Isa Western Succession. Unpublished report, 268: 177-185.

van Ruitenbeek, F.J.A., Cudahy, T.J., Hale, M. and van der Meer, F.D., 2005. Tracing fluid pathways in fossil hydrothermal systems with near infrared spectroscopy. Geology, Vol. 33, No.7, 587-600.

van Ruitenbeek, F.J.A., Cudahy, T.J., van der Meer, F.D. and Hale, M., 2007. Hydrothermal processes in the Archaean 1 – new insights from airborne imaging spectroscopy. Precambrian Research (accepted).

Volzone, C., 1992. Improvements in the method to differentiate montmorillonite from other smectites, Journal of Materials Science Letters, 11: 921-923.

Walshe, J.L., Halley, S.W., Hall., G.A. and Kitto, P., 2003. Contrasting fluid systems, chemical gradients and controls on large-tonnage, high grade Au deposits, Eastern Goldfields province, Yilgarn Craton, Western Australia, Biennial SGA Meeting 7th , Athens, Greece, Proceedings, Extended, Abstracts, p.827.

Wang, S. and Williams, P.J., 2001. Geochemistry and origin of Proterzoic skarns at the Mount Elliot Cu-Au-(-Co-Ni) deposit, Cloncurry district, NW Queensland, Australia. Mineralium Deposita, Vol. 36, 109-124.

Williams, P.J. and Pollard, P.J., 2001. Australian Proterozoic Iron Oxide-Cu-Au Deposits" an overview with new metallogenic and exploration data from the Cloncurry District, Northwest Queensland. Exploration Mining Journal. Vol. 10, No.3, 191-213.

Wyborn, L.A., Heinrich, C.A. and Jaques, A.L., 1994. Australian Proterozoic Mineral Systems: Essential ingredients and mappable criteria. AUSIMM Annual Conference, Darwin 5-9 August, 1994. http://www.ga.gov.au/image_cache/GA5228.pdf

Yang, K., Huntington, J.F., Cudahy, T.J., Mason, P. and Scott, K.M., 2001. Spectrally Mapping the Compositional Variation of White Micas in Hydrothermal Systems and the Application in Mineral Exploration. IEEE IGARSS, Sydney, July 2001., 4 pages.

Yang, K., Huntington, J.F., Quigley, M.D., Scott, K.M. and Mason, P., 2003. Mapping the Effects of Regional Metamorphism and Hydrothermal Alteration in the Mount Isa Valley, Queensland, Australia, Using Airborne Hyperspectral Data. IEEE Explores, 1555-1557.

Yamaguchi, Y., Fujisada, H., Kahle A., Tsu, H., Kato, M., Watanabe, H., Sato, I. and Kudoh, M., 2001. ASTER Instrument Performance, Operation Status, and Application to Earth Sciences. IEEE 2001 International Geoscience and Remote Sensing Symposium (IGARSS), 9-13 July. 2pp.

APPENDIX 1

Descriptions of the HyMap Blocks for all the Stage 1 and Stage 2 survey areas

Stage/region	Block Name	Nemonic	Description	Length(km) / Area(km^2)
Stage 1 Mount Isa	*Termite Range*	A and B	Century Zn mine and the Termite Range Fault	105/1575
Stage 1 Mount Isa	*Lady Loretta-Dugald River*	C and D	seismic line	118/1770
Stage 1 Mount Isa	*Pilgrim Fault*	E, F and G	major NNE-SSW trending faults between Dugald River base metal occurences, the Mary Kathleen U mine and the Tick Hill Au mine	170/2550
Stage 1 Mount Isa	*Selwyn*	H	region of significant IOCG mineralisation	55/825
Stage 1 Mount Isa	*Cloncurry*	I	Cloncurry Fault	103/1545
Stage 2 Mount Isa	*Termite Range east*	A^I	few mineral occurrences, intense folding and granites	60/900
Stage 2 Mount Isa	*Gunpowder east*	B^I	major fault and Cu mines	65/975
Stage 2 Mount Isa	*Kajabbi*	C^I		40/600
Stage 2 Mount Isa	*Mary Kathleen*	D^I	numerous Cu deposits	80/1200
Stage 2 Mount Isa	*Mount Isa west*	E^I	major Cu, Zn deposits and some U occurrences	70/1050
Stage 2 Mount Isa	*Selwyn north*	F^I	Cu, Au occurrences	55/825
Stage 2 Mount Isa	*Dajarra north*	G^I	inferred southward continuation of Mount Isa Group	50/750
Stage 2 Mount Isa	*Dajarra east-west*	H^I	geological cross section	50/750

Stage 2 Georgetown	*Croydon*	A[G]	numerous Au occurrences	25/375
Stage 2 Georgetown	*Ironhurst*	B[G]		40/600
Stage 2 Georgetown	*Mount Turner*	C[G]		60/900
Stage 2 Georgetown	*Agate Creek*	D[G]		55/825
Stage 2 Georgetown	*Broken River*	E[G]	Au, Sb and U prospects	55/825
Stage 2 Georgetown	*Kidston*	F[G]	major granite-hosted Au mine;	80/1200
Stage 2 Georgetown	*Balcooma*	G[G]		30/450
Stage 2 Georgetown	*Woolgar*	H[G]		25/375
Stage 2 Hodgkinson	*Palmerville Fault north*	A[H]	mineral potential	102/1530
Stage 2 Hodgkinson	*Palmerville Fault south*	B[H]	skarn and epithermal Au deposits	90/1530
Stage 2 Charters Towers	*Pajingo*	A[P]	epithemal Au deposits as well as skarn and mesothermal systems	40/600
Stage 2 Charters Towers	*Wirralie north*	B[H]	epithermal Au, intrusive related vein and breccia-hosted Au-Ag occurrences	45/675

APPENDIX 2

HyMap Flight line Datum and Projections

Block Name	Datum	Projection	Block Name	Datum	Projection	Block Name	Datum	Projection
Mt Isa – S1 A	WGS-84	UTM South 54	***Georgetown - A***	WGS-84	UTM South 54	***Mt Isa - S2 A***	WGS-84	UTM South 54
Mt Isa - S1 B	WGS-84	UTM South 54	***Georgetown - B***	WGS-84	UTM South 54	***Mt Isa - S2 B***	WGS-84	UTM South 54
Mt Isa - S1 C	WGS-84	UTM South 54	***Georgetown - C***	WGS-84	UTM South 54	***Mt Isa - S2 C***	WGS-84	UTM South 54
Mt Isa - S1 D	WGS-84	UTM South 54	***Georgetown - D***	WGS-84	UTM South 54	***Mt Isa - S2 D***	WGS-84	UTM South 54
Mt Isa - S1 E	WGS-84	UTM South 54	***Georgetown - E***	WGS-84	UTM South 55	***Mt Isa - S2 E***	WGS-84	UTM South 54
Mt Isa - S1 F	WGS-84	UTM South 54	***Georgetown - F***	WGS-84	UTM South 55	***Mt Isa - S2 F***	WGS-84	UTM South 54
Mt Isa - S1 G	WGS-84	UTM South 54	***Georgetown - G***	WGS-84	UTM South 55	***Mt Isa - S2 G***	WGS-84	UTM South 54
Mt Isa - S1 H	WGS-84	UTM South 54	***Georgetown - H***	WGS-88	UTM South 54	***Mt Isa - S2 H***	WGS-84	UTM South 54
Mt Isa - S1 I	WGS-84	UTM South 54	***Hodgkinson - A***	WGS-84	UTM South 55	***Pajingo - A***	WGS-84	UTM South 55
			Hodgkinson - B	WGS-84	UTM South 55	***Pajingo - B***	WGS-84	UTM South 55

Where S1 is Stage 1 (2006) HyMap Survey and S2 is Stage 2 (2007) HyMap survey (Figure 1).

APPENDIX 3

Stage 1 flight line survey times

Stage 1 Survey	Block	Run	Year	Month	Day	Hour (GMT)	Hour (local time)	Minutes	Seconds
Mount Isa	A	1	2006	8	17	3	13	7	12
Mount Isa	A	2	2006	8	17	3	13	24	23
Mount Isa	A	3	2006	8	17	3	13	41	8
Mount Isa	A	4	2006	8	17	3	13	58	24
Mount Isa	A	5	2006	8	17	4	14	15	47
Mount Isa	A	6	2006	8	17	4	14	33	53
Mount Isa	A	9	2006	8	16	4	14	42	34
Mount Isa	A	7	2006	8	17	4	14	51	1
Mount Isa	A	8	2006	8	16	4	14	59	40
Mount Isa	B	10	2006	8	16	2	12	41	35
Mount Isa	B	11	2006	8	16	2	12	55	0
Mount Isa	B	12	2006	8	16	3	13	8	32
Mount Isa	B	13	2006	8	16	3	13	21	25
Mount Isa	B	14	2006	8	16	3	13	34	1
Mount Isa	B	15	2006	8	16	3	13	47	4
Mount Isa	B	16	2006	8	16	4	14	0	32
Mount Isa	B	17	2006	8	16	4	14	13	5
Mount Isa	B	18	2006	8	16	4	14	25	38
Mount Isa	C	27	2006	8	18	3	13	13	14
Mount Isa	C	26	2006	8	18	3	13	31	46
Mount Isa	C	25	2006	8	18	3	13	49	32
Mount Isa	C	24	2006	8	18	4	14	7	27
Mount Isa	C	23	2006	8	18	4	14	25	38
Mount Isa	C	22	2006	8	18	4	14	43	53
Mount Isa	C	21	2006	8	18	5	14	8	17
Mount Isa	C	20	2006	8	18	5	15	27	28
Mount Isa	C	19	2006	8	18	5	15	45	10
Mount Isa	D	37	2006	8	15	2	12	41	34
Mount Isa	D	36	2006	8	15	2	12	58	21
Mount Isa	D	35	2006	8	15	3	13	14	39
Mount Isa	D	34	2006	8	15	3	13	31	20
Mount Isa	D	33	2006	8	15	3	13	46	55
Mount Isa	D	32	2006	8	15	4	14	2	56
Mount Isa	D	31	2006	8	15	4	14	18	13
Mount Isa	D	30	2006	8	15	4	14	39	18
Mount Isa	D	29	2006	8	15	4	14	54	10
Mount Isa	D	28	2006	8	15	5	15	10	3
Mount Isa	E	46	2006	8	16	1	11	40	30
Mount Isa	E	45	2006	8	16	1	11	53	29
Mount Isa	E	44	2006	8	16	2	12	7	11
Mount Isa	E	38	2006	8	17	0	10	33	40
Mount Isa	E	39	2006	8	17	0	10	47	25
Mount Isa	E	40	2006	8	17	1	11	0	54
Mount Isa	E	41	2006	8	17	1	11	14	39
Mount Isa	E	42	2006	8	17	1	11	27	51

Mount Isa	E	43	2006	8	17	1	11	41	51
Mount Isa	F	54	2006	8	15	0	10	53	13
Mount Isa	F	55	2006	8	15	0	10	31	26
Mount Isa	F	56	2006	8	15	0	10	14	37
Mount Isa	F	51	2006	8	15	1	11	58	27
Mount Isa	F	52	2006	8	15	1	11	36	50
Mount Isa	F	53	2006	8	15	1	11	14	42
Mount Isa	F	50	2006	8	15	2	12	19	20
Mount Isa	F	48	2006	8	16	0	10	58	59
Mount Isa	F	49	2006	8	16	0	10	37	36
Mount Isa	F	47	2006	8	16	1	11	20	8
Mount Isa	G	67	2006	8	12	0	10	15	3
Mount Isa	G	66	2006	8	12	0	10	22	57
Mount Isa	G	65	2006	8	12	0	10	32	47
Mount Isa	G	64	2006	8	12	0	10	44	44
Mount Isa	G	63	2006	8	12	0	10	59	4
Mount Isa	G	62	2006	8	12	1	11	13	16
Mount Isa	G	61	2006	8	12	1	11	27	29
Mount Isa	G	60	2006	8	12	1	11	41	34
Mount Isa	G	59	2006	8	12	1	11	55	43
Mount Isa	G	58	2006	8	12	2	12	9	54
Mount Isa	G	57	2006	8	12	2	12	21	29
Mount Isa	H	68	2006	8	11	1	11	31	43
Mount Isa	H	69	2006	8	11	1	11	43	17
Mount Isa	H	70	2006	8	11	1	11	56	50
Mount Isa	H	71	2006	8	11	2	12	12	14
Mount Isa	H	72	2006	8	11	2	12	28	2
Mount Isa	H	73	2006	8	11	2	12	43	45
Mount Isa	H	74	2006	8	11	2	12	59	31
Mount Isa	H	75	2006	8	11	3	13	15	30
Mount Isa	H	76	2006	8	11	3	13	31	27
Mount Isa	H	77	2006	8	11	3	13	46	48
Mount Isa	H	78	2006	8	11	3	13	57	44
Mount Isa	H	79	2006	8	11	4	14	4	14
Mount Isa	I	88	2006	8	10	2	12	37	35
Mount Isa	I	87	2006	8	10	3	13	4	50
Mount Isa	I	86	2006	8	10	3	13	30	53
Mount Isa	I	85	2006	8	11	4	14	28	36
Mount Isa	I	84	2006	8	11	4	14	54	20
Mount Isa	I	80	2006	8	12	3	13	2	54
Mount Isa	I	81	2006	8	12	3	13	28	51
Mount Isa	I	82	2006	8	12	3	13	54	39
Mount Isa	I	83	2006	8	12	4	14	21	4

Stage 2 flight line survey times

Stage 2 Survey	Block	Run	Year	Month	Day	Hour (GMT)	Hour (local time)	Minutes	Seconds
Mount Isa	D	13	2007	8	19	0	10	21	28
Mount Isa	D	3	2007	8	19	0	10	43	24
Mount Isa	D	2	2007	8	19	0	10	58	19
Mount Isa	D	1	2007	8	19	1	11	7	22
Mount Isa	D	4	2007	8	19	1	11	44	22
Mount Isa	D	5	2007	8	19	2	12	6	15
Mount Isa	D	6	2007	8	19	2	12	29	26
Mount Isa	D	7	2007	8	19	2	12	52	8
Mount Isa	D	8	2007	8	20	3	13	10	18
Mount Isa	D	9	2007	8	20	3	13	34	32
Mount Isa	D	10	2007	8	20	3	13	57	44
Mount Isa	D	11	2007	8	20	4	14	17	30
Mount Isa	D	12	2007	8	20	4	14	54	40
Mount Isa	H	8	2007	8	20	0	10	26	15
Mount Isa	H	7	2007	8	20	0	10	44	18
Mount Isa	H	6	2007	8	20	1	11	3	36
Mount Isa	H	5	2007	8	20	1	11	22	7
Mount Isa	H	4	2007	8	20	1	11	41	48
Mount Isa	H	3	2007	8	20	2	12	0	14
Mount Isa	H	2	2007	8	20	2	12	18	31
Mount Isa	H	1	2007	8	20	2	12	37	38
Mount Isa	F	1	2007	8	21	2	12	59	24
Mount Isa	F	2	2007	8	21	3	13	22	32
Mount Isa	F	3	2007	8	21	3	13	41	58
Mount Isa	F	4	2007	8	21	4	14	1	4
Mount Isa	F	5	2007	8	21	4	14	17	41
Mount Isa	F	6	2007	8	21	4	14	35	46
Mount Isa	F	7	2007	8	21	4	14	53	45
Mount Isa	F	8	2007	8	21	5	15	11	35
Mount Isa	G	1	2007	8	21	0	10	12	47
Mount Isa	G	2	2007	8	21	0	10	32	9
Mount Isa	G	3	2007	8	21	0	10	51	5
Mount Isa	G	4	2007	8	21	1	11	9	27
Mount Isa	G	5	2007	8	21	1	11	29	32
Mount Isa	G	6	2007	8	21	1	11	47	18
Mount Isa	G	7	2007	8	21	2	12	5	24
Mount Isa	G	8	2007	8	21	2	12	24	58
Mount Isa	B	3	2007	8	22	0	10	26	37
Mount Isa	B	4	2007	8	22	0	10	38	23
Mount Isa	B	5	2007	8	22	0	10	47	48
Mount Isa	B	1	2007	8	22	0	10	59	7
Mount Isa	B	2	2007	8	22	1	11	8	22
Mount Isa	B	6	2007	8	22	1	11	17	58
Mount Isa	B	7	2007	8	22	1	11	30	57
Mount Isa	B	8	2007	8	22	1	11	55	10
Mount Isa	B	9	2007	8	22	2	12	15	41
Mount Isa	B	10	2007	8	22	2	12	37	49

Mount Isa	B	11	2007	8	22	3	13	1	32
Mount Isa	B	12	2007	8	22	3	13	22	15
Mount Isa	B	13	2007	8	22	3	13	40	7
Mount Isa	B	14	2007	8	22	3	13	56	49
Mount Isa	B	15	2007	8	22	4	14	11	15
Mount Isa	B	16	2007	8	22	4	14	21	53
Mount Isa	C	1	2007	8	23	0	10	20	35
Mount Isa	C	2	2007	8	23	0	10	37	12
Mount Isa	C	3	2007	8	23	0	10	51	42
Mount Isa	C	4	2007	8	23	1	11	7	16
Mount Isa	C	5	2007	8	23	1	11	21	47
Mount Isa	C	6	2007	8	23	1	11	36	56
Mount Isa	C	7	2007	8	23	1	11	52	24
Mount Isa	C	8	2007	8	23	2	12	7	34
Mount Isa	E	1	2007	8	27	0	10	17	48
Mount Isa	E	2	2007	8	27	0	10	38	42
Mount Isa	E	3	2007	8	27	0	10	59	27
Mount Isa	E	4	2007	8	27	1	11	19	43
Mount Isa	E	5	2007	8	27	1	11	40	5
Mount Isa	E	7	2007	9	1	0	10	51	17
Mount Isa	E	8	2007	9	1	0	10	29	38
Mount Isa	E	6	2007	9	2	0	10	22	31
Hodgkinson	B	10	2007	9	3	2	12	9	13
Hodgkinson	B	11	2007	9	3	2	12	30	8
Hodgkinson	B	12	2007	9	8	0	10	10	18
Hodgkinson	B	13	2007	9	8	0	10	32	46
Hodgkinson	B	14	2007	9	8	0	10	23	50
Hodgkinson	B	1	2007	9	12	22	8	59	9
Hodgkinson	B	2	2007	9	12	23	9	9	7
Hodgkinson	B	3	2007	9	12	23	9	21	54
Hodgkinson	B	4	2007	9	12	23	9	37	5
Hodgkinson	B	5	2007	9	12	23	9	56	59
Hodgkinson	B	6	2007	9	13	0	10	20	44
Hodgkinson	B	7	2007	9	13	0	10	44	2
Hodgkinson	B	8	2007	9	13	1	11	7	58
Hodgkinson	B	9	2007	9	13	1	11	32	33
Hodgkinson	A	13	2007	9	10	22	8	55	30
Hodgkinson	A	12	2007	9	10	23	9	14	50
Hodgkinson	A	11	2007	9	10	23	9	33	0
Hodgkinson	A	10	2007	9	10	23	9	55	42
Hodgkinson	A	7	2007	9	11	23	9	27	23
Hodgkinson	A	6	2007	9	11	23	9	54	46
Hodgkinson	A	8	2007	9	11	22	8	59	7
Hodgkinson	A	5	2007	9	12	0	10	21	51
Hodgkinson	A	4	2007	9	12	0	10	50	10
Hodgkinson	A	3	2007	9	12	1	11	8	12
Hodgkinson	A	2	2007	9	12	1	11	21	38
Hodgkinson	A	1	2007	9	12	1	11	31	24
Hodgkinson	A	9	2007	9	12	1	11	54	0
Georgetown	A	8	2007	9	15	23	9	44	47
Georgetown	A	7	2007	9	15	23	9	54	14
Georgetown	A	6	2007	9	16	0	10	3	34

Georgetown	A	5	2007	9	16	0	10	12	41
Georgetown	A	4	2007	9	16	0	10	21	55
Georgetown	A	3	2007	9	16	0	10	31	19
Georgetown	A	2	2007	9	16	0	10	40	6
Georgetown	A	1	2007	9	16	0	10	49	40
Georgetown	B	1	2007	9	13	2	12	23	33
Georgetown	B	2	2007	9	13	2	12	36	53
Georgetown	B	3	2007	9	13	2	12	51	14
Georgetown	B	4	2007	9	13	3	13	4	41
Georgetown	B	5	2007	9	13	3	13	18	10
Georgetown	B	6	2007	9	13	3	13	31	10
Georgetown	B	7	2007	9	13	3	13	44	48
Georgetown	B	8	2007	9	13	3	13	57	59
Georgetown	C	1	2007	9	13	4	14	15	46
Georgetown	C	2	2007	9	13	4	14	33	24
Georgetown	C	3	2007	9	13	4	14	51	7
Georgetown	C	4	2007	9	13	5	15	8	57
Georgetown	C	5	2007	9	13	5	15	26	52
Georgetown	C	6	2007	9	13	5	15	44	59
Georgetown	C	7	2007	9	14	4	14	45	1
Georgetown	C	8	2007	9	14	5	15	2	15
Georgetown	D	1	2007	9	14	4	14	13	58
Georgetown	D	2	2007	9	14	3	13	57	49
Georgetown	D	3	2007	9	14	3	13	41	55
Georgetown	D	4	2007	9	14	3	13	25	30
Georgetown	D	5	2007	9	14	3	13	9	16
Georgetown	D	6	2007	9	14	2	12	52	58
Georgetown	D	7	2007	9	14	2	12	36	54
Georgetown	D	8	2007	9	14	2	12	20	11
Georgetown	E	8	2007	9	13	23	9	15	39
Georgetown	E	7	2007	9	13	23	9	38	14
Georgetown	E	6	2007	9	14	0	10	0	36
Georgetown	E	5	2007	9	14	0	10	23	31
Georgetown	E	4	2007	9	14	0	10	46	16
Georgetown	E	2	2007	9	14	1	11	31	40
Georgetown	E	1	2007	9	14	1	11	54	24
Georgetown	F	8	2007	9	15	0	10	51	19
Georgetown	F	7	2007	9	15	1	11	1	44
Georgetown	F	6	2007	9	15	1	11	12	43
Georgetown	F	5	2007	9	15	1	11	23	40
Georgetown	F	4	2007	9	15	1	11	34	44
Georgetown	F	3	2007	9	15	1	11	45	27
Georgetown	F	2	2007	9	15	1	11	56	48
Georgetown	F	1	2007	9	15	2	12	7	35
Georgetown	G	1	2007	9	15	2	12	27	27
Georgetown	G	2	2007	9	15	2	12	44	26
Georgetown	G	3	2007	9	15	3	13	1	30
Georgetown	G	4	2007	9	15	3	13	18	23
Georgetown	G	5	2007	9	15	3	13	34	53
Georgetown	G	6	2007	9	15	3	13	51	6
Georgetown	G	7	2007	9	15	4	14	6	39
Georgetown	G	8	2007	9	15	4	14	21	58

Georgetown	H	1	2007	9	14	23	9	9	34
Georgetown	H	2	2007	9	14	23	9	18	46
Georgetown	H	3	2007	9	14	23	9	28	0
Georgetown	H	4	2007	9	14	23	9	36	59
Georgetown	H	5	2007	9	14	23	9	46	4
Georgetown	H	6	2007	9	14	23	9	54	51
Georgetown	H	7	2007	9	15	0	10	3	54
Georgetown	H	8	2007	9	15	0	10	12	49
Pajingo	A	8	2007	9	16	4	14	48	46
Pajingo	A	7	2007	9	16	5	15	0	27
Pajingo	A	6	2007	9	16	5	15	12	3
Pajingo	A	5	2007	9	16	5	15	24	5
Pajingo	A	4	2007	9	16	5	15	35	48
Pajingo	A	3	2007	9	16	5	15	47	23
Pajingo	A	2	2007	9	16	5	15	58	45
Pajingo	A	1	2007	9	16	6	16	10	8
Pajingo	B	8	2007	9	16	2	12	58	20
Pajingo	B	7	2007	9	16	3	13	12	30
Pajingo	B	6	2007	9	16	3	13	25	32
Pajingo	B	5	2007	9	16	3	13	39	9
Pajingo	B	4	2007	9	16	3	13	52	41
Pajingo	B	3	2007	9	16	4	14	6	25
Pajingo	B	2	2007	9	16	4	14	19	39
Pajingo	B	1	2007	9	16	4	14	32	47
Mount Isa	A	8	2008	8	20	2	12	36	51
Mount Isa	A	7	2008	8	20	2	12	55	2
Mount Isa	A	6	2008	8	20	3	13	13	23
Mount Isa	A	5	2008	8	20	3	13	31	23
Mount Isa	A	4	2008	8	20	3	13	49	32
Mount Isa	A	3	2008	8	20	4	14	7	50
Mount Isa	A	2	2008	8	20	4	14	25	56
Mount Isa	A	1	2008	8	20	4	14	43	32

APPENDIX 4

Bureau of Meteorology weather records for Mount Isa, August 2007

stn_num	Date	Max T (°C)	Min T (°C)	Terrestrial Min T (°C)	Max Wind Gust (km/h)	Max Gust Direction	Evaporation (mm)	Bright Sunshine (hours)	Precipitation (mm)	Cloud Cover at 9am (oktas)	Cloud Cover at 3pm (oktas)
29127	1/08/07	28.1	5.8	4	37	N	5	10.8	0	0	0
29127	2/08/07	29.1	6.8	5	32	NE	5.4	10.8	0	0	0
29127	3/08/07	26.5	9.6	7.6	41	S	5	9.7	0	1	1
29127	4/08/07	21.9	12.7	11.5	42	S	7.4	10.2	0	4	1
29127	5/08/07	22.1	4.1	1.4	46	SE	6.4	10.8	0	0	0
29127	6/08/07	23.2	11	5.5	42	ESE	7.8	10.9	0	0	0
29127	7/08/07	25.4	3.4	1.2	35	ENE	5	10.9	0	0	0
29127	8/08/07	26.2	3.9	2	30	NE	4.8	10.9	0	0	1
29127	9/08/07	26.8	11.1	7.1	39	ESE	5.8	10.9	0	0	1
29127	10/08/07	27.3	11.6	7.5	32	E	7	10.9	0	0	0
29127	11/08/07	28.7	7.3	5.4	32	E	5.2	10.9	0	0	0
29127	12/08/07	30.1	8.9	6.8	32	WSW	6	10.9	0	0	1
29127	13/08/07	29.6	14.6	10.6	35	S	7	10.9	0	1	0
29127	14/08/07	28.7	13.4	8.6	35	SSE	8.2	10.9	0	1	2
29127	15/08/07	31.2	15.7	11.2	28	SSE	8.2	10.7	0	4	1
29127	16/08/07	27.1	11.6	9	39	S	5.8	2.9	0	3	7
29127	17/08/07	14.5	12.7	10.8	37	E	6.2	0	2.4	8	8
29127	18/08/07	23.1	11.8	10.2	39	S	2.2	7	1.2	7	5
29127	19/08/07	24.2	13.2	11.2	45	SE	7.2	10.9	0	1	2
29127	20/08/07	24.6	12.4	8.4	48	SE	7.4	11.1	0	0	0
29127	21/08/07	24	10.2	6.1	46	E	7.6	11.2	0	0	0
29127	22/08/07	26.7	5.2	3.5	39	S	6.2	11.2	0	0	1
29127	23/08/07	27.7	11.6	9	48	S	5.6	11.1	0	0	3
29127	24/08/07	26.7	12.6	9.9	39	SE	6.8	11.3	0	0	1
29127	25/08/07	26.5	9	6.4	30	SSE	7	11.3	0	1	1
29127	26/08/07	28.1	13.3	10.2	32	E	6.4	11.3	0	0	0
29127	27/08/07	29.7	9.6	8	33	NE	6.2	11.2	0	0	1
29127	28/08/07	30.1	12.4	10.6	32	NE	5.8	11.2	0	1	2
29127	29/08/07	28.4	14.8	10.7	46	SE	6.8	11.1	0	0	1
29127	30/08/07	28.1	13.5	10.7	37	ENE	8.2	11.2	0	1	1
29127	31/08/07	29	10.2	8.4	33	S	6.2	11	0	1	2

APPENDIX 5

HyMap band centres for Stages 1 and 2 as well as the difference between

band	Stage 1 (nm)	Stage 2 (nm)	Difference (nm)	band	Stage 1 (nm)	Stage 2 (nm)	Difference (nm)	band	Stage 1 (nm)	Stage 2 (nm)	Difference (nm)
1	453.7	458.5	-4.8	**44**	1073.3	1073.2	0.1	**87**	1715	1712.8	2.2
2	467.9	473.3	-5.4	**45**	1087.9	1087.7	0.2	**88**	1727.4	1725.1	2.3
3	482.5	488.2	-5.7	**46**	1102.7	1102.5	0.2	**89**	1739.6	1737.3	2.3
4	497.4	502.9	-5.5	**47**	1117.3	1117.1	0.2	**90**	1751.7	1749.5	2.2
5	512.3	517.8	-5.5	**48**	1131.6	1131.6	0	**91**	1764	1761.5	2.5
6	527.2	532.9	-5.7	**49**	1145.9	1145.9	0	**92**	1776.1	1773.5	2.6
7	542	547.6	-5.6	**50**	1160.4	1160.3	0.1	**93**	1788	1785.3	2.7
8	556.8	562.4	-5.6	**51**	1174.7	1174.7	0	**94**	1799.8	1797.1	2.7
9	571.7	577.1	-5.4	**52**	1188.8	1188.9	-0.1	**95**	1951.7	1949.5	2.2
10	586.4	592.1	-5.7	**53**	1202.9	1202.9	0	**96**	1970.9	1968.3	2.6
11	601.2	606.8	-5.6	**54**	1217	1217.1	-0.1	**97**	1990.4	1987.2	3.2
12	616	621.4	-5.4	**55**	1230.9	1231.1	-0.2	**98**	2009.7	2006.4	3.3
13	630.5	635.8	-5.3	**56**	1244.7	1245.1	-0.4	**99**	2028.6	2025.5	3.1
14	644.8	650.2	-5.4	**57**	1258.8	1259	-0.2	**100**	2047.3	2044.2	3.1
15	659.3	664.8	-5.5	**58**	1272.7	1273	-0.3	**101**	2066.1	2062.8	3.3
16	674	679.4	-5.4	**59**	1286.3	1286.7	-0.4	**102**	2085.1	2081.2	3.9
17	688.6	693.9	-5.3	**60**	1299.9	1300.4	-0.5	**103**	2103.8	2099.5	4.3
18	702.9	708.3	-5.4	**61**	1313.8	1314.2	-0.4	**104**	2122.2	2117.7	4.5
19	717.4	722.6	-5.2	**62**	1327.6	1328	-0.4	**105**	2140.2	2135.7	4.5
20	731.8	737	-5.2	**63**	1390.4	1389.3	1.1	**106**	2158	2153.4	4.6
21	746	751.2	-5.2	**64**	1405.3	1404.1	1.2	**107**	2175.7	2170.9	4.8
22	760.1	765.4	-5.3	**65**	1420.1	1418.7	1.4	**108**	2193.1	2187.9	5.2
23	774.3	779.6	-5.3	**66**	1434.4	1433.2	1.2	**109**	2212	2205.5	6.5
24	788.6	793.8	-5.2	**67**	1448.7	1447.7	1	**110**	2229.9	2223.9	6
25	802.8	808.3	-5.5	**68**	1463	1462.1	0.9	**111**	2247.1	2240.8	6.3
26	816.9	822.5	-5.6	**69**	1477.6	1476.4	1.2	**112**	2264.3	2258.5	5.8
27	831.3	836.7	-5.4	**70**	1491.5	1490.5	1	**113**	2281.4	2275.5	5.9
28	845.5	850.8	-5.3	**71**	1505.3	1504.2	1.1	**114**	2298.8	2292.6	6.2
29	859.5	864.8	-5.3	**72**	1519.1	1517.9	1.2	**115**	2316.1	2309.5	6.6
30	873.1	878.3	-5.2	**73**	1533	1531.7	1.3	**116**	2333.1	2326.2	6.9
31	886.4	890.8	-4.4	**74**	1546.5	1545.4	1.1	**117**	2349.7	2342.8	6.9
32	890.9	890.8	0.1	**75**	1560	1558.9	1.1	**118**	2366.1	2359.4	6.7
33	906	905.8	0.2	**76**	1573.5	1572.1	1.4	**119**	2382.4	2375.8	6.6
34	921.4	920.9	0.5	**77**	1586.7	1585.3	1.4	**120**	2399	2392	7
35	937	936.6	0.4	**78**	1599.7	1598.5	1.2	**121**	2415.5	2408.3	7.2
36	952.9	952.4	0.5	**79**	1613	1611.5	1.5	**122**	2431.9	2424.5	7.4
37	967.9	967.5	0.4	**80**	1626.1	1624.7	1.4	**123**	2447.9	2440.4	7.5
38	983	982.7	0.3	**81**	1639.1	1637.5	1.6	**124**	2463.6	2456.4	7.2
39	998.5	998.2	0.3	**82**	1651.8	1650.3	1.5	**125**	2478.8	2472.2	6.6
40	1013.7	1013.4	0.3	**83**	1664.6	1662.9	1.7	**126**	2494.1	2487.5	6.6
41	1028.5	1028.4	0.1	**84**	1677.3	1675.5	1.8				
42	1043.8	1043.5	0.3	**85**	1689.8	1688	1.8				
43	1058.8	1058.5	0.3	**86**	1702.3	1700.4	1.9				

APPENDIX 6

Stage 1: Field data and laboratory analyses

Sample site [Mixxx; xxx=site locality]	easting (mE)	northing (mN)	Description	Cover	ASD samples [mixxxyz; where xxx=site locality; yy=f1..fn (fresh) *or* =w1…wn (weathered) *or* =s1…sn (soil)]	XRD samples [mixxxyz; where xxx=site locality; yy=fn (fresh, sample n) *or* =sn (soil, sample n)]	XRD rock/outcrop sample interpretation (majors to minors)
MI001	329106	7784985	low rise of mafic metavolcanics and are felsic pods : massive epidote and chlorite schists	30% dry grass; 5% stunted gums	mi001f1, mi001f2, mi001w1, mi001w2	MI001F1; MI001F2	Epidote, quartz, actinolite, anorthite, chlorite / clinochlore, (kaolinite); Quartz, epidote, actinolite, anorthite, chlorite / clinochlore, (kaolinite)
MI002	328995	7785052	metavolcanics, N-S subvertical foliation, chlorite schist and some epidote (<15%)	35% spinifex; 10% gums	mi002f1, mi002f2, mi002w1, mi002w2	MI002F1	Quartz, chlorite/clinochlore, albite-anorthite, (magnetite)
MI003	329761	7790393	metavolcanics, massive, dark/black, epidote altered	20% grass; 5% gums; 50% rock; 25% soil	mi003af1, mi003aw1, mi003bs1	MI003F1	Quartz, epidote, actinolite, anorthite-albite, (chlorite)
MI004	335323	7799188	Metavolcanics (medium gray basalt), north side of small hill, round scallopy weathering,	45% grass; 45% rock	mi004af1, mi004af2, mi004aw1, mi004aw2, mi004bs1	MI004F1	Actinolite, anorthite, quartz, epidote, chlorite
MI005	335305	7799014	Felsic extrusive, lapilli tuff, droplets. layers of flattened shards(?), quartz-filled vugs,	40% grass; 40% rock; 5% gums; 15% soil	mi005f1, mi005f2, mi005w1, mi005w2	MI005F2	Clinochlore, albite, quartz, , actinolite, muscovite, illite, (epidote)

			cherty, epidote altered, massive,				
MI006	325611	7799724	sandstone-siltstone-shale-quartzites-conglomerates; X-bedded; 80 degrees W dip; red chert; kaolinised finer grained units	100% fresh outcrop along creek	mi006af1, mi006af2, mi006aw1, mi006aw2, mi006bs1	MI006F1; MI006F2	Anorthite, anorthoclase, orthoclase, quartz, chlorite, epidote, muscovite, (illite); ; Anorthite, anorthoclase, orthoclase, quartz, chlorite, epidote, muscovite, (illite)
MI007	390885	7703970	metasediments; subvertical 010 degrees N trend; ridge forming, amphibole/biotite/feldspar/garnet(?)-rich		mi007f1, mi007f2, mi007w1, mi007w2	MI007F1; MI007F2	Quartz, sanidine/albite, ferropargasite/ferroactinolite, clinochlore; Quartz, actinolite/hornblende, epidote, calcite, (andradite)
MI008	390922	7703989	carbonate laminated, valley-forming; dark grey-brown,	70% grass; 10% soil; 10% trees; 10% outcrop	mi008bs1, mi008bs2, mi008f1, mi008w1	MI008F1	Quartz, calcite, biotite, albite, (hornblende)
MI009	396917	7706282	Mary Kathleen Uranium Mine dumps		mi009f1, mi009f2, mi009f3, mi009w1, mi009w2, mi009w3	MI009F1; MI009F3	Potassium pargasite, actinolite, hornblende, anorthoclase/albite, (muscovite, biotite calcite?); Augite, diopside, albite, anorthoclse, chlorite, anatase
MI010	397736	7709831	felsic rock with abundant epidote and Cu CO3	40% outcrop; 50% grass; 10% trees	mi010f1, mi010w1	MI010F1; MI010F2	Albite/anorthoclase, ferropargasite, augite, (muscovite); Augite, Andradite, grossular garnet, albite/anorthite, (clinochlore)
MI011	400337	7713824	1 m wide carbonate vein in 50 m wide dolerite; dolerite 3-4 mm kaolinised feldspar (44%) + pyroxene/amphibole (60%); Carbonate white 1 cm coarse crystalline	70% gabbro float; 20% grass; 10% soil	mi011f1, mi011f2, mi011w1, mi011w2	MI011F1; MI011F2; MI011F3	Calcite, dolomite/ankerite; Magnesiohornblene/actinolite, chlorite, albite, anorthite, quartz, (muscovite); Calcite, quartz

MI012	400273	7713811	sedimentary carbonate subvertical 100 degree trend and 1 cm pink 045 trending carbonate veins; flat to elongate dark green 3mm to 1 cm "amphibole" (?) (E-W compression and vertical extension)		mi012f1, mi012f2, mi012f3, mi012f4, mi012w1, mi012w2, mi012w3	MI012F1; MI012F3; MI012F4	Calcite, dolomite/ankerite, magnesioriebeckite; Calcite, dolomite(/ankerite?), quartz, chlorite-vermiculite; Albite / anorthite, calcite, quartz, magnesioriebeckite, potassic pargasite
MI013	401141	7715287	dolerite; 15% feldspar, 2-3 mm grainsize	15% spinifex; 60% outcrop; 25% soil	mi013bs1, mi013f1, mi013w1	MI013F1	Albite / anorthite, calcite, quartz, magnesioriebeckite, potassic pargasite
MI014	374606	7768720	felsic-silicic volcaniclastic; buff coloured ad light green weathering; top of small hill/ridge; vein/S0 73/125	60% outcrop; 30% grass; 10% gums/bush	mi014f1, mi014s1, mi014w1	MI014F1	Quartz, sanidine, muscovite/illite, clinochlore
MI015	374494	7768993	feldspar porphyry (2-3 mm laths); top of ridge; light grey-buff	20% dry grass; 15% sticky bushes; 10% gums; 50% outcrop; 10% soil	mi015f1, mi015w1	MI015F1	Quartz, sanidine/anorthoclase, muscovite/illite
MI016	374494	7768981	Road cutting in felsic volcaniclastic and light green, massive 2-3mm feldspar porphyry rock		mi016f1, mi016w1	MI016F1	Quartz, albite/sanidine, muscovite/celadonite
MI017	374934	7770507	Felsic-intermediate volcaniclastic rock. Shale unit foliation subvertical trend 349 degrees. Quartz-pink feldspar 3 cm wide pegmatite vein. Massive dark grey micaceous rocks. Valley-forming	30% gums; 50% grass and dry plant material; 15% soil; 5% rock	mi017f1, mi017f2, mi017s1, mi017w1, mi017w2	MI017F1	Clinochlore, quartz, albite, illite
MI018	374318	7776997	Siliceous, white felsic volcaniclastic/quartzite. No cleavage, S0 42/290, 30 wide unit	65% outcrop; 25% spinifex; 5% gums.	mi018f1, mi018s1, mi018w1	MI018F1	Quartz, muscovite, halloysite

			flanked by pink weathering felsic rock.				
MI019	374006	7776823	Yellow-green felsic volcaniclastic with a 1-2 cm spaced cleavage.		mi019f1, mi019w1		
MI020	371233	7776325	feldspar porphyry and grey volcaniclastic, massive to weakly foliated. Fire scarred	15% spinifex; 10% dry plant material; 10% young trees; 35% soil; 35% outcrop/float	mi020f1, mi020s1, mi020w1	MI020F1	Quartz, albite/sandine/orthoclase, muscovite
MI021	376056	7778806	lag of 1-2 cm sized fine grained micaceous pink granite and quartz fragments with a light brown sandy loam	60% spinifex; 20% lag; 20% soil	mi021bs1, mi021f1, mi021w1, mi021w2, mi021w3	MI021F2; MI021F3	Quartz; Quartz, kaolinite
MI022	376362	7780576	Ferruginous, weakly foliated, ridge-forming volcaniclastic. S1 78/060. Conglomerates (quartz, banded cherts and felsic volcaniclastic clasts). Chloritic foliation? Quartz-feldspar veins subparallell to S0	35% outcrop; 25% trees; 15% soil; 25% grass	mi022f1, mi022s1, mi022w1, mi022w2	MI022F1	Quartz, kaolinite, clinochlore, hematite, magnetite
MI023	376098	7780565	Chlorite schist, dark grey to dark green, moderate Fe oxide staining. S1 80/250, close spaced 1 mm cleavage, 50 m wide unit and several hundreds of metres long	50% spinifex; 5% outcrop; 35% float; 15% soil; 5% gums	mi023f1, mi023s1, mi023w1	MI023F1	Quartz, albite/anorthite, muscovite, clinochlore
MI024	378224	7781856	Coarse grained granite with anhedral (20%) to lath-shaped euhedral	15% trees; 5% green bushes; 10% outcrop;	mi024f1, mi024s1, mi024w1	MI024F1	Albite, muscovite/illite, biotite, andradite, prehnite

			(30%) plagioclase crystals up to 40 mm with quartz (30%) and 20% dark gray groundmass with biotite(?) and amphibole (?)	50% soil/lag/grit; 10% spinifex			
MI025	418883	7756193	white-pink-grey granite with variable grainsize from 1 mm to 10mm including black amphibole laths.	45%outcrop; 35% grass/spinifex; 20% soil; <5% gums	mi025f1, mi025f2, mi025w1, mi025w2	MI025F1; MI025F2	Quartz, albite/anorthite, clinochlore, muscovite; Quartz, albite/anorthite, magnesioriebeckite, biotite, muscovite
MI026	413921	7760062	Carbonate unite (Pk3), foliated to massive grey-green-blue with abundant Cu carbonate. Southern end of drill core	60% spinifex; 5% rock; 25% float; 5% trees	mi026f1, mi026f2, mi026s1, mi026w1, mi026w2	MI026F1; MI026F2	Clinochlore, quartz, celadonite/muscovite, sandine; Clinochlore, muscovite/illite, quartz
MI027	414013	7760061	red weathering schist 1mm micaceous cleavage, S1 65/100,	30% spinifex; 55% float (1cm rock frags); 20% trees; <5% soil	mi027f1, mi027f2, mi027s1, mi027w1, mi027w2	MI027F1; MI027F2	Quartz, halite; Quartz, illite/muscovite, sanidine/anorthite, kaolinite
MI028	412772	7762600	Light buff coloured, brecciated (angular blocks) laminated (bedded) limestones (ring when hit). Outcrops 3 m wide and 50 m spaced trending 110.	80% spinifex; 15% soil; 5% outcrop.	mi028f1, mi028f2, mi028w1, mi028w2	MI028F1	Albite, quartz, calcite, hematite, illite-montmorillonite
MI029	414510	7763351	siliceous, 5m wide, ridge forming unit (aplite? dyke), quartz-feldspar-mica, very fine grained	30% spinifex; 55% outcrop; 10% trees; 5% soil	mi029f1, mi029s1, mi029w1	MI029F1	Quartz

MI030	415338	7762430	Extensive outcrop in creek. Massive to laminated (1-4 cm) siliceous grey siltstone S0 73/230 with crosscutting veins of amphibole (inner) and pink feldspar (outer) 45/230. En echelon quartz vein arrays 90/090 and 90/165 (sigma 1 horizontal 45-225)		mi030f1, mi030f2, mi030f3, mi030f4, mi030f5, mi030w1, mi030w2, mi030w3, mi030w4, mi030w5	MI030F1; MI030F2; MI030F3; MI030F4; MI030F5	Albite, Goethite/hematite, quartz, muscovite; Albite, quartz, hematite, illite, kaolinite; Albite, quartz; Albite, augite, hematite, clinochlore; Quartz, albite/anorthoclase, dolomite/calcite, illite
MI031	411937	7765436	foliated grey-green siltstone 85/265	20% spinifex; 5% outcrop; 35% float; 35% soil; 5% trees	mi031f1, mi031s1, mi031w1, mi031w2	MI031F1	Muscovite, clinochlore, quartz, albite, hematite
MI032	412128	7765497	very poor exposure along drill core, blocky lag (up to 8cm) of quartz and ferruginous grey rock	40% dry grass; 25% lag; 25% soil; 5% spinifex; 5% gums	mi032f1, mi032w1	MI032F1	Quartz, sanidine/orthocloase, muscovite/illite
MI033	412626	7765361	Gossanous, eastern end of drill line. Ferruginous and manganiferous. Float with 3 mm blebs of mica. Some quartz with Cu carbonates. 1 mm green medium grained rock + 4 mm pink spotty grey rock + light weight, dull grey zinc gossan?	20% spinifex; 40% quartz lag; 40% Mn and Fe oxide float	mi033f1, mi033f2, mi033f4, mi033w1, mi033w2, mi033w3, mi033w4, mi033w5	MI033F1; MI033F2; MI033F3; MI033F4; MI033F5	Quartz, muscovite/illite, sanidine/anothoclase, siderite/calcite-magnesian, clinochlore; Muscovite/illite, quartz, clinochlore, siderite/calcite-magnesian, hematite; Quartz, illite/muscovite, chlorite, hematite; Quartz, sanidine/orthoclase, illite/muscovite, kaolinite, montmorillonite, tourmaline; Dolomite, quartz, muscovite/illite, halloysite, kaolinite.
MI034	412561	7765676	Spotted micaceous massive to foliated rock - poor outcrop	30% spinifex; 40% soil; 10% trees; 10% quartz float; 10% rock float	mi034f1, mi034f2, mi034s1, mi034w1, mi034w2, mi035f1	MI034F1; MI034F2	Quartz, illite/muscovite, halloysite, sanidine, antigorite, hematite; Quartz, illite/muscovite, halloysite, sanidine, antigorite, hematite, talc.
MI035	412844	7765758	Micaceous grey siltstone	20% spinifex; 60% lag gravel; 10% trees; 10% soil	mi035s1, mi035w1	MI035F1	Quartz, illite/muscovite/celedonite, clinochlore, andradite, albite/anorthite

MI036	401571	7694866	altered massive carbonate S0(?) 90/265, intense alteration to pink feldspar, epidote and dark green amphibole?	35% grasses; 25% green vegetation (bushes); 5% trees; 25% outcrop/float; 10% soil	mi036f1, mi036s1, mi036w1	MI036F1	Calcite/magnesian calcite, augite, prehnite, albite/microcline, quartz, actinolite
MI037	410737	7694944	laminated (1-30 mm), light pink-green limestone S0 75/107	30% outcrop; 20% grass; 15% green bushes; 5% trees; 30% float	mi037f1, mi037s1, mi037w1	MI037F1	Calcite, quartz, muscovite/illite, clinochlore, grossular garnet
MI038	410824	7694395	laminated buff-grey siltstone S0/S1 78/098	20% spinifex; 30% rock; 15% trees; 30% soil	mi038f1, mi038f2, mi038w1, mi038w2		
MI039	376084	7635471	ridge forming, massive yellow-buff dolomite/limestone (Pkc); brecciated; chert and Fe discontinuous layers. Thicker shale horizons in the valley to the east	70% outcrop; 15% spinifex; 5% trees; 10% soil	mi039f1, mi039f2, mi039f3, mi039f4, mi039w1, mi039w2, mi039w3, mi039w4	MI039F2; MI039F3	Quartz, dolomite, chalcopyrite; Dolomite, quartz
MI040	375852	7635727	red alluvium, transported, clay to fine sand	80% soil; 20% vegetation	mi040s1		
MI041	379871	7634837	dolerite ridge. Feldspar and amphibole layering. Some Cu carbonates.	50% outcrop; 30% spinifex; 5% trees; 15% soils	mi041f1, mi041f2, mi041w1, mi041w2	MI041F1; MI041F2	Augite, riebeckite, anorthite/anorthoclase, illite/muscovite; Augite, riebeckite, albite/anorthite, chlorite, andradite
MI042	379825	7635046	Thick bedded buff-yellow limestone/dolomite associated with small Cu mines. So 86/294, quartz veins, Cu carbonates, epidote, pink albite;	20% outcrop; 50% grass; 20% trees; 10% soil	mi042f1, mi042f2, mi042f3, mi042f4, mi042f5, mi042w1, mi042w2, mi042w3, mi042w4, mi042w5, mi042w6, mi042w7	MI042F1; MI042F2; MI042F3; MI042F4; MI042F5; MI042F6	Sanidine/albite, quartz, clinochlore, magnetite; Sanidine/albite/microcline, quartz, illite/muscovite; Dolomite, quartz, calcite, magnesite, goethite; Quartz ; ; Quartz, sanidine/albite, clinochlore; Riebeckite/magnesioriebeckite,

							albite, potassium pargasite, quartz, clinochlore, calcite.
MI043	393489	7603430	Devoncourt Limestone, finely laminated (1-5 cm) buff limestone with bedding parallel foliation defined white mica.	40% outcrop; 40% soils;10% grass; 5% trees	mi043f1, mi043f2, mi043w1, mi043w2	MI043F2	Dolomite/calcite/magnesian-calcite, sanidine, quartz, muscovite/illite
MI044	389235	7605477	Saddle between mesas, white-pink felsic intrusive. Feldspar-quartz graphic intergrowth, lineation 60/260 defined by quartz. Minor zones 10cm wide of hematite and albite.	50% outcrop/float, 40% spinifex, 10% soil	mi044f1, mi044f2, mi044f3, mi044w1, mi044w2, mi044w3	MI044F1; MI044F2	Sanidine/anorthite/albite, quartz, illite/muscovite; Quartz
MI045	389265	7605527	Top of mesa, above angular unconformity. Ferruginous and clay-rich flat-lying sediments. Pebbly sandstones, quartz cobbles, fine sandstone. Ripple marks and X-bedding. X-beds 280 transport . Ripple marks 2.5 cm spaced.	80% outcrop; 5% trees; 55% soil	mi045f1, mi045f2, mi045f3, mi045w1, mi045w2, mi045w3	MI045F1; MI045F2	Quartz, kaolinite, montmorillonite; Quartz, kaolinite, montmorillonite, illite, hematite
MI046	389203	7605516	Side of mesa slope, 1 mm laminated amphibolitic gneiss, with feldspar and black	60% float; 30% spinifex; 10% outcrop	mi046f1, mi046f2, mi046w1, mi046w2	MI046F1; MI046F2	Albite/anorthite, hornblende/riebeckite, ferroactinolite, quartz, rutile, muscovite;

			amphibole fine grained <1 mm. Biotite?				Ferropargasite/ferroactinolite, albite, quartz, muscovite, clinochlore
MI047	389075	7605543	Felsic gneiss in road cutting next to water tank. Foliated, weathered, white rock with increased schistosity compared to the felsic gneiss at MI044. S1 52/235		mi047f1, mi047f2, mi047s1, mi047w1, mi047w2	MI047F1; MI047F2	Anorthite/albite/anorthoclase, quartz, muscovite/illite, clinochlore; Albite/anorthite, quartz, muscovite/illite
MI048	388891	7604667	ridge-forming amphibolites gneiss with strong foliation defined by feldspar and dark minerals 1-3 mm in size. Epidote and pink albite alteration in places. S1 52/295 in one block and then in 100 m another block S1 50/330 (i.e. 35 degrees of rotation) and then another block S150/250 (45 degrees from original block). Rotation around 060 trending subvertical fault plane.	60% outcrop; 20% spinifex; 10% trees; 10% soil.	mi048f1, mi048s1, mi048w1	MI048F1	Hornblende, ferroactinolite/ferropargasite, albite/anorthite, quartz, clinochlore
MI049	388804	7604748	felsic gneiss at top of hill. Overprinting pink albite, epidote and quartz in veins/fractures	50% float; 20% soil; 20% spinifex; 10% outcrop	mi049f1, mi049f2, mi049s1, mi049w1, mi049w2	MI049F1; MI049F2; MI049F3; MI049F4	Quartz, sanidine/albite/anorthite/microcline, illite/muscovite, barite, siderite; Quartz, sanidine/albite, muscovite/illite; Quartz ; Quartz
MI050	388743	7605098	gneiss, white and black lineated 1mm 55/280.		mi050f1, mi050s1, mi050w1	MI050F1	Quartz, marialite, anorthite/orthoclase, riebeckite(?), magnetite
MI051	387899	7618366	abundant opaline silica in alluvium/colluvium, grey, white, red, yellow silica and a spongy	60^ soil, 30% opal and other rock fragments; 10% dry grass	mi051f1, mi051s1, mi051w1	MI051F1; MI051F2	Quartz, montmorillonite, dolomite, scheelite?; Quartz, montmorillonite, dolomite, scheelite?

			light brown cracking clay soil. No calcrete.				
MI052	387928	7618274	extensive exposure of white and translucent opaline silica.	25% outcrop; 55% float; 10% grasses; 5% trees; 5% soil	mi052f1, mi052f2, mi052s1, mi052w1, mi052w2	MI052F1A; MI052F1B; MI052F2; MI052F3	Quartz, montmorillonite, dolomite, scheelite?; Quartz, montmorillonite, dolomite, scheelite? Quartz, cristobalite; Cristobalite, quartz, gutsevichte?; Quartz, cristobalite
MI053	392708	7617594	Light yellow shale, foliated, kaolinised	<2% outcrop; 40% soil; 40% float (quartz, rock); 10% spinifex; 5% trees.	mi053f1, mi053w1	MI053F1	Quartz, muscovite, kaolinite
MI054	393492	7623270	Cambrian sediments. Cherts, sandstones, pebbly sandstones. Goethite-rich	30% Spinifex; 10% outcrop; 40% float; 5% trees; 15% soil	mi054f1, mi054f2, mi054f3, mi054s1, mi054w1, mi054w2, mi054w3	MI054F1; MI054F2	Quartz, cristobalite-h.temp/tridymite, muscovite, kaolinite, anatase; Quartz, kaolinite/halloysite, muscovite, hematite
MI055	443004	7649690	granite, medium grained (2-3 mm). Buff light pink green. Quartz, feldspar, mica(?) <5% mafic minerals.	50% float (granite, quartz); 25% grass; 10% soil; 10% trees; 5% spinifex	mi055f1, mi055s1, mi055w1	MI055F1	Quartz, sanidine/albite, muscovite/illite
MI056	443654	7648990	meta-siltstone/shale, dark grey (graphitic); hackly cleavage S0/S1 63/095;	60% float; 5% outcrop; 10% spinifex; 20% grass; 10% green bushes; 5% soil	mi056f1, mi056w1	MI056F1	Quartz, albite/sanidine, ferropargasite, muscovite/illite
MI057	443902	7648936	dolerite sill/dyke. Massive, dark grey	20% outcrop; 30% float; 20% rock/soil; 5% spinifex; 10% grass; 15% tress/green bushes.	mi057f1, mi057s1, mi057w1	MI057F1	Ferropargasite/ferrorichterrite, marialite, albite, clinochlore, muscovite

MI058	447137	7601497	pelite/psammite, light grey-green and dark green, multiple foliations defined by hematite, chlorite, mica, biotite(?) S0 18/090, S1 55/280, S2 72/145, S3 90/195	40% outcrop; 40% float; 20% grass	mi058f1, mi058f2, mi058s1, mi058w1, mi058w2	MI058F1; MI058F2	Quartz, muscovite/illite, hematite; Muscovite/illite, quartz, hematite, clinochlore, montmorillonite
MI059	446826	7601310	pelite, silver in colour, very micaceous, S0 38/080, S1 parallel to S0? Kink folds,	100% outcrop/float	mi059f1, mi059f2, mi059w1, mi059w2	MI059F1; MI059F2; MI059F3	Muscovite/illite, quartz, anorthite, kaolinite, hematite; Quartz, clinochlore, hematite; Quartz, muscovite/illite, clinochlore, anorthite
MI060	446479	7601377	massive specular hematite, dark grey-black. Some Mn oxides, quartz veins.	50% outcrop; 40% float; 10% grass	mi060f1, mi060f2, mi060s1, mi060w1, mi060w2	MI060F2	Hematite, quartz, muscovite/illite, anorthite, montmorillonite, kaolinite
MI061	445739	7609432	massive epidote altered rock, poor outcrop, grey fine siltstone, dark green amphibole, pink albite.	20% outcrop; 30% float; 30% grass; 20% soil	mi061f1, mi061f2, mi061w1, mi061w2		
MI062	470383	7630788	Cambrian/Jurassic sediments at top of mesa. Subhorizontal bedded kaolinite-rich sediments and cherts.	50% float; 40% trees; <10% grass; <10% outcrop	mi062f1, mi062f2, mi062s1, mi062w1, mi062w2	MI062F2	Quartz, kaolinite
MI063	470357	7630796	chert layers in Cambrian/Jurassic sediments on side of mesa. 1 m thick, laminated ~10cm chert and kaolin layers, some coarser sands + load casts		mi063f1, mi063f2, mi063w1, mi063w2	MI063F2	Quartz, kaolinite, montmorillonite, anatase, muscovite/illite
MI064	473917	7632868	coarse grained felsic dyke within granite comprising pink albite and quartz.	20% float; 40% soil; 35% grass; 5% trees	mi064f1, mi064f2, mi064s1, mi064w1, mi064w2	MI064F1	Quartz, microcline, barite, calcite, hematite, illite/muscovite, halite
MI065	476668	7631832	Granite, light grey , white and pink, medium grained,	<10% outcrop; 20% float; 30% soil; 20%	mi065f1, mi065s1, mi065w1	MI065F1	Quartz, albite, hematite

			quartz, feldspar and few mafic minerals. A few feldspar laths 2-5 mm. Some pink albite, quartz and epidote veining.	spinifex; 20% green bushes; <5% trees			
MI066	477978	7631351	foliated sediment (fine sandstone) "within a mapped major fault. Abundant mica developed. Tourmaline and pegmatite veins of muscovite, quartz and pink feldspar. S0/S1 90/255 to 90/220, i.e. rotation of foliation around subvertical axis. Massive epidote.		mi066f1, mi066f2, mi066f3, mi066w1, mi066w2, mi066w3, mi066w4	MI066F1; MI066F2; MI066F3	Quartz, albite, kaolinite-montmorillonite; Albite, quartz, muscovite/illite; Quartz, anorthite, muscovite/illite, dolomite
MI067	478645	7631275	epidote altered metasediments, dark grey, medium grained. Some calcrete.	50% green vegetation; 30% spinifex; 20% outcrop/float	mi067f1, mi067f2, mi067f3, mi067f4, mi067s1, mi067w1, mi067w2, mi067w3, mi067w4	MI067F1; MI067F3; MI067F4	Calcite, dolomite, quartz; Anorthite/albite, amphibole/magnesiohornblende, chlorite, illite; Epidote, hornblende/ferroactinolite, quartz, muscovite/illite, clinochlore
MI068	478919	7631177	conglomerate, clasts up 20cm rounded green amphibole and 2 feldspars. Also hematite and magnetite. Deeply weathered. Massive.	80% grass; 20% float	mi068f1, mi068w1	MI068F1	Albite, hornblende/riebeckite/ferropargasite
MI069	482624	7630239	granite, light buff, muscovite-rich, few mafic minerals. Black tourmaline, pegmatite with quartz and feldspar.	50% quartz gibber; 25% outcrop; 15% spinifex; 10% soil	mi069f1, mi069s1, mi069w1	MI069F1	Quartz, sandine/albite, barite, illite/muscovite, kaolinite
MI070	483153	7630750	mica schist in granite s1 85/220 5 mm spaced cleavage	20% outcrop; 20% quartz; 20% float; 30% soil; 10% Spinifex	mi070f1, mi070s1, mi070w1	MI070F1	Quartz, albite, muscovite/illite, biotite, clinochlore, hematite, sauconite
MI071	299869	7804285	siliceous sediments, buff and white	45% trees (hakea); 30%	mi071f1, mi071f2, mi071s1, mi071w1,	MI071F1a; MI071F1b	Quartz, kaolinite/halloysite, muscovite/illite; Quartz, dickite,

			coloured, cherts and kaolinised siliceous siltstones and fine sandstone. 1-2 cm foliation. Stromatolites? Cambrian?	leaf litter; 20% float; 5% soil;	mi071w2		muscovite/illite
MI072	298770	7805567	limestone, ferruginous, massive, flat-lying.	65% grass; 20% trees; 5% gums; 5% outcrop; 5% soil	mi072f1, mi072f2, mi072s1, mi072w1, mi072w2	MI072F1	Dolomite, quartz, muscovite, kaolinite
MI073	298278	7806235	laminated buff-yellow-dark grey, mudstone with abundant trilobites (Cambrian)	60% soil; 30% float; 5% grass; 5% trees	mi073f1, mi073f2, mi073s1, mi073w1, mi073w2	MI073F2	Quartz, montmorillonite, chlorite/clinochlore, muscovite/illite
MI074	296111	7810637	foliated mudstone, yellow-white, Fe oxide banding parallel to bedding as well as X-cutting. So/S1 difficult to separate. S0 84/117, S1 90/353. Though S0 may be subhorizontal?		mi074f1, mi074f2, mi074s1, mi074w1, mi074w2	MI074F2	Quartz, illite/muscovite, sanidine, clinochlore, kaolinite
MI075	292518	7816577	grey micaceous schist S1 83/270 <1mm penetrative cleavage, extensive quartz veining; large 20cm quartz cobbles (dropstones?)		mi075f1, mi075f2, mi075w1	MI075F1; MI075F3	Quartz, illite/muscovite, clinochlore, rutlie; Quartz, dolomite
MI076	243650	7933858	indurated, siliceous siltstone, ridge-forming, riddled with quartz veins 1-10 mm wide. No apparent bedding	20% outcrop; 40% float; 30% spinifex; 10% green bushes	mi076f1, mi076s1, mi076w1	MI076F1	Quartz, muscovite/illite, chlorite, sanidine
MI077	243599	7933859	foliated, grey-red siltstone, S1/S0 57/235, 1-3 mm spaced slaty cleavage, in road cutting		mi077f1, mi077w1		
MI078	243548	7933832	brecciated quartz veins in siltstone, vein 32/310, S1 73/235		mi078f1, mi078f2, mi078s1, mi078w1, mi078w2	MI078F1	Quartz, illite/muscovite, kaolinite, montmorillonite, hematite

MI079	246625	7914796	light grey siltstone with Pb Zn mineralisation. S1/So 79/190, Fault 40/040. Thin black graphitic shale.	mi079f1, mi079f2, mi079f3, mi079w1, mi079w2, mi079w3, mi079w4	MI079F3; MI079F4	Quartz, muscovite/illite, sanidine, clinochlore, montmorillonite; Illite/muscovite, quartz, clinochlore, siderite
MI081	445780	7609400	Mal's reward gossan near MI061	mi081f1, mi081f2, mi081f3, mi081w1, mi081w2	MI081F1	Quartz, clinochlore, muscovite, hematite
MI082	445053	7598840	Starra Mine Dump - various rock samples	mi082f1, mi082f2, mi082f3, mi082f4, mi082f5, mi082f6, mi082f7, mi082w1, mi082w2, mi082w3, mi082w4, mi082w5	MI082F1; MI082F2; MI082F3; MI082F5; MI082F6; MI082F7	Clinochlore, quartz, muscovite, hematite; Albite, quartz, clinochlore, barite; Quartz, illite/muscovite, dolomite, clinochlore/chlorite; Quartz, illite/muscovite, hematite, anhydrite, kaolinite; Quartz, hematite, muscovite, magnetite, anorthite; Hematite, quartz, chalcopyrite, clinochlore, barite
MI083	445053	7598840	Starra Open Pit Mine cutting to western side haul road entry.	mi083f1, mi083w1	MI083F1	Quartz, illite/muscovite, kaolinite

Stage 2: Field data and laboratory analyses

Sample site [Mixxx; xxx= site locality]	WGS84 UTM Zone	easting (mE)*	northing (mN)*	Description and cover	ASD samples - {Nov '07 : mxxx_yz; where xxx=site locality; y=outcrop specimen "a,b,c...." or "s" for soil; z="f" for fresh/broken *or* ="w" for weathered. Note samples listed below with "X" are sawn/fresh samples and saved as "...tx_" ascii files} ; - {Apr '08 : qsxx_yz; where xx=site locality; y=outcrop specimen "1,2,3...." or "s" for soil; z="f" for fresh/broken or ="w" for weathered}	XRD samples [mixxxy; where xxx=site locality; y=rock sample specimen *or* y=s soil sample]	XRD rock/outcrop sample interpretation (majors to minors)
MI100	54	342246	7718500	Road cutting; steeply dipping slaty dolomitic siltstone, grey, pale olive; some yellow brown Fe layers. Cross cutting fractures contain very pale grey carbonate Native Bee Siltstone	m100X_a, m100_s, m100_af , m100_aw , m100_bf , m100_bw , m100_cf , m100_cw , m100_df , m100_dw , m101_af ,	m100a	quartz, muscovite/illite, dolomite, kaolinite, microcline/albite
M101	54	341880	7720815	Steep knoll pale grey shale, Fe stained at top, Some Mn and Fe on fractures. Breakaway Shale.	m101X_a, m101bX_a, m101_s, m101b_s, m101_aw , m101_bf , m101_bw , m101b_af , m101b_aw , m101b_bf , m101b_bw , m102_aw , m102_bf	m101a,m101ba	muscovite/illite, kaolinite, goethite, quartz; muscovite/illite, kaolinite, quartz
M102	54	341889	7727737	Moondarra Siltstone; minor outcrop of grey, light grey and brown siltstone. Flat plain at base of ridges to W. Spinifex, wattle, Hakea, Eucalypts, Mitchell grass.	m102_s , m102X_b, m102_bf , m102_bw	m102b	muscovite/illite, kaolinite, quartz, albite

M103	54	340350	7728684	Low outcrop of folded finely laminated blue grey siliceous? Tuff cherty siltstone. Urquhart Shale Mn intense in float boulders to E. Some pale cream siltstone too.	m103_af , m103_aw , m103_bf , m103_bw, m103X_b , m103X_b, m103_s	m103b	muscovite/illite, kaolinite, quartz, albite/microcline, calcite(?)
M104	54	339352	7729528	Gravelly soils, Fe stained quartz, No basalt. Only pale brown dolomite with calcite veins. Cromwell Metabasalt; Wattle, Eucalypts, Spinifex, Mitchell grass	m104_af , m104_aw , m104_bf , m104_bw, m104X_a , m104X_a , m104X_a, m104_s	m104a	calcite, muscovite/illite, kaolinite, quartz, albite/microcline,
M105	54	338558	7729949	Roadside cutting; Rubbly slope of ridge of pale cream grey brown to Purple quartzite. Brown moist soil. Lena Quartzite	m105_af , m105_aw , m105_bf , m105_bw, m105X_b , m105X_b, m105_s	m105b	Kaolinite, muscovite/illite, quartz, dolomite(?)
M106	54	335597	7733283	Undulating narrow plain with low outcrop rises between sharp ridges. Fine olive green somewhat sparkly meta basalt. Pickwick Metabasalt Member.grey and greasy on N side of road. Also some pale cream meta sandstone with crystals.	m106_af , m106_aw , m106_bf , m106_bw, m106X_a , m106X_a, m106_s	m106a	Chlorite, illite/muscovite
M107	54	335673	7733332	Steeply dipping grey schist; Some surface Fe staining. Lena Quartzite ridges to north.	m107_af , m107_aw , m107_bf , m107_bw, m107X_a , m107X_a	m107a	Illite/muscovite, kaolinite, quartz

M108	54	334282	7737361	Flank of Leander Quartzite to N. Comprises Cromwell meta basalt Weathered chlorite meta basalt. Mitchell grass Spinifex, Low E, Orange brown Fe stain on surface lithic gravel.	m108_af , m108_aw , m108_bf , m108_bw, m108X_b, m108_s	m108b	Chlorite, quartz, illite/muscovite, microcline(?)
M109	54	331596	7741237	In place to Colluvial regolith on Cromwell Metebasalt,Includes fragments of yellow brown schist, grey shale flakes, Mn and Fe stained angular pebbles. E and Spinifex on gentle slope to NE.Extensive Spinifex cover	m109_af , m109_aw , m109_bf , m109_bw, m109X_a, m109_s	m109a	kaolinite, Illite/muscovite, goethite
M110	54	324700	7751825	Colluvial Megalith comprises orange brown clayey soils, pebble, some cobble gravel. Milky quartz, Si Fe stone? Meta basalt, quartzite clasts. Gidgee forest with scattered Spinifex; bare areas,	m110_af , m110_aw , m110_bf , m110_bw, m110X_b, m110_s	m110a,m110b	Quartz, illite/muscovite, albite, kaolinite, chlorite, goethite; Quartz, albite/microcline, illite/muscovite, kaolinite, goethite
M111	54	337785	7688420	Rounded boulder outcrops form knoll. Abundant Spinifex; scattered E.Coarse feldspar (pink) biotite granite. Forms coarse colluviel gravels and Sand. Undulating boulder strewn terra in with scattered knolls, ridges.	m111_af , m111_aw , m111_bf , m111_bw, m111X_a, m111_s	m111a	Quartz, albite/microcline, illite/muscovite, kaolinite

M112	54	384240	7619063	Some silcrete Fe stained cobbles. Also Fe stone gravel. Mottled regedit on slope and weathered Sandstone in minor channel. Some disturbed clasts on top contain copper green clay.alluvial fan of Fe stone, milky quartz	m112_af , m112_aw , m112_bf , m112_bw , m112b_af , m112b_aw , m112b_bf , m112b_bw, m112X_b, m112_s , m112b_s	m112b,m112ba	quartz, albite, illie/muscovite, clinochlore, goethite, kaolinite; quartz, albite, illie/muscovite, clinochlore, goethite, kaolinite;
M113	54	385654	7617594	Poorly developed breakaway faces SE; scattered pavements opalise silica. Orange brown clayey soils, somewhat smectitil. W extension of silica found previously. Silica, milky quartz, Some Fe stone on surface.	m113_af , m113_aw , m113_bf , m113_bw, m113X_b, m113_s	m113b	opalline silica, illite/muscovite, kaolinite, goethite
M114	54	385950	7617286	Smectitic orange brown soils with quartz, silica, Fe stone, some jasper pebble, cobble gravels.Alluvial environment gentle slope, shallow channels , surface wash.	m114_aw , m114_bw, m114X_b, m114_s	m114b;mi114s	opalline silica, illite/muscovite, kaolinite, goethite
M115	54	386111	7617122	Light orange brown clayey soils. Surficial gravels include quartz, Fe stone. Abundant milky quartz gravel nearby. Gidgee, Spinifex. Probably influenced by high overbank flows, Undulations suggest shallow bedrock.	m115_aw , m115_bw, m115X_a, m115_s	m115a, mi115s	quartz, kaolinite, hemetite

M116	54	386735	7616290	Orange brown clayey soils on flat surface with thin surface quartz sand rare pebbles. Alluvial plain. Open gidgee; Some Spinifex.	m116_s	mi116s	
M117	54	385242	7614382	Abundant translucent and milkyquartz pebble angular gravel; some cobbles. Light orange brown soil. Slightly higher area with minor incision. Patches of milky quartz near outcrop. Minor mafic float. Infer shallow bedrock. Mice anomally must be in soil.	m117_aw, m117X_b, m117_s	m117b	quartz, kaolinite, illite/muscovite
M118	54	385689	7614375	Colluvial apron to slight rise to west. Angular milky quartz pebble gravel thinly covers brown Smectitic clay. Scattered gidgee; bare areas ; some Spinifex to west. Occasional mafic angular fragment to Cobble size.	m118_af , m118_aw, m118X_a, m118_s	m118a	ferropargasite, riebeckite, quartz, ilite/muscovite, kaolinite, hematite
M119	54	386170	7614155	Flat terrain, scattered Gidgee. Very slightly gilgai. Patches brown cracking days , milky quartz pebble to cobble gravel.Scattered hard blah mineral gravels suggest colonial rather than alluvial, despite flat terrain.	m119_aw , m119_aw , m119b_af , m119b_aw , m119b_bf , m119b_bw, m119X_a , m119bX_a, m119_s , m119b_s	m119a,m119ba	quartz, albite, hematite, illite/muscovite; dolomite, quartz, illite/muscovite, hematite

M120	54	385757	7613789	Low Amphibolite outcrop. Gentle E sloping terrain. Few trees. scattered Spinifex.Thin soil on bedrock to colluviums. Epidofe on fracture planes	m120_af , m120_aw , m120_aw , m120_bf , m120_bw, m120X_b, m120_s	m120b; mi120s	ferroactinolite, albite, microcline, quartz, calcite
M121	54	388267	7617652	Outcrop of massive slightly cavernous silica, white bleached surface; honey brown in places. Sheds angular silica gravel; orange brown clayey soils, patches grey crashing clays.Inverted drainage.	m121_af , m121_aw , m121_bf , m121_bw, m121X_a , m121X_b, m121_s	m121a,m121b; mi121s	quartz, opal, goethite, hematite
M122	54	388817	7617487	Grey slightly cracking clags with angular pebble and occasional white silica gravel scatter on surface. Grazed grass; possible local drainage channel partial in fill. Could be relictTop of silica undulating. This site in slight depression	m122_aw , m122_bf , m122_bw, m122X_b, m122_s	m122b; mi122s	quartz, opal, kaolinite
M123	54	389190	7617440	White opaline silica low rise; releases angular shard gravel. Distributed laterally onto alluvial fans. Minor incision in orange brown Colluvicl deposits; grey days in shallow channels could be "substrate	m123_af , m123_aw , m123_bf , m123_bw, m123X_a, m123_s	m123a; mi123s	quartz, opal

M124	54	388079	7617839	Grey to grey brown ercching clays, no vegetation. Ponded sleet wash deposits. Concentration of opalise Silica Cobbles 80 m WNW	m124_s	mi124s	
M125	54	388052	7618181	Less than I m soils on porous Silicified rock with pale beige brown rough texture. Appears to grade uphill into massive amorphous silica. Periphery of silica deposition. W sloping Colluvial apron to silica; minor channels Erosioual margin to higher area to SW	m125_af , m125_aw , m125_bf , m125_bw , m125_cf , m125_cw, m125X_a , m125X_b	m125a,m125b	quartz, opal, illite/muscovite; opal, quartz, illite/muscovite.
M126	54	388647	7618560	Light orange brown Soils with diverse surface gravel including quartz, Silica, muscovite rich lithics, Muscovite flakes. Sparse trees almost no grass, Some termites alluvial margin.	m126_af , m126_aw , m126_bw , m126_cf , m126_cw, m126X_a, m126_s, , m126b_s	m126a; mi126s, mi126bs	quartz, anorthite/albite, illite/muscovite, kaolinite, hematite
M127	54	388610	7618511	Poor outcrops metasediments strike 340. Fine grained; contains muscovite on fractures. Massive silica at top of ridge; grades down slope into more porous forms. Quartz vein, with muscovite further down slope.	m127_af , m127_aw , m127_bf , m127_bw, m127X_a, m127_s	m127a; mi127s	quartz, anorthite/albite, illite/muscovite, kaolinite, hematite

M128	54	388517	7618867	Near outcrop of pink fine metasediment as per earlier site. Also quartz vein, some scattered white Silica.Low bedrock controlled rise near alluvia tract. Mice in sand in channel bed.	m128_af , m128_af , m128_aw , m128_bf , m128_bw, m128X_b, m128_s	m128b; mi128s	quartz, anorthite/albite, illite/muscovite, kaolinite, hematite
M129	54	387159	7620612	Gravely rise of Corella Formation.pink to purple pink metavolcanic; dark green mineral, lots of quartz veining. Some amphibole float.Narrow bedrock Controlled low ridge; Spinifex, scattered E, termites. Generally poor outcrop. Some close boulders	m129_aw , m129_bf , m129_bw , m129_cf , m129_cw, m129X_a, m129_s	m129a; mi129s	quartz, anorthite/albite, kaolinite, hematite
M130	54	388876	7619910	Brown to orange brown soils with Surficial pebble gravel quartz, meta lithics, Fe stained, feldspar, dark brown polished Fe stone. Mapped as Corella Formation. Colluvial alluvial wash; Some bare cress, Spinifex I termites, scattered E Patches of milky quartz pebbles and hematite pebbles to Cobbles	m130_s	mi130s	

M131	54	389149	7620166	Quartz, with crystal cavities, and Corella meta fragments as cobble gravel. Top of rise mainly veg free, with pebble gravel, To north on slope is cobble gravel,Patches of cracking clays 5- 10m + between gravels and orange brown sands clays On slope to north.	m131_af , m131_aw , m131_bf , m131_bw, m131X_a, m131_s	m131a; mi131s	quartz, anorthite/albite, illite/muscovite, kaolinite, hematite
M132	54	394471	7609641	Heavily vegetated with Spinifex, wattle , some E. Surface pebble and cobble gravel includes weathered sandstone, quartzite, pale pink grey, Some rounded milky quartz, silica, silicified siltstone. Falls cuss north. Vegetation affects image pattern. Lithic gravel range indicates alluvium Also some silicified clasts.	m132_af , m132_aw , m132_bf , m132_bw, m132X_b, m132_s	m132b; mi132s	quartz, kaolinite, hematite
M133	54	394448	7616748	Plain, high in landscape; falls away, particularly south. Brown cracking clays, friable. Scattered Surficial gravel includes rounded quartz. Lithic, include quartzite, some Fe stained; opalise silica. Relict overbank deposit stranded in landscape. Overlies alluvial gravel; fragments work to surface through urchins clays.	m133_aw , m133_bw, m133X_a, m133_s	m133a; mi133s	quartz, kaolinite, illite/muscovite

M134	54	393074	7620915	Bulbous outcrop of grey Terrazo silcrete. Contains angular fine clasts in fine silica cement. Locally ferruginous to west. Weathering releases clasts as angular gravel. Two stages represented. Now high on landscape. Bedrock control. Somewhat Crenulated erosional margin to west.	m134_af , m134_aw , m134_bf , m134_bw , m134_cw , m134c_af , m134c_aw , m134c_bw , m134c_cf , m134c_cw , m134c_df , m134c_dw, m134X_a , m134cX_a, m134cX_b, m134_s , m134b_s	m134a,m134ca,m134cb; mi134s	quartz, illite/muscovite, anatase; quartz, opal, anatase; quartz, illite/muscovite, anatase, hematite
M135	54	335711	7599896	Ridges and remnants of quartzite, pale grey and Fe stained. Rice schist exposed on flank, with large quarter veins, shedding milky quartz onto colluvial apron, Orange brown very fine Sandy soils. Colluuicl wash merges with orange brown Sandy soils on local alluvial plainSome hematised Sand and gravel in small cobbles.	m135_af , m135_aw , m135_bf , m135_bw , m135_cf , m135_cw, m135X_a, m135_s	m135a	Chlorite, quartz,
M136	54	356862	7611002	Large quartz veins sled milky quartz gravels in patches. Sparsely vegetated; some E, Spinifex, grazed Mitchell grass	m136_af , m136_aw , m136_bw , m136_cw, m136X_a , m136X_b, m136_s	m136a,m136b	quartz, muscovite/illite, albite/orthoclase; quartz
M137	54	357848	7612473	Low Ridge of pale grey green fractured , Surface Fe stained silt to mudstone. Moderate to high cover of Spinifex, wattle, scattered E, especially off crest	m137_aw , m137_bw, m137X_a, m137_s	m137a	muscovite, quartz

M138	54	362713	7619683	Light orange brown clayey alluvial soils, no gravel on alluvial plain surrounding granite boulders. Throughput of alluvium more significant than granite shedding.	m138_af , m138_aw , m138_bf , m138_bw, m138X_a, m138_s	m138a	quartz, albite, muscovite/illite, biotite
M139	54	365131	7621898	Poor boulders outcrop of mafia intrusive with resorted crystals. Sheds angular lithic gravel on slope. Could be some mice in soil. Drainage channel to SW Spinifex, Mitchell grass, some E. Bare areas to NW	m139_af , m139_aw , m139_bf , m139_bw , m139_cf, m139X_b, m139_s	m139b	quartz, albite, muscovite/illite, chlorite
M140	54	447106	7677746	Bare areas with moderate Spinifex. Orange brown sandy clay 20 cm over gravely horizon of Mari mo Slate and other lithic. Thin Overbank cover on pertly sorted colluviums from lateral channels.	m140_s		
M141	54	446687	7677117	Outcrop and bouldery slope of grey fine meta sediments with some quartz veining. Spinifex and scattered E in duding ghost gums	m141_af , m141_aw , m141_bf , m141_bw, m141X_b, m141_s	m141b	quartz, albite/anorthite, muscovite/illite
M142	54	443751	7674100	Grey siltstone progressively more infused with beach hematite up slope. Earthy pink red and conglomeratic at top. Boulders colluviums produces steep slopes to alluvial plain nearby.	m142_af , m142_aw , m142_bf , m142_bw , m142_cf , m142_cw, m142X_a , m142X_c, m142_s	m142a,m142c	quartz, albite/sanidine, muscovite/illite, hematite; hematite, quartz, albite/sanidine

M143	54	440863	7673861	Orange brown stained metasediment with milky quartz clasts. Black blue manganese boulders on west Area of Mn outcrop 100m East. Surrounded by merged alluvial aprons of high bourns outcrops, Alluvial plain nearby to west.Spinifex, scattered ghost gums, other Coarse bark E.	m143_af , m143_aw , m143_bw , m143_cf , m143_cw , m144_aw, m143X_a , m143X_b, m143_s	m143a,m143b	quartz, hematite, illite/muscovite; vernadite/pyrolusite, quartz, hematite
M144	54	435072	7681579	Ridge of milky quartz flooded Clloritic mica schist. Boxworks in quartz contain hematite. Bedrock knolls and high ridges have steep colluvial aprons and more gently sloping toluide fans extending to alluvial plain.	m144_aw , m144_bf , m144_bw , m144_cw, m144X_c, m144_s	m144a,m144c	quartz, illite/muscovite, rutile
M145	54	432790	7684386	Brown maroon ridge with milky quartz breccia clasts, hooks quartzite in places. Glost gums, River Red, Spinifex, Scrubby wattle.Cobbles and boulders in creek bed.	m145_af , m145_aw , m145_bw , m145_cw , m145_cw, m145X_a, m145_s	m145a	quartz, illite/muscovite, albite, chlorite, hematite;
M146	54	431709	7684900	Fine pink quartzite, fractured, with thin surface weathering.Fine mica. Spinifex cover moderate to high. Scattered E. Numerous termites to 1 m	m146_af , m146_aw , m146_bf , m146_bw, m146X_b, m146_s	m146b	quartz, anorthite/anorthoclase, muscovite, hematite

M147	54	431454	7688191	Pale earthy pink quartzite, massive and very fine grained grey in places. Moderate Spinifex cover, scattered glost gums. Some wattle scrub. Low bedrock rise shedding angular lithic cobble to pebble gravel	m147_af , m147_aw , m147_bf , m147_bw, m147X_a, m147_s	m147a	quartz, anorthite/anorthoclase, hematite
M148	54	432609	7691212	Rubble alluvial slope and boulder outcrop Maroon to grey with weak surface Fe stain quartzite and breccias with angular and Sub round quartz.Quartz veining. Lower slopes Spinifex covered Some E. Extends onto flat alluvial alluvial plain with orange brown soils and gravels.	m148_af , m148_aw , m148_bf , m148_bw , m148_cw, m148X_a, m148_s	m148a	quartz, muscovite/illite
M149	54	438833	7705094	Poor outcrop of near vertical layered fine maroon grey metasediment with Mn impregnations. Spinifex and scattered ghost gums. Slopes onto alluvial plain to E where there are 2 bedrock knolls to NE.	m149_af , m149_aw , m149_bw , m149_cw, m149X_b, m149_s	m149b	quartz, muscovite, albite/anorthite, hematite
M150	54	438334	7706363	Grey to grey maroon quartzite to silicified conglomerate, Some massive milky quartz veins. Very localised boulders alluvial apron. Mitchell grass on plain, Spinifex on slope.	m150_af , m150_aw , m150_bw, m150X_a, m150_s	m150a	dolomite, quartz, albite/anorthite

M151	54	435959	7708993	Steeply dipping slate north offence ; quartz veining in tourmaline dolerite in low outcrop strike 120 Also some mice bearing metasediments. Low bedrock out Crops and alluvial gravel on mildly incised landscape on shallow bedrock Bare areas, patches Spinifex.	m151_af , m151_aw , m151_bw , m151_cw , m151b_af , m151b_aw , m151b_bf , m151b_bw, m151X_a , m151bX_a, m151_s , m151b_s	m151a,m151ba	quartz, dravite, rutile
M152	54	391340	7703641	Massive grey quartzite, very fine grained, and mica schist. Spinifex, scattered trees. Rugged ridge and gully country in bedrock, weakly weathered.	m152_aw , m152_bf , m152_bw , m152_cf , m152_cw , m152_df , m152_dw, m152X_b, m152_s	m152b	quartz, illite/muscovite, anorthite, hematite
M153	54	393415	7701091	Poor rubble outcrop of dark grey medium, sparkly dolerite, Some float with epi dote; also masses of ? Tourmaline. Also epidote. Gravel end soils amongst low wattle, Mitchell grass. Low rise with ridges nearby. Weak drainage incision.	m153_aw , m153_bf , m153_bw , m153_cf , m153_cw, m153X_b, m153_s	m153b	ferroactinolite, epidote, sanidine, chlorite, biotite(?)

M154	54	395521	7698720	Tabular boulder outcrop of speckled grey mica rich Wonga granite. Forms wearily channelled undulating valley floor between steep ridges east and west. Bare areas, scattered E; minor Spinifex. Coolabah Wattle in shallow drainage. Bare areas, scattered E; minor Spinifex. Coolabah Wattle in shallow drainage	m154_af , m154_aw , m154_bf, m154X_b, m154_s	m154b	quartz, illite/muscovite, anorthite/albite
M155	54	403534	7700276	Base of steep flank of Corella Formation. Outcrops of grey and pink quartzite, some epidote and quarte veins, Pink mineral could be feldspar Some Calcite float. Rubbly base of Colluvial slope. Spinifex, wattles, some E diminish upslope. No Sign of mica	m155_af , m155_aw , m155_bf , m155_bw , m155_cf , m155_cw, m155X_b, m155_s	m155b	ferropargasite, quartz, albite, chlorite
M156	54	447664	7603951	North south ridge of grey to dark grey towards carbonaceous shale; some milky quartz veining in east parallel to strike Malachite shows. Some very fine pinh grey quartzite. Narrow bedrock ridge with moderate the high Spinifex cover. Scattered E, alluvial lithic gravel.	m156_af , m156_aw , m156_bf , m156_bw , m156_cf , m156_cw , m156_df , m156_dw , m156_dw , m156_dw , m156_dw, m156X_a , m156X_b, m156_s	m156a,m156b	quartz, sanidine, muscovite, siderite(?)

M157	54	447910	7604627	Moderately steep ridge with low granite outcrop and Colluvicl gravels. Spinifex, low wattle. Scattered E.granite has pink feldspar, ? Epidotic , mica. Rugged bedrock controlled terrain Undulating valley floor between ridges to South	m157_af , m157_aw , m157_aw , m157_aw , m157_bf , m157_bw , m157_bw , m157_cf , m157_cw, m157X_a , m157X_c, m157_s	m157a,m157c	quartz, sanidine, illite/muscovite; quartz, sanidine/microcline
M158	54	447389	7604209	Very fine grained grey quartzite ridge strike about 320 Some Mn mineralisation, quartz veins.Also some interbedded chlorite schist. Narrow alluvial channel and alluvium in between ridges.	m158_af , m158_aw , m158_aw , m158_bf , m158_bw, m158X_b, m158_s	m158b	
M159	54	447015	7604355	Low Spinifex, wattle, scattered E on dissected bedrock slopes. Strong structural control on ridge gully orientation. Steeply dipping green grey schist.	m159_af , m159_aw , m159_bw , m159_cw, m159X_c, m159_s	m159c	
M160	54	442869	7600755	Contains pink feldspar and opiate green mineral. Fine. Produces Fe stained orange brown sand on light orange brown soils Biotite Abundant specula, hematite pebbles in surface gravel patches, dolerite. Locally flat terrain with bare areas & scattered patches quartz lithic cobble to pebbles. Spinifex, Hakea, Some E.	m160_af , m160_aw , m160_aw , m160_bf , m160_bw , m160b_af , m160b_aw , m160b_bf , m160b_bw , m160b_cf , m160b_cw , m160b_cwm160X_b , m160bX_a, m160bX_c, m160_s	m160b,m160ba,m160bc	

QS1	55	525016	7675472	Rise and creek bank exposures fine sst; some fractured mst	qs01_1f, qs01_1w, qs01_2f, qs01_2w, qs01_3f, qs01_3w, qs01_s	QS1_1	
QS2	55	524420	7678549	Dozer rip.	qs02_s	QS2_1,QS2_2	
QS3	55	524027	7680430	Low rise leading to knoll in east. Could have been basal Suttor	qs03_1f, qs03_1w, qs03_2w, qs03_3f, qs03_3w, qs03_4f, qs03_4w, qs03_5f, qs03_5w, qs03_6f, qs03_6w, qs03_7f, qs03_7w, qs03_s	QS3_5	
QS4	55	522842	7684983	granite exposed in bank of sandy river bed.	qs04_1f, qs04_1w, qs04_s	QS4_1	
QS5	55	522021	7688775	Top of steep rise. Poor rubble outcrop amongst grass. Ukalunda Beds	qs05_1f, qs05_1w, qs05_2f, qs05_2w, qs05_s	QS5_2	
QS6	55	522243	7689698	Erosion gullies expose mst below 1-2 m gravely Soils. Fe stained surface lithic gravel.	qs06_1f, qs06_1w, qs06_2f, qs06_2w, qs06_s	QS6_2	
QS7	55	527403	7690536	Interbedded Volcanic, and mst. steeply dipping. Some magnesite and epidotic veins; qtz Fe stone flat.	qs07_1f, qs07_1w, qs07_2f, qs07_2w, qs07_3f, qs07_3w, qs07_s	QS7_3	
QS8	55	518512	7690524	Near base of slope above creek.	qs08_1f, qs08_1w, qs08_s	QS8_1	
QS9	55	515224	7687237	Crest of low rise. knells and rises of boulder outcrops.	qs09_1f, qs09_1w, qs09_s	QS9_1	
QS10	55	447008	7727727	Star of Hope Fm. Dome and breakaway landform; variable Fe-isation	qs10_1f, qs10_1w, qs10_s	QS10_1	
QS11	55	451612	7730223	Raymond Formation. Roadside dozer rip.	qs11_1f, qs11_1w, qs11_2f, qs11_2w, qs11_3f, qs11_3w, qs11_s	QS11_1,QS11_2	
QS12	55	271178	7835936	Foliation 80 deg 140 Mag. Veg 60% grass 10% trees 20% litter. 10% soil.	qs12_1f, qs12_1w, qs12_s	QS12_1	

QS13	55	271060	7837224	Local area of clay rich Soils.Scattered Fe bark, low scrub, bare patches.	qs13_1f, qs13_1w, qs13_s	QS13_1	
QS14	55	271129	7837661	"High" plain 90% grass 5% trees; 5% soil Maps as low clay.	qs14_1f, qs14_1w, qs14_s	QS14_1	
QS15	55	269620	7841996	Flat plain, 80% grass 20% trees; numerous basalt cobbles. 20% Soil exposure.	qs15_1f, qs15_1w, qs15_s	QS15_1	
QS16	55	269715	7844270	St narrow ridge 330 deg strike W dip. 30% tree cover, 3096 grass, shrubs 40% soil, rock.	qs16_1f, qs16_1w, qs16_2f, qs16_2w, qs16_3f, qs16_3w, qs16_s	QS16_2	
QS17	55	269554	7845006	bedrock outcrop. 40% trees 10% grass ; 50% soil, rock.	qs17_1f, qs17_1w, qs17_2f, qs17_2w, qs17_3f, qs17_3w, qs17_s	QS17_1	
QS18	55	269634	7845036	Crest of basalt cobble ridge. 30% trees 20% grass 50% cobbles	qs18_1f, qs18_1w, qs18_s	QS18_1	
QS19	55	269634	7844919	Low spur ridge of exposed mudstone debris. 15% trees, no grass.	qs19_1w, qs19_1w, qs19_1w, qs19_s	QS19_1	
QS20	55	269905	7850151	30% tree cover 20% grass, 50% rock. soil.	qs20_1f, qs20_1w, qs20_2f, qs20_2w, qs20_3f, qs20_3w, qs20_s	QS20_3	
QS21	55	269925	7850083	Grey limestone ridge 15m high.	qs21_1f, qs21_1w	QS21_1	
QS22	55	270090	7850039	Towards baseof gully slope. Milky qtz gravel. 20% trees 30% grass 50? soil.	qs22_1f, qs22_1w, qs22_s	QS22_1	
QS23	55	264225	7852515	Crest of narrow high ridge strike 200 todo trees, 30% grass, 30% rock, soil.	qs23_1f, qs23_1w, qs23_2f, qs23_2w, qs23_3f, qs23_3w, qs23_s	QS23_2	

QS24	55	264229	7852414	South Side of steep sst ridge. 30% trees, 30% grass, 30% soil and rock. 3811; clay rich Hymap.	qs24_1f, qs24_1w, qs24_s	QS24_1	
QS25	55	264256	7852250	Base of steep rise. Falls away S. Fractured mst nearby. 20% trees 4o% grass 40% Soil, rock.	qs25_1f, qs25_1w, qs25_2f, qs25_2w, qs25_s	QS25_1	
QS26	55	264239	7852154	Ridge between narrow sullies. 20% trees 50% grass 30% soil, rocks	qs26_1f, qs26_1w, qs26_2f, qs26_2w, qs26_s	QS26_1	
QS27	55	264487	7851701	Big Rush mine pit. Narrow along strike mine exposes dark grey shales and pale country ms	qs27_1f, qs27_1w, qs27_2f, qs27_2w, qs27_3f, qs27_3w, qs27_4f, qs27_5f, qs27_5f, qs27_5f, qs27_6f, qs27_6w,	QS27_3, QS27_5	
QS28	55	246911	7920913	Roadside high clay. 20% soil, 80% trees shrubs grass.	qs28_s		
QS29	55	246957	7921359	gravel sand and clay layers in low face. Roadside 40% tree and shrub 30% grass 30% soil	qs29_s		
QS30	55	248467	7924329	E side of road. High clay area. 80% grass.	qs30_s		
QS31	55	248383	7924368	20% trees 20% grass. w side of road.	qs31_s		
QS32	55	248430	7924379	s end at cutting.	qs32_1f, qs32_1w, qs32_2w,	QS32_1	
QS33	55	251964	7928683	Cleared area with 800% grass. Flat terrain. Shallow stream incision to W.	qs33_s		
QS34	55	251792	7928695	Scrape area; Fe pisoliths from near surface mottled zone.	qs34_s		

QS35	55	251817	7928756	Thin cover of mottled pisolite zone on conglomerate in creek. (Tertiary). granodiorite weathered below.	qs35_s		
QS36	55	254670	7930905	accrete nodules and horizon in shallow gully	qs36_1f, qs36_1w, qs36_s	QS36_1	
QS37	55	254748	7930947	Local area of Smectitic soil above creek.grass 10-60%	qs37_s		
QS38	55	251823	7927582	Large scrape exposure pisolitic gravel slopes E. Erosions margin.	qs38a_s, qs38b_s		
QS39	55	251771	7927689	Top of land surface. Expect pisolitls at shallow depth.	qs39_s		
QS40	55	200981	7915289	Side of shallow drainage depression. Patches of exposed soil with qtz pisolith gravel. % trees 30% grass, shrubs.	qs40a_s, qs40b_s		
QS41	55	200935	7915104	30% trees 502 grass. Algal mats on surface. Moderate to high clay with unmix.	qs41a_s, qs41b_s		
QS42	55	200779	7914693	40% soil, 15% trees 45% grass. Dark grey omelette clay nearby; algal mat.	qs42_s		
QS43	55	200606	7912371	Kidston 30% trees 40% grass. Roof pendants in granite. Mica on Surface to W	qs43_1f, qs43_1w, qs43_2f, qs43_2w, qs43_3f, qs43_3w, qs43_4f, qs43_4w, qs43a_s, qs43b_s	QS43_1,QS43_2	
QS44	55	201723	7911155	5 50% Trees, 80% grass. gentle slope E	qs44_s		
QS45	55	201768	7911115	Gentle to flat grass covered slope	qs45_s		

QS46	55	198650	7911437	Kidston west. Sully exposes Weathered mica granite. Rise to N is boulder block porphyry outcrop. Mice fsp qtz send in gully.	qs46_1f, qs46_1w, qs46_2f, qs46_3f, qs46_3w, qs46a_s, qs46b_s	QS46_3	
QS47	54	761868	7918725	Crest of gentle rise. 20% trees, 70% grass High mica on road. ? Image conflict	qs47_1f, qs47_2f, qs47_2w, qs47_s	QS47_1,QS47_2	
QS48	54	761870	7916585	Weakly gullied; inter gully rise.	qs48_1f, qs48_1w, qs48_s	QS48_1	
QS49	54	761979	7916561	Rise next to gully. Moderate clay; very fine mica in schist	qs49_1f, qs49_1w, qs49_2f, qs49_2w,	QS49_1	
QS50	54	762208	7916623	Max mica abundance from schist outcrop along steep ridge. High clay response from schist.	qs50_1f, qs50_1w, qs50_s	QS50_1	
QS51	54	762479	7916136	Micro interfluves Angular quartz lithic gravel pavement with clayey orange brown soil. Some termites.Low clay (mica) unmixed.	qs51a_s, qs51b_s		
QS52	54	762730	7915688	Ridge and gully terrain. E-w qtz vein 80ám S. Mostly veg free patch. Low clay	qs52_1f, qs52_1w, qs52_s	QS52_1	
QS53	54	747921	7987393	Scrape on rise crest. Semi consol angular qtz mica granular sample overlies lithified equivalent. Ped structures on lower.	qs53_s	QS53_2	
QS54	54	764242	7970671	gentle margin of rise with shallow gullies.High clay indicated.	qs54_1f, qs54_1w, qs54_2f, qs54_2w, qs54_s	QS54_2	

QS55	54	636351	7999142	Crest of low narrow N-S ridge. Some Hakea.Pink = oxidised	qs55_1f, qs55_1w, qs55_2f, qs55_2w, qs55_s	QS55_2	
QS56	54	636322	7999062	gentle depression west of porphyry ridge.Could be graphite in porphyry,	qs56_1f, qs56_1w, qs56_1w, qs56_s	QS56_1	
QS57	54	636170	7999248	Side of broad ridge to W. Ns porphyry outcrops, 35% wattle; short grass.	qs57_1f, qs57_1w, qs57_2f, qs57_2w, qs57_s	QS57_1	
QS58	54	636290	7999141	gully by road.	qs58_1f, qs58_1w, qs58_2f, qs58_2w, qs58_3f, qs58_3w,	QS58_3	
QS59	54	632332	7995569	Flat to gently undulating bedrock terrain. Gt and Ht Fe stone gravel. Scrape edge.	qs59_1f, qs59_1w, qs59_2f, qs59_2w, qs59_s	QS59_1	
QS60	54	632363	7995709	Scrape. graphite in cavities. Querth evident on outside.	qs60_1f, qs60_1w, qs60_2f, qs60_2w,	QS60_1	
QS61	54	648683	7983790	Edge of high clay; may correlate with old mine locs. Edge of low rise to E.	qs61_1f, qs61_1w, qs61_2f, qs61_3f, qs61_3w, qs61_4f, qs61_4w, qs61_5f, qs61_5w, qs61_s	QS61_1,QS61_2	
QS62	55	224665	8105144	Red Dome, west of Chillago	qs62_1f, qs62_1w, qs62_2f, qs62_2w, qs62_4f, qs62_4w, qs62_5f, qs62_5w, qs62_6f, qs62_6w, qs62_7f, qs62_7w, qs62b_1f, qs62b_1w, qs62c_1f, qs62c_1w, qs63_s	QS62_6,QS62B_1	
QS63	55	229404	8094667	W side of rise to low hill. 20%trees,zoJogress. granite on roadside and low outcrop,	qs63_1f, qs63_1w, qs63_s	QS63_1	
QS64	55	230011	8095576	Near crest of broad low hill. 10% trees 80% grass.	qs64_1f, qs64_1w, qs64_s	QS64_1	
QS65	55	233364	8097660	Side of steep gully; intersection of Palmerville and offset far lt.	qs65_1f, qs65_1w, qs65_s	QS65_1	

QS66	55	233250	8097762	Spur of hill to NE. 20% trees 75% grass, litter. No mica. Compare fine mica in mst to S.	qs66_1f, qs66_1w, qs66_2f, qs66_2w, qs66_3f, qs66_3w, qs66_s	QS66_1	
QS67	55	233331	8097780	South Side et road 10% trees 70% grass	qs67_1f, qs67_1w, qs67_s	QS67_1	
QS68	55	241837	8093022	Abandoned quarry s of Chillagoe	qs68_1f, qs68_1w	QS68_1	

APPENDIX 7

HyMap Mineral Mapping Products – Stage 1 (3 August 2007)

Product name where * is block coverage	**Minerals/ materials detected**	**base algorithm**	**filters**	**stretch lower limit**	**stretch upper limit**	**stretch type**	**colour chart**	**accuracy**
HyMap * natural colour		Reflectance bands: R: 650nm G:550nm B:450nm Multiplicative cross track-corrected, 2nd order polynomial	none	R:700DN G:562DN B:248DN	R:2070DN G:1378DN B:750DN	linear	Black-white (each band)	Moderate. Some between block mis-calibration caused by assumptions used in the cross track correction
HyMap * false colour		Reflectance bands: Red: 750nm Green:650nm Blue:550nm Multiplicative cross track-corrected, 2nd order polynomial	none	R: 860 DN G: 117 DN B: 304 DN	R: 3120DN G: 2548DN B: 1480DN	linear	Black-white (each band)	Moderate. Some between block mis-calibration caused by assumptions used in the cross track correction
HyMap * green vegetation abundance	Green “photosynthesising’ vegetation	NDVI (Merton) $(R_{860}-R_{687})/ (R_{860}+R_{687})$	none	0.15 White :low abundance *Black is below the threshold*	0.5 Green : high abundance	Linear	Green-white	High
HyMap * dry vegetation abundance	Cellulose in dry vegetation	Normalised depth of 2080 nm absorption calculated using fitted 4th order polynomial between 2000 and 2150 nm.	none	0.99 White :low abundance *Black is below the threshold*	1.115 Green :high abundance	Linear	Green-white	High
HyMap* ferric oxide abundance	hematite, goethite, “limonite”, ferrihydrite,	Normalised depth of the 900 nm absorption calculated using a fitted	*Composite mask**	0.04 Blue : low abundance	0.11 Red : high abundance	linear	rainbow	High. Calibrated/validated by other field/lab studies#. Errors introduced by mixing with green and dry

	schwertmannite, jarosite, Fe^{3+}-pyroxene , Fe^{3+}-olivine, Fe^{3+}-carbonate	2nd order polynomial between 776 and 1074 nm.		~10%Fe_2O_3 *Black is below the threshold*	~60%Fe_2O_3			vegetation, carbon black (e.g. soil carbon) and ferrous iron in silicates/carbonates. Mixing relationship between "*transopaque*" iron oxides and "transparent" silicates/carbonates is non-linear.
HyMap* ferrous iron abundance in silicates and carbonates	Fe^{2+}-chlorites, Fe^{2+}-amphibole (e.g. actinolite), Fe^{2+}-pyroxene , Fe^{2+}-olivine, Fe^{2+}-carbonate)	$(R_{920}+R_{1650})/(R_{1230}+R_{1035})$	Composite mask*	0.85 Blue : low abundance	1.03 Red : high abundance	linear	rainbow	Moderate. Broad ferrous absorption centred at ~1100nm can be influenced by ferrous iron in a range of silicates and carbonates. Including non-OH-bearing minerals like pyroxenes and garnets, as well as ferric iron. Errors also introduced by mixing with green and dry vegetation.
HyMap * opaque group	Metal-sulphides (e.g. pyrite), magnetite, Mn-oxides (e.g. pyrolusite), carbon black (e.g. ash)	$(R_{500}+R_{520})/(R_{1600}+R_{1750})$	Composite mask* + albedo @ 1650 nm <30%	0.3 Blue : low abundance *Black is below the threshold*	0.55 Red : high abundance	linear	rainbow	Low: Errors introduced by residual aerosol scattering effects in the VNIR as well as lack of Fe^{3+} absorption in the visible, e.g. iron oxide poor clays that in theory would be masked by the <30% albedo but may be in partial "shadow".
HyMap * white mica abundance	illite, muscovite, paragonite, brammallite, phengite, margarite	Normalised depth of a fitted 4th order polynomial between 2120 and 2245 nm.	Composite mask* + $(R_{2318}+R_{2295}+R_{2369})/(R_{2333}+R_{2350}+R_{2366})$ >1.025, + $(R_{2138}+R_{2190})/R_{2156}$ <1.98 *Product mnemonic = "2200D mica"*	0.005 Blue : low abundance ~10% Al-mica *Black is below the threshold*	0.1 Red : high abundance ~50% Al-mica	linear	rainbow	Moderate: Inherent errors related to the process of masking rather than umixing (mixed-interlayer clays), especially the use of the 2350 absorption depth where pixels with carbonate/trioctahedral silicate could be masked in as white mica.
HyMap * white mica composition	Sensitive to the Al-content of the white mica that ranges from paragonite/muscovite	Wavelength of absorption minimum calculated using the 1st derivative of a fitted 4th order polynomial between 2120 and 2245	Composite mask* + *2200D mica* >0.005	2180 nm Blue is Al-rich mica (muscovite, paragonite)	2215 Red is Al-poor mica (~phengite)	linear	rainbow	Moderate: Calibrated/validated by other field/lab studies# and in this study by XRD and EMprobe. Potential error introduced with accurate fitting of a 4th order

	(Al-rich) to phengite (Al-poor) and driven by coupled "Tschermak" substitution, namely: $[(Mg,Fe^{2+})_{oct}\ Si_{tet} \Leftrightarrow Al_{oct}\ Al_{tet}]$. Note that no paragonite was identified from these airborne/field data at Mount Isa.	nm.		*Black is below the threshold*				polynomial to continuous spectra that may contain isolated "noise".
HyMap * water abundance with white mica	The molecular water abundance for only those pixels that contain white mica.	$(R_{1790}+R_{2120})/(R_{1950}+R_{1970})$ = 1900D	Composite mask*, + *2200D mica* >0.005	1.2 Blue is low water abundance *Black is below the threshold*	1.5 Red is high water abundance	linear	rainbow	Moderate: Potential errors associated with residual errors in per-pixel correction of water vapour and possible influence of other absorbing materials at these wavelengths including F-bearing minerals, carbonates and chlorites.
HyMap * water abundance relative to white mica abundance	The molecular water abundance relative to white mica abundance which is broadly correlated with the mica crystallinity as measured using the XRD 001hkl peak width (this study).	*(2200D mica) / (1900D)*	Composite mask* + *2200D mica* >0.005	0.004 Blue is low crystallinity *Black is below the threshold*	0.09 Red is high crystallinity	linear	rainbow	Moderate: The link between this spectral parameter and illite crystallinity assumes that all the molecular water in a given pixel is associated with white mica.
HyMap * Al smectite abundance	Montmorillonite, beidellite.	Normalised depth of a fitted 4th order polynomial between 2120 and 2245 nm.	Composite mask* + $(R_{2318}+R_{2295}+R_{2369})/(R_{2333}+R_{2350}+R_{2366})$ <1.025, + $(R_{2138}+R_{2190})/R_{2156}$ <1.98 *Product mnemonic = "2200D Al-smectite"*	0.005 Blue is low abundance (~10%) *Black is below the threshold*	0.085 Red is high abundance (~40%)	linear	Rainbow	Low: Validation of the presence of Al-smectite in this study by XRD. Inherent errors related to the process of masking rather than umixing (problem with all current products). Biggest confusion with poorly ordered kaolin and illite/muscovite (mixed-interlayer clays). Threshold levels on all mask parameters could exclude/include other materials

								especially for "lower" levels.
HyMap * Al smectite composition	Possibly sensitive to the Al-content of the dioctahedral smectite that ranges from high Al/Si beidellite to low Al/Si montmorillonite,	Wavelength of the absorption minimum calculated using the 1st derivative of a fitted 4th order polynomial between 2120 and 2245 nm.	Composite mask* + *2200D Al smectite* >0.005	2180 nm Blue is beidellite? (Al-rich) *Black is below the threshold*	2215 Red is montmorillonite? (Al-poor)	linear	Rainbow	Low: No confirmation of either beidellite or montmorillonite in this study using XRD. Potential error introduced with accurate fitting of a 4th order polynomial to continuous spectra that may contain isolated "noise" as swell as issue of accurate masking of kaolin and white mica. XRD analysis in this study did not identify/discriminate beidellite from montmorillonite.
HyMap * kaolin abundance	Kaolin group minerals, especially kaolinite and halloysite to a much lesser extent dickite and nacrite.	Normalised depth of a fitted 4th order polynomial between 2120 and 2245 nm.	Composite mask* + $(R_{2318}+R_{2295}+R_{2369})/(R_{2333}+R_{2350}+R_{2366})$ <1.025, + $(R_{2138}+R_{2190})/R_{2156}$ >1.98 *Product mnemonic = "2200D kaolin"*	0.005 Blue is low abundance (~10%) *Black is below the threshold*	0.12 Red is high abundance (~50%)	linear	Rainbow	Moderate: Calibrated/validated by other field/lab studies#. Inherent errors related to the process of masking rather than umixing. Biggest confusion with mixing with white mica and smectite (mixed-interlayer clays). Threshold levels on all mask parameters could exclude/include other materials especially for "lower" levels.
HyMap * kaolin 2160 nm absorption depth	Related to the kaolin structural disorder and ranging from well-crystalline kaolinite to more disordered kaolinite/halloysite including kaolinite with dickite interlayers. Pyrophyllite (and alunite) if present will be mapped as being well ordered kaolinite.	$(R_{2138}+R_{2190})/R_{2156}$	Composite mask* + 2200D kaolin >0.005	1.98 Blue is poorly ordered *Black is below the threshold*	2.045 Blue is well ordered	linear	Rainbow	Low: Calibrated/validated by other field/lab studies#. Major problem of spectrally separating the 4 diagnostic kaolin absorptions in the 2200 nm region with HyMap spectral resolution. As a result, potential error caused by imperfect separation of the 2160 nm versus the 2200 nm features. Inherent errors also related to the process of masking rather than umixing (problem with all current products), especially for mixtures with pyrophyllite, white mica and smectite.
HyMap * MgOH	Maps both tri-	$(R_{2265}+R_{2349})/(R_{2316}+R_{2333})$	*Composite mask*	1.06	1.125	linear	rainbow	High: Mineral group information

abundance	octahedral silicates like chlorite, epidote, amphibole, talc, serpentine, biotite and phlogopite as well as carbonates like calcite, dolomite, siderite and ankerite.			Blue is low abundance *Black is below the threshold*	Red is high abundance			only. Major challenge in separating the many trioctahedral silicate minerals and carbonates that have their main SWIR absorptions in the 2300-2400 nm region. One difficulty was attempting to use the 2380 nm amphibole/talc absorption for masking as this product was very noisy unlike previous study at Kalgoorlie (Cudahy *et. al*, 2005). Useful for comparison with ASTER MgOH image products.
HyMap * MgOH composition	Sensitive to the composition of the tri-octahedral silicates and carbonates.	Wavelength of the absorption minium calculated using the 1st derivative of a fitted 4th order polynomial between 2220 and 2337 nm	Composite mask + *MgOH abundance* >1.06	2300nm Blue is (magnesite [not detected in these airborne/field data from Mount Isa], dolomite, Mg-chlorite, epidote, talc) *Black is below the threshold*	2325 nm Red is calcite, siderite, amphibole)	linear	rainbow	Low: Mineral interpretation of the image colours is difficult given the large range of minerals that can absorb at these 2300-2400 nm wavelengths, including white mica and kaolinite as well as other trioctahedral clay minerals like nontronite, sepiolite, and saponite. In carbonate rocks, the interpretation is relatively simple with blue being more Mg-rich and red more Ca-rich carbonate. For MgOH-bearing rocks, blue colours tend to be minerals like talc (nontronite), with amphibole and Mg-chlorite more green-yellow and red being Fe-chlorite and epidote.
HyMap * Ferric iron and MgOH	Fe^{3+}-siderite, Fe^{3+}-ankerite, Fe^{3+}-amphibole (ankerite), Fe^{3+}-chlorite, biotite.	Normalised depth of the 900 nm absorption calculated using a fitted 2nd order polynomial between 776 and 1074 nm.	Composite mask + *MgOH abundance* >1.06	0.02 Blue: low ferric iron abundance (typically iron oxide) associated with those pixels that have MgOH (+carbonate) mineralogy	0.1 Red: high ferric iron abundance (typically iron oxide) associated with those pixels that have MgOH (+ carbonate) mineralogy	linear	rainbow	Moderate. Errors introduced by mixing with green and dry vegetation, carbon black (e.g. soil carbon) and ferrous iron in silicates/carbonates. Mixing relationship between "*transopaque*" iron oxides and "transparent" silicates/carbonates is non-linear.

				Black is below the threshold				
HyMap * Ferrous iron and MgOH group	Fe^{2+}-siderite, Fe^{2+}-ankerite, Fe^{2+}-amphibole (ankerite), Fe^{2+}-chlorite, biotite.	$(R_{920}+R_{1650})/(R_{1230}+R_{1035})$	Composite mask* + *MgOH abundance* >1.06	0.85 Blue: low ferrous iron abundance (typically in silicates/carbonates) associated with those pixels that have MgOH (+carbonate) mineralogy. *Black is below the threshold*	1.085 Red: high ferrous iron abundance (typically in silicates/carbonates) associated with those pixels that have MgOH (+carbonate) mineralogy.	linear	Rainbow	Moderate. Broad absorption centred at ~1100nm can be influenced by ferrous iron in a range of silicates and carbonates. Including non-OH-bearing minerals like pyroxenes and garnets, as well as ferric iron. Errors also introduced by mixing with green and dry vegetation.
HyMap * amphibole-chlorite mineralogy	Chlorite and Fe-amphibole (actinolite/hornblende)	"*MgOH abundance*" divided by depth of 2260 nm absorption $\{(R_{2230}+R_{2228})/(R_{2247}+R_{2265})\}$	Composite mask* + *MgOH abundance* >1.060 + *ferrous iron* >1.0 + *epidote abundance* <0.9 + hand drawn mask of Cambrian limestones around Century (+ open pit operations)	0.96 (blue ~ chlorite) *Black is below the threshold*	1.05 (red ~ actinolite)	linear	Rainbow	Low: Following on from the description for MgOH composition above, this product attempts to separate amphibole from chlorite based on the relative heights of the 2300 and 2250 nm absorptions. Many complications including the effects of vegetation. Note that the 2380 nm absorption present for amphibole (and talc) was considered but the spectral/radiometric resolution of the HyMap data at these wavelengths yielded "noisy" data that could help confirm but not be used to accurately map. Also, there remains a major issue of accurately separating chlorite from carbonate such that a hand-drawn mask was implemented on some areas. Other potential solutions include: (1) using the published geology ass a mask; (2) parameterising the asymmetry of

								the 2300 nm absorption as carbonate is strongly left-asymmetric and amphibole and chlorite are right asymmetric; (3) hyperspectral thermal infrared imagery.
HyMap * epidote abundance .	epidote	$(R_{2230}+R_{2228})/(R_{2247}+R_{2265})$	Composite mask* + *MgOH composition* >2327 nm + $(R_{1500}+R_{1585})/(R_{1532}+R_{1545})$ >1.0	1.02 Blue is low abundance *Black is below the threshold*	1.12 Red is high abundance	linear	Rainbow	Low: This product is dependent on the presence of absorption at 1550 nm which was very poorly expressed in the HyMap pixel spectra and the related image product had major residual instrument/atmospheric effects. Confusion with chlorite-amphibole.
HyMap * hydrated silica	Opal and chalcedony	Normalised depth of the broad 2250 nm Si-OH absorption calculated using a fitted 4th order polynomial between 2140 and 2365 nm.	Composite mask* + *1900D* >1.4 + *MgOH abundance* <1.035	0.075 Blue is low abundance *Black is below the threshold*	0.15 Red is high abundance	Linear	rainbow	Moderate. Confirmation in this by XRD. Possible complications related to MgOH and carbonate absorption which have been masked (in part) though could still affect this product at low abundance levels especially as carbonate also has strong absorption in the 1900 nm region.

$\boldsymbol{R_{XX}}$ where R is the reflectance and XX is the wavelength of that spectral band.

oct is mica octahedral layer
tet is mica tetrahedral layer

* Composite mask comprises:
(1) green vegetation ***out*** : NDVI Merton >0.25;
(2) dry vegetation ***out*** : 2080D >1.015;
(3) low albedo (shadows, water) ***out*** : reflectance @ 1650 nm <1000 DN (10% reflectance).

Cudahy, T.J., Caccetta, M., Cornelius, A., Hewson, R.D., Wells, M., Skwarnecki, M. Halley, S. Hausknecht, P. , Mason, P., and Quigley, M.A., 2005. Regolith geology and alteration mineral maps from new generation airborne and satellite remote sensing technologies; and Explanatory Notes for the Kalgoorlie-Kanowna 1:100,000 scale map sheet, remote sensing mineral maps. MERIWA Report No. 252, 1-114

HyMap Mineral Mapping Products – Stage 2 (9 December 2008)

Product name	Measures	Base algorithm	Filters	Lower stretch limit	Upper stretch limit	Stretch type @ Colour chart	Accuracy	Seamless within-blocks/ between-blocks/ between-surveys
** albedo		Reflectance @1650nm Multiplicative cross track-corrected, 2nd order polynomial for (See Table 3 for details)	none	1% lower clip	1% upper clip	Linear Grey-scale	High. Some between-block mis-calibrations caused by use of column/scene dependent statistics necessary for the cross track (BRDF) corrections.	Yes/No/No
** true colour		Reflectance bands: R: 650nm G:550nm B:450nm Multiplicative cross track-corrected, 2nd order polynomial for (See Table 3 for details)	none	Scene-dependent 1% clips for all three bands	Scene-dependent 1% clips for all three bands	linear	High. Some between-block mis-calibrations caused by use of column/scene dependent statistics necessary for the cross track (BRDF) corrections.	Yes/No/No
** false colour		Reflectance bands: Red: 750nm Green:650nm Blue:550nm Multiplicative cross track-corrected, 2nd order polynomial (See Table 3 for details).	none	Scene-dependent 1% clips for all three bands	Scene-dependent 1% clips for all three bands	Linear	High. Some between-block mis-calibrations caused by use of column/scene dependent statistics necessary for the cross track (BRDF) corrections.	Yes/No/No
** water vapour	Atmospheric water content (precipitable water)	Generated from HYCORR radiative transfer package using the continuum band depth of the 940 nm water vapour absorption.	none	0 (gm/cm^2) "dry" atmosphere	3 (gm/cm^2) "wet" atmosphere	Linear Rainbow	Moderate. Assumes spectrally flat and bright "background" surface materials in the NIR. Potential complications with overlapping surface (e.g. leaf and soil/rock) water absorption.	No/Yes/Yes
** green vegetation	Chlorophyll absorbing (680 nm) vegetation	$[(R_{865}-R_{694})/(R_{865}+R_{694})]$ Base level product called: ***NDVI_Merton***	none	0.15 low content	0.6 high content	Linear Rainbow	Moderate. Complications with: (1) the accuracy of the aerosol correction; (2) lichen effects; (3) BRDF cross-track	Most/Most/yes

				Black is below the threshold			effects especially multiple scattering associated with "layered" vegetation canopies; (4) water vapour residuals.	
**** dry vegetation**	Cellulose content	Normalised continuum – removed depth of the cellulose 2080 nm absorption calculated using: $[(R_{2006}+R_{2153})/(R_{2081}+R_{2100})]$ ***2080RATIO***	none	0.907 low content *Black is below the threshold*	1.006 high content	Linear Rainbow	Moderate: complications related to residual atmospheric correction especially water vapour and CO_2 as well as overlapping clay absorption in the 2200 nm and BRDF cross-track effects, especially "layered" vegetation canopies.	Most/Most/No
**** leaf water**	Leaf water content	$(R_{1958}-R_{1245})/(R_{1203}+R_{1217})$ ***Leaf water***	none	0.95	1.045	Linear Rainbow	Moderate: complicated by water vapour residual errors and surface water.	Yes/Yes/No
**** surface water content**	Molecular water in minerals, especially smectites and to a lesser degree illites and halloysite, as well free water that may be either "wet" ground after rainfall, or trapped in for example, quartz fluids inclusions.	Normalised depth of the water 1900 nm absorption calculated using: $[(R_{1785}+R_{2118})/(R_{1950}+R_{1968})]$ ***1900D***	*Composite mask**	1.1 Low water content	1.5 High water content	Linear Rainbow	Low: complications related to residual atmospheric correction especially water vapour and CO_2 as well as molecular water present in vegetation. Strongly affected by water vapour and water vapour residuals.	Some/Yes/No
**** surface water bonding**	bound water associated with smectites, illites: unbound water associated with fluid inclusions in vein quartz	$[(0.661*R_{1419}+0.339*R_{1504})/(R_{1448})]$ ***SW***	*Composite mask** 1900D > 1.1	0.75 Bound water such as in smectitic clay	0.95 Unbound water such as in "recently wet soils or fluid inclusions in quartz.	Linear Rainbow 3by3 median filter	Low: Complicated by "uncorrected" water vapour residuals, leaf water and "wet" soils following recent rainfall.	Some/Yes/No
**** ferric oxide content**	hematite, goethite, jarosite, "limonite"	Normalised depth of the 900 nm absorption	*Composite mask**	0.024 Blue : low	0.092 Red : high	Linear	Moderate. Complicated by (1) water vapour residuals; (2) mixing with green	Most/Yes/No

		calculated using a fitted 2nd order polynomial between 776 and 1074 nm ***900D***		content ~10%Fe_2O_3 *Black is below the threshold*	content ~60%Fe_2O_3	Rainbow	and dry vegetation, carbon black (e.g. soil carbon); and (3) ferrous iron in silicates/carbonates.	
**** hematite-goethite**	Hematite-goethite ratio (Cudahy and Ramanaidou, 1997)	Wavelength of 900 nm absorption minimum calculated using the 1st derivative of a fitted 2nd order polynomial between 776-1074 nm. ***900W***	Composite mask* 900D >0.024	895 nm blue=hematite	1000 nm red=goethite	Linear rainbow	Low: Complicated by cross track and along-track flight-line effects caused by (1) water vapour residuals, (2) instrument wavelength shifts; (3) and surface scattering (BRDF) effects. Wavelength accuracy of the iron oxide crystal field absorption is adversely affected by mixing with green and dry vegetation as well as ferrous-bearing carbonate and silicate minerals.	Some/Some/No
**** ferrous iron content**	Fe^{2+} in silicates & carbonates (Fe-chlorites, Fe-amphibole, Fe-pyroxene, Fe-olivine, Fe-carbonate)	$(R_{821}+R_{1650})/(R_{1028}+R_{1231})$ ***Ferrous***	Composite mask*	0.875 Blue : low content (e.g. kaolinite, quartz)	1.1 Red : high content (e.g. actinolite, ankerite)	Linear rainbow	Moderate. Broad absorption centred at ~1100nm can be influenced by ferrous iron in a range of silicates and carbonates. Including non-OH-bearing minerals like pyroxenes and garnets, as well as ferric iron. Errors also introduced by mixing with green and dry vegetation.	Most/yes/No
**** opaques 1**	"Reduced" materials such as carbon black, sulphides and magnetite as well as Mn oxides. Note sulphides and magnetite are expected to easily oxidise in the regolith to other minerals.	$(R_{458})/(R_{1650})$ *OPAQUES_450D1650*	Composite mask* + albedo @ 1650 nm <30%	0.25 Blue : low content *Black is below the threshold*	0.5 Red : high content	Linear rainbow	Moderate: Errors introduced by residual aerosol scattering effects in the VNIR as well as lack of Fe^{3+} absorption in the visible, e.g. iron oxide poor clays that in theory would be masked by the <30% albedo but may be in partial "shadow".	Yes/yes/some
**** opaques 2**	"Reduced" materials such as carbon black, sulphides and	albedo @ 1650 nm	Composite mask* + $(R_{450})/(R_{1650})$ >0.25	1000 Red: low content	3000 Blue : high content	Linear Reverse rainbow	Low: Most error is caused by topographic shading with shaded areas producing higher values.	Yes/yes/some

	magnetite as well as Mn oxides.		albedo @1650 nm <30%	*Black is below the threshold*				
** **unmixed clay content**	Total Al-clay content after the removal of green and dry vegetation to generate abundances as if there was no vegetation at all. Clays include kaolin, white mica and Al-smectite.	2200D + linear transformation based on mixing modelled projections between clay/non-clay and (1) NDVI; and (2) 2080D.	No mask	0.01 Low clay content	0.2 High clay content	Linear rainbow	Moderate: Model assumes linear mixing at the "meso" or pixel-scale (centimetres to metres). See Rodger and Cudahy (2009) for details of the method. Potential errors introduced by the accuracy and independence of the parameters used to measure the green and dry vegetation and apparent clay abundance from the image-pixel data. Both of these vegetation parameters can suffer from flight-line cross-track effects.	Most/yes/no
** **mica content**	Abundance of white mica minerals including illite, muscovite, paragonite, brammalite, phengite, lepidolite, margarite.	Normalised depth of a fitted 4th order polynomial between 2120 and 2245 nm. ***2200D***	Composite mask* + $(R_{2326}+R_{2376})/(R_{2343}+R_{2359})$ **2350De** >1.035 + $(R_{2136}+R_{2188})/(R_{2153}+R_{2171})$ **2160D2190** <1.005 Mask called **2200D_mica**	0.005 Blue : low content ~10% Al-mica *Black is below the threshold*	0.15 Red : high content ~66% Al-mica	Linear rainbow	Moderate: Inherent errors related to the process of masking rather than unmixing. That is, the threshold levels on mask parameters could exclude/include other materials especially for "lower" levels. Errors also introduced by change in HyMap bandpasses centres for different surveys (see report for details).	Yes/yes/no
** **mica composition**	Tschermak substitution of white mica which ranges from paragonite, brammalite, to illite, muscovite to phengite.	Wavelength of absorption minimum calculated using the 1st derivative of a fitted 4th order polynomial between 2120 and 2245 nm. ***2200W***	Composite mask* + **2200D_mica** >0.005	2180 nm Blue is Al-rich mica (muscovite, illite, paragonite, brammalite, lepidolite) *Black is below the threshold*	2215 Red is Al-poor mica (~phengite)	Linear rainbow	High: Potential error introduced with accurate fitting of a 4th order polynomial to continuous spectra that may contain isolated "noise". Errors also introduced by change in HyMap band-passes centres for different surveys (see report for details).	Yes/yes/no
** **mica crystallinity** index	*Illite-muscovite. Can potentially be used as (1) degree*	Relative depth of the clay and water absorptions but masked for white mica.	Composite mask* + **2200D_mica**	0.004 Blue is "wet" illitic	0.13 Red is "dry" muscovite	Linear rainbow	Low: Assumption is that all the molecular water in a given pixel is associated with white mica.	Most/yes/no

	of weathering with illite more weathered and muscovite from fresh; and (2) as a geobarometer with illite = lower temperature (P) and "dry" muscovite = higher temperature (P).	***[(2200D_mica)/(1900D)]***	>0.005	composition (low crystallinity) *Black is below the threshold*	composition (high crystallinity)		Complications can thus arise with wet ground or water in other materials (e.g. vegetation). Note that this spectral parameter is not expected to be valid as a measure of crystallinity for muscovite, which does not contain molecular water. Instead, crystallinity in muscovite and other water poor white mica is driven by other factors, including level of Tschermak substitution.	
**** Al smectite content**	Montmorillonite and beidellite.	Normalised depth of a fitted 4th order polynomial between 2120 and 2245 nm. ***2200D***	Composite mask* + $(R_{2326}+R_{2376})/(R_{2343}+R_{2359})$ **2350De** <1.025 + $(R_{2136}+R_{2188})/(R_{2153}+R_{2171})$ **2160D2190** <1.005 Mask called **2200D_smectite**	0.005 Blue is low content (~10%) *Black is below the threshold*	0.085 Red is high content (~40%)	Linear Rainbow	Moderate: Inherent errors related to the process of masking rather than unmixing (problem with all current products). Biggest confusion with poorly ordered kaolin. Threshold levels on all mask parameters could exclude/include other materials especially for "lower abundances.	Yes/yes/no
**** Al smectite composition**	Montmorillonite has longer wavelength 2200 nm absorption compared with beidellite and can undergo Tschermak substitution.	Wavelength of the absorption minimum calculated using the 1st derivative of a fitted 4th order polynomial between 2120 and 2245 nm. ***2200W***	Composite mask* + ***2200D Al smectite*** >0.005	2180 nm Blue is Al-rich dioctahedral smectite, e.g. beidellite *Black is below the threshold*	2215 Red is Al-poor dioctahedral smectite, including montmorillonite	Linear Rainbow	Moderate: Potential error introduced with accurate fitting of a 4th order polynomial to continuous spectra that may contain isolated "noise" as swell as issue of accurate masking of kaolin and white mica. Depending on the relative depths of the 2350 and 2200 nm absorption, some white micas could be misclassified as Al-smectite and vice versa. Also, some short wavelength smectite could be misclassified as kaolin.	Yes/yes/no
**** kaolin content**	Abundance of kaolin group minerals, namely	Normalised depth of a fitted 4th order polynomial between 2120 and 2245	Composite mask* + $(R_{2136}+R_{2188})/$	0.005 Blue is low content	0.12 Red is high content	Linear Rainbow	Moderate: Inherent errors related to the process of masking rather than unmixing (problem with all current	Yes/yes/no

	kaolinite halloysite, dickite and nacrite	nm. ***2200D***	(R_{2153} -R_{2171}) **2160D2190** >1.005 Mask called **2200D_kaolin**	(~10%) *Black is below the threshold*	(~50%)		products). Biggest confusion is due to mixing with white mica and smectite. Threshold levels on all mask parameters could exclude/include other materials especially for "lower" levels.	
** **kaolin composition** index	Composition and crystallinity of kaolin group minerals ranging from well-ordered kaolinite to halloysite to dickite (and nacrite).	$\frac{[(R_{2138}+R_{2173})/(R_{2156})}{[(R_{2155}+R_{2190})/R_{2173}]}$ ***KC***	Composite mask* + **2200D_kaolin** >0.005	0.93 Deep blue is dickite Blue-green is halloysite and/or poorly ordered kaolinite	1.01 Red is well ordered kaolinite *Black is below the threshold*	Linear Rainbow	Moderate: Main problem is spectrally separating the 4 diagnostic kaolin absorptions in the 2200 nm region with HyMap spectral resolution. As a result, potential error caused by imperfect separation of the 2160 nm versus the 2200 nm features and calculation of the relative height of these used for the crystallinity measurement. Inherent errors also related to the process of masking rather than unmixing (problem with all current products), especially for mixtures with white mica and smectite.	Yes/yes/no
** **MgOH content**	Abundances of both carbonates (e.g. calcite, dolomite, magnesite, ankerite, siderite) and tricotahedral silicates (e.g. chlorite, epidote, amphibole, talc, serpentine). Trioctahedral clay minerals like nontronite, sepiolite, and saponite.	$\frac{(R_{2265}+R_{2348})}{(R_{2316}+R_{2333})}$ ***2330D***	*Composite mask* + Mask called **MgOH_content**	1.06 Blue is low content *Black is below the threshold*	1.085 Red is high content	Linear rainbow	Moderate: Mineral group information only. Complicated by absorption in the 2300 region by dry/green vegetation. Useful for comparison with ASTER MgOH image products.	Yes/yes/no
** **MgOH composition**	Broad change in composition of the MgOH group from,	Wavelength of the absorption minimum calculated using the 1st	Composite mask + **MgOH_content**	2300nm Blue is magnesite,	2325 nm Red is epidote,	Linear rainbow	Moderate: Mineral interpretation of the image colours is difficult given the large range of minerals that can	Yes/yes/no

	amphibole, talc and magnesite to dolomite, chlorite and epidote to serpentine and calcite.	derivative of a fitted 4th order polynomial between 2220 and 2337 nm. **2330W**[#]	>1.06	talc, amphibole Green is dolomite *Black is below the threshold*	chlorite, calcite and siderite		absorb at these 2300-2400 nm wavelengths, including Al-clays like white mica and kaolinite. In carbonate rocks, the interpretation is relatively simple with blue being more Mg-rich and red more Ca-rich carbonate. For MgOH-bearing rocks, blue colours tend to be minerals like talc (nontronite), with amphibole and Mg-chlorite as green-yellow and red being Fe-chlorite and epidote.	
**** Ferric iron and MgOH**	Fe^{3+}-bearing MgOH minerals as in some chlorites as well as weathering of Fe^{2+} MgOH minerals.	Normalised depth of the 900 nm absorption calculated using a fitted 2nd order polynomial between 776 and 1074 nm. ***900D***[#]	Composite mask + **MgOH_content** >1.06	0.024 Blue: low ferric iron content *Black is below the threshold*	0.092 Red: high ferric iron content	Linear rainbow	Moderate. Assumes that all of the ferric oxide is contained in MgOH minerals. Errors introduced by water vapour residuals and mixing with green and dry vegetation, carbon black (e.g. soil carbon) and ferrous iron in silicates/carbonates. .	most/yes/no
**** Ferrous iron and MgOH**	Fe^{2+}-bearing MgOH minerals like actinolite, some chlorites, ankerite and siderite.	$(R_{820}+R_{1650})/(R_{1230}+R_{1035})$ ***Ferrous***[#]	Composite mask* + **MgOH_content** >1.06	0.875 Blue: low ferrous iron content (typically in silicates/carbonates) associated with those pixels that have MgOH (+carbonate) mineralogy. *Black is below the threshold*	1.1 Red: high ferrous iron content (typically in silicates/carbonates) associated with those pixels that have MgOH (+carbonate) mineralogy.	Linear Rainbow	Moderate. Broad absorption centred at ~1100nm can be influenced by ferrous iron in a range of silicates and carbonates. Including non-OH-bearing minerals like pyroxenes and garnets, as well as ferric iron. Errors also introduced by mixing with green and dry vegetation.	Yes/yes/no
**** chlorite-epidote content** .	Chlorite, epidote	$(R_{2224}+R_{2276})/(R_{2241}+R_{2258})$ **2260D**[#]	Composite mask* + **MgOH_content** >1.06	1.002 Blue is low content *Black is below*	1.03 Red is high content	Linear Rainbow	Low: Dependent on tracking the depth of a small absorption that is on the shoulders of potentially pronounced deep absorption in the 2200 and 2300 nm regions, the latter of which can	Yes/yes/no

			Mask called **chlorite-epidote content**	*the threshold*			also be related to both green and dry vegetation. Possible complications with the left asymmetry of the carbonate absorption, especially dolomite.	
** **epidote content**	epidote	$(R_{1518}+R_{1572})/(R_{1532}+R_{1545})$ **1550D#**	Composite mask* + **MgOH_content** >1.06 + **chlorite-epidote content** >1.002 3by 3 median filtered	1% lower clip Blue is low content *Black is below the threshold*	1% upper clip Red is high content	Linear Rainbow	Low: This product is dependent on the development of the1550 nm absorption which is on the shoulder of the water absorption at 1400 nm and so prone to water vapour residual and other water effects.	some/some/no
** **hydrated silica**	Opal, cristobalite	Normalised depth of the broad 2250 nm Si-OH absorption calculated using a fitted 4th order polynomial between 2118 and 2310 nm BUT omitting bands between 2136 to 2224 nm. **2250DPOLY#**	Composite mask* + *1900D* >1.2, **MgOH content** <1.035	0.075 Blue is low content *Black is below the threshold*	0.15 Red is high content	Linear rainbow	Low. Possible complications related to strong overlapping AlOH and/or MgOH absorption/s.	Some/some/no

** HyMap Block name and number

All names in **bold** are C-HyperMap base level products. Some of these products may have been levelled for either flight-line cross-track effects (BRDF) or between flight-line effects.

* Composite mask comprises:

- A) Mt Isa Blocks green vegetation ***out*** : NDVI Merton >0.3 B) Georgetown, Hodgkinson and Pajingo green vegetation out : Leaf_Water > 1.03
- dry vegetation ***out*** : 2080D >0.93;
- low albedo (shadows, water) ***out*** : reflectance @ 1650 nm <1000 DN (10% reflectance)

The HyMap radiance-at-sensor data were corrected to apparent ground reflectance using HyCORR, which is radiative transfer program based on ATREM/6S. CSIRO's *C-HyperMAP* software was used for geoscience information extraction and the generation of image mosaics.

APPENDIX 8

ASTER Geoscience Products (27 November 2007)

Product (geoTIFFs)	**base algorithm** B=band No. = ASTER band No.	**filters**	**stretch lower limit**	**stretch upper limit**	**stretch type**	**colour chart**	**accuracy**
ASTER False colour	Red: B_3 Green: B_2 Blue: B_1	none	R: 1373 DN G: 667 DN B: 383 DN	R: 3007 DN G: 2123 DN B: 1329 DN	linear	Gray-scale	Moderate. Some potential residual mis-calibration errors between scenes.
ASTER Green vegetation Content	B_3/B_2	*Composite mask*”*	1.5 Blue is low content *Black is below the threshold*	2.75 Red is high content	linear	Rainbow	Moderate: Complicated by residual atmospheric aerosols effects and iron oxides. Note also the strong seasonal affects to the type (green versus dry) and abundance of vegetation cover which can not be easily unmixed at this stage, especially given the relatively low spectral resolution of ASTER, which does not comprise any suitable bands for measuring dry vegetation content (e.g. cellulose at 2080 nm).
CSIRO Regolith ratios	R: B_3/B_2 G: B_3/B_7 B: B_5/B_7	*Composite mask*”*	R: 0.5 G: 0.5 B: 0.5 Red : iron oxides Green : ferrous iron (inverse); i.e. non-mafic rocks Blue : clays	R: 4 G: 3 B: 2.2	equalisation	Gray-scale	Moderate: Complicated by mixing with vegetation as well as any residual additive effects (e.g. aerosol scattering in the VNIR) and ASTER instrument crosstalk effects in the SWIR bands).
ASTER Ferric oxide content (hematite, goethite)	B_4/B_3 (3by3 median filtered)	*Composite mask*”*	1.1 Blue is low abundance *Black is below the threshold*	1.75 Red is high abundance	linear	Rainbow	Low: Complicated by dry vegetation (mixing effect) and lack of suitable bands positioned in the VNIR to capture diagnostic ferric oxide spectral signatures
ASTER Ferrous iron content	B_5/B_4 (3by3 median filtered)	*Composite mask*”*	0.75 Blue is low	1.05 Red is high	linear	rainbow	Moderate: Complicated by fire scars (carbon black in ash) and dry plant material (lack of).

in silicates/carbonates			abundance *Black is below the threshold*	abundance			
ASTER Opaques (sulphides, carbon black, magnetite, Mn oxides)	B_1/B_4	*Composite mask** + B_4 <2500 + hand drawn mask for aerosols.	0.445 (low content) *Black is below the threshold*	0.695 (high content)	linear	rainbow	Low: Complicated by mixtures with vegetation and dependent on the albedo of mineral mixtures endmembers and residual errors associated with: (1) masking out cloud shadows and other dark non-geologic pixels, (2) accurate correction for aerosol scattering, and (3) oxide poor bright targets that in theory would be masked by the <25% albedo but may be in partial "shadow". .
ASTER AlOH group content (illite, muscovite, Al-smectite, kaolinite)	$(B_5+B_7)/B_6$	*Composite mask**	2.06 Blue is low content *Black is below the threshold*	2.4 Red is high content	linear	rainbow	Moderate: Complicated by mixing with green/dry plant materials.
ASTER AlOH group composition (phengite red to paragonite/kaolinite blue)	B_5/B_7	*Composite mask** + $(B_5+B_7)/B_6$>2.06	1 Blue is kaolinite/paragonite *Black is below the threshold*	2 Red is phengite	equalisation	rainbow	Low: Phengite information compromised by minerals such as chlorite and carbonate while paragonite/kaolinite comprised by mixtures with pyrophyllite and alunite and some types of dry plant material.
ASTER Advanced Argillic (pyrophyllite, alunite and kaolinite)	B_6/B_5	*Composite mask**	1 Blue is low content *Black is below the threshold*	1.1 Red is high content	linear	rainbow	Low: Complicated by dry plant material (cellulose) and ALOH-poor areas dominated by "mafic"minerals.
ASTER Fe-OH group content (chlorite, epidote, jarosite, nontronite.	$(B_6+B_8)/B_7$	*Composite mask** + aerosols ROI	2 Blue is low content *Black is below the threshold*	2.15 Red is high content	linear	rainbow	Low: Complicated by carbonate (dolomite), vegetation, gibbsite, opal/chalcedony
ASTER MgOH group content (calcite, dolomite, magnesite, chlorite,	$(B_6+B_9)/(B_7+B_8)$	*Composite mask**	1.05 Blue is low content *Black is below the*	1.125 Red is high content	linear	rainbow	Low: Complicated by absorption related to dry vegetation (reddens) white mica as well as residual inaccuracies in instrument "crosstalk" correction, especially for Band 9.

epidote, amphibole, talc, serpentine)			*threshold*				
ASTER MgOH group composition (calcite, dolomite, talc, amphibole, epidote, chlorite)	B_7/B_8	*Composite mask** + *MgOH content* >1.05	0.9 Blue is dolomite, chlorite *Black is below the threshold*	1.3 Red is calcite, epidote	equalisation	rainbow	Low: Complicated by dry vegetation (more dry vegetation produces redder tones) and any contribution form MgOH minerals like talc, amphibole, serpentine, magnesite and tricoctahedral clays as well as any residual inaccuracies in instrument "crosstalk" correction, especially for Band 9.
ASTER ferrous iron content in MgOH_carbonate. (Fe-chlorite, actinolite, siderite, ankerite)	B5/B4 (3by3 median filtered)	*Composite mask** + MgOH content >1.05	0.5 Blue is low ferrous iron content in carbonate and MgOH minerals like chlorite and amphibole. *Black is below the threshold*	1.0 Red is high ferrous iron content in carbonate and MgOH minerals like chlorite and amphibole.	equalisation	rainbow	Low: Complicated by vegetation and any inaccuracies in the MgOH content mask product (see above).
ASTER ferric iron content in MgOH_carbonate. (siderite, Fe-chlorite, actinolite)	B4/B3 (3by3 median filtered)	*Composite mask** + MgOH content >1.05	0.0 Blue is low ferric iron content (e.g. iron oxide) in carbonate and MgOH minerals like chlorite and amphibole. *Black is below the threshold*	2.5 Red is high ferric iron content in carbonate and MgOH minerals like chlorite and amphibole.	equalisation	rainbow	Low: Complicated by vegetation and any inaccuracies in the MgOH content mask product (see above).

* Composite mask comprises:

(1) green vegetation **out** : ratio of bands 3/2 <2.000;
(2) cloud tops **out**; ASTER band 1reflectance <2500 (25% reflectance); and
(3) low albedo (shadows, water) ***out***: reflectance Band 4 <1200 DN (12% reflectance).

Note that strong scan-angle dependent aerosol effects were observed in small number of scenes, especially in the northern part of the ASTER mosaic. This affects the VNIR bands only.

The L1B ASTER data in hdf format were provided by Geoscience Australia. These had been corrected for SWIR crosstalk as part of ERSDAC's (Japan) standard L1B processing. CSIRO's *C-SatMAP* software was used to process all the ASTER scenes (~130 over the Mount Isa Block). The functionality of this IDL/ENVI-based *C-SatMAP* software includes:

- Extraction of ancillary metadata from the ASTER *hdf* files including date, pass, look angle etc;
- Cross calibration of all scenes using a kernel/statistical approach (band/pixel weighted offsets);
- Absolute calibration of all ASTER scenes to reflectance, given availability of appropriate ground/airborne calibration;
- Generation of 1st pass geoscience products (no masking or threshold) (e.g. continuum-ratio of $(B_5+B_7)/B_6$); and
- Generation of final geoscience products based on multiple 1st pass geoscience products and/or masks and/or thresholds. That is, large areas are expected to "black" if there is no development of that mineral (group).

APPENDIX 9

Log of cross-track correction of flight-lines (C) and levelling between blocks (L) for Stage 2 HyMap processing

	Mt Isa Block A	Mt Isa Block B	Mt Isa Block C	Mt IsaBlock D	Mt Isa Block E	Mt Isa Block F	Mt Isa Block G	Mt Isa Block H	Georgetown Block A	Georgetown Block B	Georgetown Block C	Georgetown Block D	Georgetown Block E	Georgetown Block F	Georgetown Block G	Georgetown Block H	Pajingo Block A	Pajingo Block B	Hodgkinson A	Hodgkinson B
900D				L															C/L	C/L
900W																				
1550D		C/L	C/L	C/L	C/L	C/L	C/L	C/L	C/L	C/L	C/L	C/L	C/L	C/L	C/L	C/L	C/L	C/L	C/L	C/L
1650D	C/L	C/L	C/L	C/L	C/L	C/L	C/L	C/L	C/L	C/L	C/L	C/L	C/L	C/L	C/L	C/L	C/L	C/L	C/L	C/L
1900D		C/L	C/L	C/L	C/L	C/L	C/L	C/L	C/L	C/L	C/L	C/L	C/L	C/L	C/L	C/L	C/L	C/L	C/L	C/L
2080DRATIO		C/L	C/L	C/L	C/L	C/L	C/L	C/L	C/L	C/L	C/L	C/L	C/L	C/L	C/L	C/L	C/L	C/L	C/L	C/L
2160D2190																				
2200D													C/L		C/L					C/L
2200W				L									C/L		C/L					
2250DPOLY				L					C/L		L		C/L		C/L					C/L
2260D																				
2330D				L	L				C/L		L		C/L		C/L				C/L	C/L
2330W				C/L									C/L			L	L	L	C/L	C/L
2350De				L					L											
AMPHIBOLE_CHLORITE									C/L				C/L						C/L	C/L
FERROUS																			L	
KC				L															L	
MICA_CRYSTALLINITY															C/L				C/L	
NDVI_MERTON	C	C/L	C/L	C/L	C/L	C/L	C/L	C/L	C/L	C/L	C/L	C/L	C/L	C/L	C/L	C/L	C/L	C/L	C/L	C/L
OPAQUES_450D1650															C/L					
SW				L															L	L
TRUE_COLOUR	C/L	C/L	C/L	C/L	C/L	C/L	C/L	C/L	C/L	C/L	C/L	C/L	C/L	C/L		C/L	C/L	C/L	C/L	C/L
FALSE_COLOUR	C/L	C/L	C/L	C/L	C/L	C/L	C/L	C/L	C/L	C/L	CL	C/L	C/L	C/L		C/L	C/L	C/L	C/L	C/L
LEAF_WATER																				